

**KU LEUVEN**



UNIVERSITÀ DEGLI STUDI DI NAPOLI  
**FEDERICO II**

**KU LEUVEN  
ARENBERG DOCTORAL SCHOOL**  
Faculty of Engineering Science

**UNIVERSITY OF NAPLES  
"FEDERICO II"**  
Faculty of Engineering

# Operational Modal Analysis for rotating machines

## challenges and solutions

**Emilio Di Lorenzo**

Supervisors:

Prof. dr. ir. W. Desmet

Prof. dr. ir. F. Marulo

Prof. dr. ir. B. Peeters

Dissertation presented in partial fulfillment of the requirements for the degree of:

- Doctor of Engineering Science(PhD): Mechanical Engineering (KU Leuven)
- Doctor of Aerospace, Naval and Quality Engineering (University of Naples "Federico II")

April 2017



# **Operational Modal Analysis for rotating machines**

challenges and solutions

**Emilio DI LORENZO**

Examination committee:

Prof. dr. ir. H. Heynen, chair  
Prof. dr. ir. W. Desmet, supervisor  
Prof. dr. ir. F. Marulo, supervisor  
Prof. dr. ir. B. Peeters, supervisor  
Prof. dr. ir. P. Guillaume  
Prof. dr. ir. S. De Rosa  
Prof. dr. ir. G. Lombaert

Dissertation presented in partial fulfillment of the requirements for the degree of:

- Doctor of Engineering Science(PhD): Mechanical Engineering (KU Leuven)
- Doctor of Aerospace, Naval and Quality Engineering (University of Naples "Federico II")

April 2017

© 2017 KU Leuven – Faculty of Engineering Science  
Uitgegeven in eigen beheer, Emilio Di Lorenzo, Celestijnenlaan 200A box 2402, B-3001 Leuven (Belgium)

Alle rechten voorbehouden. Niets uit deze uitgave mag worden vermenigvuldigd en/of openbaar gemaakt worden door middel van druk, fotokopie, microfilm, elektronisch of op welke andere wijze ook zonder voorafgaande schriftelijke toestemming van de uitgever.

All rights reserved. No part of the publication may be reproduced in any form by print, photoprint, microfilm, electronic or any other means without written permission from the publisher.

# Acknowledgements

Trying to describe the past years in few words is definitely a challenging task. When you see approaching the end, then all the past moments come to your mind and there is a bit of confusion. At this point it is time to thank all the people who crossed my steps and helped me to grow up day by day during this adventure.

Actually, making one step back in the past I need to say THANKS (with capital letters) to my University and Life Promotor, Prof. Francesco Marulo. It is thank to you that I had the great opportunity to spend the first 6 months in LMS at the time of my final thesis. Thanks to that I had then the chance to start the PhD and you were again there supporting all ideas. I will never forget the infinite support and help that I received from you during the past years. You always believed in me and I always trusted you. I must say that when people across these years asked me an opinion about you, I simply replied: "He is like a second father".

Within LMS/Siemens I met many people, but of course the most important ones, from whom I learned as much as I could, are Dr. Bart Peeters and Simone Manzato. You both always believed in me and gave me all the help that I needed on a daily basis. If you were not there I don't know if I could have made it. It has been fantastic to share all these experiences with you. I am looking forward to continue being part of your team and enjoying working with you.

On the other side the support of Prof. Wim Desmet has been very important across these years. Your valuable suggestions and opinions have been fundamental to reach the final status of the work. It has been a pleasure to be part of your huge group of PhD students.

A special thank goes also to the Master students from Naples who helped me a lot with several topics that have been discussed in this dissertation: Umberto Musella, Giancarlo Kosova and Antonio Cutolo. Your precious work needs to be acknowledged and you know that I am very grateful to you. It was a nice experience from my side and I hope that you also enjoyed the time spent on your thesis.

Now let's move to the less academical part of the acknowledgments. Well, it is difficult to thank everyone and there are so many important people who crossed my path that it is impossible to remember all of them. On the other hand it would be a pity to just remember some of them. I will give a try and I hope that I will not make people unhappy.

*Ovviamente, e non potrebbe essere il contrario, ringrazio infinitamente i miei maestri di vita, le persone che più di ogni altra hanno creduto in me e mi hanno seguito costantemente nel percorso di una vita. 30 anni sono passati velocemente, ma non ricordo un giorno in cui non vi ho avuti accanto. Anche se da diversi anni oramai viviamo a qualche chilometro di distanza, io sono sempre la persona più felice del mondo quando sono con voi. Mamma, papà, GRAZIE MILLE!*

...and of course a fundamental role in my life was played by my two brothers Vincenzo and Matteo. Vincenzo, I can say that you are my best friend before being my brother. We shared a room for many many years and we keep sharing our experiences day by day even from far away. I am pretty sure that it will be like this in the future too. You keep making me laugh even in bad days. Matteo, you played very well the role of the youngest brother. You came to the world when we were already old and it is impressive to see how in the last 16 years you grew up and became a boy. It seems yesterday that you were falling asleep on my legs and that I was keeping you in my arms or throwing you in the air. I feel sorry for not being on your side during these important years of your life, but luckily they invented social media and we can keep in touch day by day in order to see all your steps. Ah, I almost forgot: wait for me that in the summer I will teach you again how to play basketball on the court.

A big thank goes to the entire Family. All of you, grandmas, aunts, uncles, cousins from the north to the south across Italy. It is always wonderful to meet all together several times per year during our holidays. This has always been one of the milestones during each of these years from the childhood until now. Let's continue with the old friends to come then to the most recent time: the first rows of this paragraph go without any doubts to Mafalda and Daniela. You play a fundamental role in my life. We know each other since 17 years. Woow! It was back in 2000 when our paths crossed and now we are still more than simple friends since we know each other by hearth. I will never forget all the time spent together, all our trips and our red camping tent. By the way I am still waiting for both of you here in Belgium. ...

Antonio, Mimmo, Peppe, Roberta, Federica, Marina, Elisa, Berto, the friends of a life who are still there even if we cross each other very rarely. You keep being part of my life and, after so many years that we know each other, this is just impressive.

The Aerospace group from the University of Naples: Matteo, Maurizio and Nicola, friends, brothers and great colleagues. We spent so much time together

during the University that it seems that we know each other since the childhood. Of course now it is a bit more difficult to see each other on a daily basis, but it is very nice that as soon as we can spend some time together we do it and we keep laughing for hours and hours.

Before concluding, it is mandatory to go one step further and thank all the people who shared my experiences abroad. First the ones who shared my Erasmus experience in Paris. It is impossible to list all your names. I can say that it was a great time and a wonderful experience, one of the best of my life. It changed my life and it will be forever in my mind. My Paris flatmate Lucia needs to be especially thanked since she changed my way of being and helped me in growing up. There were very hard period but we were able to go through them by supporting each other. I wish you all the best in your new adventure in Spain and I hope that sooner or later we will be living again close to each other.

And finally back to Belgium. In Leuven I met so many people that I would need many pages to write down all your names. All of you are an important part of this Belgian experience. It seems yesterday when everything started, but apparently it was almost 5 years ago. It is so nice to be part of such a young (?) and international (even if mostly Italian) group: Claudio, Simona, Alessandro, Umberto, Mariano, Steffen, Enrico, Kim, Giampiero, Roberta, Carina, Fabio, Emanuela, Stefano, Eleonora, Melania, Paolo and I could keep continuing listing names. Nice trips, nice days, nice evenings, nice dinners, nice parties.

A special mention is needed for the Casa Lepore people: Alessandro (again!), Antonio, Pippo, Davide and Roberto for the nice time spent together in Leuven and for all our trips. To be continued very soon...

Last but absolutely not the least, it's YOU. Knowing you day by day has been an amazing experience. I don't know how you made it, but you came into my life and it seems that we know each others since many years. Sharing most of my time with you in the last months has been a great choice that I will never regret. And.....now that I found you, I will never let you fly away!





# Abstract

Operational Modal Analysis (OMA) is widely employed and became an industrial standard technique for identifying the modal parameters (i.e. resonance frequencies, damping ratios and mode shapes) of mechanical structures. Its main applications are in the automotive, aerospace, civil engineering domains and many others. The advantage, if compared with Experimental Modal Analysis (EMA), is that it is not necessary to stop the machine, but its modal characteristics can be estimated during its operating cycles. In other words, OMA does not rely on known and deterministic excitation, but it uses exclusively the natural vibrations of the structure. It is very useful in cases in which the forces cannot be measured or when it is very difficult to excite a structure and it is more convenient to exploit the natural ambient excitation. The input forces are unknown and the main concept behind OMA is that the structure can be identified from a dynamic perspective by analyzing only the measured output signals. Several hypothesis need to be verified in order to apply OMA. First of all the structure must be Linear Time Invariant (LTI), but this is not the case if several parts are moving with respect to each other. Secondly, the forces acting on the structure must be represented by white noise in the frequency range of interest. This means that all the frequencies must be uniformly excited. This is often the case for wind excitation, but it is not valid anymore if periodical loads due to rotating elements are introduced in the system. The main scope of this dissertation is to fully understand and propose solutions to the challenges and the limitations occurring when applying classical OMA techniques in case of rotating machines. Several simulation and test cases will be discussed in order to validate the proposed solutions.



# Nomenclature

## List of abbreviations

<b>AD</b>	Angle Domain
<b>AE</b>	Acoustic Emission
<b>ANPSD</b>	Averaged Normalized Power Spectral Density
<b>ARMA</b>	Auto-Regressive Moving Average
<b>BEM</b>	Blade Element Momentum
<b>BW</b>	Backward
<b>CMS</b>	Condition Monitoring System
<b>CM</b>	Condition Monitoring
<b>DFT</b>	Discrete Fourier Transform
<b>DOF</b>	Degree-Of-Freedom
<b>DTE</b>	Dynamic Transmission Error
<b>EMA</b>	Experimental Modal Analysis
<b>EMP</b>	Exponentially Modulated Periodic signal
<b>ERA</b>	Eigensystem Realization Algorithm
<b>FA</b>	Fore-Aft
<b>FDD</b>	Frequency Domain Decomposition
<b>FE</b>	Finite Element

---

<b>FFT</b>	Fast Fourier Transform
<b>FRF</b>	Frequency Response Function
<b>FS</b>	Fixed Sampling
<b>FT</b>	Floquet Theory
<b>FW</b>	Forward
<b>HAWT</b>	Horizontal Axis Wind Turbine
<b>HCF</b>	Harmonic Confidence Factor
<b>HPS</b>	Harmonic Power Spectrum
<b>HSS</b>	High Speed Shaft
<b>HTF</b>	Harmonic Transfer Function
<b>IRF</b>	Impulse Response Function
<b>LR</b>	Lower Residual
<b>LSCF</b>	Least Squares Complex Frequency-domain
<b>LSFD</b>	Least Squares Frequency Domain
<b>LSS</b>	Low Speed Shaft
<b>LS</b>	Least Squares
<b>LTI</b>	Linear Time Invariant
<b>LTP</b>	Linear Time Periodic
<b>LTV</b>	Linear Time Variant
<b>MAC</b>	Modal Assurance Criterion
<b>MBC</b>	Multi-Blade Coordinate
<b>MDOF</b>	Multiple-Degree-Of-Freedom
<b>ML</b>	Maximum Likelihood
<b>MSCI</b>	Modal Shape Curvature Index
<b>NE<sub>x</sub>T</b>	Natural Excitation Technique
<b>NNF</b>	Normalized Natural Frequency

---

<b>OBMA</b>	Order-Based Modal Analysis
<b>OCM</b>	Orthogonality Compensation Matrix
<b>ODS</b>	Operational Deflection Shape
<b>OMAX</b>	Operational Modal Analysis with eXogeneous inputs
<b>OMA</b>	Operational Modal Analysis
<b>OT</b>	Order Tracking
<b>PP</b>	Peak-Picking
<b>PSD</b>	Power Spectral Density
<b>PS</b>	Power Spectrum
<b>RWT</b>	Reference Wind Turbine
<b>S2S</b>	Side-to-Side
<b>SDOF</b>	Single-Degree-Of-Freedom
<b>SEA</b>	Structural Element Assembly
<b>SHM</b>	Structural Health Monitoring
<b>SSI-COV</b>	Covariance driven Stochastic Subspace Identification
<b>SSI-DATA</b>	Data driven Stochastic Subspace Identification
<b>SVD</b>	Singular Value Decomposition
<b>SWT</b>	Samcef Wind Turbines
<b>TDC</b>	Top Dead Center
<b>TE</b>	Transmission Error
<b>TF</b>	Transmissibility Function
<b>TOBMA</b>	Torsional Order Based Modal Analysis
<b>TVDFFT</b>	Time Variant Discrete Fourier Transform
<b>UR</b>	Upper Residual
<b>VB</b>	Vibration-Based
<b>VK</b>	Vold-Kalman filter

**List of symbols**

$\alpha_r$	Denominator matrix polynomial coefficient
$\beta$	Window decay rate
$\beta_r$	Numerator matrix polynomial coefficient
$\Delta o$	Order resolution
$\epsilon(n)$	Structural equation error term
$\eta(n)$	Data equation error term
$\lambda_i$	System pole, root of the characteristic equation
$\mu$	Floquet exponent
$\nu$	Poisson's ratio
$\Omega$	Rotational speed
$\omega$	Frequency
$\omega_A$	Amplitude modulation frequency
$\omega_n$	Undamped natural frequency
$\overline{C}_{r,l}$	Fourier coefficients for the $r$ -th mode
$\Phi(t)$	Fundamental transition matrix
$\phi_r$	Edgewise displacement for the $r$ -th mode
$\psi_b$	Azimuth angle of the $b$ -th blade
$\rho_E$	Ice density
$\sigma_y$	Minimum yield strength
$\Theta(t)$	Phase reference signal
$\xi$	Damping ratio
$A(t)$	Dynamic matrix
$A_i$	Residue matrix
$C$	Damping matrix
$C(t)$	Observation matrix

$c_c$	Critical damping
$c_{max}$	Maximum chord length
$c_{min}$	Chord length at the blade tip
$E$	Young's modulus
$E(\bullet)$	Expected value
$F(\omega)$	Input vector in frequency domain
$F(s)$	System input in Laplace domain
$f(t)$	System inputs in time domain
$F_n^b$	Normal force to the $b$ -th blade
$F_t^b$	Tangential force to the $b$ -th blade
$F_p$	Progressive whirling force
$F_r$	Regressive whirling force
$F_{x_R}$	Force components along the $x_R$
$F_{y_R}$	Force components along the $y_R$
$g_i$	Operational reference factor
$H(\omega)$	Frequency Response Function (FRF)
$H(s)$	Transfer function
$K$	Stiffness matrix
$k$	Time lags
$l_i$	Modal participation factor
$M$	Mass matrix
$M_B$	Blade modal mass
$n\Delta\theta$	$n$ -th angular interval
$n\Delta t$	$n$ -th time interval
$o_m$	Order number
$o_{Nyq}$	Angular Nyquist rate

$o_s$	Angular sampling rate
$p$	Polynomial order
$p(t)$	Period of the primary order
$Q$	Monodromy matrix
$q_{\bullet,i}$	Multiblade coordinate
$r$	Harmonic Confidence Factor
$R_{xx}(k)$	Auto- and cross-correlation output matrix
$S_B$	Moment on inertia about the blade root
$S_{uu}(\omega)$	Auto- and cross-power spectra input matrix
$S_{yy}(\omega)$	Auto- and cross-power spectra output matrix
$U(\omega)$	Displacement vector in frequency domain
$v_b(r, t)$	Edgewise displacement for the $b$ -th blade
$v_i$	Mode shape
$w_k$	Window function
$x(n)$	Complex envelope
$x(t)$	Displacement in time domain
$Z(s)$	Damping stiffness
$z_r$	z-domain variable

### List of operators

$\bullet^*$	Complex conjugate
$\bullet^H$	Hermitian transpose
$\bullet^T$	Regular transpose
$\bullet^{-1}$	Inverse matrix
$adj(\bullet)$	Adjoint transpose



# Contents

<b>Abstract</b>	<b>v</b>
<b>Contents</b>	<b>xiii</b>
<b>List of Figures</b>	<b>xvii</b>
<b>List of Tables</b>	<b>xxix</b>
<b>1 Introduction</b>	<b>1</b>
1.1 Research context . . . . .	1
1.2 Introduction to the dissertation topics . . . . .	3
1.2.1 Time variant nature of dynamic systems . . . . .	4
1.2.2 Harmonics in Operational Modal Analysis . . . . .	5
1.2.3 “End-of-order” effect during transient events . . . . .	6
1.2.4 OMA for Structural Health Monitoring . . . . .	7
1.3 Focus and outline of the thesis . . . . .	7
1.4 Original contributions in this work . . . . .	9
1.5 Organization of the text . . . . .	10
<b>2 Dynamic characterization of structures in operating conditions</b>	<b>13</b>
2.1 Introduction . . . . .	13

2.2	Modal model identification algorithms . . . . .	14
2.2.1	Single-Degree-Of-Freedom system . . . . .	15
2.2.2	Multiple-Degree-Of-Freedom system . . . . .	16
2.2.3	Operational Deflection Shapes . . . . .	17
2.2.4	Overview of modal parameter estimation techniques . . . . .	19
2.3	Operational Modal Analysis . . . . .	22
2.3.1	Operational Polymax . . . . .	24
2.4	OMA vs EMA: advantages and drawbacks . . . . .	28
2.5	Going further: OBMA . . . . .	30
<b>3</b>	<b>Time variant nature of dynamic systems</b>	<b>33</b>
3.1	Time-periodic system techniques . . . . .	33
3.1.1	Floquet theory . . . . .	34
3.1.2	Multi-Blade Coordinate transformation (MBC) . . . . .	37
3.1.3	Harmonic Power Spectrum method (HPS) . . . . .	41
3.2	Whirling mode definition . . . . .	45
3.3	Whirl mechanism . . . . .	46
3.4	Application cases . . . . .	50
3.4.1	2D model . . . . .	50
3.4.2	5MW vs 10MW wind turbine . . . . .	63
<b>4</b>	<b>SHM considerations: rotor sensitive parameters</b>	<b>91</b>
4.1	The need of Structural Health Monitoring for wind turbines . . . . .	91
4.2	Sensors and non-destructive testing methods . . . . .	93
4.2.1	Conventional accelerometers . . . . .	94
4.2.2	Displacement sensors . . . . .	95
4.3	Damage detection techniques . . . . .	96
4.4	Whirling modes as damage indicators . . . . .	97

4.5	Mode shape curvatures as damage indicators . . . . .	101
4.6	Damage detection on a wind turbine blade . . . . .	104
4.6.1	Wind turbine blade . . . . .	104
4.6.2	Experimental results . . . . .	108
4.6.3	Model validation . . . . .	110
4.6.4	Damage detection in standing still conditions . . . . .	113
4.6.5	Damage detection in operating conditions . . . . .	119
<b>5</b>	<b>Order Based Modal Analysis: theory and practical aspects</b>	<b>125</b>
5.1	Introduction . . . . .	125
5.2	Order Tracking techniques . . . . .	127
5.2.1	Time domain sampling based Fourier transform order tracking (FS) . . . . .	129
5.2.2	Resampling based Order Tracking . . . . .	131
5.2.3	Time Variant Discrete Fourier Transform (TVDFFT) . . . . .	138
5.2.4	Vold-Kalman filter based order tracking (VK) . . . . .	140
5.3	Polymax method for OBMA . . . . .	144
5.4	Algorithm for rotating accelerometers . . . . .	146
5.4.1	Motion transmission error . . . . .	147
5.4.2	Measurement system description . . . . .	148
5.5	Best practice for OBMA . . . . .	152
5.5.1	Best practice for tacho measurements . . . . .	152
5.5.2	Best practice for order estimation . . . . .	161
<b>6</b>	<b>Order Based Modal Analysis: application cases</b>	<b>163</b>
6.1	2D model . . . . .	163
6.1.1	Model description . . . . .	163
6.1.2	Operational Modal Analysis . . . . .	165

6.1.3	Order-based Modal Analysis . . . . .	170
6.2	Industrial gear test-rig . . . . .	198
6.2.1	Test-rig description . . . . .	198
6.2.2	Experimental Modal Analysis . . . . .	199
6.2.3	Analysis in operating conditions . . . . .	203
6.2.4	Rotating accelerometers post-processing . . . . .	225
6.3	Wind turbine gearbox . . . . .	228
6.3.1	Experimental campaign . . . . .	228
6.3.2	Operational Modal Analysis . . . . .	232
6.3.3	Order-Based Modal Analysis: order tracking step . . . . .	233
6.3.4	Order tracking for harmonic removal purpose . . . . .	234
6.3.5	Order-Based Modal Analysis: modal analysis step . . . . .	236
<b>7</b>	<b>Conclusions and Recommendations</b>	<b>245</b>
7.1	Conclusions on OMA for LTP systems . . . . .	245
7.2	Conclusions on OMA for SHM purposes . . . . .	246
7.3	Conclusions on Order-Based Modal Analysis . . . . .	247
7.4	Recommendations and future directions . . . . .	248
	<b>Bibliography</b>	<b>253</b>
	<b>Curriculum vitae</b>	<b>263</b>
	<b>List of publications</b>	<b>265</b>

# List of Figures

1.1	Examples of rotating parts: gears, bearings, shafts, wheels . . .	2
1.2	Examples of rotating machinery: wind turbines and gearboxes .	2
1.3	Operational Modal Analysis concept: $U$ =unknown input, $H$ =structure, $Y$ =measured output . . . . .	3
1.4	Colormaps for the wind turbine gearbox in different conditions.	5
1.5	"End-of-order" effect. . . . .	6
1.6	Whirling modes as damage indicators. . . . .	8
1.7	Normalized curvatures of the 1st and 2nd mode shapes as damage indicators. Damage extension 120cm represented by red dots.	9
2.1	Single-Degree-Of-Freedom (SDOF) system . . . . .	15
3.1	Multi-Blade Coordinate transformation flowchart for OMA application . . . . .	40
3.2	Amplitude modulation . . . . .	42
3.3	LTI vs LTP systems. . . . .	43
3.4	Harmonic Power Spectrum flowchart for OMA application . . .	44
3.5	Wind turbine model . . . . .	46
3.6	Whirling forces illustration . . . . .	50
3.7	2D model representation . . . . .	51
3.8	2D model - mode shapes. . . . .	55

3.9	2D model - stabilization diagrams. . . . .	57
3.10	2D model - MAC without any pre-processing step. . . . .	58
3.11	2D model - stabilization diagram after MBC transformation. . . . .	59
3.12	2D model - auto-MAC after MBC transformation. . . . .	59
3.13	2D model - synthesized vs. measured crosspowers after MBC transformation. . . . .	60
3.14	2D model - Autopowers related to several channels before and after MBC transformation and comparison with tower signal. . . . .	61
3.15	2D model - stabilization diagram after HPS. . . . .	62
3.16	2D model - auto-MAC after HPS. . . . .	63
3.17	2D model - HPS vs MBC. . . . .	64
3.18	5 MW vs 10 MW wind turbine models. . . . .	64
3.19	SWT example. . . . .	65
3.20	5 MW - absolute wind speed. . . . .	67
3.21	5 MW - wind speed in X, Y and Z directions. . . . .	67
3.22	5 MW - generated power. . . . .	68
3.23	5 MW - virtual accelerometers positions. . . . .	69
3.24	5MW - ice condition simulation in parked configuration. . . . .	72
3.25	5MW - ice condition in operating configuration. . . . .	74
3.26	5MW - parked vs operating conditions. . . . .	75
3.27	5MW - PSDs comparison before and after the use of MBC transformation. . . . .	76
3.28	5MW - PSDs comparison between multiblade coordinates and tower top signal. . . . .	77
3.29	5MW - Autopowers comparison between parked and rotating conditions. . . . .	78
3.30	10 MW - blade designed by using SWT. . . . .	82
3.31	10 MW - drivetrain kinematic chain. . . . .	82
3.32	10 MW - controller scheme. . . . .	83

3.33	10 MW model - mode shapes. . . . .	84
3.34	10 MW - blade instrumentation. . . . .	85
3.35	10MW - stabilization diagram in parked conditions. . . . .	86
3.36	10MW - auto-MAC matrix in parked conditions. . . . .	87
3.37	10MW - autopowers related to the tower sensors - parked vs rotating conditions. . . . .	88
3.38	10MW - autopowers related to a blade tip sensor - parked vs rotating conditions. . . . .	89
3.39	10 MW - stabilization diagrams. . . . .	90
4.1	Damage effects on operating wind turbines . . . . .	92
4.2	Capacitive accelerometers . . . . .	94
4.3	Servo accelerometers . . . . .	95
4.4	Piezoelectric accelerometers . . . . .	95
4.5	Healthy case - backward whirling mode. . . . .	98
4.6	Healthy case - collective mode. . . . .	99
4.7	Stiffness reduction ( $k_1=0.99$ ) - backward whirling mode. . . . .	99
4.8	Stiffness reduction ( $k_1=0.97$ ) - backward whirling mode. . . . .	100
4.9	Stiffness reduction ( $k_1=0.95$ ) - backward whirling mode. . . . .	100
4.10	Stiffness reduction ( $k_1=0.99$ ) - collective mode. . . . .	101
4.11	Stiffness reduction ( $k_1=0.97$ ) - collective mode. . . . .	102
4.12	Stiffness reduction ( $k_1=0.95$ ) - collective mode. . . . .	102
4.13	Wind turbine blade airfoils. . . . .	105
4.14	Angle of twist and chords distribution of the blade. . . . .	106
4.15	Different material properties along the blade span - Generic section. . . . .	107
4.16	FE model of the turbine blade. . . . .	107
4.17	Neutral axis and gravity centers of the blade. . . . .	108
4.18	Inertia moments $I_{xx}$ , $I_{yy}$ torsional constant $J$ . . . . .	109

4.19	Test specimen and instrumentation . . . . .	110
4.20	Autopowers pre and post buckling at a tip node in out-of-plane direction. . . . .	111
4.21	Stabilization diagrams. . . . .	112
4.22	Displacement comparison along $x$ and $y$ axes between the two models loaded with the same force. . . . .	113
4.23	1 <sup>st</sup> mode shape for different conditions: Healthy and by reducing the stiffness of several percentage values. . . . .	116
4.24	2 <sup>nd</sup> mode shape for different conditions: Healthy and by reducing the stiffness of several percentage values. . . . .	116
4.25	3 <sup>rd</sup> mode shape for different conditions: Healthy and by reducing the stiffness of several percentage values. . . . .	117
4.26	4 <sup>th</sup> mode shape for different conditions: Healthy and by reducing the stiffness of several percentage values. . . . .	117
4.27	Curves of the first derivative of the first mode shape for different configurations from the undamaged one to the 50% stiffness reduction with a step of 10%. . . . .	118
4.28	Normalized curvatures of the 1 <sup>st</sup> and 2 <sup>nd</sup> mode shapes. Damage extension 80cm. . . . .	119
4.29	Normalized curvatures of the 1 <sup>st</sup> and 2 <sup>nd</sup> mode shapes. Damage extension 120cm. . . . .	120
4.30	Natural frequencies variation with the rotational speed for the 1 <sup>st</sup> and 2 <sup>nd</sup> mode for three different conditions (healthy, 30% stiffness reduction (40cm damage extension), 30% stiffness reduction (140cm damage extension)) . . . . .	121
4.31	Accelerometers position (red dots). . . . .	123
4.32	Normalized curvatures of the 1 <sup>st</sup> and 2 <sup>nd</sup> mode shapes in operational conditions. Damage extension 80cm. . . . .	123
4.33	Normalized curvatures of the 1 <sup>st</sup> and 2 <sup>nd</sup> mode shapes in operational conditions. Damage extension 120cm. . . . .	124
5.1	Source-Receiver-Transfer model: $U$ =input, $H$ =structure, $Y$ =measured output . . . . .	126



5.2	Fixed Sampling order tracking processing . . . . .	129
5.3	Time domain sampling based FFT order tracking concept . . .	130
5.4	Angle domain resampling order tracking procedure . . . . .	131
5.5	Resampling issue: rpm oscillations within a single revolution .	133
5.6	Resampling issue: pulse per revolution not coinciding with time sample . . . . .	134
5.7	Resampled order tracking processing . . . . .	136
5.8	Angle domain resampling order tracking concept . . . . .	136
5.9	Angle domain resampling order tracking procedure . . . . .	137
5.10	Order 57 extracted with (red) and without (green) phase reference.	138
5.11	Order 57 extracted considering Order 57 as phase reference (red) and Order 114 as phase reference (green). . . . .	138
5.12	Order 114 extracted considering Order 57 as phase reference (red) and Order 114 as phase reference (green). . . . .	138
5.13	Reference signal and "zero-crossings" detection . . . . .	140
5.14	Order-Based Modal Analysis illustration . . . . .	144
5.15	Definition of the motions of gears along the LA and OLA directions	148
5.16	In-plane measurement system . . . . .	149
5.17	Out-of-plane measurement system . . . . .	151
5.18	Linear accelerometers configuration . . . . .	154
5.19	Torsional laser principle based on Doppler effect . . . . .	155
5.20	Coder-based measurement principle . . . . .	157
5.21	Zebra tape shaft instrumentation . . . . .	158
5.22	Zebra tape butt joint correction . . . . .	159
5.23	Incremental encoder . . . . .	159
5.24	Incremental encoder signals . . . . .	160
6.1	Schematic representation of the numerical model . . . . .	164

6.2	Time-Frequency plot for the 8-DOF model . . . . .	166
6.3	Stabilization diagram obtained by applying Operational Polymax.	167
6.4	Spectrum of the input forces exciting the 8DOF system . . . . .	168
6.5	Measured vs. synthesized crosspower after having applied Operational Polymax. . . . .	169
6.6	Stabilization diagram obtained by applying Operational Polymax.	170
6.7	rpm signals: 10s vs 100s runup. . . . .	171
6.8	1000s runup: comparison between order tracking techniques (FS, OT, AD) and the theoretical order (True). . . . .	172
6.9	1000s runup: comparison between order tracking techniques (TVDFT, VK) and the theoretical order (True). . . . .	173
6.10	100s runup: comparison between order tracking techniques (FS, OT, AD) and the theoretical order (True). . . . .	173
6.11	100s runup: comparison between order tracking techniques (TVDFT, VK) and the theoretical order (True). . . . .	174
6.12	10s runup: comparison between order tracking techniques (FS, OT, AD) and the theoretical order (True). . . . .	175
6.13	10s runup: comparison between order tracking techniques (TVDFT, VK) and the theoretical order (True). . . . .	175
6.14	1000s runup: Influence of input parameters for FS order. . . . .	176
6.15	100s runup: Influence of input parameters for FS order. . . . .	176
6.16	10s runup: Influence of input parameters for FS order. . . . .	177
6.17	1000s runup: Influence of input parameters for OT order. . . . .	177
6.18	100s runup: Influence of input parameters for OT order. . . . .	178
6.19	10s runup: Influence of input parameters for OT order. . . . .	178
6.20	1000s runup: Influence of input parameters for AD order. . . . .	179
6.21	100s runup: Influence of input parameters for AD order. . . . .	179
6.22	10s runup: Influence of input parameters for AD order. . . . .	180
6.23	Stabilization diagrams for different order tracking techniques . . .	181

6.24	Stabilization diagrams for different order tracking techniques . .	181
6.25	Stabilization diagrams for different order tracking techniques .	182
6.26	Stabilization diagrams for different order tracking techniques .	185
6.27	Stabilization diagrams for different order tracking techniques .	185
6.28	Stabilization diagrams for different order tracking techniques .	186
6.29	Stabilization diagrams for different order tracking techniques .	187
6.30	Stabilization diagrams for different order tracking techniques .	187
6.31	Stabilization diagrams for different order tracking techniques .	188
6.32	Synthesized vs measured models for different order tracking techniques . . . . .	188
6.33	Synthesized vs measured models for different order tracking techniques . . . . .	189
6.34	Synthesized vs measured models for different order tracking techniques . . . . .	189
6.35	Synthesized vs measured models for different order tracking techniques . . . . .	190
6.36	Synthesized vs measured models for different order tracking techniques . . . . .	190
6.37	Synthesized vs measured models for different order tracking techniques . . . . .	191
6.38	Synthesized vs measured models for different order tracking techniques . . . . .	191
6.39	Synthesized vs measured models for different order tracking techniques . . . . .	192
6.40	Synthesized vs measured models for different order tracking techniques . . . . .	192
6.41	MAC diagram comparison between different order tracking techniques . . . . .	193
6.42	MAC diagram comparison between different order tracking techniques . . . . .	194

6.43	MAC diagram comparison between different order tracking techniques . . . . .	194
6.44	MAC diagram comparison between different order tracking techniques . . . . .	195
6.45	MAC diagram comparison between different order tracking techniques . . . . .	195
6.46	MAC diagram comparison between different order tracking techniques . . . . .	196
6.47	MAC diagram comparison between different order tracking techniques . . . . .	196
6.48	MAC diagram comparison between different order tracking techniques . . . . .	197
6.49	MAC diagram comparison between different order tracking techniques . . . . .	197
6.50	Test rig three-dimensional representation. 1. Test gears; 2. Reaction Gears; 3. Bearings support plates; 4. Flexible couplings; 5. Flywheel; 6. Clutch flange for preload. . . . .	198
6.51	Test rig picture. . . . .	199
6.52	SCADAS measurement system. . . . .	200
6.53	Shaker installation. . . . .	200
6.54	Accelerometers locations along the test rig. . . . .	201
6.55	Frequency Response Function (FRF): test repeatability and consistency. . . . .	201
6.56	Measured FRF vs. Synthesized FRF . . . . .	202
6.57	Mode shape example . . . . .	202
6.58	Test rig measurement points. . . . .	203
6.59	Run-up and run-down cases . . . . .	204
6.60	Rundown colormap plot (left: fast; right: slow). . . . .	205
6.61	Runup colormap plot (left: fast; right: medium). . . . .	205
6.62	FS vs OT vs AD - Fast run-up - Order 57. . . . .	207

6.63 TVDFT vs VK - Fast run-up - Order 57. . . . .	207
6.64 FS vs OT vs AD - Fast run-up - Order 114. . . . .	208
6.65 TVDFT vs VK - Fast run-up - Order 114. . . . .	208
6.66 FS vs OT vs AD - Medium run-up - Order 57. . . . .	209
6.67 TVDFT vs VK - Medium run-up - Order 57. . . . .	209
6.68 FS vs OT vs AD - Medium run-up - Order 114. . . . .	210
6.69 TVDFT vs VK - Medium run-up - Order 114. . . . .	210
6.70 Stabilization diagrams for different order tracking techniques . .	211
6.71 Stabilization diagrams for different order tracking techniques . .	211
6.72 Stabilization diagrams for different order tracking techniques .	212
6.73 Synthesized vs measured models for different order tracking techniques . . . . .	213
6.74 Synthesized vs measured models for different order tracking techniques . . . . .	214
6.75 Synthesized vs measured models for different order tracking techniques . . . . .	215
6.76 MAC diagram comparison between different order tracking techniques . . . . .	215
6.77 MAC diagram comparison between different order tracking techniques . . . . .	216
6.78 MAC diagram comparison between different order tracking techniques . . . . .	216
6.79 MAC diagram comparison between different order tracking techniques . . . . .	217
6.80 Stabilization diagrams for different order tracking techniques .	218
6.81 Stabilization diagrams for different order tracking techniques .	218
6.82 Stabilization diagrams for different order tracking techniques .	219
6.83 Synthesized vs measured models for different order tracking techniques . . . . .	220

6.84 Synthesized vs measured models for different order tracking techniques . . . . .	221
6.85 Synthesized vs measured models for different order tracking techniques . . . . .	221
6.86 MAC diagram comparison between different order tracking techniques . . . . .	222
6.87 MAC diagram comparison between different order tracking techniques . . . . .	222
6.88 MAC diagram comparison between different order tracking techniques . . . . .	223
6.89 MAC diagram comparison between different order tracking techniques . . . . .	223
6.90 Test rig plate mode shapes . . . . .	224
6.91 Test rig plate mode shapes . . . . .	224
6.92 Synthesized vs measured models in rotating conditions . . . . .	226
6.93 Auto-MAC diagram . . . . .	226
6.94 Test rig mode shapes - Fast run-up: 310.0 Hz and 481.2 Hz . . . . .	227
6.95 Test rig mode shapes - Fast run-up: 638.6 Hz and 767.6 Hz . . . . .	227
6.96 Picture taken during the measurement campaign at ZF Wind Power, Lommel, Belgium . . . . .	229
6.97 P3 gearbox picture. . . . .	230
6.98 P2 gearbox picture. . . . .	230
6.99 Time-frequency plot during stationary conditions (constant speed). . . . .	231
6.100 Time-frequency plot during runup conditions (increasing speed). . . . .	231
6.101 "End-of-order" effect. . . . .	232
6.102 TVDFT vs VK - Order 12.36. . . . .	234
6.103 TVDFT vs VK - Order 27. . . . .	235
6.104 Harmonic removal filter - Order 12.36. . . . .	236
6.105 Harmonic removal filter - Order 27. . . . .	237

6.106	Stabilization diagram before applying VK as harmonic removal filter . . . . .	237
6.107	Stabilization diagram after applying VK as harmonic removal filter	238
6.108	Order-based Modal Analysis with TVDFT order tracking - relative variation of natural frequencies with torque level. . . . .	238
6.109	Order-based Modal Analysis with VK order tracking - relative variation of natural frequencies with torque level. . . . .	239
6.110	Synthesized vs measured models for VK order tracking technique	240
6.111	Synthesized vs measured models for VK order tracking technique	240
6.112	Auto-MAC for VK order tracking technique . . . . .	241
6.113	Auto-MAC for TVDFT order tracking technique . . . . .	241
6.114	MAC comparison between VK and TVDFT order tracking techniques . . . . .	242
6.115	Wind turbine gearbox mode shape: test-rig symmetric mode. . . . .	242
6.116	Wind turbine gearbox mode shape: bending/twisting movement of the high-speed housing. . . . .	243
7.1	Condition monitoring system + Virtual sensing + OMA + Damage detection . . . . .	252





# List of Tables

3.1	2D model specifications . . . . .	51
3.2	2D model - modal identification ( $\Omega = 0Hz$ ) . . . . .	54
3.3	2D model - modal identification ( $\Omega = 0.16Hz$ ) . . . . .	56
3.4	2D model - modal identification after MBC transformation ( $\Omega = 0.16Hz$ ). . . . .	58
3.5	2D model - modal identification after HPS ( $\Omega = 0.16Hz$ ) . . .	62
3.6	5 MW specifications . . . . .	65
3.7	5 MW - SWT model validation . . . . .	66
3.8	5 MW - model validation . . . . .	70
3.9	Modal parameters comparison between "ice on all blades" and "ice on all blades but one" conditions . . . . .	73
3.10	Whirling modes identification . . . . .	79
3.11	10 MW specifications . . . . .	80
3.12	10 MW tower properties . . . . .	81
3.13	10 MW rotor properties . . . . .	81
3.14	10 MW - model validation . . . . .	83
4.1	Wind turbine characteristics . . . . .	105
4.2	Core and laminate mechanical properties . . . . .	106
4.3	Experimental natural frequencies and damping ratios of the blade.	110

4.4	Modal frequencies comparison. . . . .	111
4.5	Sensitivity analysis of the natural frequencies of the 1D model for different damage extensions and stiffness reduction. . . . .	114
4.6	Mechanical properties of the laminate under undamaged and damaged condition. . . . .	114
4.7	Numerical and experimental natural frequencies of the damaged blade. . . . .	115
4.8	Variation due to the rotation of the numerical natural frequencies of the blade - First mode. . . . .	122
4.9	Variation due to the rotation of the numerical natural frequencies of the blade - Second mode. . . . .	122
5.1	Sensor assignment for each type of measurement . . . . .	153
6.1	2D model: input parameters . . . . .	165
6.2	Modal parameters identification . . . . .	165
6.3	OMA - Modal parameters identification and comparison with numerical analysis . . . . .	168
6.4	Order Tracking step: sensitivity analysis parameters . . . . .	171
6.5	Order Tracking step: selection of the optimal parameters . . . . .	171
6.6	OBMA - Natural frequencies identification - 1000s . . . . .	182
6.7	OBMA - Damping identification - 1000s . . . . .	183
6.8	OBMA - Natural frequencies identification - 100s . . . . .	183
6.9	OBMA - Damping identification - 100s . . . . .	184
6.10	OBMA - Natural frequencies identification - 10s . . . . .	184
6.11	OBMA - Damping identification - 10s . . . . .	184
6.12	Test rig specifications . . . . .	199
6.13	EMA - Modal parameters identification . . . . .	201
6.14	Order Tracking step: selection of the optimal parameters . . . . .	206
6.15	OBMA - Natural frequencies identification - Fast run-up . . . . .	213

---

6.16 OBMA - Damping identification - Fast run-up . . . . .	214
6.17 OBMA - Natural frequencies identification - Medium run-up . .	219
6.18 OBMA - Damping identification - Medium run-up . . . . .	220
6.19 OBMA - Modal parameters identification by considering rotating accelerometers . . . . .	225
6.20 Measurement points list . . . . .	230



# Chapter 1

## Introduction

This Chapter contains a general introduction and motivation of the research that was conducted in the framework of the thesis. The research context is described in Section 1.1. The different topics and their challenges are discussed in Section 1.2. Finally, the goals and the main contributions of the thesis are underlined in Section 1.3 and 1.4.

### 1.1 Research context

Rotating machines have always been used in a wide variety of industrial applications. Nowadays it is very difficult to find machines or mechanical systems which do not have any rotating component such as shafts, gears, bearings, wheels and so on (Figure 1.1). Wind turbines, gearboxes, combustion and electrical engines, generators and gas turbines are few examples of objects with several rotating substructures (Figure 1.2). These machines face very complex and non-linear conditions during their operating cycles. They are often subjected to the fatigue problem. It is fundamental to design more reliable systems and to detect faults or damages well in advance in order to reschedule the maintenance cycles. This is especially true for big machines (i.e. wind turbines) where the maintenance costs are a huge part of the total costs.

Any problem to the machine will have an effect on its structural properties. As such, structural properties should be continuously monitored. Several benefits could be obtained from Structural Health Monitoring (SHM) strategies based on the estimation of the modal parameters. In fact, faults or cracks will have an



Figure 1.1: Examples of rotating parts: gears, bearings, shafts, wheels

effect on the natural characteristics of the system such as natural frequencies, damping ratios and mode shapes.

A classical technique used since decades for estimating the modal properties of all kind of structures is Experimental Modal Analysis (EMA). This technique supposes that the user has some knowledge both about inputs and outputs, but unfortunately it is not always possible to measure both of them, especially in operating conditions. This is the main reason why several years ago a technique named Operational Modal Analysis (OMA) was introduced. This is the dual of EMA, but it is suitable for operating machines because it relies only on the measured outputs and it does not require any knowledge about the input forces.



Figure 1.2: Examples of rotating machinery: wind turbines and gearboxes

The OMA parameter estimation could be automated and together with a proper SHM strategy could keep track of the variation of the modal parameters and inform the user when an unforeseen maintenance service needs to be done. Of course some assumptions are needed for applying OMA in a straightforward manner and some of them are not valid when a mechanical system has several rotating parts which are moving with respect to each other. Section 1.2 will introduce the main assumptions of OMA and the cases in which these assumptions are violated. A SHM strategy for detecting faults in beam-like structures based on the estimated modal parameters will also be proposed.

## 1.2 Introduction to the dissertation topics

Operational Modal Analysis (OMA) is widely employed and became an industrial standard technique for identifying the modal parameters (i.e. natural frequencies, damping ratios and mode shapes) of mechanical structures. Its main applications are in the automotive, aerospace, civil engineering domains and many others. There are several advantages with respect to the classical Experimental Modal Analysis (EMA) [1], [2], [3]. In fact, in traditional EMA an artificial excitation is normally used for measuring the Frequency Response Functions (FRFs) or Impulse Response Functions (IRFs). These quantities would be very difficult or even impossible to be measured in field tests and/or for large structures. Additionally, EMA is normally conducted in a laboratory environment. However, many industrial applications show real operating conditions which may be quite different from those applied in the lab experiments. Finally, in the laboratory a single component is tested instead of the entire assembled structure. For this reason, it is very important to assign the proper boundary conditions. These reasons were the basis for the development of the OMA technique. It does not rely on known excitation, but it uses exclusively the ambient excitation of the structure. It is very useful in cases in which the forces cannot be measured or when it is very difficult to excite a structure and it is more convenient to exploit the natural ambient excitation [4]. By using OMA the true mode shapes are obtained while the structure is operating with all the components assembled. The OMA concept is shown in Figure 1.3, where a wind turbine is excited by the wind. The input  $U$  is unknown and the main concept behind OMA is that the structure  $H$  can be identified from a dynamic perspective by analyzing only the measured output signals  $Y$ .

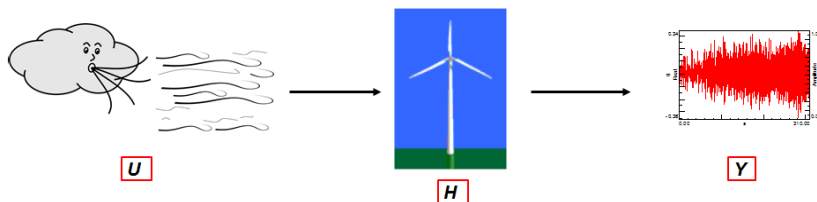


Figure 1.3: Operational Modal Analysis concept:  $U$ =unknown input,  $H$ =structure,  $Y$ =measured output

Several hypothesis need to be verified in order to apply OMA. First of all, the structure must be Linear Time Invariant (LTI), but this is not the case if several parts are moving with respect to each other. Secondly, the forces acting on the structure must be represented by white noise in the frequency range of interest. This means that all the frequencies must be uniformly excited. This

is often the case for wind excitation, but it is not valid anymore if periodical loads due to rotating elements are acting on the system. The main scope of this dissertation is to fully understand and propose solutions to the challenges and the limitations occurring when applying classical OMA techniques in case of rotating machines. Several simulation and test cases will be discussed in order to validate the proposed solutions.

### 1.2.1 Time variant nature of dynamic systems

One of the main hypothesis of OMA requires the structure being Linear Time Invariant (LTI). This is not the case for rotating machines where several parts are rotating. Several techniques will be proposed to take into account the time-varying nature of the system and to allow applying OMA also in these challenging cases. A further distinction can be made between Linear Time Variant (LTV) systems and Linear Time Periodic (LTP) ones. The first case includes all the situations occurring in real life where the rotational speed can vary with the time. In the second case the equations of motion are described by periodic terms with period  $T$  and this is, for instance, the case in which a machine is rotating at constant speed (stationary conditions). In fact, in this case, a similar behavior is happening at the same "angular reference position". Within a period  $T$ , the same events will regularly repeat. Several techniques have been implemented and tested in a simulation environment with a particular focus on the wind turbine domain:

- Floquet Theory (FT) [5], [6];
- Multi-Blade Coordinate transformation (MBC) [7], [8];
- Harmonic Power Spectrum method (HPS) [9], [10].

In fact, a very good example of a time-periodic structure is a wind turbine in operating conditions. This kind of structure has been considered for validating the implemented techniques. If the brake is engaged and the blades are not rotating, such a structure can be considered as a LTI system if the interactions between the blades and the wind flow are neglected. On the other hand, if the wind turbine is in operating conditions, the structure cannot be considered anymore as LTI. If the angular speed can be approximated with a constant value, then it can be considered as a LTP system. The mentioned techniques will take into account the relative motion between the substructures and will allow the use of OMA for characterizing the dynamic behavior of the entire structure.



## 1.2.2 Harmonics in Operational Modal Analysis

Another assumption of OMA is violated if harmonic excitation due to rotating components is present, i.e. the pulsation of a pump, the rotation of a shaft, the rotor of a wind turbine, the meshing gear pairs in gearboxes. In fact they cause periodical loads which excite deterministic frequencies (multiples of the rotational speed) and do not allow considering the excitation spectrum as stochastic white noise. The harmonic components could be considered as numerical modes during the identification process, but if they are very close to eigenfrequencies the standard OMA approach breaks down and it cannot be applied in a straightforward way. In these cases it is quite difficult to distinguish among a true mode and a peak due to an harmonic. Harmonics could also be due to a bad electrical insulation of cables and sensors during the measurements. It is not rare to have the 50 Hz (or 60 Hz if in the US) component and its odd multiples which are masking a great part of the dynamics of the system. A solution could be the one of selecting small frequency bands and excluding the frequencies at which harmonics are showing. For example, if an harmonic is present at 25 Hz, the identification process could be completed by selecting two frequency bands: from 0 Hz to 24 Hz and from 26 Hz to the maximum frequency. This is normally possible because harmonics (especially the electrical ones) are represented by very sharp peaks that do not spread energy on many frequency lines around them. Figure 1.4 shows the harmonics appearing at several frequencies when the machine (in this case a wind turbine gearbox) is operating at a constant rotational speed. On the other hand, when the same machine is working in transient conditions (i.e. a run-up case) the harmonics are sweeping through a certain frequency band and they are also known as orders.

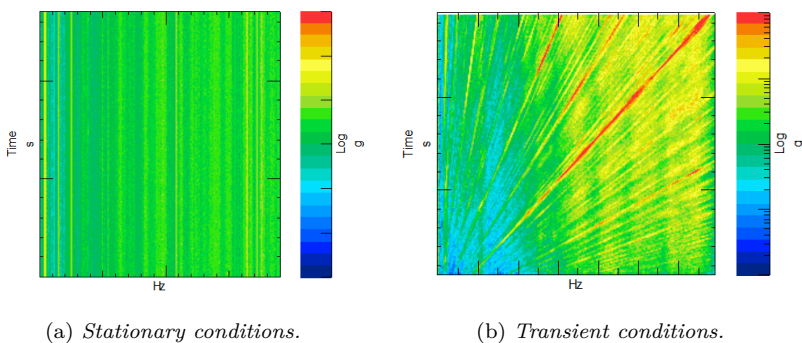


Figure 1.4: Colormaps for the wind turbine gearbox in different conditions.

Different harmonic removal tools could be employed to filter out the harmonics before the modal analysis step takes place. In this dissertation, the potential of Vold-Kalman filter order tracking will be used for filtering out harmonics before using OMA techniques [11]. In the literature this filter is normally used as order tracking technique, but with some adaptations it could be easily used for filtering out harmonics instead of extracting the orders.

### 1.2.3 “End-of-order” effect during transient events

Last but not least problem of applying OMA to rotating machineries is due to the so-called “end-of-order” effect. This effect appears during transient events such as run-up or coast-down measurements. This is related to order components which suddenly end at the maximum rotational speed of the machine at the end of the measurements. They cause the presence of sharp peaks in the spectra which are then identified as poles by any modal parameter estimation technique (Figure 1.5). These peaks are also present if the transient event is not fully controlled and the rotational speed is increased manually by the user. In this case it can happen that the machine is keeping the same rotational speed for few more instants of time causing a peak in the spectrum. In both cases the problem of applying OMA is due to the violation of the assumption of white noise spectrum for the input.

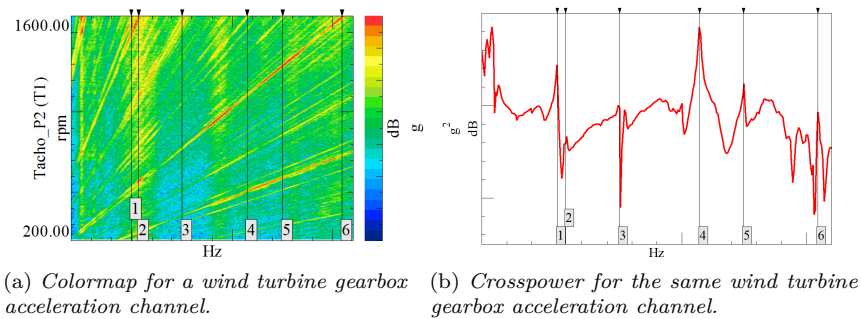


Figure 1.5: "End-of-order" effect.

In order to solve this problem, a technique named Order-Based Modal Analysis (OBMA) has been developed [12]. This method is able to overcome the limitation of classical OMA to interpret the “end-of-order” poles. The concept behind OBMA can be explained in few words by saying that it has been proven that OMA could be applied on orders instead of applying it on cross-power spectra. It consists of two main steps: Order Tracking (OT) and OMA. The combination

of several order tracking techniques with Operational Modal Analysis will be evidenced and the best processing flowchart will be drawn. Several works demonstrated the applicability of such technique to a wide range of rotating machinery: a gear test rig, a wind turbine gearbox test rig, jet engine blades, a locomotive and a car during an engine run-up [13], [14].

### **1.2.4 OMA for Structural Health Monitoring**

Structural Health Monitoring (SHM) is a technology which is able to provide a continuous indication of the health and the reliability of the structure along its lifecycle. A damage detection technique is an essential part of any SHM system. Its scope consists in the identification of some structural and environmental parameters which have to be monitored regularly during the operation of the machine. This technique should be able to distinguish if the damage is present or not in the structure, but it should also locate and quantify the same damage. A damage can be seen as a change in material and/or geometric properties of a structure, including variation of boundary conditions and structural connections [15]. Modal parameters are a structural property and they are often recognized as possible damage-sensitive features. A typical effect happening in case of a small crack or a small damage is the loss of stiffness. This is reflecting into shifts of natural frequencies towards lower values, but these shifts are not always identifiable. Several studies have been performed and two different SHM strategies have been defined. The first one is based upon the whirling phenomenon [16]. The whirling modes are the most identifiable modes in operating conditions and they appear to be very sensitive to changes of stiffness. Their amplitude and phase can be used as damage indicators because they allow to identify losses of isotropy in the rotor (Figure 1.6). A second parameter which is quite sensitive even to small changes of stiffness is the curvature of the mode shape or, in other words, the second derivative of the mode shape. For beam-like structure it has been demonstrated to be a very good damage indicator (Figure 1.7). Several simulations have been run together with some experimental validation on a wind turbine blade.

## **1.3 Focus and outline of the thesis**

The main objectives of this thesis are:

- the implementation of techniques that overcome the limitations of applying OMA in the rotating machinery field;

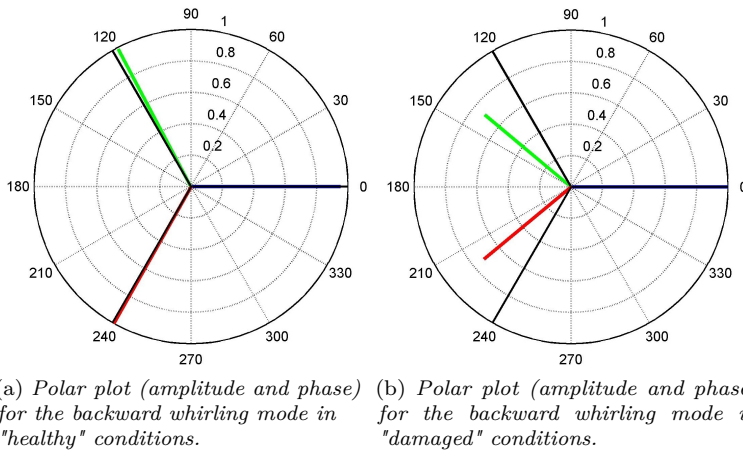


Figure 1.6: Whirling modes as damage indicators.

- the definition of SHM strategies suitable for slender structures in rotating conditions;
- the further development of OMA based on orders: Order-Based Modal Analysis (OBMA);
- the definition of the best practices for applying OBMA for industrial applications in the rotating machinery domain.

The Chapter 2 focuses on the introduction of modal parameter estimation techniques in operating conditions by highlighting their advantages and drawbacks. Chapter 3 describes the limitations in applying OMA in case of time variant structures and several solutions are proposed and validated. Chapter 4 proposes two SHM strategies for rotating structures and shows some examples in the wind turbine domain. Finally Chapter 5 underlines the advantages of performing OBMA instead than classical OMA in case of rotating machinery and introduces a novel approach for considering rotating sensors. Chapter 6 gives several examples in simulation and test environments: a simple 2D model, an industrial test-rig and a wind turbine gearbox.

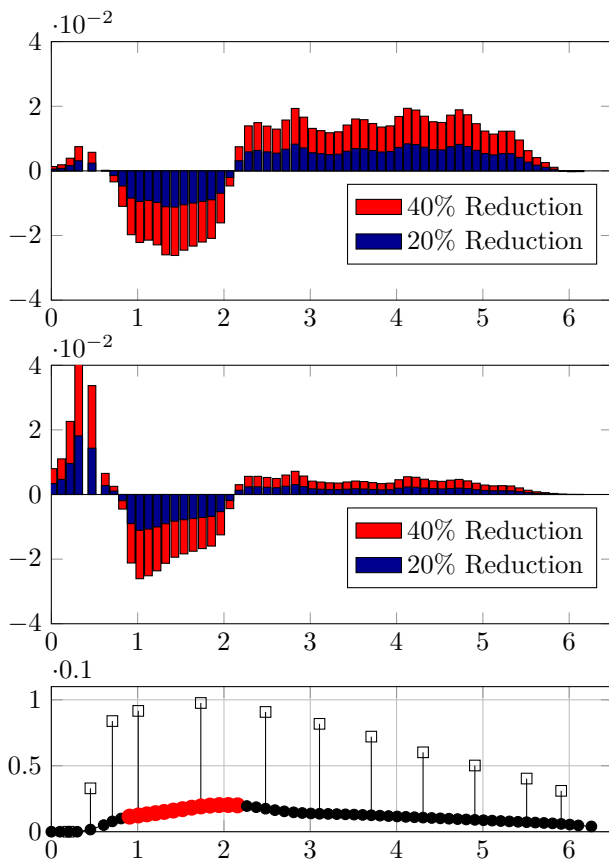


Figure 1.7: Normalized curvatures of the 1st and 2nd mode shapes as damage indicators. Damage extension 120cm represented by red dots.

## 1.4 Original contributions in this work

The research presented in this thesis is based on several presentations given at international events, published conference and journal papers and unpublished articles. In this Section an overview of the most important contributions is given:

- Operational Polymax was combined together with several pre-processing techniques in order to allow the modal parameter estimation for operating wind turbines (LTP systems);

- two SHM strategies were proposed based on the whirling modes estimation for identifying anisotropies in the rotor and on the curvature of the mode shapes in rotating conditions for identifying the presence of cracks along the blades;
- the matter of the phase referencing for OBMA was solved by considering as phase reference channel during the order extraction a sine sweep with a frequency equal to the instantaneous rotational speed of the machine;
- the problem of defining the best practices in terms of sensors both for measuring the rotational speed and the measurement channels was addressed and some guidelines were defined depending on the application;
- a novel approach for taking into account the rotating sensors was developed and validated in a test-rig environment.

## 1.5 Organization of the text

The thesis can be divided in three main parts. The first part sets the framework in which the entire work has been performed in the context of time-varying systems. Throughout this part, numerical simulations and simulated cases are used to illustrate and verify the proposed methods and solutions. Based on these outcomes, the second part extend the analysis to the Structural Health Monitoring domain. Two different SHM strategies for beam-like structures have been proposed and validated. Finally the third part focuses on the Order-Based Modal Analysis technique. Both theory and application cases are discussed in order to validate the proposed approach in laboratory conditions as well as in industrial cases.

**Chapter 1** outlines the problems and motivates the work. The objectives and the novel contributions of the work are highlighted.

**Chapter 2** introduces the framework in which the work has been done. Operational Modal Analysis is introduced and its limitations in a rotating machinery context are underlined. The advantages and drawbacks when compared to standard Experimental Modal Analysis technique are discussed and finally the Order-Based Modal Analysis method is introduced.

**Chapter 3** starts by introducing the concept of time-periodic or, more in general, time-variant systems. Three different methods to deal with such systems are discussed: Floquet theory, Multi-Blade Coordinate transformation and Harmonic Power Spectrum. The whirling phenomenon is presented. Finally

these techniques are applied in a simulation environment using wind turbine models results.

**Chapter 4** is based on the results of Chapter 3 and extend them to the Structural Health Monitoring domain. Two different SHM strategies are discussed. The first one uses the whirling modes as damage indicators. The second one analyzes the effect of damages using the mode shape curvatures as damage indicators. Finally the damage detection procedure is tested on a wind turbine blade.

**Chapter 5** enters in the third and last part of the thesis. The Order-Based Modal Analysis technique is discussed deeply into details. This technique is a combination of Order Tracking and Operational Modal Analysis. For this reason, both methods are discussed in this chapter. The best practices for applying the method in a real-life environment are also highlighted.

**Chapter 6** introduces several simulation and test cases to underline the improvements obtained by applying the OBMA method instead of classical modal analysis techniques. First of all a simple 2D model shows the basic concepts. Then OBMA is applied to an industrial gear test-rig and compares EMA, OMA and OBMA results. Finally, a very industrially oriented example is presented considering a wind turbine gearbox in a test-rig configuration before being installed in a wind turbine.

**Chapter 7** summarizes the most important conclusions of the thesis and gives recommendations for further research.





## Chapter 2

# Dynamic characterization of structures in operating conditions

This Chapter contains a discussion about the modal parameter estimation techniques in operating conditions. After a brief introduction in Section 2.1, the modal model identification algorithms are discussed in Section 2.2. The development of the Operational Modal Analysis (OMA) to overcome some of the limitations of EMA is shown in Section 2.3. Section 2.4 illustrates a comparison between EMA and OMA underlining advantages and drawbacks of each of the two techniques. Finally the Order-Based Modal Analysis (OBMA) method is introduced in Section 2.5.

### 2.1 Introduction

The experimental identification of modal parameters is a key topic in structural dynamics. In the last decades it has been explored from researchers all over the world and it has become a well-accepted standard for the industry. It started to be applied in the mechanical engineering field to identify the dynamic behavior of relatively small structures in laboratory conditions. For this purpose the first approach was based on the measurement of the structural response when the specimen is excited by a force which is also measured. This technique took the name of Experimental Modal Analysis (EMA). The evolution of EMA

techniques has been impressive in the last decades both in terms of testing equipment and post-processing algorithms. Nowadays it is a well-established technique which is founded on solid theoretical basis [1], [2], [3]. It is used in many fields (civil, aerospace, automotive, naval engineering and many others) and it also allows to identify the modal characteristic of huge structures such as bridges, buildings, airplanes, off-shore platforms, etc. Of course in these cases the user has to take into account additional challenges. In fact, the use of a controlled and measurable dynamic excitation requires the use of heavy and expensive devices and sensors. The main problem associated with forced vibration tests on such big structures is connected with the difficulties in exciting the most significant modes of vibration of the structure with a sufficient level of energy. This is one of the main reasons behind the development of Operational Modal Analysis (OMA) which uses ambient excitation sources such as wind, traffic, waves, seismic activity, etc. Since it is impossible to measure these forces, the response measurements are the only information which can be used for the determination of the modal model of the structure. The fundamental idea behind OMA is that the structure being tested is excited by a certain force which has white noise characteristics. This means in other words that the energy is distributed over a wide frequency range that includes the one of interest [4]. Recently combined modal testing techniques have been explored. They are known as Operational Modal Analysis with eXogeneous inputs (OMAX). In this case an artificial force is used in operating conditions and it is applied while operational forces are acting on the same structure [17].

## 2.2 Modal model identification algorithms

The main objective of modal analysis is the estimation of the modal characteristics of a dynamic system. The modes are inherent properties of a structure and they depend on the material properties (mass, damping and stiffness) and boundary conditions of the structure. Each mode is identified by means of the modal parameters (natural frequencies, damping ratios and mode shapes) and the dynamic behavior of the system is explained in terms of superposition of modes of vibration. The number of modes depends on the number of Degree-Of-Freedom (DOF) that describe the system. Real structures are continuous systems and for this reason they have an infinite number of modes. In practice dynamic studies are aimed to characterize the modal model of the structure in a limited frequency interval. Within this interval the most dominant modes can be identified and the machine can be considered to behave as a system with a finite number of DOFs.

## 2.2.1 Single-Degree-Of-Freedom system

The most simple case is the one of the Single-Degree-Of-Freedom (SDOF) system which is described by using Equation 2.1. The model is shown in Figure 2.1.

$$m\ddot{x}(t) + c\dot{x}(t) + kx(t) = f(t) \quad (2.1)$$

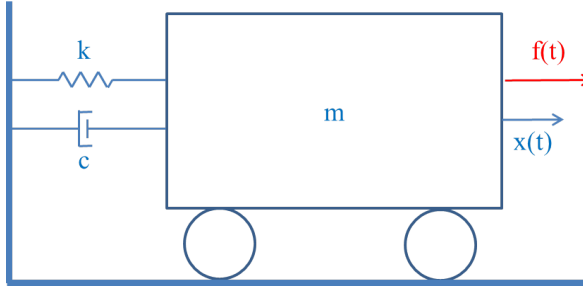


Figure 2.1: Single-Degree-Of-Freedom (SDOF) system

$m$  is the mass,  $c$  the damping coefficient and  $k$  the stiffness. This equation represents the force equilibrium and expresses the balance between inertial ( $m\ddot{x}(t)$ ), damping ( $c\dot{x}(t)$ ), elastic ( $kx(t)$ ) and external forces ( $f(t)$ ).  $\ddot{x}(t)$ ,  $\dot{x}(t)$  and  $x(t)$  are the acceleration, velocity and displacement in the direction of motion. Equation 2.1 can be transformed to the Laplace domain by assuming zero initial values yielding to Equation 2.2.

$$(ms^2 + cs + k)X(s) = F(s) \quad (2.2)$$

By defining the dynamic stiffness  $Z(s) = ms^2 + cs + k$ , the transfer function  $H(s)$  between displacement and force can be defined as the inverse of this quantity, as shown in Equation 2.3.

$$H(s) = \frac{1}{Z(s)} = \frac{1}{ms^2 + cs + k} \quad (2.3)$$

The denominator of Equation 2.3 can be put equal to zero. The roots of the so-called system characteristic equation are the system poles calculated in Equation 2.4.

$$\lambda = -\frac{c}{2m} \pm i\sqrt{\left(\frac{c}{2m}\right)^2 - \frac{k}{m}} = -\sigma \pm i\omega_d \quad (2.4)$$

If  $c = 0$ , then the system is not damped and the undamped natural frequency  $\omega_n$  can be defined (Equation 2.5).

$$\omega_n = \sqrt{\frac{k}{m}} \quad (2.5)$$

The critical damping  $c_c$  is the value for which the term under the square root in Equation 2.4 becomes zero. The damping ratio  $\xi$  is defined as the ratio between  $c$  and  $c_c$ .

$$\xi = \frac{c}{c_c} = \frac{c}{2m\omega_n} \quad (2.6)$$

The relationship between the forces and displacements has been expressed in the Laplace domain but it could be represented in the frequency domain ( $s = i\omega$ ) yielding to the Frequency Response Function (FRF)  $H(\omega)$ .

$$H(\omega) = \frac{1}{(k - m\omega^2) + ic\omega} \quad (2.7)$$

From Equation 2.7 the resonance frequency  $\omega_n$  can be obtained by putting  $c = 0$ . Of course physical systems cannot be represented as SDOF systems, but the properties of such simple systems are very important. In fact, if a Multiple-Degree-Of-Freedom (MDOF) system is Linear Time Invariant (LTI), it can always be represented as the linear superposition of a certain number of SDOF systems.

## 2.2.2 Multiple-Degree-Of-Freedom system

The concepts introduced for a SDOF system can be extended to a Multiple-Degree-Of-Freedom (MDOF) scenario. In this case the terms  $m$ ,  $c$  and  $k$  becomes matrices, as shown in Equation 2.8.

$$M\ddot{x}(t) + C\dot{x}(t) + Kx(t) = f(t) \quad (2.8)$$

$M$  is known as mass matrix,  $C$  is the damping matrix and  $K$  the stiffness matrix. In this case, the transfer function matrix  $H(s)$  can be defined as in Equation 2.9.

$$H(s) = [Ms^2 + Cs + K]^{-1} = \frac{adj(Ms^2 + Cs + K)}{|Ms^2 + Cs + K|} \quad (2.9)$$

The system characteristic equation is given by the denominator of Equation 2.9 which is the determinant of the inverse of the transfer function matrix  $H(s)$ . Equation 2.9 can be rewritten in a pole-residue form, as shown in Equation 2.10.

$$H(s) = \sum_{i=1}^N \frac{A_i}{s - \lambda_i} + \frac{A_i^*}{s - \lambda_i^*} \quad (2.10)$$

$A_i$  are the residue matrices which are related to the mode shapes  $v_i$  by the following relationship.  $N$  is the number of DOF of the system.

$$A_i = v_i v_i^* \quad (2.11)$$

The derivation of this relationship can be found in [1]. It can be concluded that the transfer function matrix of a LTI MDOF system with  $N$  DOFs is the sum of  $N$  SDOF transfer functions. This is also known as modal superposition principle. The full transfer function matrix is completely characterized once that the modal parameters are known, i.e. the poles  $\lambda_i$  and the mode shape vectors  $\Psi_i$ ,  $i = 1, \dots, N$ .

### 2.2.3 Operational Deflection Shapes

Very close to the natural frequency of a mode, the overall vibration shape of a system is dominated by the mode shape of the resonance, but small contributions are coming also from the other modes. This is the substantial difference between an Operational Deflection Shape (ODS) and a mode shape. Traditionally, an ODS has been defined as the deflection of a structure at a particular frequency of excitation. In general it can be defined as any motion of two or more points on a structure produced by an excitation. An Operational Deflection Shape contains both forced and natural vibration components, whereas the mode shape is an inherent characteristic of the structure and contains only natural (resonant) vibration components. The basis equation for ODS studies is the forced response which is expressed in Equation (2.12).

$$\{U(\omega)\} = [H(\omega)] \{F(\omega)\} \quad (2.12)$$

In this equation the displacement vector  $\{U(\omega)\}$  is obtained as a multiplication in the frequency domain between the forces  $\{F(\omega)\}$  which are considered being unknown and the frequency response matrix  $[H(\omega)]$ . The most important thing to be noticed is that the frequency response function acts as a filter on the input force which results in some output response. If the excitation contains all the frequencies, all the modes will be activated and the response can be seen as a linear superposition of all these modes. In case of ODS, the excitation does not contain all frequencies, but only excites a single frequency line. In any case all the modes contribute to the ODS. The main differences between natural modes of vibration and ODSs can be listed here:

- An ODS can be defined at any frequency. Each mode is related to a specific natural frequency.
- ODSs can be defined for non-linear and non-stationary structures. Modes are generally defined only for linear and stationary structures.
- A mode shape is associated with resonant vibration of the system. An ODS can be related to both resonant and nonresonant vibrations.
- Modes do not depend on the forces acting on the system, but their superposition determines how the system respond to such forces. ODSs strongly depend on the forces and they will change if the loads change. Modes only change if there are structural modifications or boundary condition variations.

The ODS analysis is normally used for analyzing and solving several problems related to noise and vibration. The main advantages of such technique if compared to modal analysis are that:

- There is no assumption of linear model
- The structure is subjected to the actual operating forces
- True boundary conditions are applied

On the other hand this technique has also some disadvantages:

- Modal parameters (natural frequencies, damping ratios and mode shapes) cannot be determined

- ODS reflect the cyclic motion at a single frequency line, but no conclusions can be obtained for the behavior at different frequencies

The following steps need to be followed in order to perform an ODS measurement:

- decides the points to be measured and define a local and a global coordinate system;
- build a geometry model of the structure under test by considering all the measurement points;
- measure the points by using sensors (i.e. accelerometers) during steady-state (Spectral ODS) or transient (Run-up/down ODS) conditions;
- if all measurement points cannot be measured simultaneously, it can be necessary to measure during different runs. In this case some sensors need to be used as reference and they must be kept in the same location along the entire measurement campaign. The reference points must be selected such that they show clear peaks at the frequencies of interest;
- compute spectra (Spectral ODS) or compute orders (Run-up/down ODS) of all measured points by selecting one of the reference channels as phase reference;
- extract the amplitude and phase at the frequencies of interest (the ones showing clear peaks) and store them in a shape vector;
- animate the shape vector to analyze the vibration pattern at a certain frequency.

## 2.2.4 Overview of modal parameter estimation techniques

Although ODS represents a powerful tool for understanding the dynamic behavior of a system, it cannot be used for troubleshooting and root-cause analysis. In fact it becomes quite complicated to understand if the measured response is caused by the presence of a structural resonance or if it is due to the excitation or again to a combination of the two. For this reason, in order to determine the modal characteristics of a structure, several modal parameter estimation methods have been developed. In the literature they are classified as frequency domain or time domain methods.

## Peak-Picking (PP)

The simplest method to obtain a first estimate of the modal parameters of a structure subjected to ambient loading is the so-called Peak-Picking (PP) method. It allows to estimate the natural frequencies by selecting the peaks of the auto-spectra of the measured outputs. It is based on the assumptions of very low damping and well separated modes. If these conditions are not violated, the mode shape can be approximated by a single row or column of the spectrum matrix evaluated at the identified peak [18]. If these conditions are violated, then two or more closely spaced modes can be superposed yielding to the conclusion that an Operational Deflection Shape (ODS) was identified instead of the mode shapes. The main problem of this method is the damping ratio estimation. The half-power bandwidth method can be used, but this is not a very accurate method. Another problem is related to the subjectivity of the peak selection task which can be very difficult if the spectra are not very clear. A practical implementation of the PP technique has been proposed by Felber [19]. In this method, the natural frequencies are determined as the peaks of the averaged normalized power spectral densities (ANPSDs). It assumes that the coherence function computed for two simultaneously recorded response signals is close to 1 at the natural frequencies and that the dynamic response at a resonance is only determined by a single mode. These assumptions help to identify the natural frequencies of the structure.

## Frequency Domain Decomposition (FDD)

A slightly more advanced curve-fitting method is the Frequency Domain Decomposition (FDD) [20]. It is also a non-parametric frequency domain method which is computing the Singular Value Decomposition (SVD) of the output spectrum matrix and which is overcoming some of the limitations of the PP method. The method is based on the fact that a transfer function or spectrum matrix evaluated at a certain frequency can be determined by only few modes. The number of important modes identifies the rank of the matrix. The SVD is typically used for estimating the rank of a matrix: the number of non-zero singular values equals the rank. In order to get the natural frequencies, the singular values can be plotted as a function of frequency identifying the local maxima. This method is able to separate among closely spaced modes. On the other hand the main drawback of the Peak-Picking method is still there. In fact the initial selection of peaks in singular value plots remains a subjective task.



## Parametric frequency domain methods

In order to overcome the limitations of the previous methods, several parametric methods have been proposed in the past years. These methods are able to fit models to the measured data and allow an objective selection of model order and physical poles based on the so-called stabilization diagram. Parametric methods do not consider only one mode at a time, but allow to estimate the spectrum matrix as a whole. The fitting of experimental data to a model is an optimization problem based on a cost function which can be solved through the linear Least Squares (LS) method or with the Maximum Likelihood (ML) estimator [21]. The ML method results in non-linear equations and it can be solved by using an iterative procedure. For this reason it requires a high computational load and it is not suitable for handling a large amount of data. In the last years the algorithm has been improved in order to reduce the computational time. In its first development, the method was applied to FRFs, but then it was extended to use spectra as primary data so that it could be used for OMA applications. In [22] several possible combinations of these models and fitting procedures have been explored together with a different class of methods (realization algorithms) that use frequency domain state-space models. In [23] an alternative frequency domain identification algorithm based on the concept of Transmissibility Functions (TF) was developed.

### **Poly-reference Least Squares Complex Frequency domain method (p-LSCF) - Polymax**

The poly-reference Least Squares Complex Frequency domain method (p-LSCF) is also known as Polymax and in its first development was used for identifying the modal parameters from FRFs, which means for EMA studies [24], [25]. It was in a second time extended to the OMA case by taking into account the similarities between the modal decomposition of the output half-spectrum of a system excited by white noise input and its transfer function. It originates from the so-called least-squares complex frequency-domain (LSCF) estimation method which was introduced to find initial values for the iterative maximum likelihood method. It was found that these values yielded very accurate modal parameters with a very small computational effort. The main advantage of this technique is its very clear stabilization diagrams if compared to the other modal parameter estimation techniques. The drawbacks of the classical LSCF method are mainly due to the fact that neither participation factors nor mode shapes are available at first instance and that closely spaced poles will be erroneously seen as a single pole. For these reasons the Polymax method was developed. By following this approach, also the participation factors are available when

constructing the stabilization diagram. Closely spaced modes can then be separated. The output-only version was presented in [26] and it is known as Operational Polymax. This technique is widely applied in the industrial environment and it is implemented in the commercial software Siemens Test.Lab.

### **Time domain methods**

The similarity between the mathematical representation of the transfer function and the output spectrum of a system excited by a white noise input in the frequency domain finds its dual in the time domain. In fact, in the time domain the similarity is between the impulse response and the output correlations of a system excited by white noise. In the early stage of OMA development, these similarities were explored mainly in the time domain in order to extend the existing technique to the operational case. As a result, the first technique extended to OMA application was the well-known ERA (Eigensystem Realization Algorithm) method [27]. [28] converted it into the Natural Excitation Technique (NExT) method. Nowadays the available time domain methods are mainly included in two different groups: the discrete-time stochastic state-space models and the ARMA (Auto-Regressive Moving Average) models [29]. Two methods are based on the state-space formulation: Covariance driven Stochastic Subspace Identification (SSI-COV) which identify the modal model from the covariances of the outputs and the Data driven Stochastic Subspace Identification (SSI-DATA) which uses directly the time series collected by putting sensors on the structure to be tested. [30]. The two methods are very similar to each other, but it can be underlined the advantage of the SSI-COV to be faster while the SSI-DATA allows to get some further information with some post-processing as for instance, the decomposition of the measured response in modal contributions.

## **2.3 Operational Modal Analysis**

In general, we can state that the identification methods used for operational modal analysis are very similar, if not identical, to those for input-output modal analysis. The main difference lies in the fact that they are based on auto- and cross correlations in the time domain and on auto- and cross spectra in the frequency domain. On the other hand, the methods developed for classical modal analysis are based on the impulse and frequency responses respectively [1]. Under the assumption of white noise input, the output spectra can be modelled in a very similar way as Frequency Response Functions (FRFs). The

FRF matrix  $H(\omega)$  is expressed in Equation (2.13) as a function of the modal parameters.

$$[H(\omega)] = \sum_{i=1}^n \frac{\{v_i\} \langle l_i^T \rangle}{j\omega - \lambda_i} + \frac{\{v_i^*\} \langle l_i^H \rangle}{j\omega - \lambda_i^*} \quad (2.13)$$

$n$  is the number of complex conjugated mode pairs,  $*$  is the complex conjugate of a matrix,  $^H$  is the complex conjugate transpose (Hermitian) of a matrix,  $v_i$  are the mode shapes and  $l_i$  are the modal participation factors.  $\lambda_i$  are the poles which are related to the eigenfrequencies  $\omega_i$  and damping ratios  $\xi_i$  as shown in Equation (2.14).

$$\lambda_i, \lambda_i^* = -\xi_i \omega_i \pm i \sqrt{1 - \xi_i^2} \omega_i \quad (2.14)$$

For stationary stochastic processes, the auto- and cross power spectral density matrix between the outputs  $S_{yy}$  is given in Equation (2.15).

$$[S_{yy}(\omega)] = [H(\omega)][S_{uu}][H(\omega)]^H \quad (2.15)$$

$S_{uu}$  is the auto- and cross power spectral density matrix between the input forces. In case of operational data, the output spectra are the only available information and some hypothesis regarding the input forces need to be made. In fact, under the assumption of white noise inputs, the input matrix is not frequency dependent and equals a constant matrix. By combining Equation (2.13) and Equation (2.15), the auto- and cross power spectral density matrix between the outputs can be decomposed in modal components, as shown in Equation (2.16).

$$[S_{yy}(\omega)] = \sum_{i=1}^n \frac{\{v_i\} \langle g_i \rangle}{j\omega - \lambda_i} + \frac{\{v_i^*\} \langle g_i^* \rangle}{j\omega - \lambda_i^*} + \frac{\{g_i\} \langle v_i \rangle}{-j\omega - \lambda_i} + \frac{\{g_i^*\} \langle v_i^* \rangle}{-j\omega - \lambda_i^*} \quad (2.16)$$

$g_i$  are the so-called operational reference factors which are the corresponding of the modal participation factors in case of OMA. It is quite difficult to interpret their physical meaning because they are a function of the modal parameters of the system and the constant input spectrum matrix. The last equation is the basis for most of the frequency domain operational modal identification techniques. In all cases, the unknown input is assumed to be represented by white noise.

In order to get the basis for what concerns the time domain methods, the discrete-time inverse Fourier transform of the last equation can be taken. The results are the auto- and cross correlation function matrix of the outputs  $[R_{xx}(k)]$  which are expressed as a sum of decaying sinusoidal signals, for positive and negative time lags  $k$ , as shown in Equation 2.17.

$$[R_{xx}(k)] = \begin{cases} \sum_{i=1}^n (\{v_i\} \langle g_i \rangle e^{\lambda_i k T} + \{v_i^*\} \langle g_i^* \rangle e^{\lambda_i^* k T}) & \text{for } k \geq 0; \\ \sum_{i=1}^n (\{g_i\} \langle v_i \rangle e^{\lambda_i |k| T} + \{g_i^*\} \langle v_i^* \rangle e^{\lambda_i^* |k| T}) & \text{for } k < 0; \end{cases} \quad (2.17)$$

where  $T$  is the sampling period.

In Section 2.3.1, the Operational Polymax method will be described in a more detailed manner. This technique will be extensively used in the following chapters for identifying the modal parameters in operational conditions.

## 2.3.1 Operational Polymax

### Pre-processing techniques

The only inputs needed for all OMA techniques in the frequency domain, as it was already pointed out in the previous sections, are the power spectra between the outputs. They are defined as the Fourier transforms of the correlation vectors. Two main non-parametric methods can be used for estimating the spectra:

- weighted averaged periodogram;
- weighted correlogram.

The term ‘weighted’ in both names is related with the fact that the signal is weighted by using one of the classical windows (Hanning, Hamming, etc.) for reducing the leakage, an error which effect lies in the spreading of the spectrum components along other frequencies. This is due to the finite nature of the time segments and to the non-periodicity of the time blocks. The window is reducing the contribution of the data at the beginning and at the end of each block. For this reason some overlap between the blocks is needed [3].

**Weighted averaged periodogram** The weighted averaged periodogram is also known as modified Welch's periodogram [31]. It is based on the computation of the Discrete Fourier Transform (DFT) of the weighted outputs. As a first step the measured responses are divided into  $N$  segments  $y_k$  with the same length which normally have a certain percentage of overlap. Then, the second step consists in the DFT calculation of each block after having applied a proper window  $w_k$  (Equation (2.18)).

$$Y(\omega) = \sum_{k=0}^{N-1} w_k y_k e^{-j\omega k \Delta t} \quad (2.18)$$

An unbiased estimate of the output spectrum matrix can be obtained by using Equation (2.20). Its variance can be reduced by averaging the spectra associated with the several overlapping data blocks obtained with the use of the DFT.

$$S_{yy}^{(b)}(\omega) = \frac{1}{\sum_{k=0}^{N-1} |w_k|^2} Y(\omega) Y^H(\omega) \quad (2.19)$$

$$S_{yy}(\omega) = \frac{1}{P} \sum_{b=1}^P S_{yy}^{(b)}(\omega) \quad (2.20)$$

Of course, the length of each block and their number  $P$  is selected by taking into account both the frequency resolution and the irregularity of the spectra or the variance of the estimates. If longer blocks are selected, the resolution increases and the effect of leakage reduces, but the uncertainties are higher because the number of averages is smaller.

**Weighted correlogram** Another non-parametric spectrum estimate is the so-called weighted correlogram. This technique calculates the output spectrum from the DFT of the output correlation matrix which can be estimated by using Equation (2.21).

$$R_i = \frac{1}{N} \sum_{k=0}^{N-1} y_{k+1} y_k^T \quad (2.21)$$

Several implementations based on the use of FFT exist to compute the correlations. By inserting the Equation (2.21) in Equation (2.22), a weighted estimate of the output spectrum matrix can be obtained.

$$S_{yy}(\omega) = \sum_{k=-L}^L w_k R_k e^{-j\omega k \Delta t} \quad (2.22)$$

$L$  is the maximum number of time lags at which the correlations are estimated. This number is typically smaller than the number of data samples in order to avoid the greater statistical variance associated with the higher lags of correlation estimates. If the DFT is extended to both positive and negative time lags of the correlation function, a spectrum is obtained. If only positive values are taken into account, a half-spectrum is the result of the calculation. Also in this case a window is used for reducing the leakage problem. By using windows such as Hanning, Hamming, etc., the decay of the correlations will be influenced by the window application. This will cause problems for what concerns the damping estimation. The solution is the use of an exponential window which effect can be corrected from the estimated modal damping ratios. The window is also able to reduce the influences of noise in the tails of the correlations. It is defined as a symmetric function shown in Equation (2.23).

$$w_k = e^{-\beta|k|\Delta t}, -j_m \leq k \leq j_m \quad (2.23)$$

$\beta$  defines the decay rate of the window and influences directly the value of the window related to the maximum time lag of the correlation functions  $j_m$ . The correction can be performed afterwards by removing the artificial damping added by  $\beta$  from the estimated damping ratios, as shown in Equation (2.24).

$$\xi_{estimated} = \xi_{real} + \frac{\beta}{\omega} \quad (2.24)$$

It can be noticed that the added damping is inversely proportional to the frequency  $\omega$ , which means that the modes at lower frequencies are more influenced by the  $\beta$  effect.

**Weighted correlogram advantages** For modal analysis purposes, the weighted correlogram approach has several advantages if compared to the weighted periodogram one. Several discussions on the estimation of spectra from the measured time histories in a modal analysis context can be found in [32], [22], [33]. The two main advantages can be summarized as follows:

- By using the correlogram method, the calculation of the half-spectra is enough for performing the modal analysis step. The half-spectra is

obtained by considering only the positive time lags, as shown in Equation (2.25).

$$S_{yy}^+(\omega) = \frac{\omega_0 R_0}{2} + \sum_{k=1}^L \omega_k R_k e^{-j\omega k \Delta t} \quad (2.25)$$

The relationship between the half-spectra and the full spectra is expressed by Equation (2.26).

$$S_{yy}(\omega) = S_{yy}^+(\omega) + S_{yy}^+(\omega)^H \quad (2.26)$$

The modal decomposition of the half-spectra consists only of the first two terms of Equation (2.16). In this way, models of lower order can be fitted without affecting the quality.

- The output correlations are equivalent to the impulse response under the white noise assumption. Therefore, it is a good choice to apply the exponential window  $w_k$  to the correlations before using the DFT. The application of such a window is compatible with the modal model and the pole estimates can be corrected. This is not true if other windows such as a classical Hanning window are used.

## Operational Polymax method

The poly-reference Least Squares Complex Frequency method (p-LSCF), also known as Polymax is based on the weighted correlogram technique for estimating the output spectra which are the main input needed in case of OMA. The next step, after having identified the spectra, is to fit a modal model through a modal parameter estimation step. The method is formulated in the z-domain which is a frequency-domain derived from a discrete-time signal. The so-called right matrix-fraction model is assumed to represent the measured half spectrum matrix (Equation (2.27)).

$$S_{yy}^+(\omega) = \sum_{r=0}^p z^r [\beta_r] \left( \sum_{r=0}^p z^r [\alpha_r] \right)^{-1} \quad (2.27)$$

$p$  is the order of the polynomials,  $\beta_r$  are the numerator matrix polynomial coefficients,  $\alpha_r$  are the denominator ones. The number of lines of the half-spectrum matrix is equal to the number of measured responses, while the number of columns is equal to the number of channels selected as references.

In fact, in order to estimate the modal parameters, the cross-spectra can be calculated between all outputs and a limited number of reference channels. In common practice, for testing real large structures with a limited number of sensors several setups are built. Some sensors are moved around, while the others are fixed in the same positions for linking between them the different datasets. The last ones are selected as reference channels in these cases and they should be able to measure the response with the higher modal components for all the modes in the frequency band of interest. Finally the unknown model coefficients  $\alpha_r$  and  $\beta_r$  are obtained by minimizing the differences between the half-spectrum estimated from the measured output and the theoretical one obtained by Equation (2.27). The minimization step can be performed after the linearization of the equation in a least-squares sense. For the mathematical steps, [25] and [24] can be consulted. Once the denominator coefficients  $\alpha_r$  are obtained, the system poles  $\lambda_i$  and the operational reference factors  $g_i$  can be found respectively as the eigenvalues and eigenvectors of their companion matrix. This procedure allows constructing the so-called stabilization diagram for increasing model orders  $p$  and using stability criteria for natural frequencies, damping ratios and operational reference vectors. Natural frequencies and damping ratios can finally be calculated. It is not possible to know in advance which model order needs to be selected for having the best results. The last step of the entire process consists in the calculation of the mode shapes which can be done by using Equation (2.28).

$$[S_{yy}^+(\omega)] = \sum_{i=1}^n \frac{\{v_i\} \langle g_i \rangle}{j\omega - \lambda_i} + \frac{\{v_i^*\} \langle g_i^* \rangle}{j\omega - \lambda_i^*} + \frac{LR}{j\omega} + j\omega UR \quad (2.28)$$

$LR$  and  $UR$  are respectively the lower and upper residuals and they need to be there in order to model the influence of the modes outside of the considered frequency band. Equation (2.28) can be solved in a least-squares sense giving as results the mode shapes  $v_i$  and the residuals. Since the mode shapes are estimated in a second step, the stabilization diagram has to be built before their estimation and it is based exclusively on the poles and operational reference vectors.

## 2.4 OMA vs EMA: advantages and drawbacks

OMA has several advantages if compared to EMA, but it has also some drawbacks [33]. Important advantages are:



- The structure remains in its real operational conditions during OMA and the dynamic of the system is excited in a real-life environment. Normally these conditions are different from the laboratory ones which are less realistic.
- OMA does not require the use of any artificial excitation device. In fact it is based only on the ambient excitation.
- OMA is suitable for being used in continuous monitoring of systems subjected to ambient noise.
- Ambient excitation is causing problems to perform EMA measurements, but it can be used as input for OMA measurements.

The main drawbacks are:

- OMA cannot estimate all modal parameters. As results, the mode shapes remain unscaled. In case of rotating machines, also in case of EMA the mode shapes are unscaled because the right and left eigenvectors are different.
- The main assumption of white noise input is not always respected. If there are peaks in the input spectrum there will be extra peaks in the output data which could be erroneously estimated as structural modes.
- The results could be quite noisy if the ambient excitation is not high enough and if there is a limitation on the available amount of data. This situation will lead to modal parameters which are uncertain.

In case of rotating machines, two more limitations can be underlined distinguishing by stationary operations (constant rotational speed) and transient operations (run-up/coast-down events):

- Stationary conditions: Harmonic components appear in the measured spectra as sharp peaks at fixed frequencies coloring the spectrum of the input forces. These peaks are hampering the identification process and they are masking the dynamics of the system in the frequency range close to the harmonic frequencies.
- Transient conditions: The harmonics are sweeping through a certain frequency band and, when calculating the cross-correlations, before applying the OMA technique, all these contributions are averaged and the excitation could be considered quite flat. On the other hand, it has

been demonstrated [12] that also in this case sharp peaks appear in the spectra. These peaks are in correspondence of the frequencies at which the orders are ending at the maximum rotational speed. Moreover, in case of manually-controlled run-up/coast-down, there can be some rotational speeds at which the machine is rotating longer than at other frequencies. This will also cause the presence of a peak in the spectra. In general, the frequencies at which these sharp peaks appear are identified as natural frequencies by applying any OMA technique. Moreover these peaks mask also the dynamics of the system in a certain range of frequencies. This effect has been named “end-of-order” effect.

## 2.5 Going further: OBMA

Due to its simplicity of use in commercial software and to the fact that often it is rather complicated to perform a complete modal analysis on a structure, nowadays the ODS analysis is widely used in the industrial environment. Its main scope is to understand the behavior of the structure in operating conditions at a particular frequency line (or rotational speed). This is the reason why for rotating machinery applications, this is one of the most used tools. The scope of this dissertation is to demonstrate that both ODS and OMA have some limitations when the objective is the characterization of the dynamic behavior of rotating machines. Some of these problems can be solved using the techniques introduced by [12]. A new method was introduced to apply operational modal identification techniques also to rotating machines during transient operations. The main idea behind the method is that instead of estimating the spectra and apply OMA by using them, the orders can be extracted and used as input for the OMA technique. It can be assumed that the measured responses are mainly caused by the rotational excitation. In this case, run-up and coast-down events can be assimilated to multi-sine sweep excitation in the frequency band of interest.

A deep study has been performed to identify the best practice for OBMA both in terms of Order Tracking (OT) techniques and in terms of their combination with Operational Modal Analysis (OMA). Based on the boundary conditions, on the structure under-test and on the effective operational conditions a technique can be more powerful than another one. The main step for OBMA technique is the order extraction step. Once very good orders have been extracted, the OMA step is quite straightforward and it is giving very good results. The steps needed for performing OBMA in an efficient way can be described as follows:

- selection of the equipment both for measuring the rotational speed (zebra tape, encoders, ...) and the measurement channels (accelerometers, strain

- gauges, ...);
- selection of response degree of freedom;
  - selection of run-up/down conditions;
  - perform preliminary measurements for selecting the most excited orders and the best technique for the order extraction step;
  - data acquisition of interesting orders;
  - data quality analysis to verify if data are good for parameter extraction;
  - modal parameters extraction;
  - verification of obtained modal parameters.

OBMA allows overcoming the limitations of applying classical OMA to the auto- and cross-spectra. A complete analysis can be performed without focusing only on frequency lines selected manually by the users, as done by using the ODS technique. A very important difference which must be underlined at this point is the fact that for ODS the relative phase between the measurement points is enough to understand how the structure is moving at a certain frequency line. This is not true for OBMA which goes one step further and it is going to identify a modal model for the entire structure. So, the orders must be calculated by considering a reference signal  $\Theta(t)$  which is synchronous with the excitation coming from the rotating source. This is one of the main differences also if OBMA is compared with OMA where the reference signal is chosen as one or more of the measurement channels in several directions. The choice of the reference signal for OMA is crucial in order to get a reliable modal model. In the OBMA case this signal has been chosen as a sine sweep with a frequency which is equal to the instantaneous rotational speed  $\omega(t)$  of the machine multiplied by the order  $o_m$  which is going to be extracted, as shown in Equation (2.29).

$$\Theta_m(\tau) = \cos \left( \int_0^\tau o_m \omega(t) dt \right) \quad (2.29)$$

Therefore, for each order a different reference signal has to be considered. There are no doubts about choosing the correct reference signal, as it can be the case for classical OMA.

The Order-Based Modal Analysis technique is extensively described in Chapter 5.



# Chapter 3

## Time variant nature of dynamic systems

This Chapter introduces the concept of time-varying structures. A review of pre-processing techniques to deal with the time variant nature of dynamic systems is given in Section 3.1. An introduction concerning the so-called whirling modes and their origin is given in Section 3.2 Some application cases in the wind turbine domain are shown in Section 3.4.

### 3.1 Time-periodic system techniques

The modal analysis of a wind turbine has been generally handled with the assumption that this structure can be accurately modeled as a Linear Time-Invariant (LTI) system. This assumption can be misleading for stability analysis because of the huge increase in terms of size and power of the new wind turbines. The complex dynamic behavior can be due to the aeroelastic coupling, the nonlinearity and the time-periodic dynamics. Therefore, the time-periodicity needs to be taken into account while estimating the modal parameters of operating wind turbines. Of course, it is quite difficult to measure the input forces acting on this kind of structure, so for this purpose OMA seems to be the best technique. OMA application on parked wind turbines is a straightforward task. In fact such a structure can be considered as a bridge, a building or a stadium since there are no rotating parts in these conditions. The OMA assumption are fulfilled as the wind excitation can be considered as a white noise broadband excitation. Problems arise when the wind turbine is in operating

conditions. In fact such a structure is a Linear Time Variant (LTV) system or a Linear Time Periodic (LTP) one if the rotational speed is constant. Moreover the rotor rotation introduces peaks at the rotational frequency and at its integer multiples (the most dominant is the 3P component, also known as blade passing frequency: every time a full rotation of the rotor is completed three blades are passing in front of the tower). In this way the excitation is not random and broadband as needed. The harmonic excitation can cover the dynamics of the system and needs to be filtered out by using, for example, an harmonic removal tool. In order to overcome these problems, several techniques have been developed mainly for wind turbine rotor analysis, but they could also be extended to helicopter rotor analysis:

- Floquet analysis;
- Multi-Blade Coordinate transformation (MBC);
- Harmonic Power Spectrum method (HPS).

### 3.1.1 Floquet theory

#### Dynamic model

Dynamic systems can be represented in several ways. One of the most common way to represent such a system is the state-space representation which can be written in continuous-time [34] as shown in Equation (3.1).

$$\begin{aligned}\dot{x}(t) &= A(t)x(t) + v(t) \\ y(t) &= C(t)x(t) + w(t)\end{aligned}\tag{3.1}$$

$x(t)$  is the state vector and  $y(t)$  the output vector. The first equation is named the state equation and the second one is known as the observation or output equation. The vector  $v(t)$  and  $w(t)$  are the two noise processes represented by white Gaussian noise. Finally, the matrices  $A(t)$  and  $C(t)$  are respectively named the dynamic matrix and the observation matrix. If these matrices contain periodic terms with a period  $T$ , then the system can be considered as periodic. The system periodicity condition is shown in Equation (3.2).

$$\begin{aligned}A(t+T) &= A(t) \\ C(t+T) &= C(t)\end{aligned}\tag{3.2}$$

In general, the period of the system  $T$  is related to the constant rotation speed of the machine  $\omega$ , as shown in Equation (3.3).

$$T = \frac{2\pi}{\omega} \quad (3.3)$$

### Floquet modal analysis

The Floquet theory is a mathematical theory of Ordinary Differential Equations (ODE) with time-periodic coefficients. Therefore, it can be used in case of constant rotational speed for a wind turbine in operating conditions. It was introduced by Floquet [5] and it is the first complete theory for the class of periodically time-varying systems. The key steps are recalled here, but more details can be found in [6]. Let's start considering the periodic differential system (Equation (3.4)).

$$\dot{x}(t) = A(t)x(t) \quad (3.4)$$

$x(t)$  is again the state vector and  $A(t)$  is the transition matrix which is continuous in time and periodic with period  $T > 0$ :  $A(t + T) = A(t)$ .

If the independent variable  $t$  is replaced by  $t + T$ , the system (3.4) remains invariant. Therefore, if  $x(t)$  is a solution vector of the system, then also the vector  $x(t + T)$  will be a solution of the same system. This observation may be stated conveniently in terms of fundamental solution matrices.

Let  $X(t)$  be a fundamental solution matrix of (3.4).  $X(t)$  is a matrix with each of its columns consisting of a linearly independent solution vector of (3.4). This is also known as fundamental transition matrix. In particular, the  $i^{th}$  column vector can be chosen such that it satisfies an initial condition for which each of the scalar components of  $x(0)$  is equal to zero, except for the  $i^{th}$  scalar component which is unity. This gives  $X(0) = I$ , where  $I$  is the identity matrix. The columns of  $X(t)$  are linearly independent and for this reason they form a basis for the solution space of (3.4). Thus, any other fundamental solution matrix  $Z(t)$  may be written as in Equation (3.5).

$$Z(t) = X(t)C \quad (3.5)$$

$C$  is a nonsingular matrix. Equation (3.5) means that each of the column of  $Z(t)$  may be written as a linear combination of the columns of  $X(t)$ .

Replacing  $t$  by  $t + T$  in  $X(t)$  produces a new fundamental solution matrix  $X(t + T)$ . At this point, each of the columns of  $X(t + T)$  may be written as a linear combination of the columns of  $X(t)$ , as shown in Equation (3.6).

$$X(t + T) = X(t)C \quad (3.6)$$

It can be noted that at  $t = 0$ , Equation (3.6) becomes Equation (3.7).

$$X(T) = X(0)C = IC = C \quad (3.7)$$

Equation (3.7) states that the matrix  $C$ , also known as monodromy matrix, is equal to the value of the fundamental solution matrix  $X(t)$  evaluated at the time  $T$ , which means after one period.

In order to solve Equation (3.6), the transformation to normal coordinates is needed. Let  $Y(t)$  be another fundamental solution matrix. Each of its columns can be written as a linear combination of the columns of  $X(t)$ , as shown in Equation (3.8).

$$Y(T) = X(T)R \quad (3.8)$$

$R$  is an unknown nonsingular matrix. Combining together Equation (3.6) and (3.8), we obtain Equation (3.9).

$$Y(t + T) = Y(t)R^{-1}CR \quad (3.9)$$

Let us suppose that the matrix  $C$  has  $n$  linearly independent eigenvectors. If the columns of  $R$  are chosen as these  $n$  eigenvectors, then the matrix product  $R^{-1}CR$  becomes a diagonal matrix with the eigenvalues  $\lambda_i$  of  $C$  on its main diagonal. These eigenvalues are also known as the characteristic multipliers of the system. A Floquet exponent is a complex  $\mu$  such that  $e^{\mu T}$  is a characteristic multiplier of the system. It can be noticed that Floquet exponents are not unique since Equation 3.10 is valid for  $k$  integers.

$$e^{(\mu + \frac{2\pi ik}{T})} = e^{\mu T} \quad (3.10)$$

### Floquet stability analysis

The stability analysis of a periodic system is based on the Floquet exponents. In order to establish if a system is stable or unstable, the real parts of the Floquet exponents (also known as Lyapunov exponents) need to be evaluated and the following statements are valid:



- If all the damping ratios are positive (or all the Floquet exponents have negative real parts), then the system is asymptotically stable (all the solutions converge to the null solution).
- If there exists a damping ratio negative (or a Floquet exponent with a positive real part), then the system is unstable (there is a solution diverging from the null solution).
- If some damping ratios are null (or some Floquet exponents have null real parts), then the system is in a critical state of neutral stability: it can be stable or unstable.

### 3.1.2 Multi-Blade Coordinate transformation (MBC)

A different approach for performing modal and stability analysis in case of operating wind turbines was developed by Bir [7]. Under isotropy assumption, the system can be approximated by a LTI model where the equations of motion are written in the whirling coordinate frame. This transformation is known as Multi-Blade Coordinate (MBC) transformation or Coleman transformation [8]. Initially MBC was proposed for helicopter analysis and then it was extended for wind turbine applications. Coleman used this method to analyze the rotor-in-plane motion, also known as lag motion, and he was able to identify the ground resonance problem. Johnson [35] was the first one to give a mathematical basis to the MBC and Bir [36] developed a numerical MBC approach providing insights into the rotor in-plane motion. Hansen [37] started applying the technique to a three-bladed wind turbine and, then, MBC was used to study aeroelastic characteristics of a 5-MW wind turbine in different configurations [38]. This work was based on several assumptions: the three blades have to be identical both aerodynamically and structurally and the rotor speed must be constant. In order to overcome these limitations, in successive studies, a new approach was developed [7]. The transformation allows to convert the rotating Degrees-Of-Freedom (DOFs) into a non-rotating frame. This technique offers several benefits. In fact, first of all, it properly models the dynamic interaction between the non-rotating system entities (tower, nacelle, etc.) and the spinning rotor. Secondly, it offers physical insights into rotor dynamics and how the rotor is interacting with wind, controls and tower-nacelle substructure. Finally, MBC allows to filter out all periodic terms except those ones which are multiple of  $\Omega N$ , where  $\Omega$  is the rotor angular speed and  $N$  is the number of blades (in the wind turbine case it is normally equal to 3). A wind turbine can be considered as a periodic system if the angular speed is constant. In this case, the blade equations usually contain all the harmonics, while the equations in the new reference frame only contain a subset of these harmonics. It can be stated that

MBC acts as a filter and this filtering renders the system equations numerically well-conditioned because all non-essential periodic terms are filtered out. In order to eliminate all the periodic terms (including the  $3\Omega$  component), the MBC approach should be combined with the previously mentioned Floquet theory or with a harmonic removal tool. Let us consider a rotor with 3 blades, which is the typical wind turbine rotor. First of all we need to assume that the three blades are equally spaced around the rotor azimuth. In this case, the azimuth angle of the  $b$ -th blade can be obtained using Equation (3.11).  $\psi_1$  is the instantaneous azimuth angle of a blade considered as the reference one. When this blade is vertically up, then  $\psi_1 = 0$ .

$$\psi_b = \psi_1 + (b - 1)\frac{2\pi}{3}, b = 1, 2, 3 \quad (3.11)$$

Let us consider  $q_{b,i}$  as a particular rotating DOF for the  $b$ -th blade. For instance, it could be an acceleration in a certain direction measured by a sensor placed at the location  $i$  along the blade. The MBC is a linear transformation which allows to move from the rotating blade coordinate system to the multi-blade non-rotating one, as shown in Equation (3.12).

$$\begin{aligned} q_{0,i} &= \frac{1}{N} \sum_{b=1}^N q_{b,i} \\ q_{c,i} &= \frac{2}{N} \sum_{b=1}^N q_{b,i} \cos \psi_b \\ q_{s,i} &= \frac{2}{N} \sum_{b=1}^N q_{b,i} \sin \psi_b \end{aligned} \quad (3.12)$$

It is quite difficult to give a physical interpretation of these new coordinates. They actually depend upon the considered DOF. A first distinction can be done between the first coordinate that represents the collective symmetric behavior of the blades, and the other two coordinates which describe the asymmetric one. For example, two different cases can be described:

- $q_b$ =flapwise DOF:
  - $q_0$ =rotor coning
  - $q_c$ =rotor fore-aft tilt about an horizontal axis normal to the rotor shaft

- $q_s$ =rotor side-side tilt about a vertical axis normal to the rotor shaft
- $q_b$ =edgewise DOF:
  - $q_0$ =rotor collective edgewise
  - $q_c$ =horizontal displacement of the rotor center of mass in the rotor plane
  - $q_s$ =vertical displacement of the rotor center of mass in the rotor plane

Most of the wind turbines in the world have nowadays 3 blades, therefore we can assume  $N = 3$  and obtain Equation (3.13) and consider these equations in the rest of the discussion.

$$\begin{aligned}
 q_{0,i} &= \frac{1}{3} \sum_{b=1}^3 q_{b,i} \\
 q_{c,i} &= \frac{2}{3} \sum_{b=1}^3 q_{b,i} \cos \psi_b \\
 q_{s,i} &= \frac{2}{3} \sum_{b=1}^3 q_{b,i} \sin \psi_b
 \end{aligned} \tag{3.13}$$

At this point,  $q_0$  can be defined as the coning mode,  $q_c$  and  $q_s$  are respectively the cosine and sine cyclic modes. The last equations allow to transform the blade coordinates into the new reference system. The inverse transformation which is shown in Equation (3.14) is needed in order to get back to the blade coordinates.

$$q_{b,i} = q_{0,i} + q_{c,i} \cos \psi_b + q_{s,i} \sin \psi_b \tag{3.14}$$

Concluding, it can be stated that in order to perform OMA on an operating wind turbine, a possible solution is the use of MBC transformation prior the estimation of the modal parameters. The procedure to be followed can be synthesized in the next steps and it is also summarized in Figure 3.1:

- acquire data (i.e. accelerations, strains, etc.) at several locations along the blades and along the tower-nacelle;

- apply MBC transformation to the blade data by using Equation 3.13 and by taking into account the measured azimuth angle;
- combine the two set of data (multi-blade and tower-nacelle) and perform OMA by using Operational Polymax for estimating natural frequencies, damping ratios and multi-blade mode shapes;
- apply Equation 3.14 to come back to the physical coordinates in order to animate the mode shapes and give them a proper interpretation.

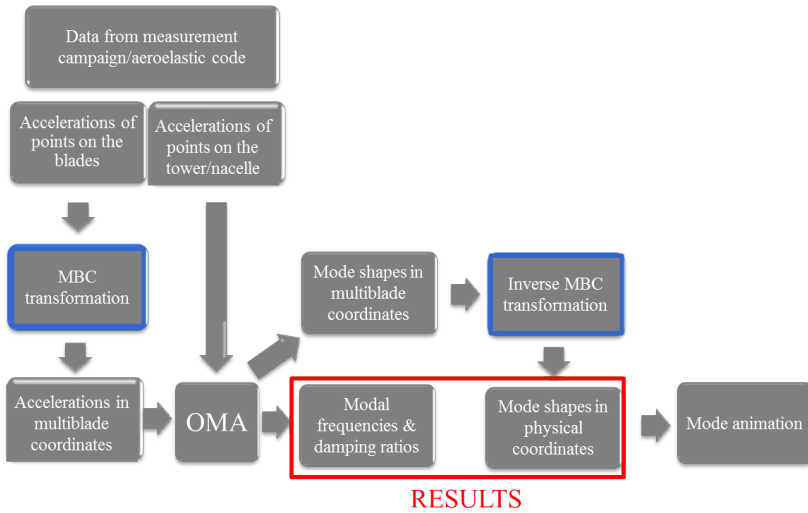


Figure 3.1: Multi-Blade Coordinate transformation flowchart for OMA application

Several studies demonstrated the applicability of this procedure to wind turbines in operating conditions built by using aeroelastic codes [39], [40]. The same technique has also been applied in the experimental field, where some more difficulties were encountered [41], [42]. In the literature several misconceptions regarding MBC are frequently arisen both in the helicopter and wind turbine fields:

- The rotor must spin at constant speed
- MBC transforms a time-variant system into a time-invariant one
- The rotor blades must have identical structural and aerodynamic properties

These three statements are all false. In fact, MBC relations are derived assuming that the rotor speed  $\Omega$  varies with the time. MBC is thus applicable to variable-speed turbines. The second statement is also often used in the literature, but it is not fully true. In fact MBC does not eliminate all the periodic terms, so it does not transform the system into a time-invariant one. In order to get a LTI system, a harmonic removal tool (or the Floquet theory) needs to be used. It can be stated that MBC acts like a filter since it lets through terms that are integral multiples of  $3\Omega$  and filters out all the other periodic terms. This is true if we assume that the blades are identical and that the operating conditions are not varying with the time. On the other hand, while deriving the MBC transformation equations, any assumption has been made concerning the isotropy of the rotor blades. It means that it is not needed to have equal blades both structurally and aerodynamically. Of course, these dissimilarities will be reflected in the system matrices and MBC will not be able to filter out any periodic term, even the ones which are not multiple of  $3\Omega$ . Therefore, harmonics will continue being present in the data and this will not be compliant with the OMA assumptions. The only restriction assumed in the derivation of the equations is that the blades must be equally spaced around the rotor azimuth. On the other hand, these dissimilarities could be used to eventually detect the presence of anisotropies in the rotor during its operating cycles.

### 3.1.3 Harmonic Power Spectrum method (HPS)

Wereley [9] introduced a linear operator or transfer function for LTP systems which is completely analogous to the well-known transfer function for LTI systems. In general, the dynamics of a LTI system can be described in the time domain by a  $n$ -th order matrix differential equation with constant coefficients. In steady state conditions, the response of a LTI system to a sinusoidal input (or complex exponential signal) of a given frequency is a sinusoidal output signal of the same frequency, but with possibly different amplitude and phase. In these conditions the Laplace transform can be applied for deriving the LTI transfer function. The Bode diagrams can be obtained by computing the magnitude and the phase of the complex-valued LTI transfer function over the frequency range of interest. The same concepts are not applicable for LTP systems in a straightforward manner.

In order to underline the differences, we can consider an example of LTP system represented by the amplitude modulation of a signal, as shown in Figure 3.2.

The amplitude modulation takes place at the so-called pumping frequency  $\omega_A$ . In case of a sinusoidal input (which can be represented by an exponential input signal), the output signal is obtained as the sum of three complex exponential, as shown in Equation (3.15).

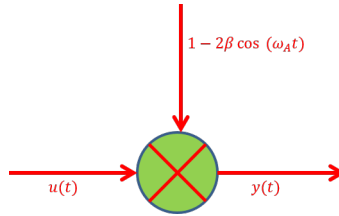


Figure 3.2: Amplitude modulation

$$y(t) = e^{st} - \beta e^{(s-j\omega_A)t} - \beta e^{(s+j\omega_A)t} \quad (3.15)$$

Therefore, when such an input is injected into a LTP system, several harmonics of the pumping frequency may appear in the output signal, all modulated by the input complex exponential. So the LTP system maps a complex exponential to a complex exponential modulation of a possibly infinite number of harmonics of the pumping frequency. Wereley addressed this difficulty using an Exponentially Modulated Periodic (EMP) signal space in which  $u(t)$  and  $y(t)$  are represented by Equation (3.16).

$$u(t) = \sum_{n=-\infty}^{\infty} u_n e^{(j\omega + jn\omega_A)t} \quad (3.16)$$

$$y(t) = \sum_{n=-\infty}^{\infty} y_n e^{(j\omega + jn\omega_A)t}$$

An EMP input signal will cause an EMP output signal, with possibly different magnitude and phase at each frequency.

In this way, the transfer function concept becomes completely analogous to the LTI case and the so-called Harmonic Transfer Function (HTF) can be defined. The main difference between the two transfer functions is that the standard one relates the output at a single frequency to the input at the same frequency, whereas the HTF relates the input at a collection of frequencies each separated by  $\omega_A$  to the output at the same collection of frequencies. Theoretically, an infinite number of harmonics should be used for characterizing a LTP system, but practically most systems can be approximated by a finite, even small, number of harmonics. For LTI systems, the Power Spectrum (PS) is the correspondent of the Transfer Function (TF) in case of output-only systems. The PS is expressed in Equation (3.17).

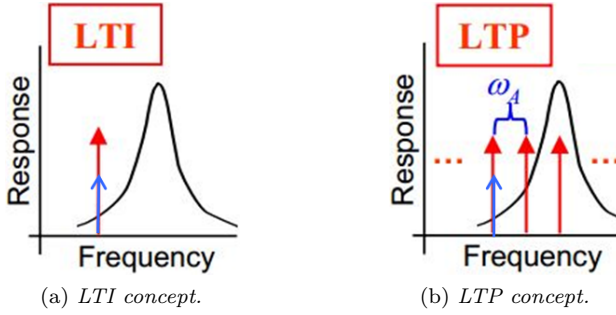


Figure 3.3: LTI vs LTP systems.

$$S_{yy}(\omega) = E(Y(\omega)Y(\omega)^H) = \sum_{r=1}^N \frac{\psi_r S_{uu}(\omega) \psi_r^H}{[j\omega - \lambda_r][j\omega - \lambda_r]^*} \quad (3.17)$$

This function has a peak in the spectrum when the excitation frequency  $\omega$  is close to a natural frequency and this peak can be curve-fitted in order to identify the modal parameters (natural frequencies, damping ratios and mode shapes). The same approach can be considered for LTP systems. In this case, the Harmonic Power Spectrum (HPS) can be defined in an analogous manner, as shown in Equation (3.18).

$$S_{yy}(\omega) = E(Y(\omega)Y(\omega)^H) = \sum_{r=1}^N \sum_{l=-\infty}^{\infty} \frac{\bar{C}_{r,l} W(\omega)_l \bar{C}_{r,l}^H}{[j\omega - (\lambda_r - jl\Omega)][j\omega - (\lambda_r - jl\Omega)]^H} \quad (3.18)$$

The procedure for obtaining such a signal remains the same: the EMP signal is divided into several blocks, a Hanning window can be applied and the Discrete Fourier Transform (DFT) of each block is performed and finally an averaging step is needed. The formula is shown in Equation (3.18) where  $E$  denotes the expectation and  $^H$  indicates the Hermitian operator.  $Y(\omega)$  is the frequency domain representation of the EMP output signal. The terms  $W(\omega)_r$  is a function of the input spectrum and the characteristic of the system. As valid also for LTI systems, the autospectrum of the output can be approximated by a sum of modal contributions if the excitation is reasonably flat in the frequency band of interest (white noise input assumption). The terms  $\lambda_r - jl\Omega$  cause the HPS to have a peak near the system's eigenvalues or Floquet exponents  $\lambda_r$  and also at the eigenvalue plus some integer multiple of the fundamental frequency  $l$ . On

the other hand, the mode vector  $\overline{C}_{r,l}$  is not the typical mode vector describing the mode shape at different points. It contains the Fourier coefficients for the  $r$ -th mode but with the position of the elements shifted by  $l$  in the coefficient vector [10].

Also in this case, we can summarize the steps needed for applying the HPS method in a practical case. Figure 3.4 shows the applicability scheme of the technique.

- acquire data (i.e. accelerations, strains, etc.) at several locations along the blades and along the tower-nacelle;
- construct the EMP signal by considering shifted copies of the output signal  $y(t)$ ;
- compute the autospectrum of the EMP signal by averaging multiple blocks of the time history;
- use Operational Polymax system identification technique to estimate the modal parameters from the autospectrum;
- reconstruct the time-periodic mode shapes using the identified Fourier coefficients  $\overline{C}_{r,l}$ .

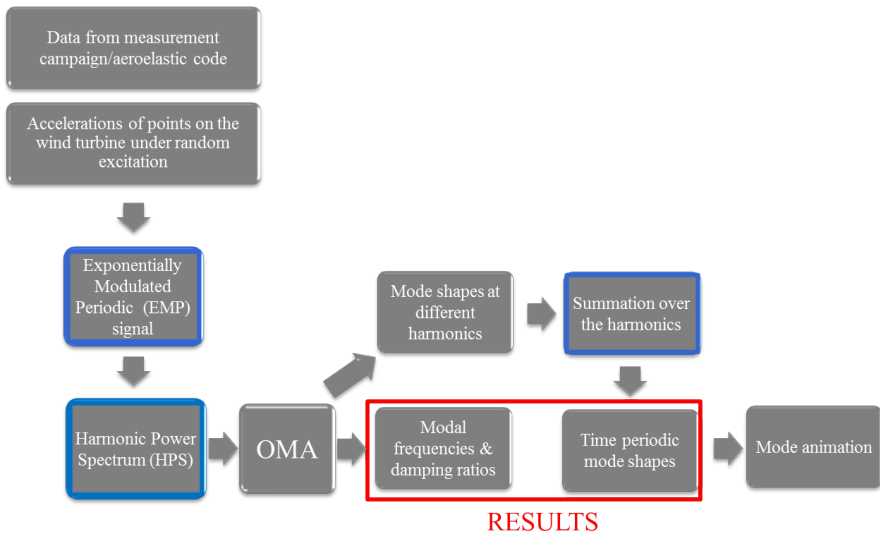


Figure 3.4: Harmonic Power Spectrum flowchart for OMA application



This technique has also been applied in several cases both in simulation and test environment and demonstrated to help the user to identify differences in modal parameters.

## 3.2 Whirling mode definition

A well-known phenomenon occurring in case of rotating machines such as wind turbines is the so-called whirling phenomenon. The whirl mode behavior is associated with the rotor shaft whirl and with the in-plane (or edgewise) motion of the blades. This phenomenon started receiving a lot of attention in the last years because it can lead to high vibration levels. In order to fully understand it, Bir [16] developed an analytical formulation. In his work he shows that the whirl-causing force is generated by two cyclic in-plane modes of the rotor. In a single-frequency whirl mode, the rotating force vector on the shaft is a resultant of two components: a regressive force vector rotating at lower frequency and a progressive force vector rotating at higher frequency. Therefore, the resultant force vector, when observed with respect to the spinning rotor, traces an elliptical path.

In a wind turbine, the rotor modes can be grouped in three categories: flapwise motion (out-of-rotor-plane motion), edgewise motion (rotor-in-plane motion) and blade torsion motion. Flapwise modes are usually dominant in wind turbines, but they are well aerodynamically damped. Torsion modes are normally at very high frequencies if compared to the ones of the other modes and also have low amplitudes. As consequence, there are not many concerns about them. Finally, dominant edgewise modes must be carefully avoided because they can lead to aeroelastic instabilities. These modes are associated with the whirl mechanism. In 1994 the first problem related with this mechanism was observed. In fact a stall-induced excessive edgewise vibration was reported on a 500kW wind turbine [43]. In the next years, considering also the increasing diameter of the new wind turbines, this problem gained importance and several studies tried to understand the low aerodynamic damping associated with edgewise modes [44], [45], [46]. It has been demonstrated that there is a significant coupling between the local edgewise blade modes (also known as local blade whirl modes) and the global rotor whirl modes. In other words, the local blade whirl is the deformation associated with the in-plane inertia force which describes an elliptical path in the rotor plane. On the other hand, the global rotor whirl represents the hub movement along an elliptical orbit when the rotor tilt-yaw modes are excited. The main concern is the interaction between these two phenomena. These two frequencies should be very well separated and certain frequency ranges should be totally avoided.

### 3.3 Whirl mechanism

Let us consider the wind turbine model shown in Figure 3.5. The  $x_H$  and  $y_H$  represent the hub-centered axes that do not rotate with the rotor, while  $x_R$  is an axis directed along blade 1 and rotates with it.  $y_R$  is perpendicular to it in the rotor plane. The azimuth angle can be obtained by using equation 3.11. We will be focusing mainly on the first blades mode which shows a dominant edgewise component, the so-called edgewise mode. This mode will also have a very small contribution from the flap and twist motion, but this will be ignored.

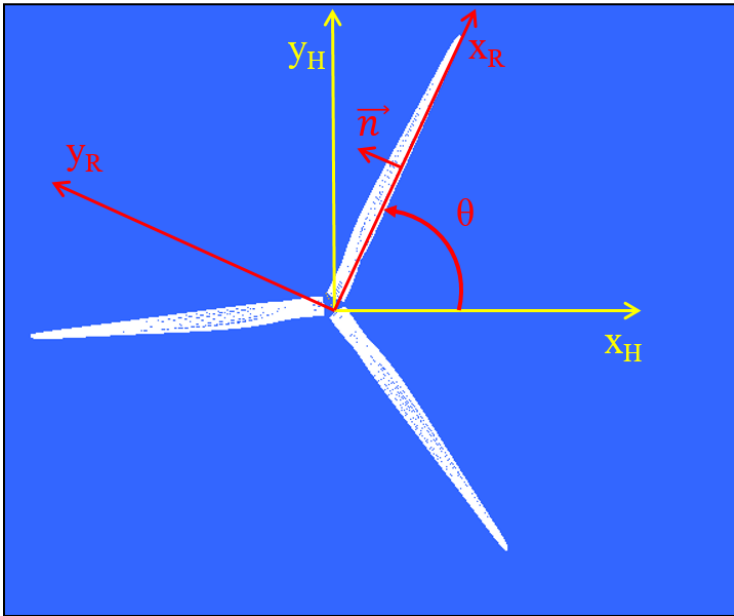


Figure 3.5: Wind turbine model

$\phi_r$  is the edgewise displacement in this mode. This displacement can be normalized such that  $\phi(r) = 1$ .  $r$  represents the distance along the blade measured from the hub center.  $v_b(r, t)$  is the edgewise displacement of the rotating blade  $b$  at radial location  $r$  and time  $t$ . The blade mass per unit length at this location can be indicated as  $m(r)$ . At this point we can calculate the differential inertia force normal to and along the blade, as shown in Equation (3.19).

$$\begin{aligned} dF_n^b &= m(\Omega^2 v_b - \ddot{v}_b) dr \\ dF_t^b &= m\Omega^2 r dr \end{aligned} \quad (3.19)$$

The components of the centrifugal force perpendicular to and along the blade have been considered in Equation (3.19). According to the definitions introduced for the MBC transformation,  $q_b$  are the tip deflections of the blades at the time  $t$ , where  $b = 1, 2, 3$ . The displacements in the rotor plane along the blade  $b$  can be expressed as in Equation (3.20).

$$v_b(r, t) = \phi(r)q_b(t) \quad (3.20)$$

Integrating Equation (3.19) along the blade and taking into account Equation (3.20), we can get the in-plane forces on blade  $b$  (Equation (3.21)).

$$\begin{aligned} F_n^b &= M_B(\Omega^2 q_b - \ddot{q}_b) \\ F_t^b &= S_B \Omega^2 \end{aligned} \quad (3.21)$$

$M_B$  is the blade modal mass and  $S_B$  is its first mass moment of inertia about the root. Assuming that the three blades are equally spaced in the rotor plane (one blade each  $120^\circ$ ), then the force components along the  $x_R$  and  $y_R$  axes are given by Equation (3.22).

$$\begin{pmatrix} F_{x_R} \\ F_{y_R} \end{pmatrix} = \begin{bmatrix} 0 & -\sin 120^\circ & -\sin 240^\circ \\ 1 & \cos 120^\circ & \cos 240^\circ \end{bmatrix} \begin{pmatrix} F_n^1 \\ F_n^2 \\ F_n^3 \end{pmatrix} + \begin{bmatrix} 0 & \cos 120^\circ & \cos 240^\circ \\ 1 & \sin 120^\circ & \sin 240^\circ \end{bmatrix} \begin{pmatrix} S_B \Omega^2 \\ S_B \Omega^2 \\ S_B \Omega^2 \end{pmatrix} \quad (3.22)$$

The last part of Equation (3.22) vanishes, so the equation can be simplified to Equation (3.23).

$$\begin{pmatrix} F_{x_R} \\ F_{y_R} \end{pmatrix} = \begin{bmatrix} 0 & -\frac{\sqrt{3}}{2} & -\frac{\sqrt{3}}{2} \\ 1 & -\frac{1}{2} & -\frac{1}{2} \end{bmatrix} \begin{pmatrix} F_n^1 \\ F_n^2 \\ F_n^3 \end{pmatrix} \quad (3.23)$$

The tip displacements can be explicated in Equation (3.24).

$$\begin{pmatrix} q_1(t) \\ q_2(t) \\ q_3(t) \end{pmatrix} = \begin{pmatrix} 1 \\ 1 \\ 1 \end{pmatrix} q_0(t) + \begin{pmatrix} \frac{2}{\sqrt{6}} \\ -\frac{1}{\sqrt{6}} \\ -\frac{1}{\sqrt{6}} \end{pmatrix} q_c(t) + \begin{pmatrix} 0 \\ \frac{1}{\sqrt{2}} \\ -\frac{1}{\sqrt{2}} \end{pmatrix} q_s(t) \quad (3.24)$$

where

$$\begin{pmatrix} q_0(t) \\ q_c(t) \\ q_s(t) \end{pmatrix} = \begin{bmatrix} \frac{1}{3} & \frac{1}{3} & \frac{1}{3} \\ \frac{2}{\sqrt{6}} & -\frac{1}{\sqrt{6}} & -\frac{1}{\sqrt{6}} \\ 0 & \frac{1}{\sqrt{2}} & -\frac{1}{\sqrt{2}} \end{bmatrix} \begin{pmatrix} q_1(t) \\ q_2(t) \\ q_3(t) \end{pmatrix} \quad (3.25)$$

The column vectors associated with  $q_0$ ,  $q_c$  and  $q_s$  have a physical meaning. For instance, the one associated with  $q_c$  represents the ratio of the three blade tip displacements if the blades were assumed stationary and the hub was oscillating around the  $y_R$  direction in the rotor plane. On the other hand, the one associated with  $q_s$  represents the same but referred to the  $x_R$  direction in the rotor plane. Finally the vector associated with  $q_0$  represents the ratio of the blade tip displacements if the hub was oscillating about the  $z_R$  axis normal to the rotor plane. The three equations are linearly independent and relate the blade coordinates  $q_1$ ,  $q_2$  and  $q_3$  with the rotor coordinates  $q_0$ ,  $q_c$  and  $q_s$ . If the blades are vibrating at a frequency  $\omega$ , the rotor coordinates can be written as in Equation (3.26).

$$\begin{aligned} q_0 &= Q_0 \sin(\omega t + \alpha_0) \\ q_c &= Q_c \sin(\omega t + \alpha_c) \\ q_s &= Q_s \sin(\omega t + \alpha_s) \end{aligned} \quad (3.26)$$

Combining together Equation (3.23) and Equation (3.24) we can write Equation (3.27).

$$\begin{pmatrix} F_{x_R} \\ F_{y_R} \end{pmatrix} = M_B(\Omega^2 + \omega^2) \begin{bmatrix} 0 & -\frac{\sqrt{3}}{2} & -\frac{\sqrt{3}}{2} \\ 1 & -\frac{1}{2} & -\frac{1}{2} \end{bmatrix} \begin{bmatrix} 1 & \frac{2}{\sqrt{6}} & 0 \\ 1 & -\frac{1}{\sqrt{6}} & \frac{1}{\sqrt{2}} \\ 1 & -\frac{1}{\sqrt{6}} & -\frac{1}{\sqrt{2}} \end{bmatrix} \begin{pmatrix} Q_0 \sin(\omega t + \alpha_0) \\ Q_c \sin(\omega t + \alpha_c) \\ Q_s \sin(\omega t + \alpha_s) \end{pmatrix} \quad (3.27)$$

With some simplifications, the resultant of the in-plane forces describes an elliptical path if observed in the  $x_R - y_R$  reference frame which is rotating with the rotor. This is shown in Equation (3.28).

$$\vec{F} = \begin{pmatrix} F_{x_R} \\ F_{y_R} \end{pmatrix} = \sqrt{3/2}M_B(\Omega^2 + \omega^2) \begin{pmatrix} -Q_s \sin(\omega t + \alpha_s) \\ Q_c \sin(\omega t + \alpha_c) \end{pmatrix} \quad (3.28)$$

This force is represented by two counter-rotating vectors of constant amplitude. Let's define  $F_p$  as the magnitude of the vector rotating in the same direction as the rotor (progressive whirling force) and  $F_r$  the one of the counter-rotating vector (regressive whirling force). The projection of  $F_p$  and  $F_r$  onto the  $x_R$  and  $y_R$  axes can be put equal to the projection of the resultant  $F_R$  obtaining Equation (3.29).

$$\begin{pmatrix} F_{x_R} \\ F_{y_R} \end{pmatrix} = \begin{bmatrix} \cos(\omega t + \alpha_p) & \cos(\omega t + \alpha_r) \\ \sin(\omega t + \alpha_p) & -\sin(\omega t + \alpha_r) \end{bmatrix} \begin{pmatrix} F_p \\ F_r \end{pmatrix} \quad (3.29)$$

All these observations are true in a frame which is spinning with the rotor, but it is quite important to understand how the whirling forces and the associated motion are appearing in a fixed reference frame  $x_H$  and  $y_H$  which is non-rotating even if the rotor is spinning. Equation (3.30) can be written.

$$\begin{pmatrix} F_{x_H} \\ F_{y_H} \end{pmatrix} = \begin{bmatrix} \cos(\Omega t) & -\sin(\Omega t) \\ \sin(\Omega t) & \cos(\Omega t) \end{bmatrix} \begin{pmatrix} F_{x_R} \\ F_{y_R} \end{pmatrix} \quad (3.30)$$

Combining together Equation (3.29) and Equation (3.30) yields to Equation (3.31).

$$\begin{pmatrix} F_{x_H} \\ F_{y_H} \end{pmatrix} = \begin{bmatrix} \cos[(\omega + \Omega)t + \alpha_p] & \cos[(\omega - \Omega)t + \alpha_r] \\ \sin[(\omega + \Omega)t + \alpha_p] & -\sin[(\omega - \Omega)t + \alpha_r] \end{bmatrix} \begin{pmatrix} F_p \\ F_r \end{pmatrix} \quad (3.31)$$

Therefore, it can be concluded that in a non-rotating reference frame the resultant force is represented by two circularly orbiting forces: a progressive force  $F_p$  that whirls in the same direction as the rotor at an angular speed  $\omega + \Omega$  and a regressive force  $F_r$  that whirls in the opposite direction at a lower angular speed of  $\omega - \Omega$ . This is clearly shown in Figure 3.6

In the rotor dynamic field it is convenient to refer the equations to a fixed reference system. In the wind turbine domain and in the rotorcraft one is very common the introduction of the multiblade coordinates for this purpose.

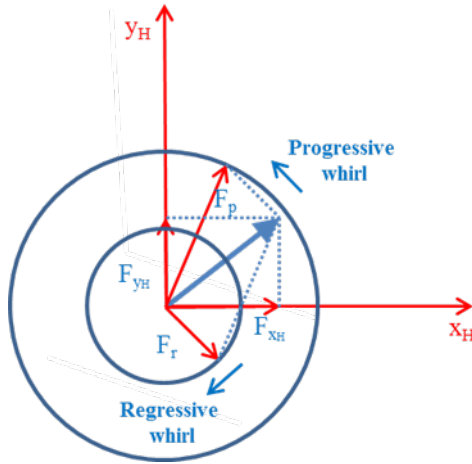


Figure 3.6: Whirling forces illustration

### 3.4 Application cases

In order to prove the applicability of these methods, several models have been built. The first one that will be presented is a simple 2D model developed by using Matlab. Afterwards, two full wind turbine models will be introduced. They have been built by using Samcef Wind Turbines (SWT) and represent respectively a 5 MW and a 10 MW wind turbines. The first one has been proposed by the National Renewable Energy Laboratory (NREL) in the US [47] and the second one by the DTU Wind Energy in Denmark [48].

#### 3.4.1 2D model

The 2D wind turbine model consists of a 5 Degree-Of-Freedom (DOF) three-bladed rotor system in which each blade is modelled as a two beams assembly [49]. It is shown in Figure 3.7. The beams are connected by means of a hinge with a linear angular spring with stiffness  $k_j$ , where  $j$  stands for the blade index ( $j = 1, 2, 3$ ). A lumped mass  $m_j$  is attached at the end of the outer beam. Finally the rotor is attached to the tower modelled by using two springs with stiffness  $k_H$  and  $k_V$  in the horizontal (H) and vertical (V) directions and with a mass  $m_T$ .  $r_1$  represents the distance between the root of the blade and the torsional spring location.  $r_2$  is the distance between the torsional spring and the blade tip.  $R$  is the rotor radius. The blades are evenly distributed over the rotor.  $\Omega$  represents the angular speed at which the rotor is spinning around

the point C. The value of all the parameters are chosen in order to reproduce the ones of the DTU 10 MW reference wind turbine. They are shown in Table 3.1. The vector  $y$  represents the 5 DOFs of the system:  $\phi_1$ ,  $\phi_2$  and  $\phi_3$  are the rotations of the three blades,  $x_H$  and  $x_V$  are the translational movements of the mass  $m_T$  in the horizontal and vertical directions.

$$y = \{\phi_1; \phi_2; \phi_3; x_H; x_V\}^T \quad (3.32)$$

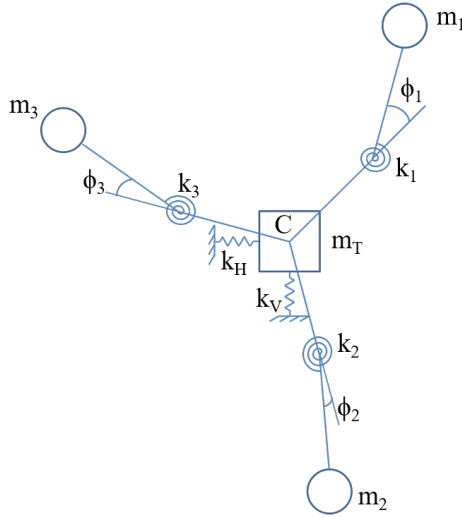


Figure 3.7: 2D model representation

Parameter	Value
$m_1 = m_2 = m_3$	$41.7 * 10^3 kg$
$m_T$	$446 * 10^3 kg$
$k_1 = k_2 = k_3$	$2.01 * 10^8 N * m/rad$
$k_H$	$2.6 * 10^6 N/m$
$k_V$	$5.2 * 10^8 N/m$

Table 3.1: 2D model specifications

## Equations of motion

This section shows the construction of the equations of motion which are describing the wind turbine model in operating conditions. If the blades are not rotating ( $\Omega = 0$ ), the centrifugal forces are in equilibrium. When the blades are rotating at a speed equal to  $\Omega$ , several terms appear in the stiffness matrix in Equation (3.33) which is obtained by evaluating the direct and coupled reactions.

$$K = \begin{bmatrix} k_1 + \frac{1}{2}m_1\Omega^2 Rr_2 & 0 & 0 & 0 & 0 \\ 0 & k_2 + \frac{1}{2}m_2\Omega^2 Rr_2 & 0 & 0 & 0 \\ 0 & 0 & k_3 + \frac{1}{2}m_3\Omega^2 Rr_2 & 0 & 0 \\ -\frac{1}{2}m_1\Omega^2 R \cos \psi_1 & -\frac{1}{2}m_2\Omega^2 R \cos \psi_2 & -\frac{1}{2}m_3\Omega^2 R \cos \psi_3 & k_H & 0 \\ \frac{1}{2}m_1\Omega^2 R \sin \psi_1 & +\frac{1}{2}m_2\Omega^2 R \sin \psi_2 & +\frac{1}{2}m_3\Omega^2 R \sin \psi_3 & 0 & k_V \end{bmatrix} \quad (3.33)$$

In order to linearize the problem, the hypothesis of small deformation needs to be done. According to this hypothesis, the Equations (3.34) are valid.

$$\begin{aligned} \sin(\phi_i) &= \phi_i \\ \cos(\phi_i) &= 1 \end{aligned} \quad (3.34)$$

Several observations can be listed:

- The centrifugal forces  $\frac{1}{2}m_i\Omega^2 R$  along the diagonal in the first three rows add a torsional stiffness to the blades.
- The terms out of the diagonal  $K_{i,j}$  vary with the azimuth angles which vary with the rotational speed  $\Omega$ .
- The rotation of the rotor at a constant speed makes the wind turbine a Linear Time Periodic (LTP) system.

The representation of the mass matrix  $M$  is shown in Equation (3.35).



$$M = \begin{bmatrix} m_1 r_2^2 & 0 & 0 & m_1 r_2 \cos \psi_1 & -m_1 r_2 \sin \psi_1 \\ 0 & m_2 r_2^2 & 0 & m_2 r_2 \cos \psi_2 & -m_2 r_2 \sin \psi_2 \\ 0 & 0 & m_3 r_2^2 & m_3 r_2 \cos \psi_3 & -m_3 r_2 \sin \psi_3 \\ m_1 r_2 \cos \psi_1 & m_2 r_2 \cos \psi_2 & m_3 r_2 \cos \psi_3 & m_T & 0 \\ -m_1 r_2 \sin \psi_1 & -m_2 r_2 \sin \psi_2 & -m_3 r_2 \sin \psi_3 & 0 & m_T \end{bmatrix} \quad (3.35)$$

In case of unbalanced rotor mass, the sum of the centrifugal forces will not be a null vector, but the resultant will have some components acting on the rotor support. The main input force, according to the assumptions of OMA, is a broadband white noise, but in case of unbalanced rotor some harmonics will be introduced in the input spectrum at the rotational frequency  $\Omega$  and at its multiples. In this case the hypothesis of OMA are not anymore respected and the results will be less stable and in presence of errors that need to be taken into account. In this study, no damping  $C$  is introduced in the system, so the equation can be written as shown in Equation (3.36).

$$[M(t)]\{\ddot{y}(t)\} + [K(t)]\{y(t)\} = \{f(t)\} \quad (3.36)$$

### Numerical analysis

In standing still conditions, the azimuth angle is fixed and the mass and stiffness matrices are not time-periodic. It is then possible to extract the eigenvalues and eigenvectors from the dynamic matrix in order to get the natural frequencies and the mode shapes of the LTI system. As the system has 5 DOF, we are expecting to find the following five modes:

- 3 blade modes
- 2 support modes

Transforming the time domain equation into the Laplace domain (variable  $p$ ) and assuming the initial displacement and velocities are zero, yields to Equation (3.37) and Equation (3.38) in the general case in which also the damping is present.

$$(p^2[M] + p[C] + [K]) \{X(p)\} = \{F(p)\} \quad (3.37)$$

$$[Z(p)] \{X(p)\} = \{F(p)\} \quad (3.38)$$

where  $Z(p)$  is the dynamic stiffness matrix. The determinant of this matrix is the system characteristic equation. Its roots are known as system poles and they define the resonance frequencies of the system. They can be obtained by solving the general eigenvalue problem expressed in Equation (3.39).

$$|Z(p)| = 0 \quad (3.39)$$

Table 3.2 lists the identified natural frequencies together with a brief description of the mode shape.

Mode n.	Natural frequency [Hz]	Description
1	0.3777	Tower side-to-side (S2S)
2	0.8412	Asymmetric rotor with vertical motion
3	0.8426	Collective edge
4	0.9247	Asymmetric rotor with horizontal motion
5	5.8710	Tower up-down

Table 3.2: 2D model - modal identification ( $\Omega = 0Hz$ )

By changing the position of the rotor, the coupling between the blades and the tower also changes, as shown in Equation 3.33 and 3.35. As consequence, the natural frequencies will vary and they will be again the same when a complete rotation will be done. In case of constant rotational speed, their values will be slightly higher as shown in Table 3.3 because of the increase of torsional stiffness due to the rotation of the rotor. In Figure 3.8, the blue rotor represents the initial configuration, while the red one is the mode shape for the case in which  $\Omega = 0$  and the 1<sup>st</sup> blade is vertically up ( $\psi_1 = 0$ ).

### OMA without preprocessing step

After having identified the modes in the so-called parked conditions, the model can be put into rotation under a white noise excitation (simulating the wind excitation). Gravity is also taken into account. Long time histories are usually required for confident modal parameters estimation. As a good compromise between this requirement and the computational time, the simulations last 700 seconds and the sampling frequency is chosen to be equal to 100 Hz. Since

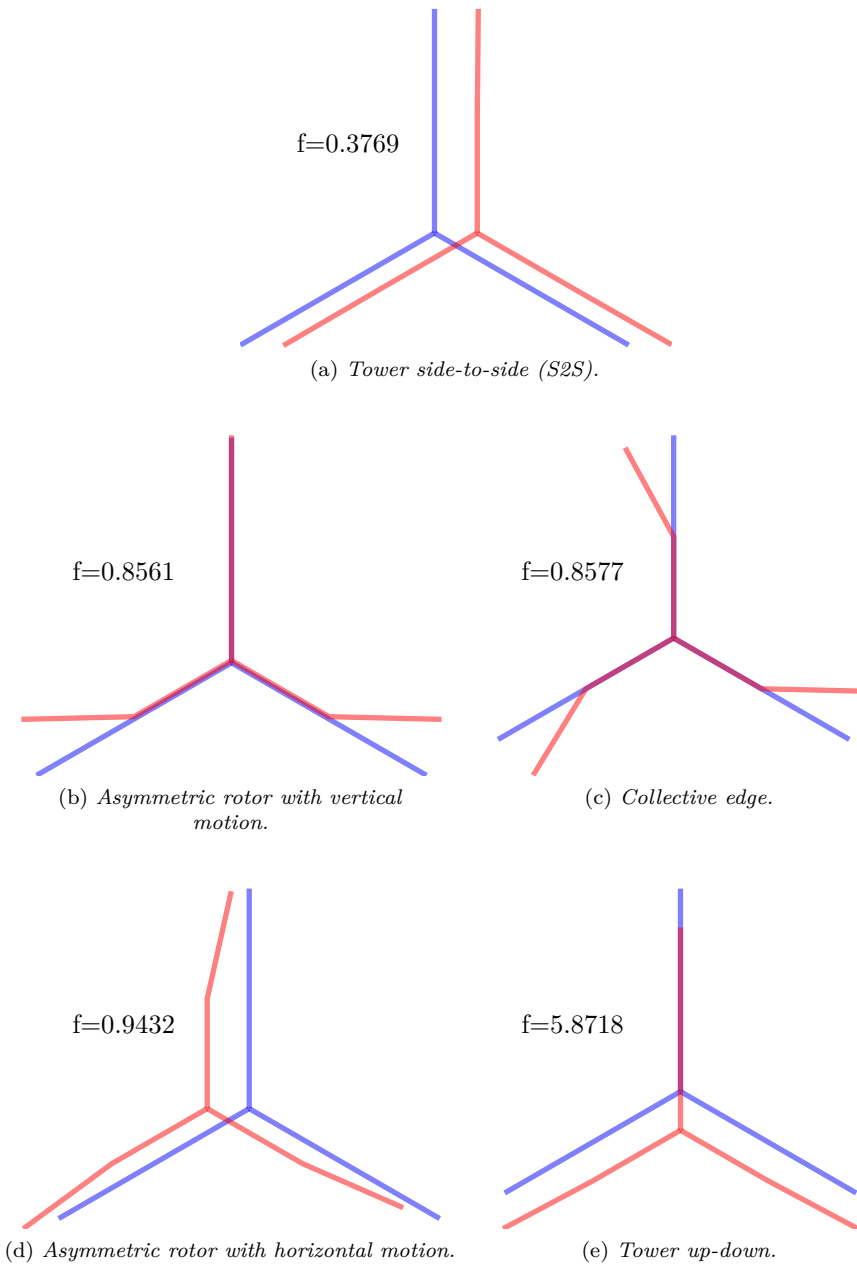


Figure 3.8: 2D model - mode shapes.

Mode n.	Natural frequency [ $Hz$ ]	Description
1	0.3769	Tower side-to-side (S2S)
2	0.8561	Asymmetric rotor with vertical motion
3	0.8577	Collective edge
4	0.9432	Asymmetric rotor with horizontal motion
5	5.8718	Tower up-down

Table 3.3: 2D model - modal identification ( $\Omega = 0.16Hz$ )

the highest mode is around  $6Hz$ , the signals have been downsampled to  $14Hz$ . The displacements of the rotating masses as well as the ones of the support are recorded. Crosspowers are calculated and Operational Polymax is then used for estimating the modal parameters. A perfect match with the numerical results can be found in the case in which the rotor is in parked conditions. When the rotor is rotating, the stabilization diagram is less clear and there are a lot of harmonics which are hampering the identification process. In fact, by selecting a nominal rotational speed of  $0.16Hz$ , several peaks in the spectra are present at this frequency and at its multiples, as shown in Figure 3.9. The symbols have following meaning: "o": new pole, "f": stable frequency, "d": stable frequency and damping, "v": stable frequency and eigenvector, "s" all criteria stable. Figure 3.10 represents the Modal Assurance Criterion (MAC) [50]. The so-called auto-MAC is shown and it compares the modeset obtained with itself. It shows that several modes are repeated in the frequency band which has been analyzed. Furthermore, the modes that should be present at certain frequencies (according to the numerical analysis) are not there. This is because the system is being analyzed by considering a combination of fixed reference frame displacements (at the tower top) and rotating reference frame ones (along the blades). This demonstrates the need of using a preprocessing tool such as the ones shown in Section 3.1.2 and 3.1.3: MBC and HPS, respectively.

### OMA after MBC transformation

In case of use of MBC transformation, the recorded displacements are converted into the multiblade coordinates. At this point, the data can be combined with the fixed reference system ones. The calculation of crosspowers (with the use of an exponential window) and the use of the stabilization diagram allow to identify with a very good level of accuracy the modal parameters, as shown in Figure 3.11 and Figure 3.12. In order to assess if a good modal model has been obtained, the so-called synthesized crosspowers (the ones obtained by

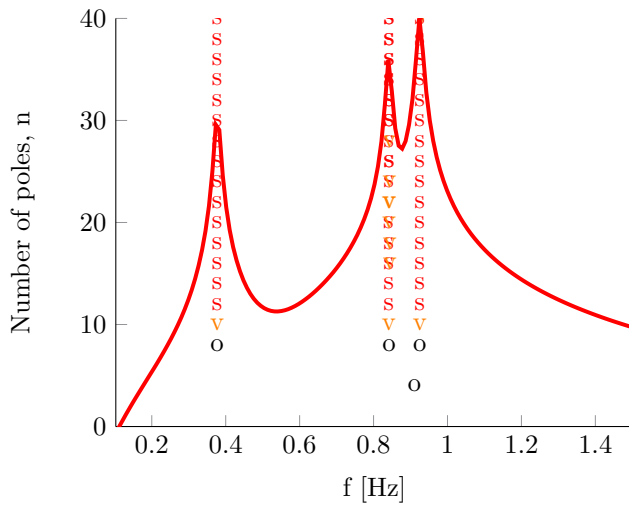
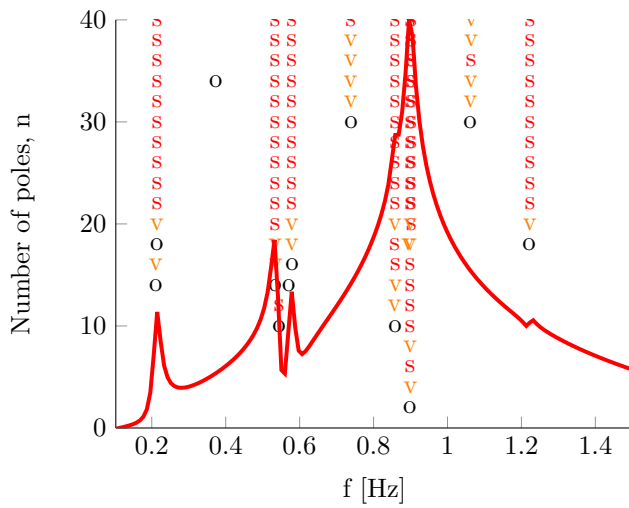
(a) *Parked.*(b) *Rotating.*

Figure 3.9: 2D model - stabilization diagrams.

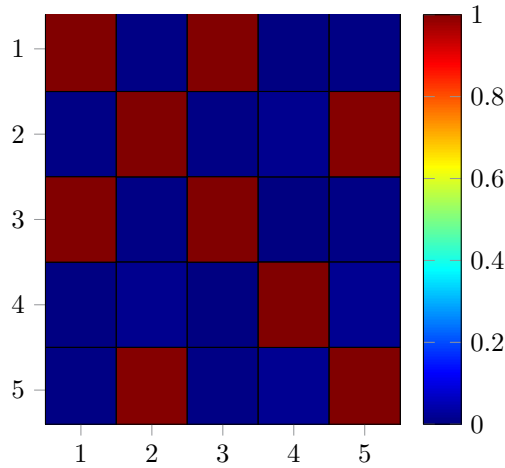


Figure 3.10: 2D model - MAC without any pre-processing step.

using the estimated modal parameters) can be compared with the measured crosspowers. In this case, a very good match with very small errors ( $<1\%$ ) has been obtained thanks to the use of MBC both in terms of magnitude and phase. Two crosspowers are shown as examples in Figure 3.13. In order to animate the mode shapes, the inverse MBC transformation needs to be applied to the multiblade mode shapes. In this process, we focused mainly on the tower and rotor modes and since the torsional mode of the drivetrain is not coupled with the other DOFs, then it has been neglected. Therefore, five modes have been identified, as shown in Table 3.4.

Mode n.	Natural frequency [Hz]	Description
1	0.3739	Tower side-to-side (S2S)
2	0.7389	Backward whirling mode
3	0.8576	Collective edge
4	1.0628	Forward whirling mode
5	5.8712	Tower up-down

Table 3.4: 2D model - modal identification after MBC transformation ( $\Omega = 0.16Hz$ ).

The effect of the rotation is much evident on the rotor modes. The new modes in the rotor plane are known as whirling modes, named backward (BW) and forward (FW). They are spaced by  $2\Omega$ , so their frequency is dependent by

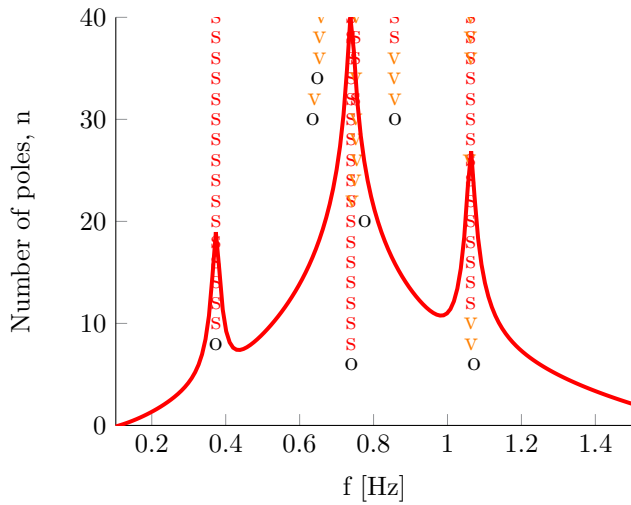


Figure 3.11: 2D model - stabilization diagram after MBC transformation.

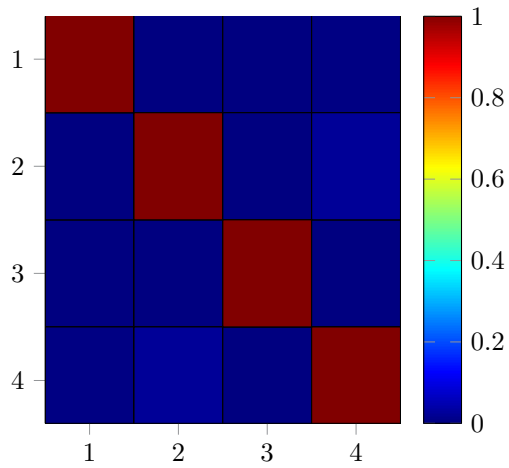


Figure 3.12: 2D model - auto-MAC after MBC transformation.

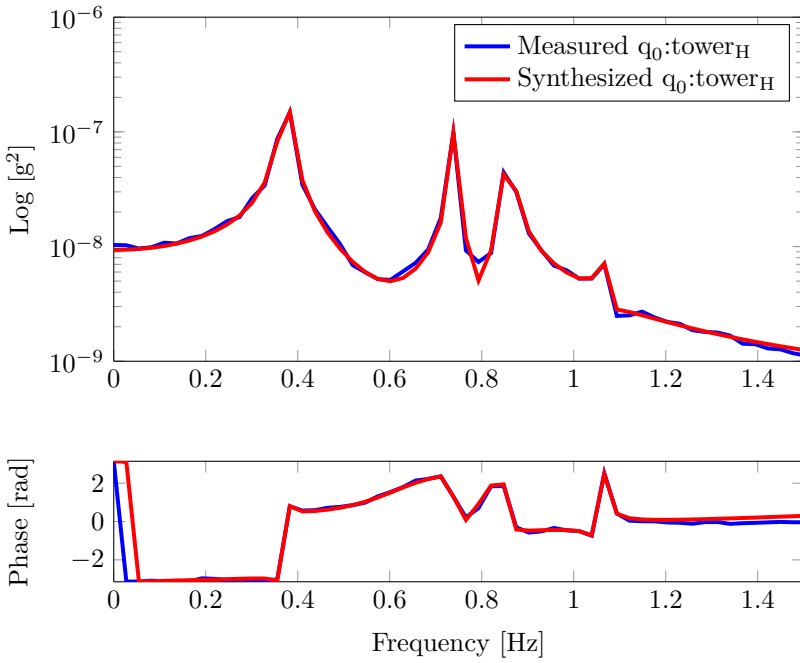
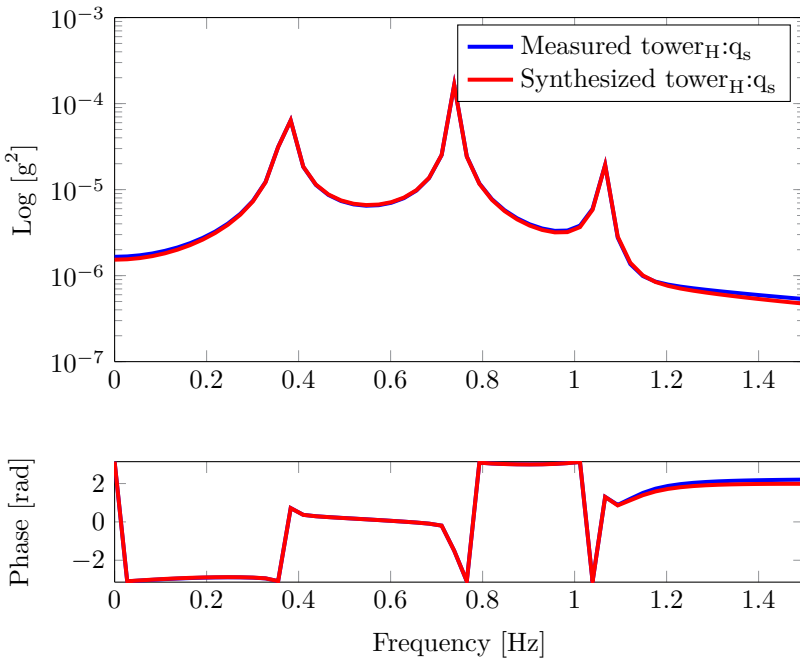
(a)  $q_0:\text{tower}_H$ .(b)  $\text{Tower}_H:q_s$ .

Figure 3.13: 2D model - synthesized vs. measured crosspowers after MBC transformation.



the rotational speed of the wind turbine. Figure 3.14 shows the importance of applying a preprocessing tool before the Operational Modal Analysis step takes place. In fact we can look at the autopowers of the displacement of a point on the blade in the rotor plane and we can identify a sharp peak in correspondence of the collective edgewise mode and another peak corresponding to the asymmetric mode shapes (they are identified at two frequencies very close to each other). By looking at the autopower of the point representing the support structure ( $tower_H$ ), two peaks separated by  $2\Omega$  (whirling modes) are identified instead of a double peak at the same frequency. After applying MBC, these two modes separated by  $2\Omega$  are also identified by the autopower of the multiblade coordinates confirming their physical meaning.

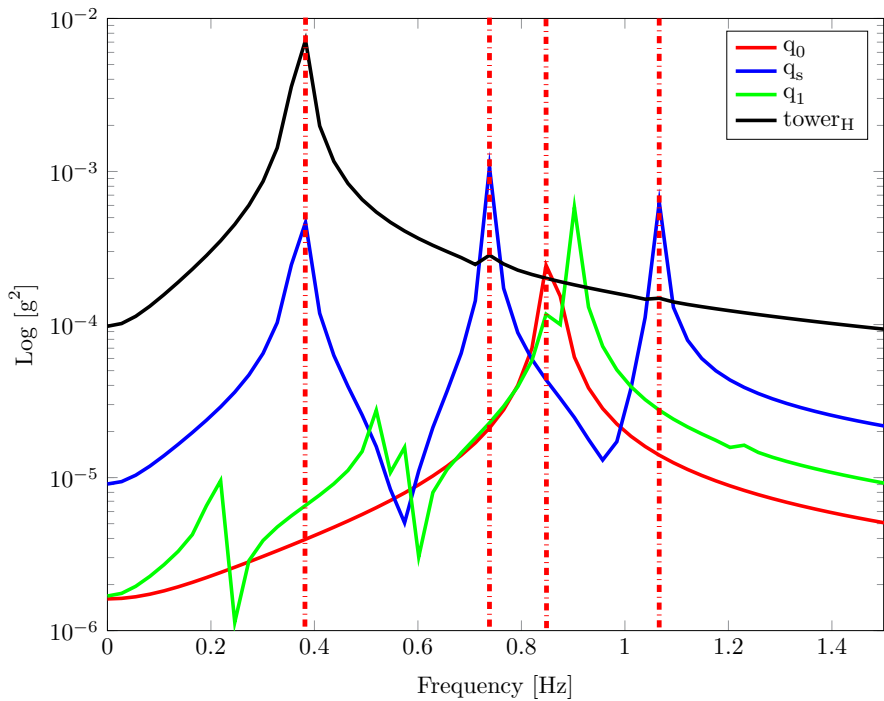


Figure 3.14: 2D model - Autopowers related to several channels before and after MBC transformation and comparison with tower signal.

## OMA after HPS

When HPS technique is used, the output of the simulation signals are exponentially modulated. Theoretically an infinite number of harmonics should be used to approximate the signal. Practically speaking, only few harmonics are more than enough to get a very good estimation of the initial signal. In this case, five harmonics have been used. The so-defined EMP signals contain the original signal and other time histories which also have an imaginary part. The crosspowers can be calculated and finally the stabilization diagram can be built also in this case. The stabilization diagram is shown in Figure 3.15 and the selected natural frequencies are listed in Table 3.5.

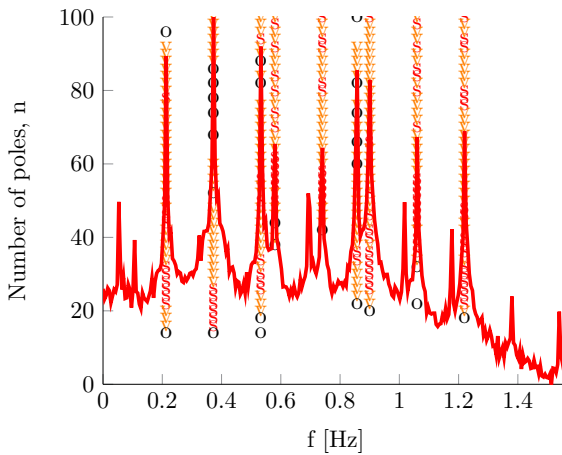


Figure 3.15: 2D model - stabilization diagram after HPS.

Mode n.	Natural frequency [Hz]	Description
1	0.369	Tower side-to-side (S2S)
2	0.736	Backward whirling mode
3	0.858	Collective edge
4	1.063	Forward whirling mode
5	5.863	Tower up-down

Table 3.5: 2D model - modal identification after HPS ( $\Omega = 0.16Hz$ )

If compared with the MBC calculation, the HPS stabilization diagram contains a lot of harmonics which are introduced in the data by the exponential modulation.

By selecting only the frequencies obtained by using MBC, the true modes of the system can be obtained and the auto-MAC is shown in Figure 3.16 by considering the reduced modeset. An a priori knowledge is then needed if HPS method is going to be applied.

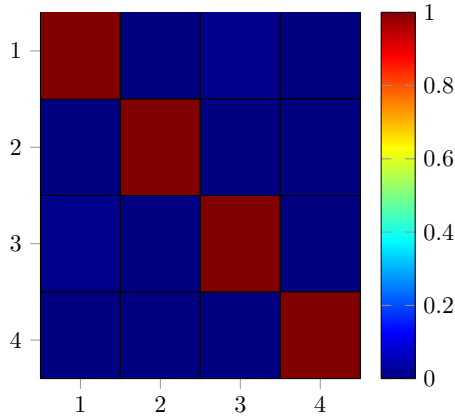


Figure 3.16: 2D model - auto-MAC after HPS.

At this point, the modes obtained by using MBC can be compared to the ones that we got by means of HPS method. The MAC between the two modesets is shown in Figure 3.17. The modes are almost exactly the same. The two techniques allow to get both very good results in terms of natural frequencies and mode shapes.

### 3.4.2 5MW vs 10MW wind turbine

The potential of the introduced methods has been proven in a controlled Matlab environment in Section 3.4.1. The next natural step is the construction by means of an aeroelastic software, Samcef Wind Turbines (SWT), of offshore wind turbine models. The two selected models are the one proposed by the NREL [47], a 5 MW wind turbine and a model proposed by DTU Wind Energy [48] which allows to reach a power equal to 10 MW. The two models are shown in Figure 3.18.

SWT is an aeroelastic finite element multi-body code. The multi-body approach allows the user to define the different substructures separately and then combine them in order to build the entire system (i.e. wind turbine). The substructures are modelled by using the finite element code Samcef which is embedded in SWT. The assembly of the substructures is done by means of a lookup table

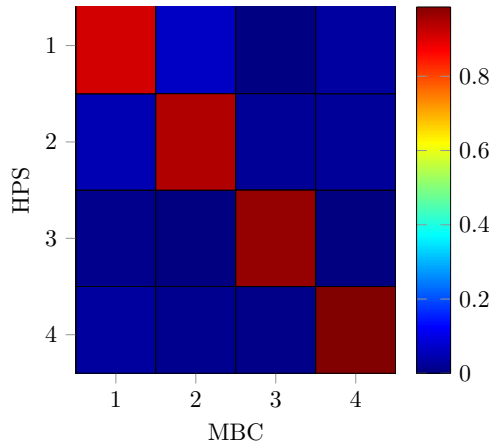


Figure 3.17: 2D model - HPS vs MBC.

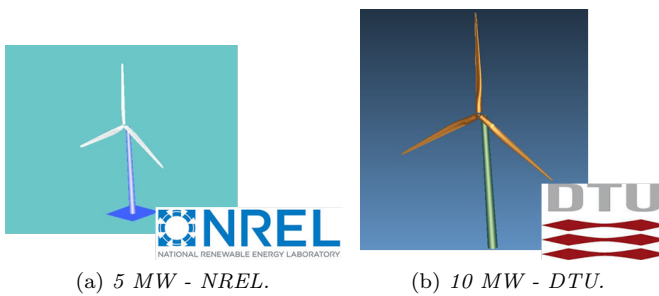


Figure 3.18: 5 MW vs 10 MW wind turbine models.

according to the Craig-Bampton method. The connector nodes need to be assigned in order to link the substructures between them. The example in Figure 3.19 shows a combination of high and low fidelity models.

High fidelity and low fidelity components can both be incorporated into a single model of the complete Wind Turbine (WT) and the analysis can be focused on a particular component.

### 5MW model

**Model description** The first wind turbine model which will be presented here is a 5 MW wind turbine model. It has been proposed in 2009 by the

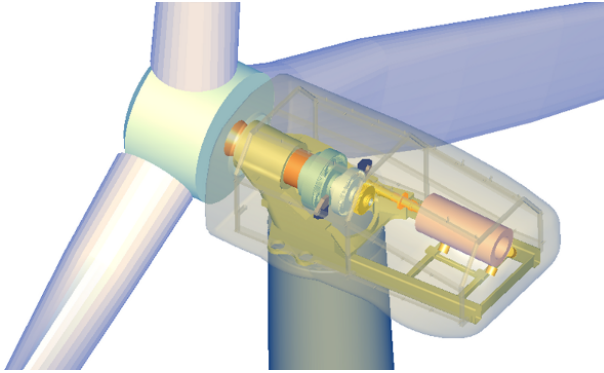


Figure 3.19: SWT example.

U.S. Department of Energy's (DOE's) National Renewable Energy Laboratory (NREL) and it is well-known as the NREL offshore 5-MW baseline wind turbine. This wind turbine has been used to establish the reference specifications for several research projects supported by the U.S. DOE's Wind & Hydropower Technologies Program [51], [52], [53]. Additionally, the European UpWind research program adopted the same wind turbine as reference case. Let's describe briefly the main properties of the model. They are listed in Table 3.6.

Rating	5 MW
Rated rotor speed	12.1 rpm
Rotor orientation	upwind, 3 blades
Control	Variable speed, Collective pitch
Drivetrain	High-speed, multiple-stage gearbox
Gearbox ratio	97:1
Rotor, Hub Diameter	126 m, 3 m
Hub Height	90 m
Rotor Mass	110000 kg
Nacelle Mass	240000 kg
Tower Mass	347460 kg

Table 3.6: 5 MW specifications

It is a three-bladed model. The rotor diameter is equal to 126 m and the hub is located at an elevation of 90 m above the ground. Important parameters are the rated rotor speed (12.1 rpm), the rated generator speed (1173.7 rpm) and the

gearbox ratio (97:1). The gearbox was assumed to be a typical multiple-stage gearbox but with no frictional losses. The last element to be discussed here is the controller. For this wind turbine a conventional variable-speed, variable blade-pitch-to-feather configuration was chosen. In such wind turbines, the conventional approach for controlling power-production operation relies on the design of two basic control systems: a generator-torque controller and a full-span rotor-collective blade-pitch controller. The two controller systems are designed to work independently, for the most part, in the below-rated and above-rated wind speed range, respectively. The goal of the generator-torque controller is to maximize power capture below the rated operation point. On the other hand, the goal of the blade-pitch controller is to regulate generator speed above the rated operation point. The first step, as done also for the 2D model, is the calculation of the natural frequencies and mode shapes. They are compared in Table 3.7 with the ones listed in the NREL 5-MW wind turbine definition. A very good correspondence has been obtained by using SWT, therefore the model can be used for further studies.

Mode n. n.	SWT Natural frequency [Hz]	NREL Natural frequency [Hz]	Mode description
1	0.31	0.31	Tower side-to-side (S2S)
2	0.32	0.32	Tower fore-aft (FA)
3	0.66	0.67	1 <sup>st</sup> Flap Yaw
4	0.66	0.67	1 <sup>st</sup> Flap Pitch
5	0.67	0.70	1 <sup>st</sup> Flap Sym
6	1.07	1.08	1 <sup>st</sup> Edge Pitch
7	1.07	1.09	1 <sup>st</sup> Edge Yaw

Table 3.7: 5 MW - SWT model validation

Several operating conditions have been analyzed and consistent results have been obtained. The wind main component is defined in the X direction (from the Low Speed Shaft (LSS) to the High Speed Shaft (HSS) and perpendicular to the rotor plane). Turbulent fluctuations are added also in the other two directions. The Kaimal turbulence model is used for performing the analysis [54]. The absolute wind speed is shown in Figure 3.20 and its components in Figure 3.21. Figure 3.22 shows the power which is generated by the wind turbine. The power is oscillating around the nominal power (5 MW).

Virtual sensors are placed at several locations along the blades and along the tower. The accelerations are recorded in a local reference system (simulating a real accelerometer placed at the same location). The accelerometers

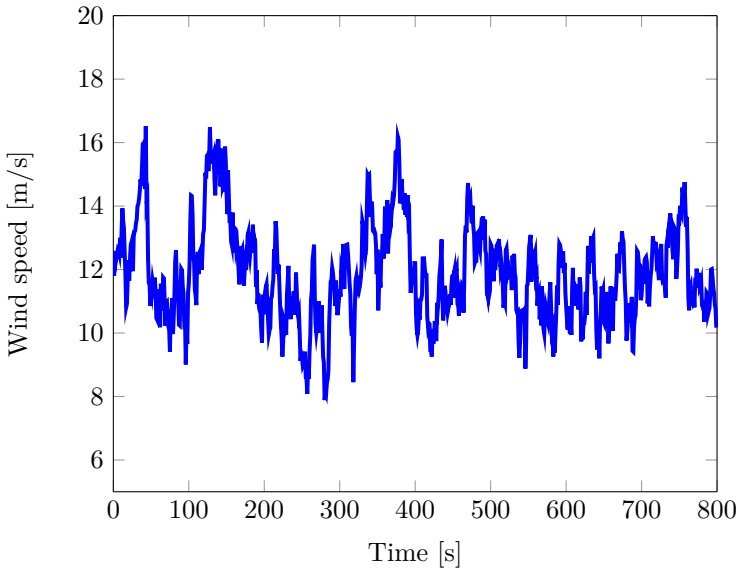


Figure 3.20: 5 MW - absolute wind speed.

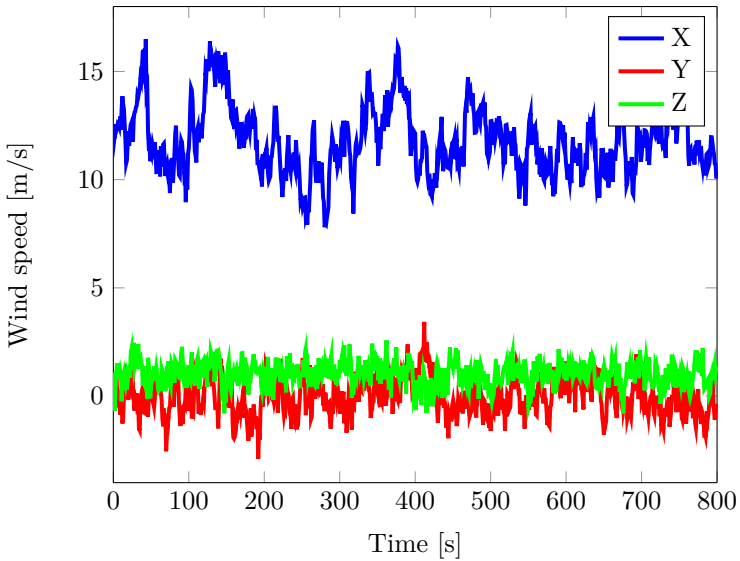


Figure 3.21: 5 MW - wind speed in X, Y and Z directions.

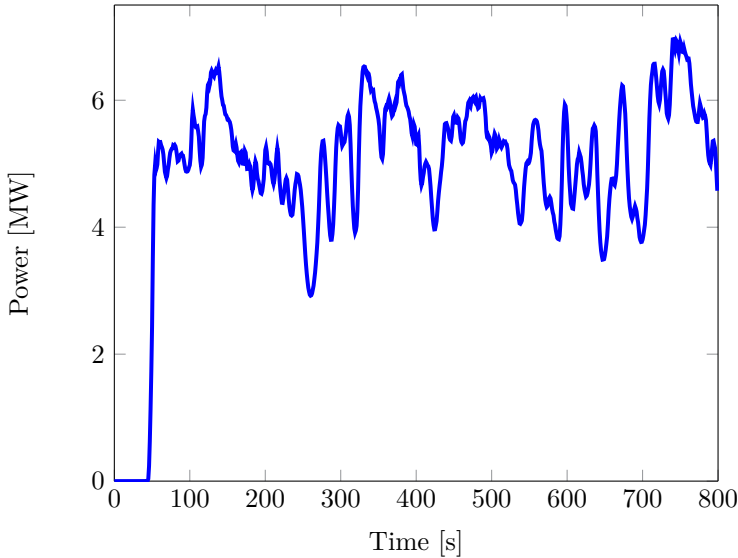


Figure 3.22: 5 MW - generated power.

configuration is shown in Figure 3.23. Five accelerometers are placed along each blade ( $x$  direction is aligned with the blade extension,  $y$  and  $z$  are the in-plane accelerations in the edgewise and flapwise directions) and the tower is instrumented by means of three accelerometers.

In this reference, the X axis is the blade axis (oriented toward the blade tip), the Y axis is aligned with the chord line and belongs to the blade section plane (oriented toward the leading edge) and finally the Z axis is normal to the chord line and belongs to the same plane. In this configuration, the edgewise modes are described by bending along the Y axis, while flapwise modes bend the structure along the Z direction. Axial modes along the blade pitch axis can be neglected since they appear at frequencies much higher than those which are included in the frequency range of interest.

**Parked configuration** The first configuration to be analyzed in detail is the one in which the wind turbine is in a parked condition. In this case, the blades are parked and the first seconds are used to place the pitch in its parking position (Parking Pitch Angle). When the simulation starts, the rotor is released, but the pitch is fixed. The generator is disconnected so that there is no resisting torque and the brake is released to allow the rotor to be free to spin if it is not in the equilibrium position. Several configurations are also imposed by



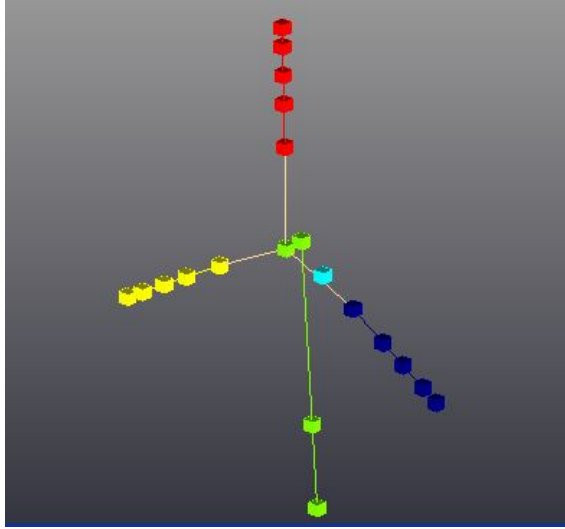


Figure 3.23: 5 MW - virtual accelerometers positions.

modifying the number of accelerometers placed along the blades. The measured accelerations are then imported in Test.Lab to calculate auto- and cross-powers and to perform OMA by considering the wind spectrum as white noise with a good level of approximation. The modal parameters can be estimated (natural frequencies, damping ratios and mode shapes) and their correspondence with the ones obtained numerically from the model can be checked. Long time histories are usually required for having a confident modal parameters estimation, but on the other side a low sampling frequency is needed to better determine low frequency modes. As a good compromise among the two requirements, the simulations last 800 seconds and the sampling frequency is 100 Hz. Since the interesting modes are at very low frequencies, a downsampling to 10 Hz has been performed as first step in the analysis. The point on top of the tower is chosen as reference for the correlations and spectra computation which are then used to estimate the modal parameters by means of Operational Polymax method. In order to simplify the entire procedure, the accelerations along the blade axis are neglected. The identified modes are then compared to the ones obtained using both the FAST model and the ADAMS model; in FAST the natural frequencies are calculated by performing an eigenanalysis on the first-order matrix created from a linearization analysis, while in ADAMS a command that linearizes the complete model and compute eigendata is used. A very good level of accuracy both in terms of natural frequencies and mode shapes is reached for the first ten modes. Results are reported in Table 3.8 where Yaw and Pitch mean that

the blades asymmetric modes couple with the nacelle yaw and pitching motions respectively.

Mode n. n.	OMA [Hz]	FAST [Hz]	ADAMS [Hz]	Mode description
1	0.312	0.312	0.319	Tower side-to-side (S2S)
2	0.329	0.324	0.316	Tower fore-aft (FA)
3	0.666	0.666	0.630	1 <sup>st</sup> Flap Yaw
4	0.675	0.668	0.669	1 <sup>st</sup> Flap Pitch
5	0.720	0.700	0.702	1 <sup>st</sup> Flap Sym
6	1.056	1.079	1.074	1 <sup>st</sup> Edge Pitch
7	1.059	1.089	1.088	1 <sup>st</sup> Edge Yaw
8	1.853	1.934	1.651	2 <sup>nd</sup> Flap Yaw
9	1.888	1.922	1.856	2 <sup>nd</sup> Flap Pitch
10	1.900	2.021	1.960	2 <sup>nd</sup> Flap Sym

Table 3.8: 5 MW - model validation

By using Operational Polymax, all the first 10 modes can be identified and the biggest differences exist in the predictions of the blades second asymmetric flapwise yaw and pitch modes. At this stage, some “damages” can be introduced in the structure in order to see their effects on the modal parameters if compared with the ideal condition. In a preliminary step, two main damages can be introduced by using SWT code: ice formation on the blades (i.e. on all the blades or on two of them), presence of an unbalancing mass on a blade. The presence of ice on the blades can cause high vibration levels and can modify the natural frequencies of the blade modes as well as increase the fatigue loads. In the academic literature and in the industrial world, a long list of studies concerning the ice formation can be found. The final objective is to predict when the icing phenomena is occurring. The main effects of adding ice on the blades are two: on one hand it modifies the blade shape by increasing the drag and decreasing the lift at the same time, on the other hand the presence of an additional mass which is not uniformly distributed can cause an unbalancing force on the rotor. Within the software SWT, the conditions in which the wind turbine is operating can be specified. The calculation is based on Germanischer Lloyd’s Wind Guideline and it allows to consider the ice formation on none of the blades, all blades or all blades but one. The ice on blades option will apply an additional mass along the blade. It is suggested that the mass distribution (mass/unit length) is assumed at the leading edge of the rotor blade. It increases linearly from zero at the rotor axis to the maximum value  $\mu_E$  at half the radius

and then it remains constant up to the outermost radius. The value  $\mu_E$  is calculated as shown in Equation 3.40.

$$\mu_E = \rho_E k c_{min} (c_{max} + c_{min}) \quad (3.40)$$

$\rho_E$  is the density of the ice,  $R$  is the rotor radius,  $c_{max}$  is the maximum chord length and  $c_{min}$  is the cord length at the blade tip, linearly extrapolated from the blade contour.  $k$  is a parameter which depends on the rotor radius and it is calculated by using Equation 3.41.

$$k = 0.00675 + 0.3e^{-0.32R} \quad (3.41)$$

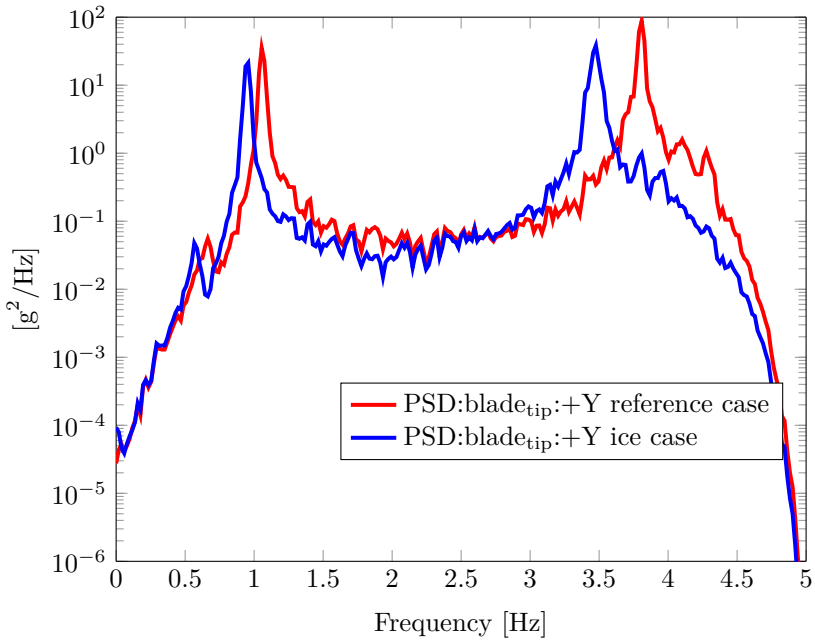
The second damage condition which has been simulated is the presence of an unbalanced mass that is added to a particular location on one of the wind turbine blades. A little cubic mass ( $m=30$  kg) placed not far from the rotor center was considered. Table 3.9 list the natural frequencies and the estimated damping values for two different configurations:

- Ice on all blades
- Ice on all blades but one

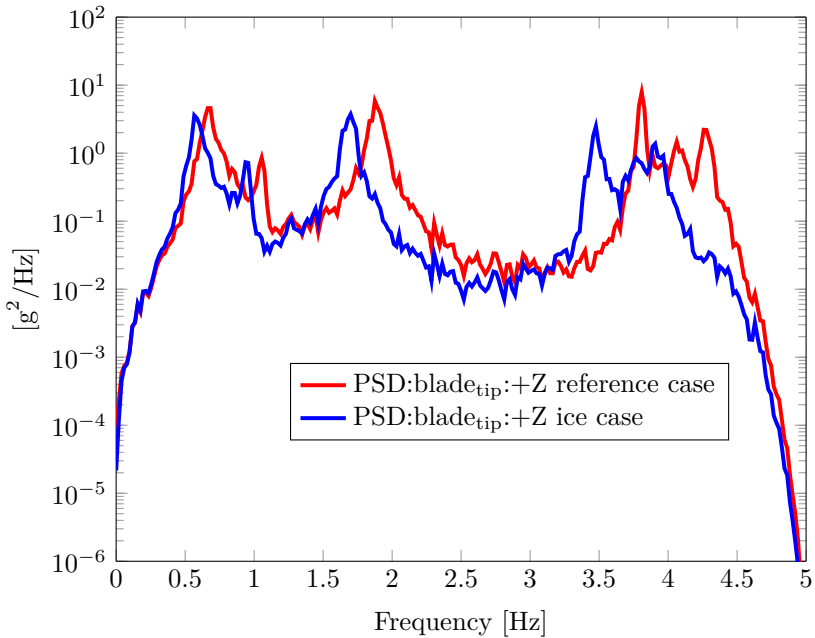
A frequency shift towards lower frequencies due to the added ice mass on the blades can be observed by comparing 3.9 results with 3.8 ones. On the other hand, not so many conclusions can be drawn for what concerns the damping values. In fact, a global trend cannot be identified, but it should be analyzed mode by mode. In general we could say that the increase of the mass reduces the damping ratio for each mode.

For a qualitative analysis of the signals, the Power Spectral Density (PSD) of signals recorded from the virtual sensors placed at the blades tip are shown in Figure 3.24 for both directions (in-plane  $Y$  and out-of-plane  $Z$ ). It can be noticed that almost all the peaks are shifted to lower frequencies as a consequence of the mass increase.

**Rotating configuration** In a parked configuration, the modes are corresponding with a very good accuracy to the ones identified numerically. If the wind turbine is rotating things change, as demonstrated for the 2D model. Also in this case the so-called whirling modes can be identified after having applied the two proposed techniques (MBC and HPS). Figure 3.25 shows the PSDs in operating conditions for different configurations. The reference case is compared



(a) PSDs at the blades tip in Y direction.



(b) PSDs at the blades tip in Z direction.

Figure 3.24: 5MW - ice condition simulation in parked configuration.

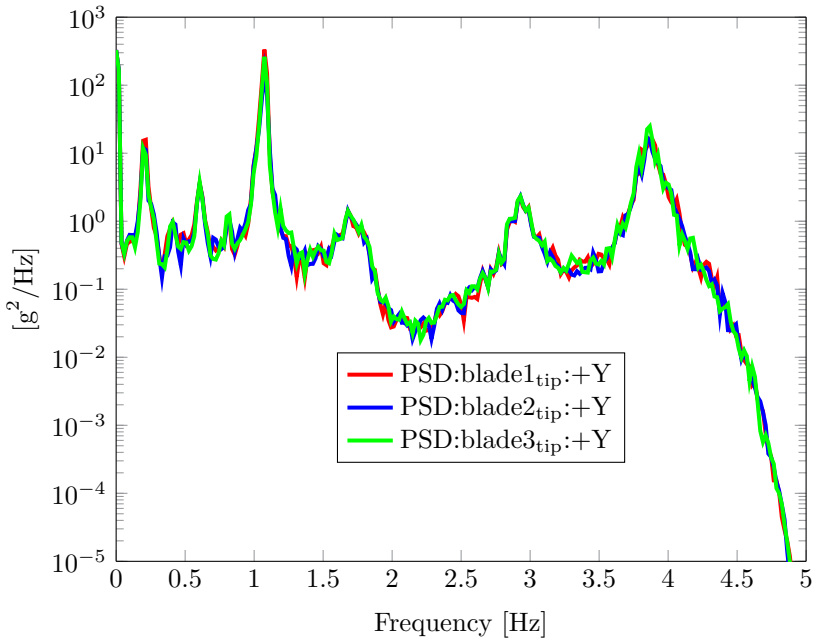
Mode description no.	Ice on all blades		Ice on all blades but one	
	Natural frequency [Hz]	Damping ratio [%]	Natural frequency [Hz]	Damping ratio [%]
1 <sup>st</sup> Tower FA	0.324	5.13	0.324	5.24
1 <sup>st</sup> Flap Yaw	0.588	7.05	0.585	7.06
1 <sup>st</sup> Edge Yaw	0.948	0.95	0.948	0.99
2 <sup>nd</sup> Flap Yaw	1.696	2.05	1.695	2.33

Table 3.9: Modal parameters comparison between "ice on all blades" and "ice on all blades but one" conditions

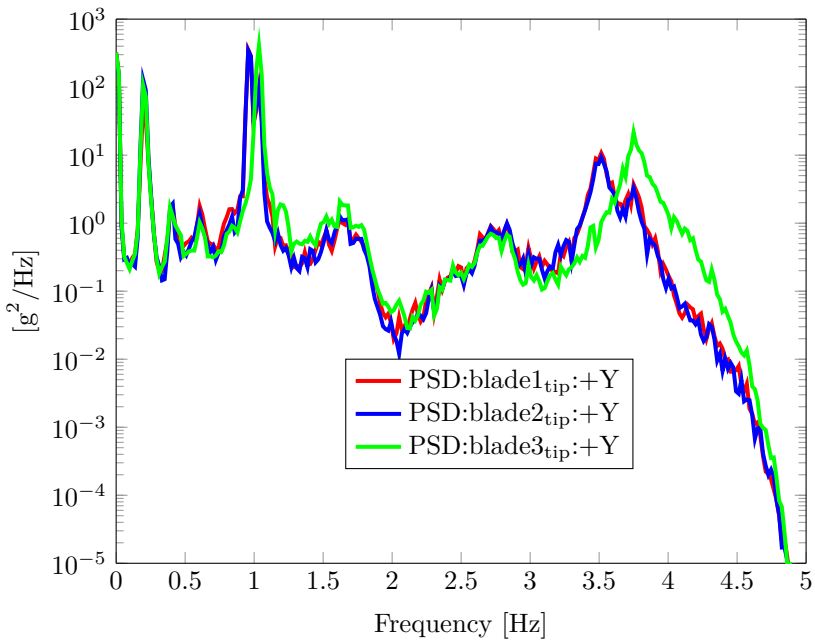
to the one with ice on all blades but one. The PSD amplitude decreases for ice configuration in comparison with the reference case. The same considerations can be done regarding the mass unbalance configuration, even if the blade mass is much bigger than the unbalanced mass and the difference between the curves is not so evident. In these cases, the modes are shifting to lower frequencies, while the harmonics are fixed at the same frequency if the rotational speed continues being constant. It is evident from Figure 3.25 that the 3<sup>rd</sup> blade is the one without ice. In fact no shifts can be seen by looking at the PSD from the tip of that blade.

The presence of harmonics is evidenced in Figure 3.26 in which the PSDs are compared among the parked and operating conditions at the blade tip in the edgewise direction for the reference case. The frequency shift toward higher frequencies for the 1<sup>st</sup> and 2<sup>nd</sup> edgewise modes due to the centrifugal stiffening can be underlined, while the different harmonics dominate the response of the system in operating conditions.

Some preliminary considerations can be done by calculating the PSD of the time signal before and after the MBC transformation. The PSDs have been calculated by using the Welch's estimator for several points (blade-tip and tower-top are the most interesting ones). The time data have been divided up into smaller blocks to improve the resolution. In order to achieve a high calculation performance, the algorithm requires that the block size be a power of 2. A value of 512 has been chosen with an overlapping between the blocks of 66% to compensate the effect of using Hanning windows in time domain. Figure 3.27 highlights the presence of the whirling modes in operating conditions. The PSDs related to the blade tip are shown before and after the use of the MBC transformation.



(a) PSDs at the blades tip in  $Y$  direction - "reference" conditions.



(b) PSDs at the blades tip in  $Y$  direction - "ice but one" conditions.

Figure 3.25: 5MW - ice condition in operating configuration.

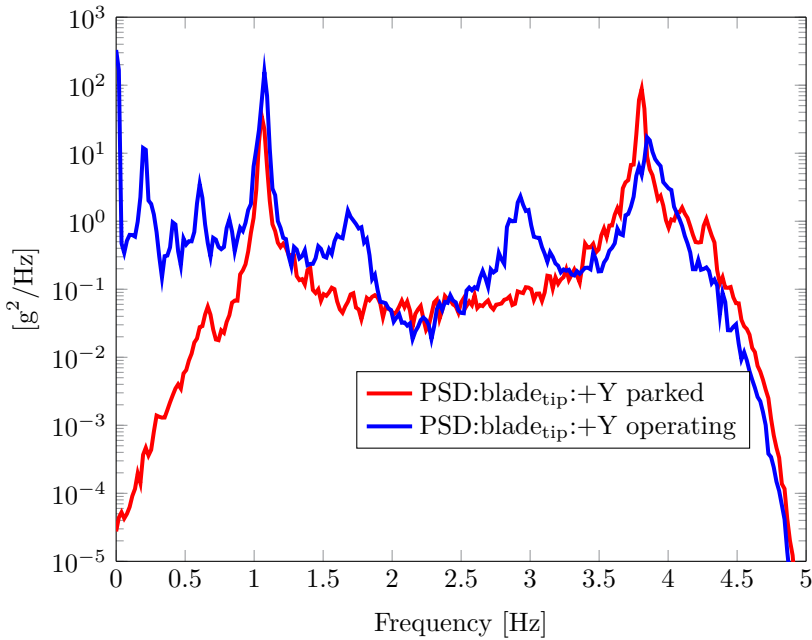


Figure 3.26: 5MW - parked vs operating conditions.

The whirling phenomenon is not observable from experimental data because the blade responses are measured in the rotating coordinate system, while whirling can be observed in a fixed reference system. MBC transformation enables the observability and the identification of whirling modes transforming the blade responses into a new reference system. The two whirling modes are separated by  $2\Omega$ . In Figure 3.28 PSDs of accelerations at the blade tip after MBC transformation are compared to the PSD obtained considering the acceleration at tower-top. The asymmetric coordinates (named  $a_c$  and  $a_s$ ) follow each other with a very good approximation, while the symmetric component ( $a_0$ ) has a different behavior as expected. It can be stated that MBC allows to separate the collective blade components from the asymmetric ones.

It is also quite important to notice that the peaks that are present in the MBC PSDs are found back in the tower-top PSD. It can be translated in the statement for which many of the rotor modes can be identified only using tower and nacelle data. Of course, instrumenting the blades can give some more details which can be very useful especially in case of Structural Health Monitoring or Damage Detection systems to set in place. But, on the other hand, instrumenting blades is a very delicate topic among the industrial partners. In fact, most of the blade

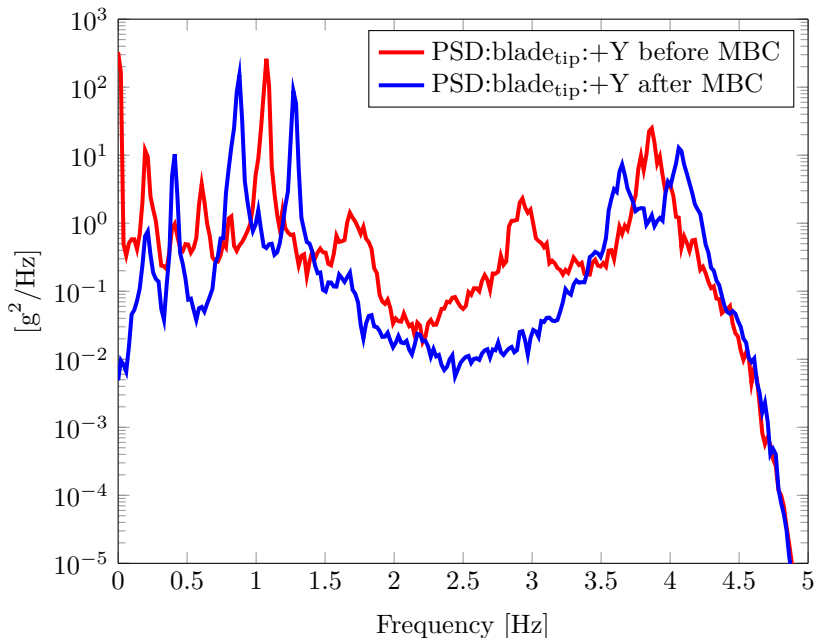


Figure 3.27: 5MW - PSDs comparison before and after the use of MBC transformation.

manufacturers do not allow to acquire data on the blades or do not share them because of confidentiality issues. The instrumentation of the blades requires state-of-the-art technology and it is not a straightforward task. Nowadays several blades are instrumented by means of accelerometers, strain gauges, but especially fiber optics, mostly for SHM purposes.

However, when the brake is released and the rotor starts rotating, the so-called harmonics are present in the recorded data if any transformation is applied. If we consider the case in which the rotational speed is equal to 0.20 Hz (nominal value), the stabilization diagram will show a peak at this frequency and at all the multiples of this frequency within the frequency band of interest. These harmonics are due to the rotation and they mask the dynamic behavior of the system and hamper the identification process. The auto- and cross-powers obtained from the fixed accelerometers signals and from the rotating accelerometers after the application of MBC or HPS techniques are combined together. After applying the MBC transformation, only the harmonics at the blade passing frequency ( $3\Omega$ ) are still present in the data. These harmonics are caused by an unbalancing force change as the blades pass in front of the tower. Three blades per rotation of the rotor pass in front of the tower and this is the



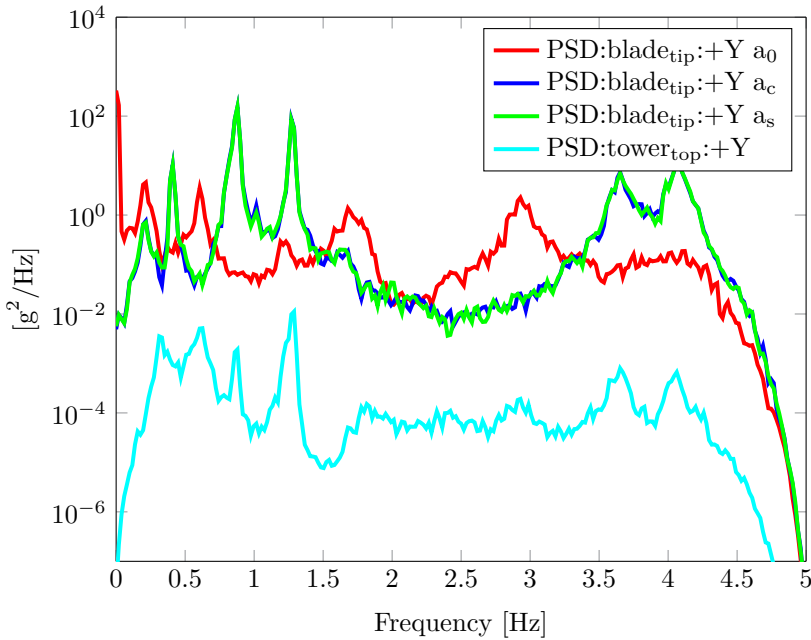


Figure 3.28: 5MW - PSDs comparison between multiblade coordinates and tower top signal.

reason why the  $3\Omega$  component is the dominant one. In case of helicopter, for instance, the dominant component is the  $4\Omega$  which is due to the fact that in this case, normally, 4 blades are composing the rotor. Figure 3.29 continues considering always the edgewise contributions. It shows the autopowers obtained at the tower top and at the blade tip in parked and in operating conditions. Once more, the presence of the whirling modes can be underlined. In fact the two edgewise modes (which were at the very close frequencies) split into two modes at different frequencies separated by  $2\Omega$ .

Next step is the identification procedure by means of Operational Polymax for estimating the modal parameters in operating conditions. The results for what concerns the interesting edgewise modes are listed in Table 3.10. Natural frequencies and damping ratios can be obtained directly, while the mode shapes need to be transformed back to the physical coordinates in order to be animated.

Some considerations can be again done by referring to the edgewise modes, but the same analysis could be performed in the flapwise direction. As underlined also for the 2D case, the two edgewise modes split into two modes at different

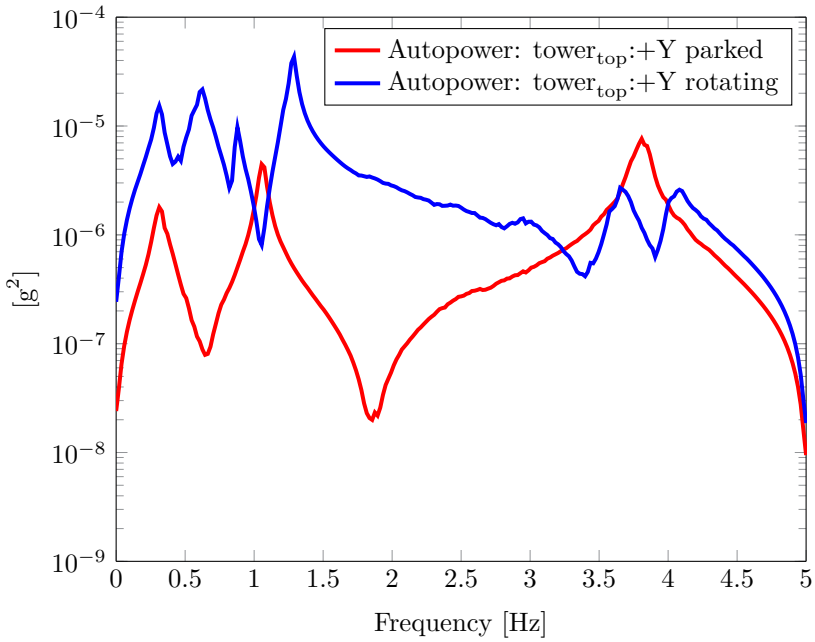
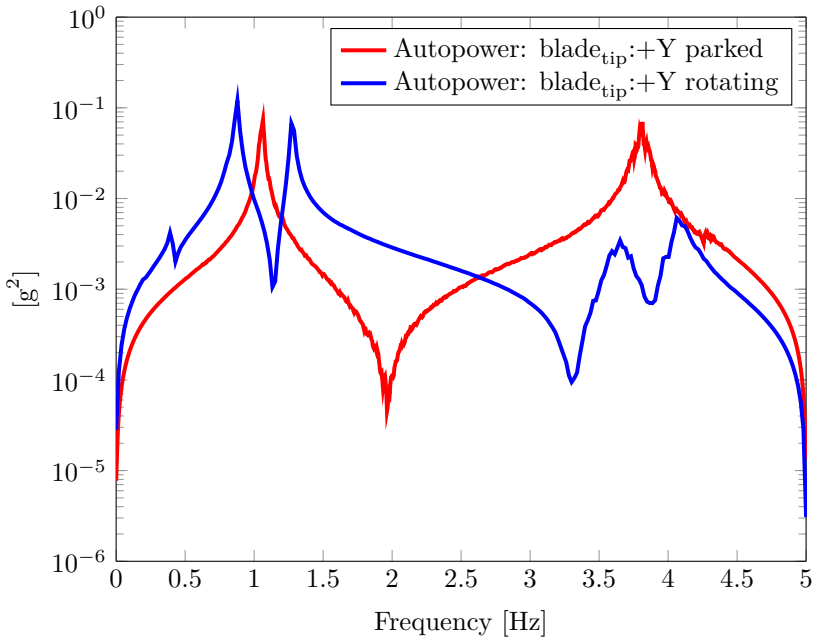
(a) *Tower top.*(b) *Blade tip.*

Figure 3.29: 5MW - Autopowers comparison between parked and rotating conditions.

Mode description	OMA Parked [Hz]	MBC + OMA Rotating [Hz]	Mode description
1 <sup>st</sup> Edge Pitch	1.07	0.87	1 <sup>st</sup> BW mode
1 <sup>st</sup> Edge Yaw	1.07	1.27	1 <sup>st</sup> FW mode
2 <sup>nd</sup> Edge Pitch	3.82	3.63	2 <sup>nd</sup> BW mode
2 <sup>nd</sup> Edge Yaw	3.83	4.07	2 <sup>nd</sup> FW mode

Table 3.10: Whirling modes identification

frequencies. In parked conditions, they are around the same frequency, while in operating conditions they are always separated by  $2\Omega$ , where  $\Omega$  is the fundamental frequency. In the literature they are known as backward (BW) and forward (FW) whirling modes. MBC transformation helps to identify and understand the whirling phenomenon. By using HPS, the procedure for estimating the system poles is not very easy, but the whirling modes continue being the dominant ones and they can be identified without many problems.

## 10MW model

**Model description** The 10-MW Reference Wind Turbine has been designed following the model developed by the DTU Wind Energy. Its general properties are shown in the Table 3.11. The idea of creating a new reference wind turbine arose because the largest wind turbines on the market have a power of around 7-8 MW. Upscaling causes a challenge because the mass of the turbine increases with the cube of the rotor radius with linear upscaling.

In order to address this challenge, several projects are trying to optimize the design of the blades to increase the overall performances of the rotor taking into account aerodynamics, structural and aero-servo-elastic considerations. Even if in most cases, the focus of the work was the optimization of the rotor, the entire wind turbine is needed in order to assess the performance by taking into account the interaction between the rotor and the other structural entities. The 10-MW Reference Wind Turbine (10MW RWT) was inspired by the artificial NREL 5-MW one (introduced in the previous section). Although it was thought as a natural and direct upscaling of the 5-MW model, the design procedure followed by DTU brought to a new model by taking into account the next generation of large wind turbines that will soon enter the market. The objectives of the DTU 10MW RWT are the following:

- have a basis for designing and optimizing rotors;

Rating	10 MW
Rated rotor speed	9.6 rpm
Rotor orientation	upwind, 3 blades
Control	Variable speed, Collective pitch
Drivetrain	Medium-speed, multiple-stage gearbox
Gearbox ratio	50:1
Rotor, Hub Diameter	178.3 m, 5.6 m
Hub Height	119 m
Rotor Mass	227962 kg
Nacelle Mass	446036 kg
Tower Mass	628442 kg

Table 3.11: 10 MW specifications

- show the results of a traditional design process;
- design an entire wind turbine which could be reproduced by other institutions for further studies.

The existence of a document providing the detailed description of the wind turbine from an aerodynamic, aeroelastic and structural point of view inspired us to reproduce the same model by using SWT [55]. The wind turbine has a rated power of 10 MW and was designed for offshore siting for an IEC class 1A wind climate. It is a three-bladed upwind wind turbine. The new model can be compared with the upscaled 5-MW and some considerations can be drawn. The hub height is lower because a short tower is possible offshore. The drivetrain concept changed from a high speed gearbox to a medium speed one. Finally the blades have a certain prebend to ensure the tower clearance. The following SEAs have been used in SWT:

- Tower: connected to the drivetrain through the yaw node;
- Rotor: connected to the drivetrain through the blades root link nodes;
- Drivetrain: connected to the tower through the yaw node and to the rotor through the blades root nodes;
- Controller: not connected to other SEAs, but it reads the measured rotor speed in order to properly modify the aerodynamic torque by varying the blade pitch angle.

The tower has been modelled as a ten-segments tower. Its material is the steel alloy S355 which properties are reported in Table 3.12.

Young's modulus	$E$	210 $GPa$
Poisson's ratio	$\nu$	0.3
Density	$\rho$	8500 $kg/m^3$
Minimum yield strength	$\sigma_y$	355 $MPa$

Table 3.12: 10 MW tower properties

In order to take into account the presence of joints and flanges masses, an increase in the material density has been considered. The outer diameter is linearly decreasing from 8.3 m at the tower-base to 5.5 m at the tower-top. The thickness is kept constant along each segment and it is decreasing from 76 mm at the base to 40 mm at the top. The tower length is equal to 115.63 m. The rotor general properties are listed in Table 3.13. The blades are made of glass fiber reinforced composites and wood was used as sandwich core material.

Number of blades	3
Material	Glass fiber reinforced composites
Rotor diameter	178.3 m
Hub diameter	5.6 m
Blade length	86.366 m

Table 3.13: 10 MW rotor properties

The wind turbine blade is shown in Figure 3.30. The rotor design is the result of an optimization of aerodynamic and structural properties. The aerodynamic performances have been calculated by using the Blade Element Momentum (BEM) theory, while the structural properties have been studied according to the classical lamination theory.

The drivetrain has been modeled as a rigid body in which all the components are included (i.e. bedplate, gearbox, generator, hub and nacelle). Several kinematic chains have been investigated in order to analyze the influence of the drivetrain on the dynamics behavior of the entire wind turbine. Figure 3.31 shows the chosen kinematic chain. The hub consists of three rigid connections between the blade root nodes and the blades-hub link node. This node is then connected to the drivetrain chain by means of the LSS. The drivetrain connects the LSS to the HSS by means of a hinge. The gearbox ratio is consistent with the one proposed by DTU (50:1), which represents a medium-speed gearbox.

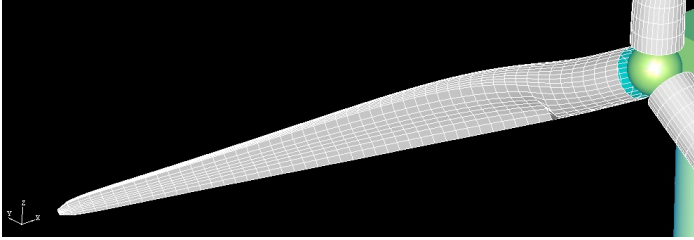


Figure 3.30: 10 MW - blade designed by using SWT.

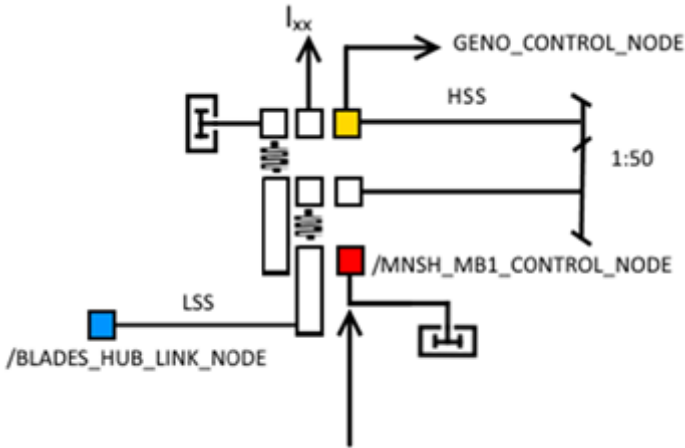


Figure 3.31: 10 MW - drivetrain kinematic chain.

The controller of the wind turbine would require a dedicated chapter to be described in details. The SAMTECH controller is reported in Figure 3.32. It is based on two main blocks: a generator controller and a pitch controller. A low-pass and a notch filters are also included in order to cut out input speed undesired oscillations.

As for the 5 MW wind turbine model, also in this case a first validation of the model has been done by comparing the masses of the entire wind turbine and of each separate component with the ones provided by DTU. Then the model has been validated by comparing the modal parameters with the ones listed in the DTU document. The first 7 modes identified in Table 3.14 are shown in Figure 3.33.

After the validation step, the same procedure used for the 5 MW model has

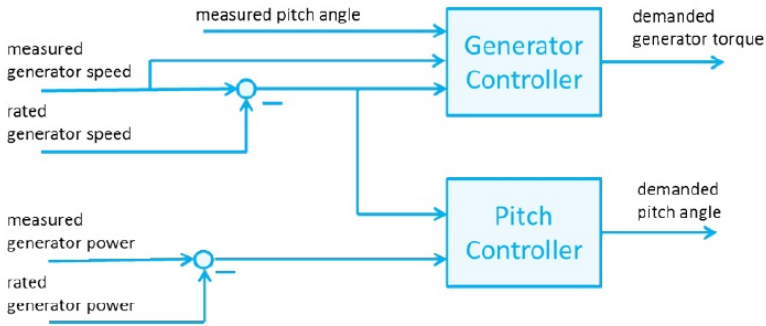


Figure 3.32: 10 MW - controller scheme.

Mode description	DTU Natural frequency [Hz]	SWT Natural frequency [Hz]	Error [%]
Tower FA	0.249	0.247	<1%
Tower S2S	0.251	0.251	<1%
1 <sup>st</sup> Flap Yaw	0.547	0.549	<1%
1 <sup>st</sup> Flap Pitch	0.590	0.598	1.3%
1 <sup>st</sup> Flap Sym	0.634	0.636	<1%
1 <sup>st</sup> Edge Pitch	0.922	0.942	2.2%
1 <sup>st</sup> Edge Yaw	0.936	0.959	2.4%
2 <sup>nd</sup> Flap Yaw	1.376	1.413	2.7%
2 <sup>nd</sup> Flap Pitch	1.550	1.573	1.5%
2 <sup>nd</sup> Flap Sym	1.763	1.812	2.7%

Table 3.14: 10 MW - model validation

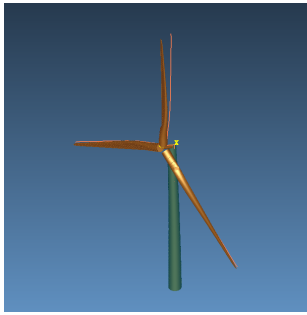
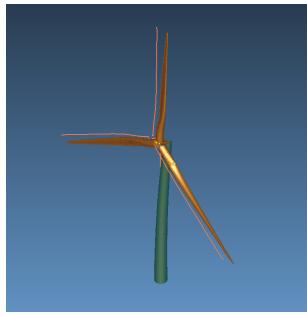
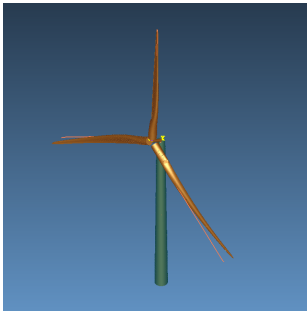
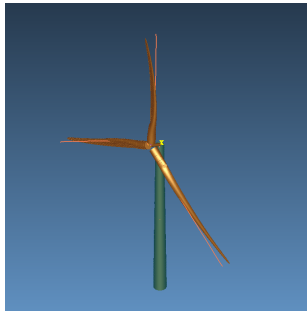
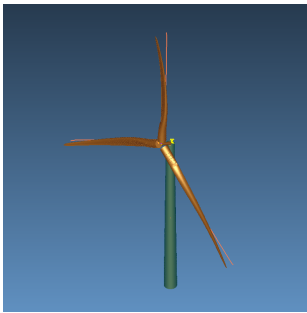
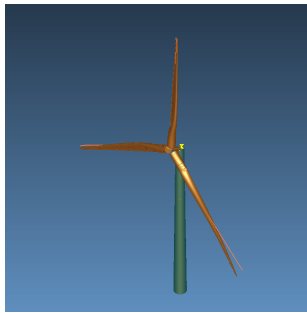
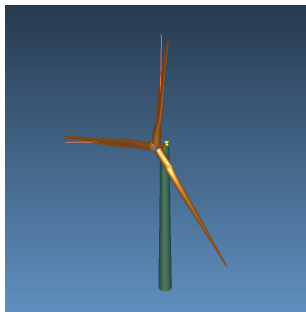
(a) *Tower FA.*(b) *Tower S2S.*(c) *1<sup>st</sup> Flap Yaw.*(d) *1<sup>st</sup> Flap Pitch.*(e) *1<sup>st</sup> Flap Sym.*(f) *1<sup>st</sup> Edge Pitch.*(g) *1<sup>st</sup> Edge Yaw.*

Figure 3.33: 10 MW model - mode shapes.



been followed. The wind turbine has been instrumented by using several virtual accelerometers and accelerations during its operating cycles are recorded.

**Parked configuration** The first case to be analyzed is the parked configuration in which the blades are not rotating and the wind is the only excitation which is effectively acting on the structure. In this situation, classical OMA can be applied in a straightforward manner because the system can be considered a LTI system excited by an input force which can be assumed as white noise in the frequency range of the first ten modes. The same procedure followed for the 5 MW model can be used. In this case a simulation time of 1000 s was chosen together with a sampling frequency equal to 200 Hz. A configuration with 4 sensors placed on the tower at several locations and 6 accelerometers along the blades (divided into 51 uniform sections) at the sections 10, 15, 30, 40, 48, 51 was used and it is shown in Figure 3.34. Also configurations with more sensors were used, but they did not improve the estimation while they were increasing the computational time.

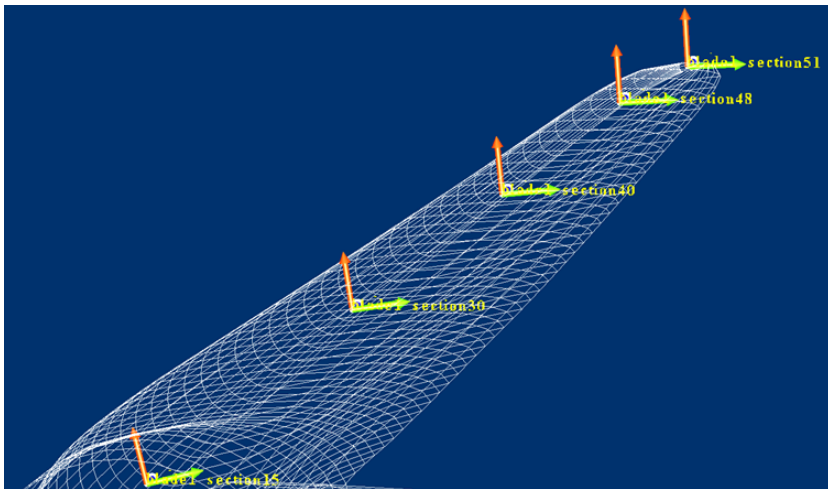


Figure 3.34: 10 MW - blade instrumentation.

Different wind conditions as well different “damages” were introduced and their effects on the model parameter estimation were analyzed. Figure 3.35 shows the stabilization diagram obtained in parked conditions. It is possible to see clear columns indicating the presence of stable poles. All the first ten modes were identified at frequencies very close to the ones listed in Table 3.14.

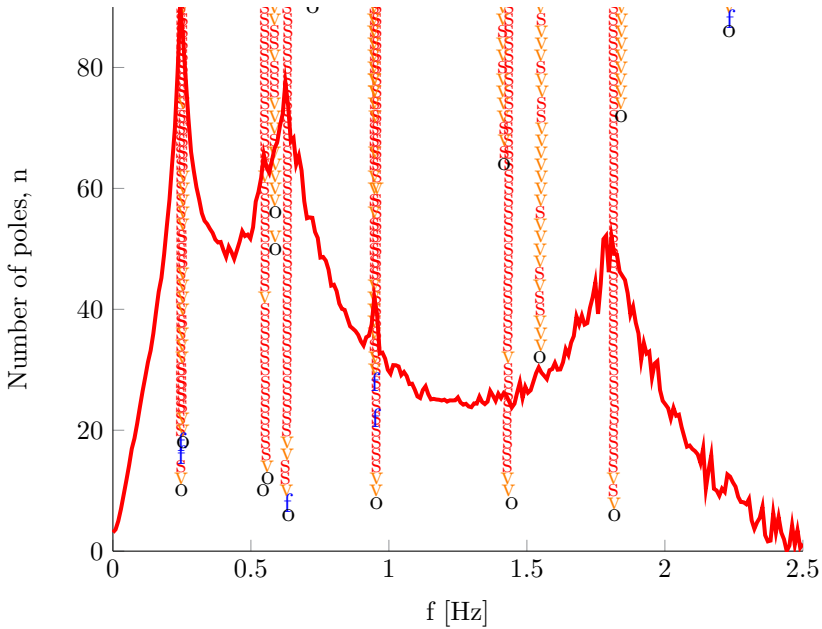


Figure 3.35: 10MW - stabilization diagram in parked conditions.

Figure 3.36 shows the auto-MAC matrix. It shows that we identified properly all the modes. The high value of the auto-MAC between modes 3, 4, 5 and 9, 10, 11 (around 60%) is due to the low number of sensors used for the analysis. Indeed, this value decrease quite a lot if we increase the number of sensors along the blade. It can be stated that 6 sensors placed at those locations were not enough to appreciate the differences between the first and the second blades bending modes in the flapwise direction. Also the auto-MAC between mode 2 and mode 5 is quite high (around 50%) and this can be explained with the fact that in the global side-to-side mode shape the rotor follows the tower and the channels placed along the blades detect almost the same behavior detected for the rotor flap with pitch mode.

**Rotating configuration** The final step is again the analysis in power production conditions. This configuration, as already explained, is more trivial. In fact the system is changing its configuration during each operating cycle. In general, it is a Linear Time Variant (LTV) system, but when the rotational speed is kept constant it can be considered as a LTP system. In this case most of the considerations are similar to the ones obtained for the 5 MW model, but of

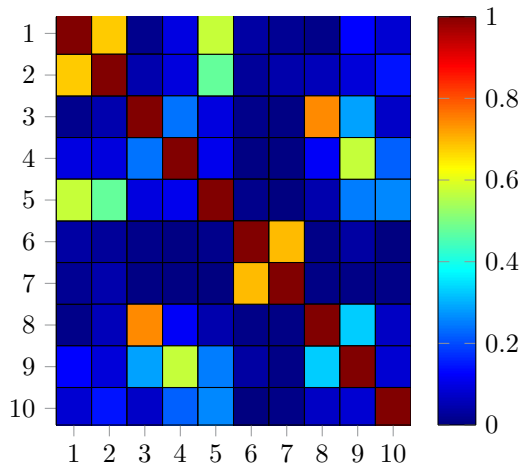


Figure 3.36: 10MW - auto-MAC matrix in parked conditions.

course some more complications are present in the new case. In fact, the 10MW wind turbine is much bigger than the other and as consequence the modes are at lower frequencies. The same is true for the rated rotational speed which is also lower, which means more harmonics in the data. After applying the MBC transformation only the  $3\Omega$  components are still present in the data and the whirling modes can be easily identified from the stabilization diagram due to their dominance in the structural response. These modes show the same properties highlighted for the 2D model and for the 5 MW model. Figure 3.37 shows the autopowers calculated for the channels in the lateral Y direction of the tower. Three different cases are shown: the one in which the rotational speed is constant and equal to 8 rpm, the one in which it is 9.6 rpm and finally the parked conditions. In the power production conditions, high peaks at integer multiples of  $3\Omega$  can be seen (also named 3P harmonics). They mask the dynamic behavior of the wind turbine in their frequency range. Also the whirling modes (which are normally the dominant modes in the Y direction) are masked by the  $9\Omega$  component. Only the BW mode can be seen at around 0.8 Hz in the case of higher rotational speed. It is remarkable to see that for such a big system, the amplitude of the harmonics is much higher than the dynamics of the system.

Figure 3.38 allows to see even better the differences in amplitude of the harmonics with respect to the system dynamic. In this case, the autopowers calculated for the channels in the edgewise direction Y of the blade tip (components in the rotor plane) are shown. For what concerns the blades, without applying

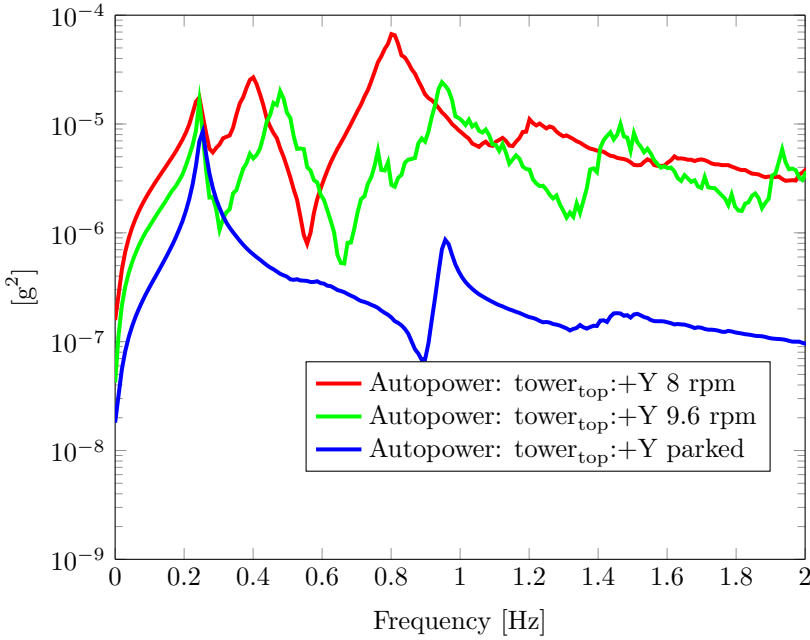


Figure 3.37: 10MW - autopowers related to the tower sensors - parked vs rotating conditions.

any transformation, all the multiples of  $\Omega$  harmonics are visible when the wind turbine is in operating conditions. Therefore, MBC and HPS transformations are needed in order to have some knowledge about the dynamics of the blades.

Finally, Figure 3.39 compares the stabilization diagram obtained by using the blade tip as reference in two cases: before applying any transformation and after applying MBC transformation. In the first case mostly harmonics are identified, while in the second case the  $3\Omega$  harmonics are still identified, but on top of them some physical poles can also be selected (the tower modes, the whirling modes and some flapwise modes). Not all the modes are identified because of the presence of the harmonics, but with a good harmonic filter the problem could be solved. On the other hand, after MBC the whirling modes continue being the dominant modes also for the 10 MW case and in Chapter 4 some SHM considerations regarding these modes are underlined.

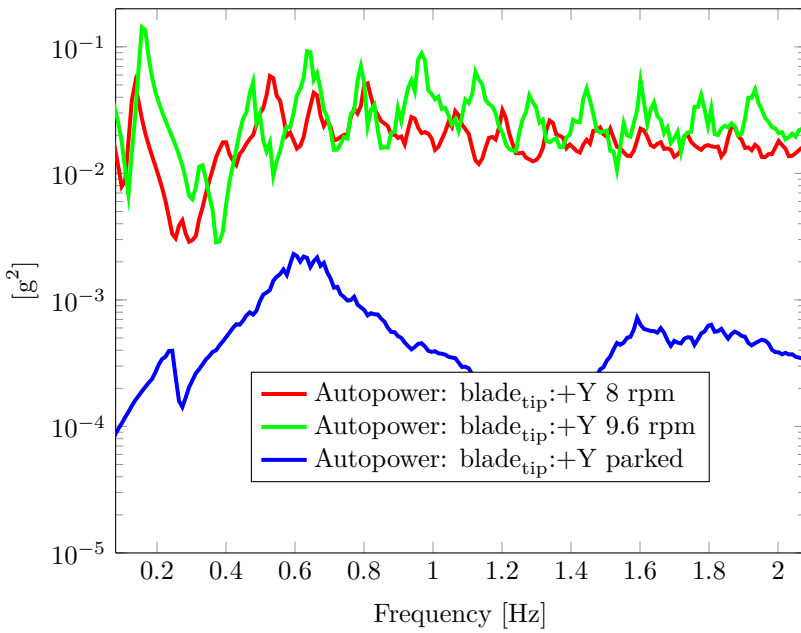
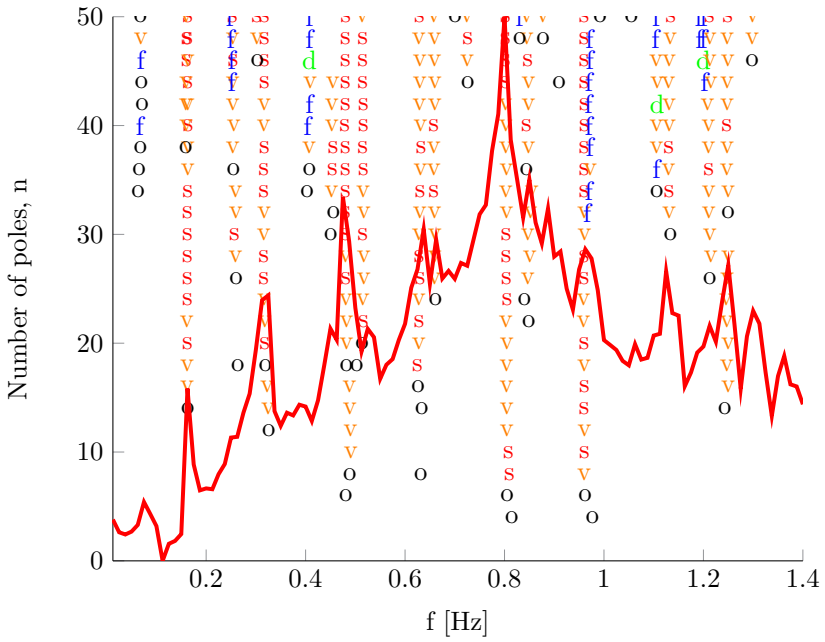
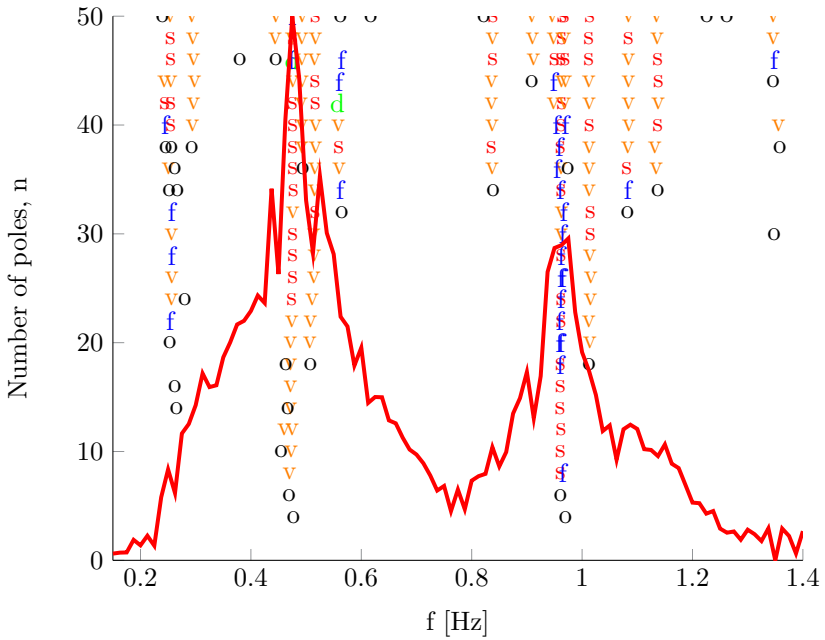


Figure 3.38: 10MW - autopowers related to a blade tip sensor - parked vs rotating conditions.



(a) 10 MW - stabilization diagram before MBC.



(b) 10 MW - stabilization diagram after MBC.

Figure 3.39: 10 MW - stabilization diagrams.

## Chapter 4

# SHM considerations: rotor sensitive parameters

This Chapter underlines the need of Structural Health Monitoring (SHM) techniques for wind turbines in Section 4.1. A list of sensors which could be used for this scope is given in Section 4.2. In order to perform SHM, a damage detection strategy needs to be defined. This topic is covered in Section 4.3. Then two different Structural Health Monitoring (SHM) strategies for wind turbine rotors are discussed. Section 4.4 shows how the whirling modes could be used as damage indicators. On the other hand, Section 4.5 introduces another SHM technique based on the use of the mode shape curvatures as damage indicators. Finally the damage detection procedure has been tested on a wind turbine blade and the results are shown in Section 4.6.

### 4.1 The need of Structural Health Monitoring for wind turbines

In recent years, wind energy has become one of the most exploited renewable energy technologies. In fact, even if wind turbines exist since decades, in the last twenty years huge improvements have been realized in terms of technology, size and produced mechanical power. Nowadays, 6-8 MW wind turbines with up to 160 m diameters have already been built and the trend shows that in the next years a power higher than 10 MW will be reached by offshore wind turbines. On the other hand, by increasing the power and consequently the size

of the wind turbines, structural problems can arise and they need to be solved in an early stage to avoid catastrophic effects (Figure 4.1).



Figure 4.1: Damage effects on operating wind turbines

This is one of the main reasons why wind turbine owners, operators and customers would receive huge benefits if a proper Structural Health Monitoring (SHM) strategy is set in place. This technology can provide an indication of the health and reliability of the entire structure or of its substructures during the operating lifecycle of the wind turbine. Several researchers are active in this field and a few techniques have been proposed and can be found in the literature [56], [57]. Their aim is to identify damages in wind turbine components such as blades, gearbox, generator, tower, etc before they actually occur in a real life situation. It is very important to underline the fact that a standard scheduled maintenance for a single wind turbine can require up to 24 hours, which means that it is a long process for what concerns an entire wind park. This is normally done twice per year in case of Horizontal Axis Wind Turbines (HAWTs). Furthermore, when a wind turbine is not operating, the loss of energy production translates into a huge loss of money for the wind farm owner. A SHM strategy should be able to identify damages well in advance in order to reschedule the maintenance ahead of time and reducing the associated costs. If damages or failures have already occurred, the maintenance can be up to 5 times more expensive or the situation can be already compromised and a substitution of single or multiple components can be required.

Hahn [58] acquired a huge dataset from more than 1500 HAWTs to understand and classify the damage occurring in operating wind turbines. The main aim of this study is the reliability characterization of HAWTs. Its outcome is that the components which are failing the most are the hydraulic pitch actuators and the bearings. They have the highest chance to fail once per year (25%). The main components such as the rotor blades and the gearbox have a chance of experiencing a damage in the same period equal to respectively 20% and 18%. Adams [59] addressed the potential of using blade operational measurements for detecting faults not only in the blades, but also in the drive train and nacelle both in a simulation and a test environment. The main damage indicators



selected in this prior study were the Modal Assurance Criterion (MAC) and the dynamic displacements in the span and edge-wise directions along the blades. It is clear that any SHM system should be based on a damage detection technique. In fact it is essential to identify some structural and environmental parameters which can be monitored continuously during the operation of the wind turbine. Such a technique should identify if a damage is present in the structure, but it should also be able to localize and quantify the damage itself. When a certain threshold has been reached, a warning signal should be sent to the wind farm operator in order to eventually reschedule the maintenance cycle. In general, damages could be seen as changes in material or geometric properties of a structure, including also variations of the boundary conditions and structural connections [60], [61]. Therefore, a damage can modify the normal operating conditions of the machine and it is crucial to identify them well in advance to avoid to stop the wind farm because of unforeseen accidents.

## 4.2 Sensors and non-destructive testing methods

A sensor is defined as a device which detects or measures some conditions or properties and records the information received. It converts a stimulus (mechanical, electromagnetic, acoustic) into a measured signal (electrical, optical, pneumatic). The selection of the proper sensor for a certain application is a difficult task for an engineer. Several studies tried to give guidelines on the use of sensors depending by the objectives to be achieved [62]. It can be distinguished among several kind of sensors for SHM applications. We can limit the attention to sensors which can detect displacements, strain, velocities and accelerations. The velocity sensors can be divided into contact-type sensors (electromagnetic, piezoelectric and cable-extension based) and non-contact ones (optical and microwave). Accelerometers are the most common sensors for vibration measurements. They are used, as their name suggests, to measure accelerations. The fiber optics and the strain gauges also became very popular in the last years and their main applications are in the SHM field. Although velocity and acceleration are the first and second derivatives of displacement with respect to the time, velocity and acceleration measurements are not usually achieved by time differentiation due to the noise in the signals. Sorensen [63] demonstrated the cost-benefits in embedding the sensors in the blades for identifying possible damages. Several solutions have been compared in terms of efficiency and costs: acoustic emission (AE) sensors, embedded fiber optics and conventional accelerometers. The last solution showed to be the cheapest one, but the second one is the most attractive because the wires in the blades can be eliminated and problems in case of lightening can be avoided. Another possible solution consists in the use of electrical strain gauges which are able to measure

the strain distribution along the blades. In conclusion, we can distinguish among several kind of sensors and each of them has its own advantages and drawbacks. On the other hand different information can be extracted and added to each other. Sections 4.2.1 and 4.2.2 describe the concept behind the most used sensors for SHM applications. A complete SHM system should be able to read information from all these sensors and to combine all the information together in order to detect and identify damages.

### 4.2.1 Conventional accelerometers

Accelerometers use the mass of an element to convert acceleration into a force, according to the 2<sup>nd</sup> Newton law. The imposed acceleration causes a relative displacement of the inertial mass with respect to the housing or a force on the force-sensing element (i.e. piezoelectric materials) by the inertial mass. Several types of accelerometers can be found in the market.

- Capacitive accelerometers:  
They operate by detecting the changes in the spacing of two capacitor plates of which one is attached to the housing and the other is attached to the inertial mass. Temperature calibration is needed to get accurate measurements. (Figure 4.2)

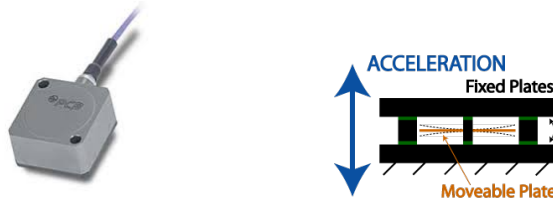


Figure 4.2: Capacitive accelerometers

- Servo accelerometers:  
Servo accelerometers are used in the inertial navigation systems. They use the deflection signal as feedback in the servo system that moves the inertia mass back to the equilibrium position. They have higher resolution, accuracy and stability, but they can be used for measuring only up to 300 Hz. (Figure 4.3)
- Piezoelectric accelerometers:  
Piezoelectric accelerometers are equipped with a piezoelectric crystal placed between the seismic mass and the sensor housing. The acceleration

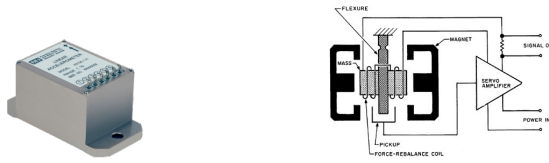


Figure 4.3: Servo accelerometers

of the inertial mass causes a force on the crystal which induces a charge. This charge is detected by the charge amplifier. They have a wide frequency range from 0.1 Hz to 20 kHz. (Figure 4.4)



Figure 4.4: Piezoelectric accelerometers

## 4.2.2 Displacement sensors

Several types of displacement sensors are available in the market. They can be contact sensors or non-contact ones:

- **Capacitive sensors:**  
Capacitive sensing is a non-contact technology suitable for detecting the position of several kind of materials (metal, non-metal, solids and liquids). A change in the spacing of the capacitor plates results in a change in the measured capacitance.
- **Eddy current sensors:**  
Eddy current sensing is also a non-contact technology which allows to detect electrically conductive objects. These sensors generate an electromagnetic field. They use two coils: one as reference and the other one for sensing the currents induced in the conductive target. The closer the target to the sensing coil, the greater the change in the magnetic impedance.
- **Video extensometers:**  
Video extensometers are also among the non-contact technologies. They

use a CCD camera to send displacement data to an image processing system in order to evaluate the displacement of a target.

- **Strain gauges:**  
Strain gauges are resistive sensors consisting of a wire, a photographically etched foil or a semiconductor element bonded to an insulating base. When the wire get strained, a change in resistance can be detected which is proportional to the strain itself. The resistance is measured by using a bridge circuit. Temperature compensation is needed.
- **Fiber optics:**  
Fiber optics utilizes the fact that the propagation of light through an optical fiber is strongly affected by bending the fiber. A sensor of this type can be produced at a very low cost, but it is sensitive to displacements only at the sensor position. Therefore, a certain number of sensors need to be placed in order to get a satisfactory spatial resolution. Fiber optic cables can be mounted in locations that would be otherwise inaccessible to other types of sensors. They could also be embedded in the material.

### 4.3 Damage detection techniques

In the last years, several damage detection techniques and algorithms have been developed. Among the most interesting ones there are the AE method [64], [65], the impedance-based method [66], the wave propagation-based method and the vibration-based (VB) methods [67]. The AE approach can be considered a standard practice for damage detection purposes during blade tests, but it requires the availability of a lot of AE sensors in order to cover the interested regions [64], [65]. The VB methods are based on the fact that when a damage is occurring and growing, it affects mainly the structural stiffness of the system . At this point, changes in the modal parameters of the structure, such as natural frequencies, damping ratios, mode shapes and derived properties can be seen. All these methods are based on the comparison between a “healthy” condition and a “damaged” one. Some techniques are based on the mode shapes and their derivatives effectiveness for damage localization [68], [69], other methods use the Frequency Response Functions (FRFs). For instance, the frequency response curvature method considers the FRF at different locations along the structure for each frequency and compares the curvatures in the damaged and undamaged cases [70]. The interpolation damage detection method is also based on the FRFs, but it uses a spline interpolation in order to identify the damage [71]. All these techniques are not applied only in the wind turbine domain, but they can be applied in a huge variety of a damage detection related cases.

The main topics in the literature for what concerns wind turbines are the blades and the gearbox. There are several studies in which SHM techniques are applied to these two components. SHM applied to blades has been faced by several researchers. Ghoshal [66] described the SHM of composite wind turbine blade. An extensive review study about SHM and non-destructive testing methods applied to wind turbine blades was described by Sutherland [65]. Adams [59] introduced active damage detection methods based on the use of accelerometers that recorded the dynamic response of a rotor blade during static testing performed by the Sandia National Laboratory at the National Renewable Energy Laboratory (NREL). Rumsey [67] gave an overview of SHM techniques based on vibration, acoustic emission and impedance measurements taken during a wind turbine blade test. Schroeder [72] used fiber Bragg grating strain sensors for monitoring rotor blades. On the other hand, for what concerns the drivetrain, several studies described sensing techniques and algorithms for Condition Monitoring (CM) of critical components such as bearings and gears. Sensors installed on the drivetrain have been used for fault detection. Adams [59] explored the potential of using blade measurements to detect faults in the drivetrain and nacelle.

An important aspect related with all damage detection techniques concerns the environmental effects. Several studies demonstrated that it is not easy to separate abnormal changes from normal changes in the dynamic behavior. Normal changes are caused by environmental condition variations such as humidity, wind and temperature. The temperature can affect both the boundary conditions and the material properties. On the other hand, abnormal changes can be due to several factors such as damages and they can be critical for the structure. In [73] the Z24-Bridge in Switzerland was monitored during almost one year before it was artificially damaged. Black-box models are determined from the healthy-bridge data. These models describe the variations of eigenfrequencies as a function of temperature. New data are compared with the models. If an eigenfrequency exceeds certain confidence intervals of the model, there is probably another cause than the temperature that drives the eigenfrequency variations, for instance damage. These issues have not been taken into account in the following discussion.

## 4.4 Whirling modes as damage indicators

The first step in a Structural Health Monitoring (SHM) algorithm is the identification of damage sensitive parameters. It has been proven that the whirling modes are the most identifiable modes in operating conditions both in a simulation and in a test environment. They can be considered as damage

indicators. Figure 4.5 shows the polar plot for the backward whirling mode. In green, blue and red there are the three blades. It can be noticed that in a perfectly symmetric case, this mode is characterized by the fact that all the blades have the same amplitude and they are shifted in phase by a factor equal to  $120^\circ$ . This is a characteristic behavior of both backward and forward whirling modes. On the other hand, the collective edgewise mode can be seen in Figure 4.6. This mode is characterized by an equal amplitude and a  $0^\circ$  phase among the three blades. These two features could be used for SHM purposes. If these properties get lost during the operation of a three-bladed system, then there is an asymmetry which could be associated to an incipient damage. It is also possible to identify which one is the "damaged" blade. Of course, in real life the three blades are not equal to each other because of the manufacturing process and the material properties. This will lead to an asymmetry at the initial stage, when the blades are all "healthy". Anyhow the underlined features could be used by looking at the differences between the initial conditions and the actual ones.

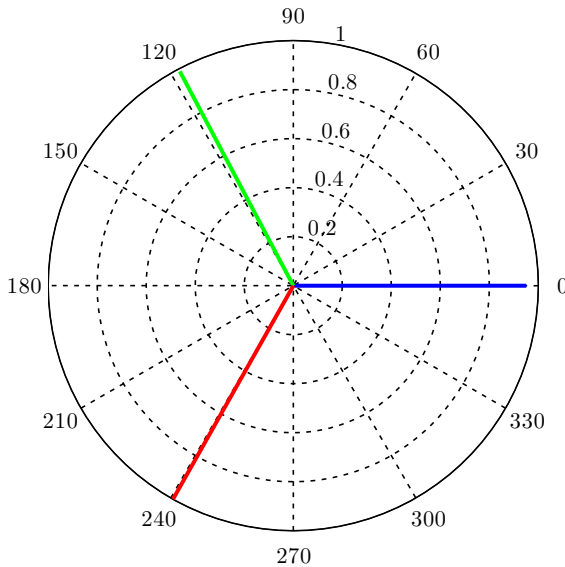


Figure 4.5: Healthy case - backward whirling mode.

In a preliminary study a reduction of the stiffness of one of the blades has been applied in order to simulate a possible damage. Figure 4.7, Figure 4.8 and Figure 4.9 show a progressive reduction of the stiffness of blade 1 (blue color) of a percentage (99%, 97% and 95% respectively) of the nominal value.

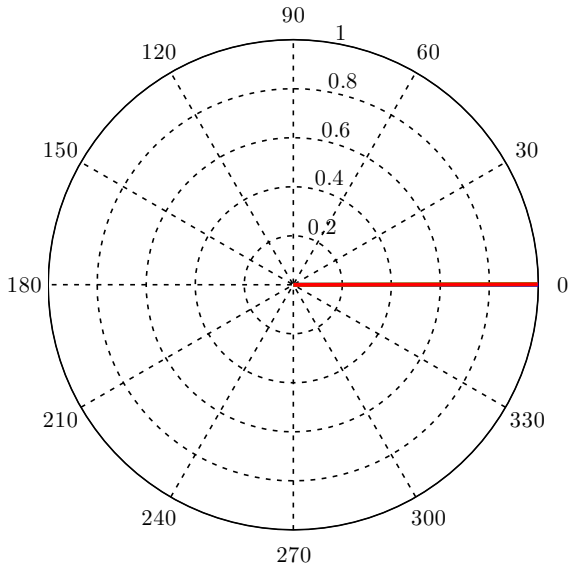


Figure 4.6: Healthy case - collective mode.

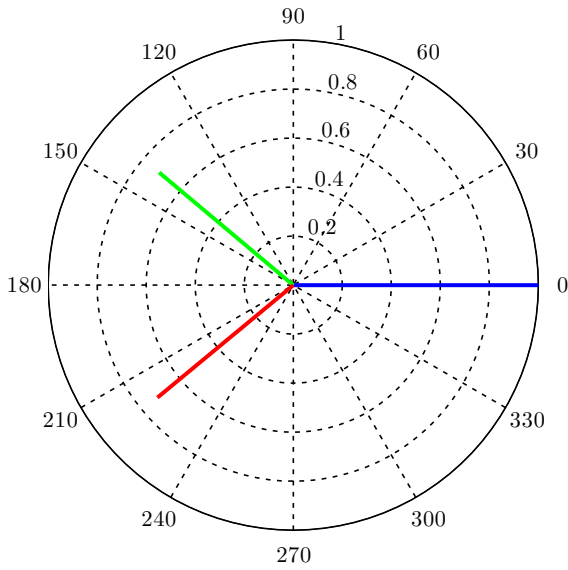


Figure 4.7: Stiffness reduction ( $k_1=0.99$ ) - backward whirling mode.

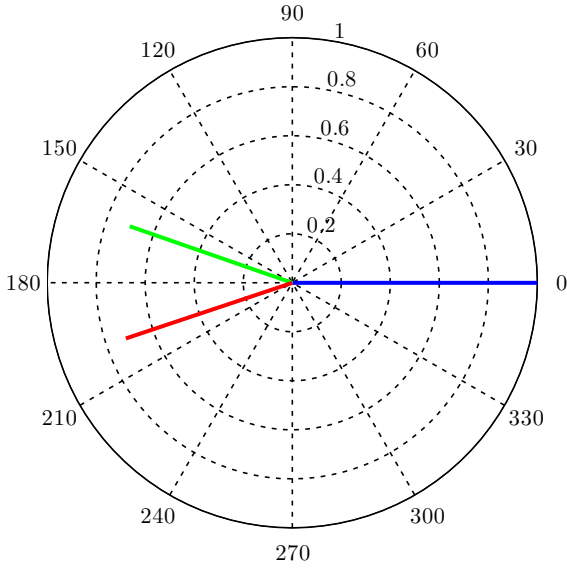


Figure 4.8: Stiffness reduction ( $k_1=0.97$ ) - backward whirling mode.

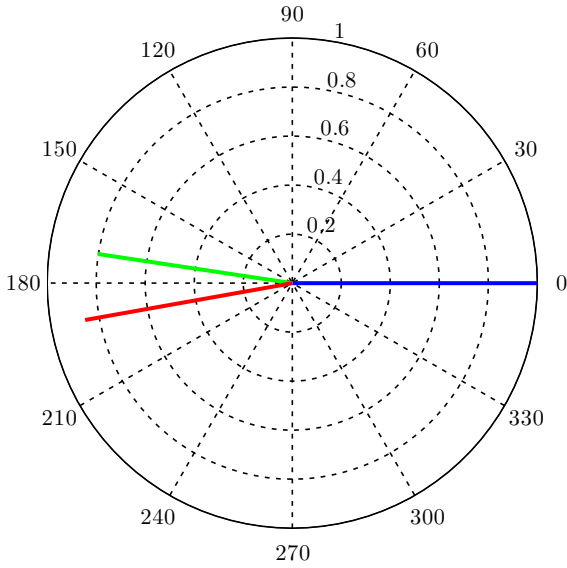


Figure 4.9: Stiffness reduction ( $k_1=0.95$ ) - backward whirling mode.



It can be clearly noticed how the phase lag between the blades is not anymore equal to  $120^\circ$  and the amplitude of the damaged blade is higher than the ones of the other two blades. So finally, both amplitude and phase of these modes can be used as damage indicators since they are able to detect even small changes in the stiffness of the blades. For what concerns the collective edgewise mode, different conclusions can be drawn. In fact, in this case, we are looking at a collective mode. As its name says all the blades move in phase with each other and this is not altered by the asymmetry. At least it is not for small stiffness reductions. On the other hand, the amplitude of the mode shapes for the different blades change in a significant manner, as it is shown in Figure 4.10, Figure 4.11 and Figure 4.12.

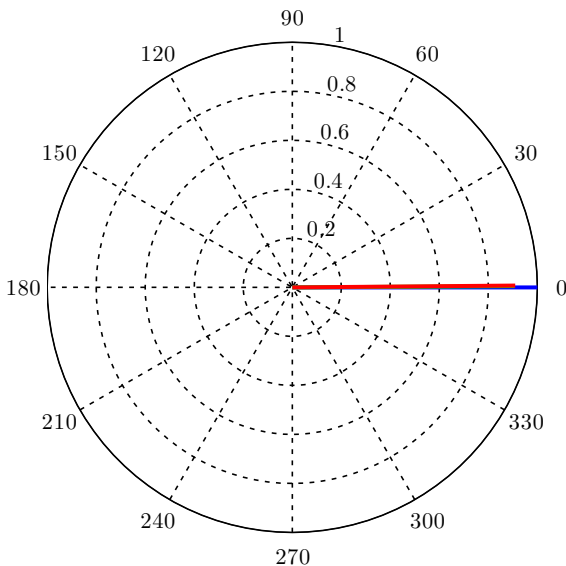


Figure 4.10: Stiffness reduction ( $k_1=0.99$ ) - collective mode.

## 4.5 Mode shape curvatures as damage indicators

It is well-known that the presence of a crack or a damage in a structure will cause a reduction of stiffness which can be seen as a reduction of its natural frequencies. Many researchers [74] [75] [76] have attempted to detect damages in structures by comparing the natural frequencies of the undamaged and the damaged structure. For example, the Normalized Natural Frequency ( $NNF_r$ )

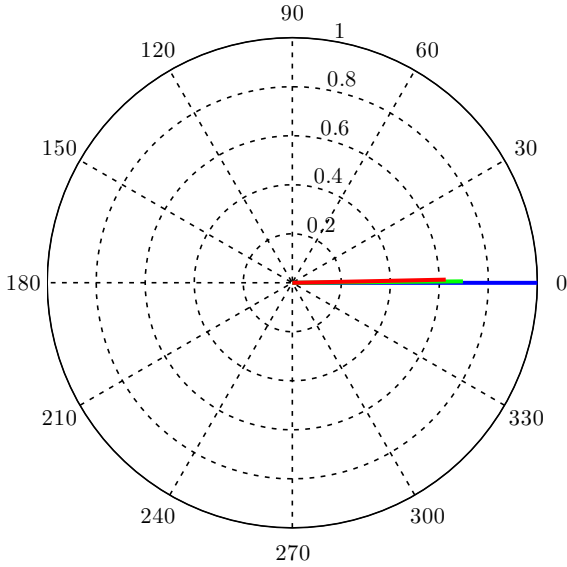


Figure 4.11: Stiffness reduction ( $k_1=0.97$ ) - collective mode.

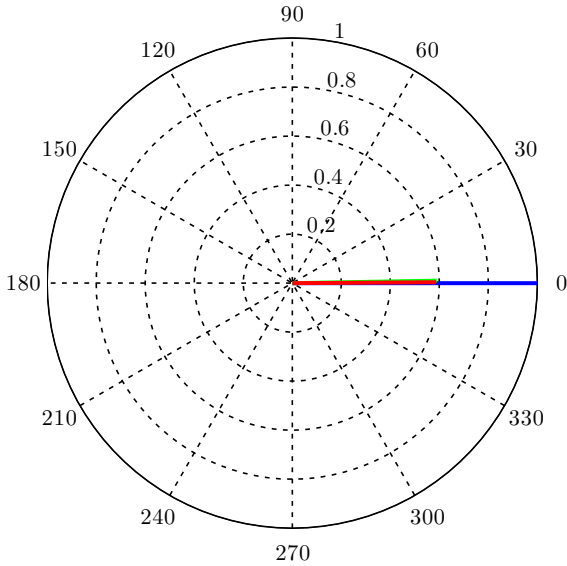


Figure 4.12: Stiffness reduction ( $k_1=0.95$ ) - collective mode.

defines the ratio between the damaged natural frequency and the undamaged one, as shown in Equation (4.1).

$$NNF_r = \frac{\omega_r^{damaged}}{\omega_r^{undamaged}} \quad (4.1)$$

Another parameter which can be used is the percentage changes in the natural frequency (Equation (4.2)).

$$\%C_r = 100 \times \frac{\omega_r^{undamaged} - \omega_r^{damaged}}{\omega_r^{undamaged}} \quad (4.2)$$

Normally, in order to detect the presence of a damage, the natural frequencies of the undamaged structure need to be carefully estimated. In fact, the change in percentage of these frequencies can be lower than 1% for small cracks propagating in the structure. So, uncertainties on the natural frequencies of the undamaged structure may lead to erroneous conclusions by hiding the small amount of frequency change. A mode shapes approach (as shown also for the so-called whirling modes) can lead to better results both in term of identification and localization of the structurally damaged regions. Moreover, the variation of mode shapes depends on both the severity and the location of the damage. The presence of a crack results in a change in the mode shape of a structure which manifests itself as a discontinuity in the response close to the crack location. In case of small cracks along a cantilever beam it can be hard to detect the problem by only looking at the mode shape. In fact only a small variation of the curves if compared to the undamaged case can be seen. In this case it can be very helpful to look at the first, second and third derivatives of the displacement mode shapes, which correspond to the slope, curvature and rate of curvature of the same beam. They give progressively a better indication of the presence of a damage, but on the other hand “noise” effect due to the difference approximation error also magnify at higher derivatives. A good compromise, for this purpose, is the use of the first two derivatives (slope and curvature). For instance, a reduction of the bending stiffness  $EI$  in a specific region of a beam will cause a growth of curvature in that region: hence the fault locations can be detected by comparing the curvature of the undamaged and damaged beam. In order to compute the curvature from the mode shapes ( $\Phi$ ), a central approximation (Equation (4.3)) can be used.

$$\ddot{\Phi}_{s,r} = \frac{\Phi_{i+1,r} - 2\Phi_{i,r} + \Phi_{i-1,r}}{\Delta h^2} \quad (4.3)$$

Where  $\Delta h$  is the coordinate difference between measured points  $i$  and  $i + 1$ , while  $r$  indicates the  $r$ -th mode shape. The need for an accurate evaluation of mode shapes in a starting condition (healthy or undamaged) and in case in which damages are occurring must be emphasized. This is not always possible in case of complex structure and in operating conditions. On the other hand, several kind of structure (i.e. aircraft wings, bridges, wind turbine blades) can be considered as beam-like structures with their own boundary conditions (i.e. clamped-free in case of wings and blades, clamped-clamped in case of bridges and so on). In these cases it is possible to reduce the complex structure to an equivalent beam and its dynamics can be studied by analyzing the dynamics of the equivalent beam. The first step is the evaluation of the modal curvatures of the undamaged structure. They can then be used as normalization parameters of the modal curvatures of the damaged structure. The Modal Shape Curvature Index ( $MSCI_i$ ) can be defined as shown in Equation (4.4) [77].

$$MSCI_i = \ddot{\Phi}_{i,r}^{undamaged} - \ddot{\Phi}_{i,r}^{damaged} \quad (4.4)$$

$i$  stands for the measurement point location. If  $MSCI_i$  has a discontinuity in some regions, a structural fault can be identified in these regions. For an undamaged structure, the derivatives of the mode shapes are smooth curves. Local peaks or discontinuities on the slope (first derivative) can underline an abnormal mode shape change. Both for the first and second derivative case, the damage detection is evidenced by the crossing behavior of the damaged curves with the undamaged ones. In particular, the second derivative (curvature) can be used to estimate the position of the damaged region of the structure: the intersection between the curvature in the undamaged and damaged case indicate the beginning and the end of the damaged area. The curves can be normalized with respect to the initial state curves (considered as undamaged) by subtracting them so that the curves representing the damaged structure will be negative in the damaged zone. The presence of the damage, its position and its extension can be obtained by using this method.

## 4.6 Damage detection on a wind turbine blade

### 4.6.1 Wind turbine blade

The wind turbine blade under investigation is a 6.5 m fiberglass from a small wind turbine (30kW). Eolpower Group performed the needed aerodynamics and structural design of the blade under the project Wind4Life. Its main technical characteristic are shown in Table 4.1 [15].

Figure 4.13 shows the two airfoils used for the section of the blade. The first one has a maximum thickness of 25% of the chord length and it is used from the root up to 27% of the radius. The second one has a maximum thickness of 21% of the chord length and it is used from 30% of the radius up to the tip of the blade.

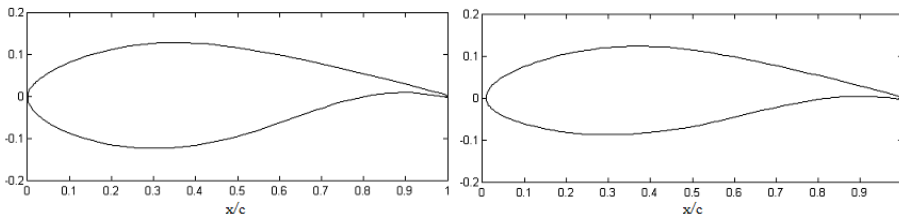


Figure 4.13: Wind turbine blade airfoils.

Both the chord and the twist distribution along the blade were obtained by using an optimization code in which the maximum area was fixed and the requirement was the nominal rotation speed equal to 80 rpm. Figure 4.14 shows the chord and twist distribution along the span.

The wind turbine blade is made of a high-performance foam core (DIAB Divinycell H45), offering excellent mechanical properties and low weight. Two different configurations of laminates (unidirectional and fabric) are present and the properties of the core and the laminates are reported in Table 4.2. The material properties of the foam are the ones referred to in the datasheet, while the mechanical properties of the laminates are obtained by carrying on static tests according the relative standards.

Wind turbine WL 30	
Rotor type	3-bladed, horizontal axis
Nominal power	30 kW
Rotor diameter	13.6 m
Blade length	6.5 m
Rated rotor speed	80 rpm
Cut-in wind speed	3 m/s
Cut-out wind speed	20 m/s
Nominal power wind speed	10.8 m/s
Hub height	24.8 m

Table 4.1: Wind turbine characteristics

A Finite Element (FE) model of the blade has been developed based on the geometry and structural information. Several configurations for what concerns the sequence and the number of plies of the composite material have been used. In Figure 4.15, the different material configurations along the blade span are shown by using different colors.

The most common approach for understanding the dynamic behavior of a structure is to construct a FE model and validate it with measurement data. Then, once the model is able to reproduce the behavior of the real structure, it can be used for vibration-based SHM purposes. The full-scale model can be very accurate, but on the other hand it requires a high computational power. It was modeled using 4-node quadrilateral elements (CQUAD4) for the skins

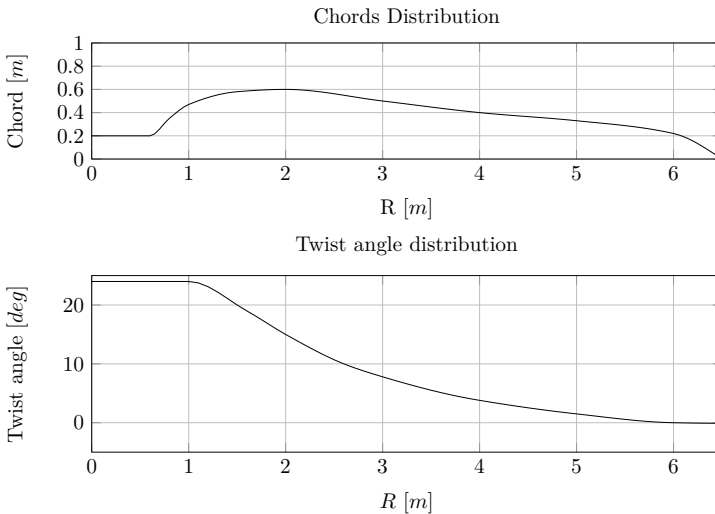


Figure 4.14: Angle of twist and chords distribution of the blade.

Elastic constants	Units	Foam H45	Unidirectional laminate	Fabric laminate
$E_1$	[GPa]	59	30.0	15.6
$E_2$	[GPa]	-	7.0	15.6
$G_{12}$	[GPa]	15.9	4.0	4.0
$\nu$		0.32	0.22	0.27
$\rho$	[kg/m <sup>3</sup> ]	48	2200	2200

Table 4.2: Core and laminate mechanical properties

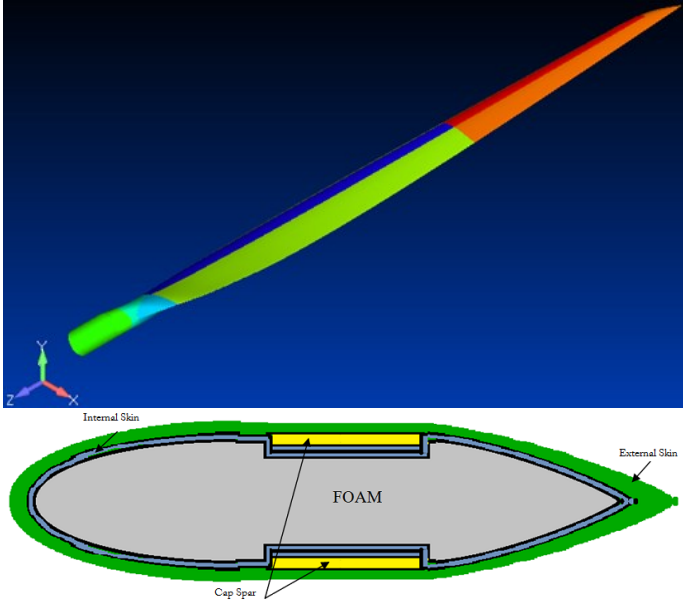


Figure 4.15: Different material properties along the blade span - Generic section.

of the blade and rigid elements (RBE3) for the ribs and constraints. A total number of 11805 nodes and 10867 elements have been used. A picture of the FE model can be seen in Figure 4.16.



Figure 4.16: FE model of the turbine blade.

In order to simplify it and reduce the computational cost, it is common practice to reduce blade models to beam-like structures. Therefore the complex 3D full blade model was converted into a simplified equivalent 1D beam model consisting of 62 nodes and 61 CBEAM elements along the blade. These elements are indicated with black dots in Figure 4.17. 11 concentrated mass elements (CONM2) are also present in the model and they are indicated as white squares. The new model simulates the mass and stiffness characteristics of the 3D one with a minimum loss of accuracy. The same distribution of dynamic stiffness (bending stiffness  $EI$  and torsional stiffness  $GJ$ ) along the span has to be

guaranteed. Therefore, using the Euler-Bernoulli beam theory, the inertia and the torsional moments can be found by using Equation (4.5) section by section by performing a static test.

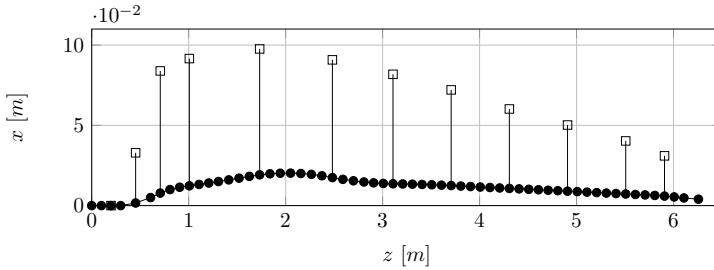


Figure 4.17: Neutral axis and gravity centers of the blade.

$$\begin{aligned}\Delta\theta_x &= \frac{1}{(EI_x)_AB} \int_A^B M_x dz \\ \Delta\theta_y &= \frac{1}{(EI_y)_AB} \int_A^B M_y dz \\ \Delta\phi &= \frac{1}{(GJ)_AB} \int_A^B T_x dz\end{aligned}\quad (4.5)$$

$M_x$  and  $M_y$  are the bending moments and  $T$  is the torque.  $\Delta\theta_x$  and  $\Delta\theta_y$  and  $\Delta\phi$  are the three rotations of the cross section. The inertia distributions along the span are reported in Figure 4.18.

## 4.6.2 Experimental results

Operational Modal Analysis was used for estimating the dynamic properties of the blade. Two tests were performed: pre-buckling and post-buckling. They were useful for investigating the change of modal parameters due to the presence of a damage. The phenomenon of the buckling is very well-known and it is widely studied since decades in the aerospace field. It consists of a failure of the structure caused by a strong deformation which distorts the geometrical topology and the associated load-carrying capabilities. Most of the studies were performed on aluminum structures, which means on isotropic materials. On the other hand some studies were already done in presence of fiber-reinforced composite structures. The wind turbine blade under investigation was fixed



to a rigid structure by using bolts at only one end resulting in a cantilever beam. On the other side, it was manually excited. Ten tri-axial accelerometers were used for recording the response of the system. They were placed on two lines along the blade with the objective to evaluate both the flexural and the torsional mode shapes. Operational Polymax was used for extracting the modal parameters in the selected frequency range (0-256Hz). The experimental setup together with the locations of the accelerometers is shown in Figure 4.19.

Figure 4.20 shows the autopowers calculated by considering the acceleration signals at the tip node in the out-of-plane direction in both cases (pre- and post-buckling).

In this case, the shift of the natural frequencies toward lower values can be easily noticed. This is due to the stiffness reduction of the structure. In fact a damage can be seen as a reduction of the mechanical properties of a structure. Figure 4.21 shows the so-called stabilization diagram in the two cases. Several poles are identified, but taking into account the Modal Assurance Criterion (MAC) and the synthesized spectra, only the ones listed in Table 4.3 are selected as physical poles of the structure.

The same table lists also the damping ratios obtained for each mode and a huge increase in these values can be seen with reference to the second mode.

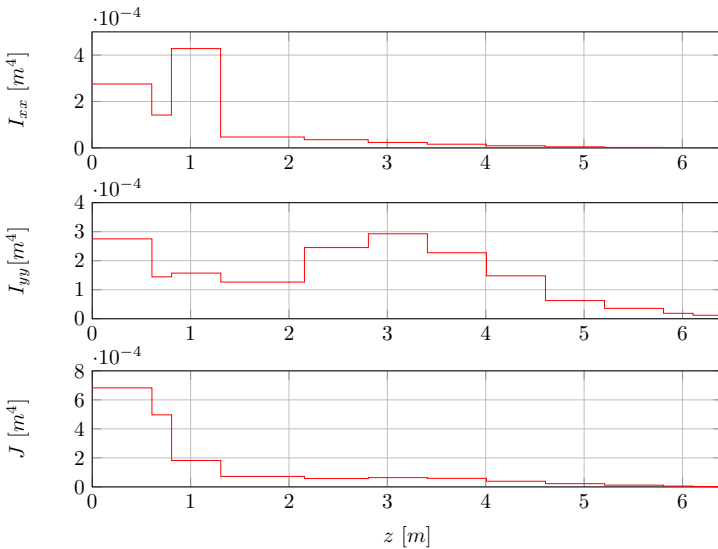


Figure 4.18: Inertia moments  $I_{xx}$ ,  $I_{yy}$  torsional constant  $J$ .

Mode n.	Pre-buckling		Post-buckling	
	[Hz]	[%]	[Hz]	[%]
1	3.93	2.06	3.20	1.98
2	7.92	0.74	6.09	2.90
3	11.33	1.35	9.98	1.01
4	24.78	0.65	22.93	0.47

Table 4.3: Experimental natural frequencies and damping ratios of the blade.

### 4.6.3 Model validation

For validating the reduced-beam model, static and dynamic analysis have been performed on both the 1D and the 3D models. For what concerns the static analysis, the two models have been loaded with the same static force along the x and y directions ( $F_x = F_y = 100\text{N}$ ). The results of the two static analysis are reported in Figure 4.22 in which the displacements of the two models have been plotted. The error is in both cases less than 5%.

On the other hand, modal analysis was performed on the two models using the commercial finite element solver NX Nastran. The results show that the

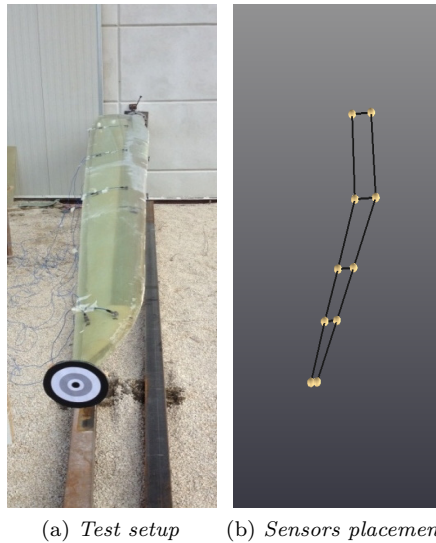


Figure 4.19: Test specimen and instrumentation

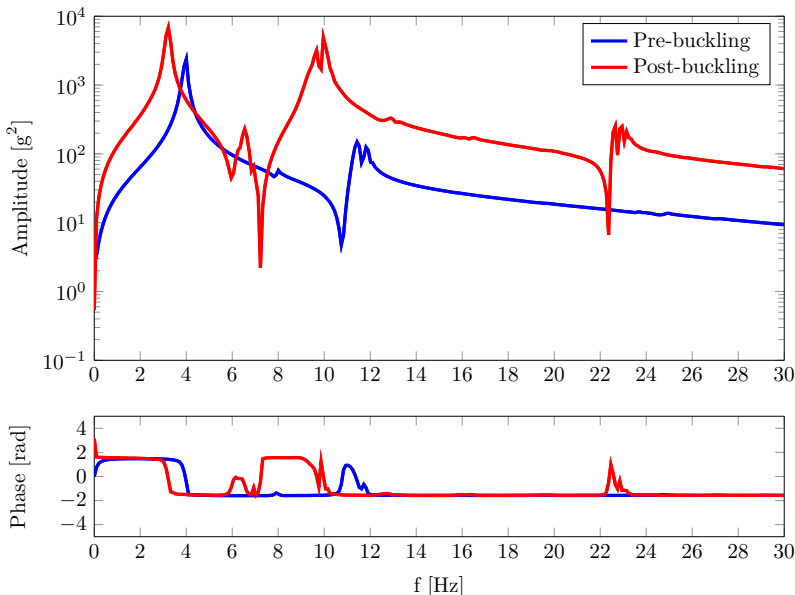


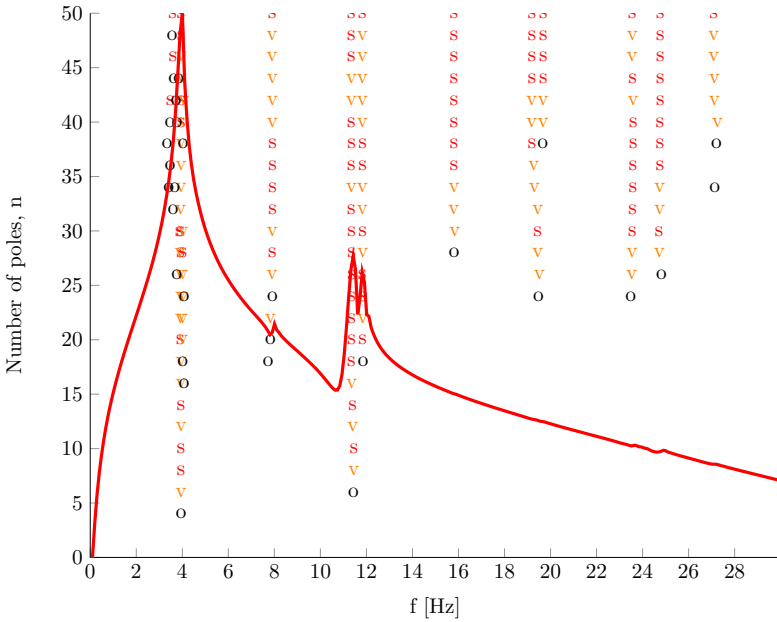
Figure 4.20: Autopowers pre and post buckling at a tip node in out-of-plane direction.

reduced-order beam reproduces the dynamic behavior of the wind turbine blade in the frequency range [0-30Hz]. The natural frequencies are listed in Table 4.4.

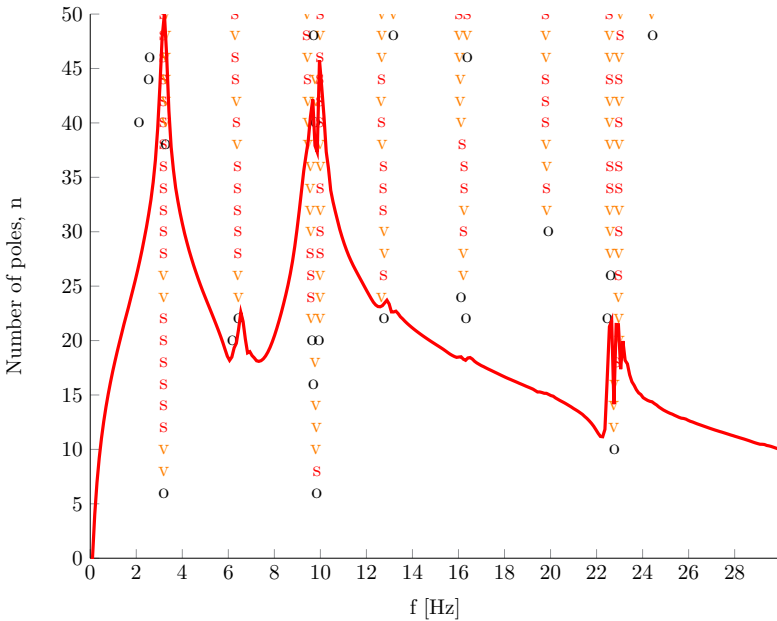
	3D model [Hz]	Beam [Hz]	Experimental	Error [%]
Mode 1	3.952	3.963	4.005	1.05%
Mode 2	8.317	8.040	7.994	0.58%
Mode 3	12.960	12.014	11.376	5.61%
Mode 4	24.910	24.706	24.887	0.73%

Table 4.4: Modal frequencies comparison.

They are also compared to the ones identified by performing OMA on the real wind turbine blade. This analysis confirms that the beam model is able to ensure good results and for this reason it will be used for subsequent damage detection studies.



(a) Pre-buckling



(b) Post-buckling

Figure 4.21: Stabilization diagrams.

### 4.6.4 Damage detection in standing still conditions

The wind turbine 1D model discussed in the previous sections has been used for studying natural frequencies and mode shapes variations in case of a damage located in a specific area. In a simulation environment, a damage can be introduced by reducing the mechanical properties of the beam material in a certain region. The *MSCI* technique has been used for identifying and localizing the damage. In order to replicate the same damage occurred during the experimental campaign, the damage was simulated in a section close to the root of the blade. A sensitivity study for defining the proper damage extension and material properties reduction has been performed. Several damage extension (40cm, 80cm, 120cm and 140cm) and percentage stiffness reduction (10%, 20% and 40%) were used in this study. The parameters to optimize were the natural frequencies of the 1D model to be as close as possible to the experimental ones. From all the investigated configurations (listed in Table 4.5), the beam with a damage extension of 140cm and a reduction of 40% of the mechanical properties of the material was selected.

The same study was performed also for the 3D model. In this case the presence of a damage was modelled as a local reduction of the mechanical properties of some elements of the entire structure, as listed in Table 4.6. In order to replicate the damage occurred during the experimental test, the damage was simulated in the section close to the blade root also in this case. The same damage extension

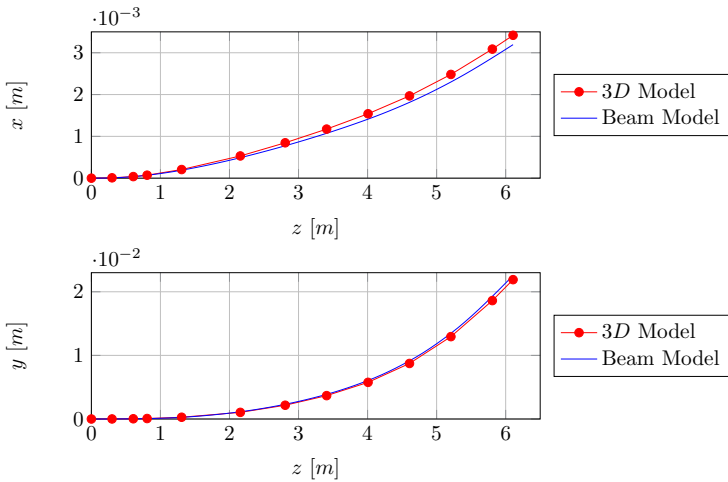


Figure 4.22: Displacement comparison along  $x$  and  $y$  axes between the two models loaded with the same force.

Stiffness reduction	Mode	Damage size			
		40 cm	80 cm	120 cm	140 cm
Healthy	1	3.96	3.96	3.96	3.96
	2	8.04	8.04	8.04	8.04
	3	12.01	12.01	12.01	12.01
	4	24.71	24.71	24.71	24.71
10%	1	3.93	3.89	3.86	3.85
	2	7.97	7.92	7.86	7.87
	3	11.94	11.87	11.84	11.83
	4	24.55	24.35	24.25	24.21
20%	1	3.88	3.81	3.75	3.72
	2	7.88	7.77	7.70	7.68
	3	11.84	11.7	11.65	11.64
	4	24.35	23.93	23.72	23.65
40%	1	3.76	3.59	3.46	3.41
	2	7.64	7.37	7.22	7.18
	3	11.59	11.28	11.17	11.13
	4	23.81	22.81	22.34	22.19

Table 4.5: Sensitivity analysis of the natural frequencies of the 1D model for different damage extensions and stiffness reduction.

of the 1D case was chosen (140cm) and a stiffness reduction equal to 22%.

Mechanical	Units	undamaged	damaged
$E_1$	$GPa$	30	23
$E_2$	$GPa$	7.0	4.0
$G_{12}$	$GPa$	4.0	3.0
$\nu$	-	0.22	0.22
$\rho$	$kg/m^3$	2200	2200

Table 4.6: Mechanical properties of the laminate under undamaged and damaged condition.

Table 4.7 shows the first four natural frequencies obtained for the full-scale model, the one-dimensional model and the experimental results.

It is very difficult to perform a damage detection step by only comparing the natural frequencies in the healthy and damaged cases. In fact they must be measured with a very good level of accuracy in order to detect changes. It is

Mode no.	Full-scale model [Hz]	1D model [Hz]	Experimental results [Hz]
1	3.24	3.41	3.20
2	6.84	7.18	6.09
3	11.91	11.13	9.98
4	22.78	22.19	22.93

Table 4.7: Numerical and experimental natural frequencies of the damaged blade.

quite clear from our example that the natural frequencies in the damaged case are lower than the ones in the healthy one. But, on the other hand, it must be noticed that the change in percentage may be very low and inferior to 1% for small cracks or for specific locations of the cracks. Therefore uncertainties on the natural frequencies can hide the small amount of frequency change. A mode shapes approach could normally lead to better results in terms of identification and localization of the damaged region of the structure under analysis. The change of mode shapes depends on both the severity and the location of the damage. The presence of a crack results in a slight change in the mode shape of a structure which is manifested as a small discontinuity in the response at the crack location. Figure 4.23, Figure 4.24, Figure 4.25 and Figure 4.26 show the first four mode shapes of the beam for a damage extension of 140 cm and six different damage levels (stiffness reduction from 0 to 50%). Mode shapes have been shown by scaling them with respect to their maximum components.

In case of small damages it is quite difficult to detect them by only looking at the mode shapes. In fact, their variations with respect to the healthy case are quite small. In this case the first, second and third derivatives of the displacement mode shapes, that are the slope, curvature and rate of curvature, respectively, of the cracked cantilever beam provide a progressively better indication of the presence of a crack. However, "noise effects" due to the difference approximation error also begin to be magnified at higher derivatives. This is the main reason why only the first and second derivatives have been considered in this study. In Figure 4.27 the curves of the first derivative of the first mode shape are shown for six different configurations from the undamaged one to the 50% stiffness reduction with a step of 10%. Though there is a slight difference in the shapes of the derivatives at the different configurations, it is very difficult to underline the presence of a damage by looking at these curves. This is the reason for which the second derivatives have been investigated.

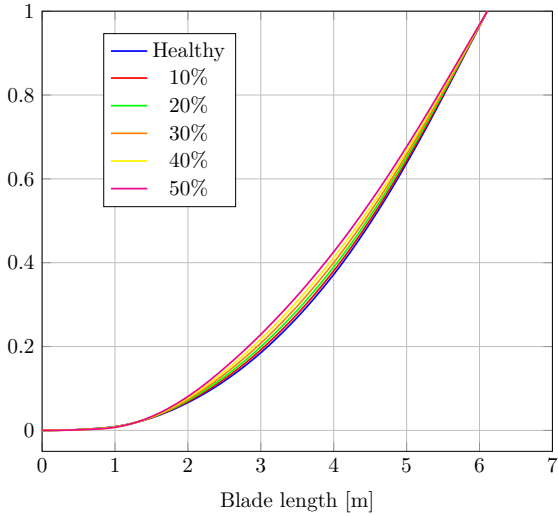


Figure 4.23: 1<sup>st</sup> mode shape for different conditions: Healthy and by reducing the stiffness of several percentage values.

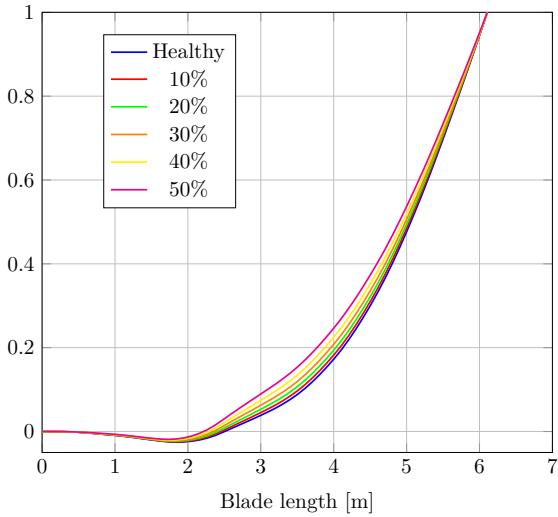


Figure 4.24: 2<sup>nd</sup> mode shape for different conditions: Healthy and by reducing the stiffness of several percentage values.



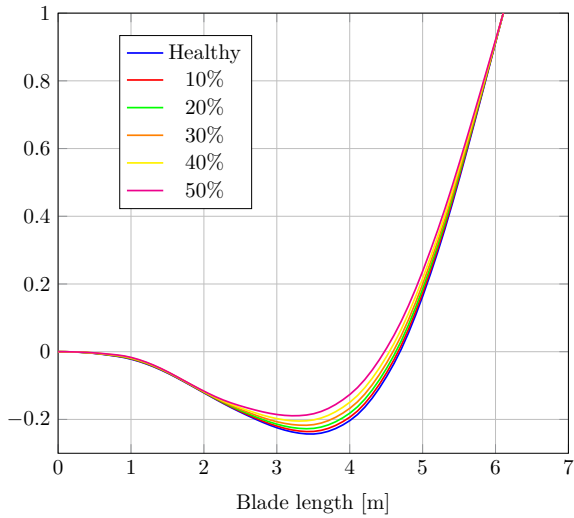


Figure 4.25: 3<sup>rd</sup> mode shape for different conditions: Healthy and by reducing the stiffness of several percentage values.

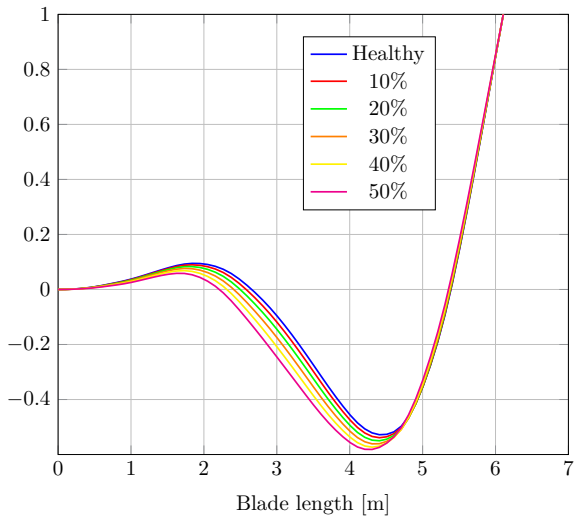


Figure 4.26: 4<sup>th</sup> mode shape for different conditions: Healthy and by reducing the stiffness of several percentage values.

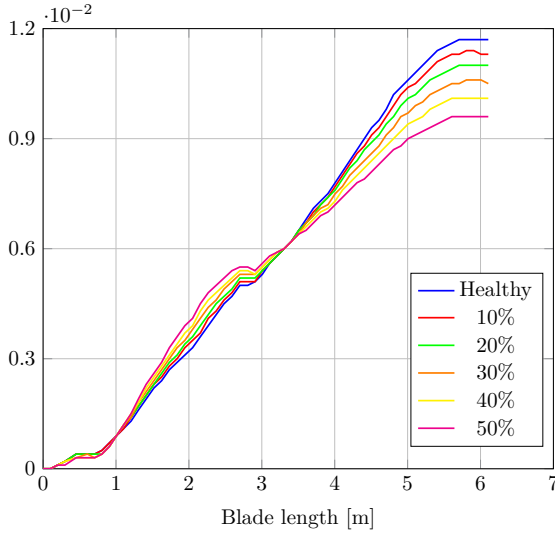


Figure 4.27: Curves of the first derivative of the first mode shape for different configurations from the undamaged one to the 50% stiffness reduction with a step of 10%.

For the healthy structure, these derivatives are smooth curves, so the local peaks or discontinuity on the slope (first derivative) can be used to indicate abnormal mode shape changes at those positions. For both cases of first and second derivatives the detection of damage is evidenced by the crossing behaviour of the damaged curves with the undamaged ones, as shown in Figure 4.27. In particular, the second derivative can be used to evaluate the position of the damaged region of the structure: the intersections between the curvature of healthy structure and the curvature of damaged structure, indicate the beginning and the end of the damaged area, as it can be seen in Figure 4.28 and in Figure 4.29. The curves representing the 2<sup>nd</sup> derivatives of the first two mode shapes were normalized with respect to the undamaged ones by subtracting them from each other. The curves representing the damaged structure are negatives in correspondence of the damage. In this case it can be highlighted both the presence of the damage, its position and its extension. The damaged area has been indicated on the blade by using red dots instead of black ones.

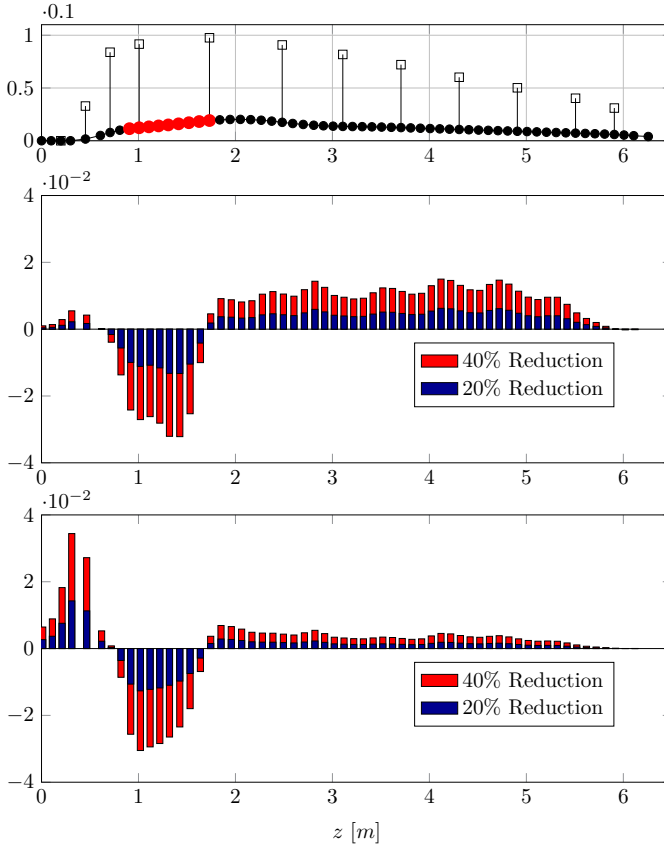


Figure 4.28: Normalized curvatures of the 1st and 2nd mode shapes. Damage extension 80cm.

### 4.6.5 Damage detection in operating conditions

The method demonstrates to work quite well in a simulation environment. In order to be applicable in a real life situation and in operating conditions, several observations need to be taken into account. First of all, for simulating a damage detection on a wind turbine blade which is rotating, the rotational velocity of the rotor needs to be considered. The centrifugal force effects will cause an increase of the global stiffness of the blade and of the entire rotor. This will translate into an increase of the natural frequencies. The variation of these frequencies is shown in Table 4.8 and Table 4.9 for different damage extensions and by increasing the rotational speed from 0rpm to 90rpm. Figure 4.30 shows

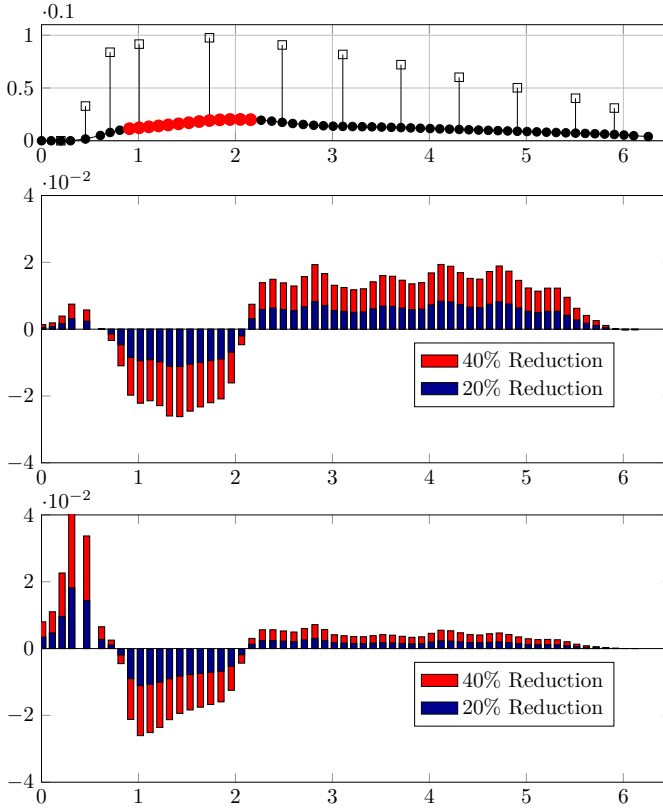


Figure 4.29: Normalized curvatures of the 1st and 2nd mode shapes. Damage extension 120cm.

this trend for the first two modes. For the purpose to include the rotational speed effects, modal analysis has been performed by using the StatSub routine in NX Nastran.

The equations of motion of a rotating beam can be written as done in Equation (4.6) by including also the rotational stiffening effect [78].

$$[M_S]\ddot{x} + [C_S]\dot{x} + ([K_S] + [K_G(\Omega)])x = [M_A]\ddot{\alpha} + [C_A]\dot{\alpha} + [K_A]\alpha \quad (4.6)$$

The matrices subscripted  $S$  (structural) and  $A$  (aerodynamic) are composed of elemental mass, damping and stiffness terms. The stiffness matrix subscripted  $G$  stands for the centrifugal stiffening contribution due to the rotational speed. This equation allows the use of a standard aeroelastic solution as implemented

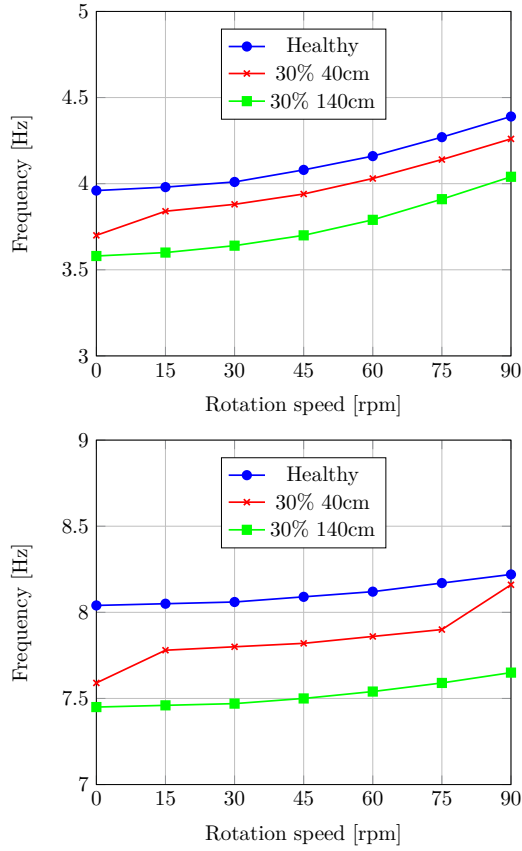


Figure 4.30: Natural frequencies variation with the rotational speed for the 1<sup>st</sup> and 2<sup>nd</sup> mode for three different conditions (healthy, 30% stiffness reduction (40cm damage extension), 30% stiffness reduction (140cm damage extension))

Mode 1	0 rpm [Hz]	30 rpm [Hz]	60 rpm [Hz]	90 rpm [Hz]
Healthy	3.96	4.01	4.16	4.39
30% stiffness reduction (40cm)	3.70	3.88	4.03	4.26
30% stiffness reduction (140cm)	3.58	3.64	3.79	4.04

Table 4.8: Variation due to the rotation of the numerical natural frequencies of the blade - First mode.

Mode 2	0 rpm [Hz]	30 rpm [Hz]	60 rpm [Hz]	90 rpm [Hz]
Healthy	8.04	8.06	8.12	8.22
30% stiffness reduction (40cm)	7.59	7.80	7.86	8.16
30% stiffness reduction (140cm)	7.45	7.47	7.54	7.65

Table 4.9: Variation due to the rotation of the numerical natural frequencies of the blade - Second mode.

in a commercial software like NX Nastran provided that the terms  $K_G$  is added. This matrix can be computed separately and properly added to the structural stiffness before the aeroelastic computation takes place. This operation is allowed using the ALTER options described in [79]. The procedure computes the term  $K_S + K_G(\Omega)$  from a static case of the blade model loaded by the centrifugal forces proportional to the rotational speed  $\Omega$ . The new stiffness matrices are then stored to be recalled by the aeroelastic solution. They will replace the stiffness matrix computed before the computation of the aeroelastic effect. This approach is not an automatic one because it requires a two-step procedure. The validity of this approach has been tested for structural dynamics computation by calculating the variation of the natural frequencies due to the rotational speed  $\Omega$ . Mode shapes are normally not affected for simple structures. Finally, the damage detection technique can be performed in operating conditions. In order to estimate mode shapes and then the curvatures, virtual accelerometers need to be placed along the blade at several locations while the blade itself is rotating. The chosen configuration foresees six accelerometers placed as shown in Figure 4.31. The final results are shown in Figure 4.32 and Figure 4.33 for the two cases of damage extension equal to 80cm and 120cm and for a rotational speed

of 30rpm. The damaged area (identified by using red dots) can be detected with a quite good level of confidence in both cases.

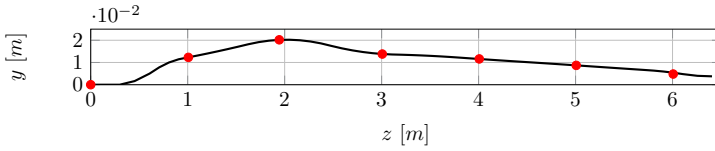


Figure 4.31: Accelerometers position (red dots).

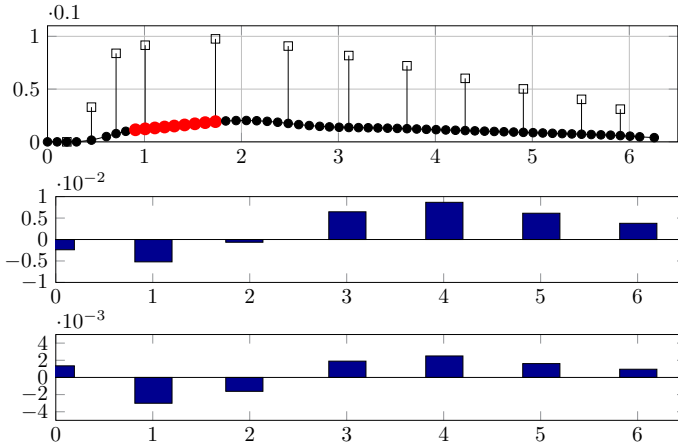


Figure 4.32: Normalized curvatures of the 1st and 2nd mode shapes in operational conditions. Damage extension 80cm.

The *MSCI* method allows to establish if a damage is present or not, but also its position and extension along the beam-like structure. The next step in this direction would be the use in a real-life environment on an operating wind turbine. The variation of mode shapes and curvatures could be detected by constantly or periodically monitoring the blades by using a SHM system.

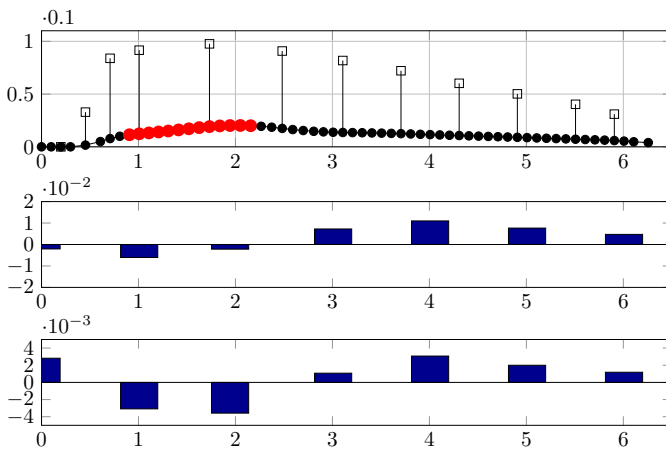


Figure 4.33: Normalized curvatures of the 1st and 2nd mode shapes in operational conditions. Damage extension 120cm.



## Chapter 5

# Order Based Modal Analysis: theory and practical aspects

This Chapter introduces the technique named Order Based Modal Analysis (OBMA) and several application cases. As suggested by its own name, this technique is a combination of Order Tracking and Operational Modal Analysis (OMA). For this reason, after a brief introduction in Section 5.1, the state-of-the-art techniques for extracting the orders as well as innovative order extraction algorithms will be described in Section 5.2. The main concepts behind the use of OBMA and its advantages if compared with Operational Deflection Shapes (ODS) and OMA will be explained in Section 5.3. Section 5.5 illustrates the best practices for applying the method in a real-life environment.

### 5.1 Introduction

The dynamic characterization of structures in operating conditions is a challenging step. It becomes more difficult if the structure is composed by several substructures interacting with each other. The situation becomes even more complicated if some parts of the structure under study are rotating with respect to each other. In fact, it is well known that such structures face several complex and non-linear conditions during their operating life. On one side, Operational Deflection Shapes are widely used in the industrial domain to visualize the deformation of the structure at certain critical frequencies. On the other side, Operational Modal Analysis is often used for the dynamic characterization of big and complex structures. It is also known as output-only

modal analysis because it is based only on measurements of the response of the system without the need of measuring the forces acting on it. In its first development, it was used for civil engineering structures like buildings, bridges and wind turbines. Today it is a well-established technique which is widely used for the dynamic identification of all kind of structures such as aircraft, helicopters, vehicles, ships, stadiums, bridges and every kind of industrial machinery. OMA is used instead of classical experimental modal analysis for an accurate modal identification under operating conditions and when it is very difficult to artificially excite the structure. Historically there has always been a distinction between techniques that characterize the dynamic behavior of a structure and the ones that attempt to identify the response signals measured while the same structure is operating. The first category comprises Modal Analysis, whereas the second one includes the Order Tracking procedure. The main distinction between the two categories can be explained by introducing the classical Source-Transfer-Receiver model which is shown in the example of Figure 5.1. In the Modal Analysis case the scope is to identify the system (Transfer) by measuring the output ( $Y$ ) in all cases and eventually also the input ( $U$ ). The scope of the signature testing, for which the Order Tracking step is usually taken, is the identification of the source of noise and vibration for rotating machinery (gearboxes, engines, drive mechanisms, compressor, pumps, etc.). This technique relies on the fact that the system is well-known and it was already dynamically characterized. This is usually employed in laboratory test facilities, engine test benches, artificial road dynamometers, but also in operational conditions in a real environment. The quality and the performance of both Modal Analysis and Order Tracking are of fundamental industrial importance.

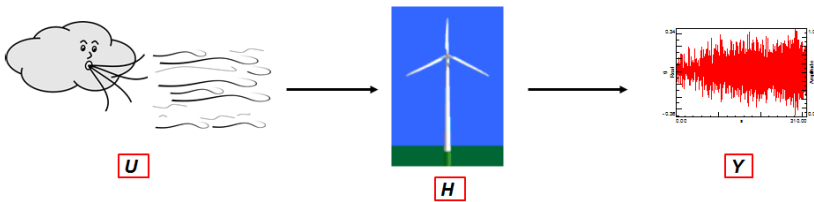


Figure 5.1: Source-Receiver-Transfer model:  $U$ =input,  $H$ =structure,  $Y$ =measured output

The two categories can be brought together by introducing an Operational Modal Analysis technique based upon the orders extracted by using state-of-the-art order tracking algorithms. Several order tracking techniques will be discussed by identifying their advantages and drawbacks for modal analysis

purposes. Then the concept of Order-Based Modal Analysis (OBMA) will be extensively described [12].

## 5.2 Order Tracking techniques

The term Order Tracking represents the analysis of frequency components whose frequency is related to the rotational speed  $\omega$  of the machine being studied. If the machine is running at constant speed ( $\omega = \omega_0$ ), these frequencies are constant and they are also known as harmonics. If the rotational speed is varying with the time ( $\omega = \omega(t)$ ), then the conditions are non-stationary. In this case, the frequency components are also time varying and they are known as orders. From a mathematical point of view, an order can be defined as a time-varying phasor that rotates with an instantaneous frequency which is related to the rotational frequency of the reference shaft [80]. It generates a sinusoidal function with varying frequency. From a mathematical point of view, a single order can be described by using Equation 5.1.

$$x(t) = A_k(t)e^{2\pi j \frac{k}{p} t} \quad (5.1)$$

$A_k(t)$  is a complex number that represents the amplitude and phase of the  $k^{th}$  order. This is not a constant and it normally depends on the structure conditions (torque, temperature, rotational speed, etc.). Most of these parameters are kept constant during a test, but the rotational speed  $\omega$  is typically swept over a certain range.  $p(t)$  is the period of the primary order in seconds. If we consider an operating machine, several orders are present due to several components and multiples, so the combination of orders can be described by a summation of time-varying phasors, as shown in Equation 5.2.

$$x(t) = \sum_{k=-\infty}^{\infty} A_k(t)e^{2\pi j \frac{k}{p} t} \quad (5.2)$$

Under controlled conditions (e.g. on a roller bench), the response of the system at a fixed location can be expressed as  $x(t)$ . The objective of the Order Tracking step is to estimate  $A_k(t)$ , which means to split up the response  $x(t)$  in its components  $A_k(t)$ . The order numbers  $k$  are often known in advance. In most cases an order has frequencies that are integer multiples of the rotational frequency of the reference shaft (e.g. teeth numbers in gears). In other words, an order is a phenomenon which is occurring a fixed number of times per revolution of the reference shaft. For instance, the first order represents an event that

happens once per revolution, the second order is an event that happens twice per revolution and so on. Also non-integer multiples of the primary frequency can be present in the data, especially in case in which gearboxes are being analyzed. In this case fractional orders show up and this situation can make the analysis more difficult.

The oldest order tracking techniques were based on analog devices. Vibration signals are fed to a bandpass filter whose center frequency is controlled by a tachometer signal. The output of the filter is then sent to a peak or RMS detector in order to obtain the amplitude of the filtered signal. The amplitude can then be plotted against the rotational speed. With the huge development of digital equipment and software, order tracking techniques have been extensively implemented and studied in the past years. Most of the techniques are very fast and they can be implemented in real time. It can be distinguished among two main categories: non-reconstruction and reconstruction waveform schemes. The first category includes all the techniques that do not need to reconstruct the time histories of the orders for obtaining the required information. They only extract the amplitude and phase of the orders in the frequency or order domain. The parameters obtained by using these techniques are averaged values over a certain time interval that can be given in terms of constant time interval, angular interval or number of revolutions. The choice of the interval is strictly related with the technique to be used and depends by the test conditions. These techniques are ranging from simple techniques based on Fourier transform to more sophisticated techniques such as resampling based Order Tracking and Time-Variant Discrete Fourier Transform.

On the other hand, the second category, as its name says includes techniques which are based on the reconstruction of the time histories of the orders. Instead of estimating the average amplitude and phase of the orders over a certain blocksize, the time history allows the determination of instantaneous values at any time. They are the most accurate techniques in terms of resolution, but they also require extensive computations which limit their use in real time cases and for long analysis. Techniques such as the Vold-Kalman filter based order tracking and the Gabor based order tracking are part of this category.

The following methods will be briefly described and then employed in several simulation and test cases in the next sections:

- Time domain sampling based Fast Fourier Transform order tracking (FS);
- Resampling based order tracking (OT or AD);
- Time Variant Discrete Fourier Transform (TVDFFT);
- Vold-Kalman filter based order tracking (VK);

## 5.2.1 Time domain sampling based Fourier transform order tracking (FS)

The time domain sampling based Fourier transform order tracking require time domain data sampled with constant time intervals. As its name suggests, it is based upon standard Discrete Fourier Transform (DFT) implementation on time domain data. This is the simplest and commonly applied digital order tracking technique. Since the Fast Fourier Transform (FFT) is the most computationally efficient algorithm to perform DFT, the signal is divided into a number of blocks with power of two blocksize. FFT is performed for each block and the results are displayed as FFT waterfall or spectrogram plot. The waterfall plot is a 3D plot in which the FFT spectra are displayed in cascaded form. It is quite useful for detecting the resonances while the machine speed sweeps through a certain frequency range. Another way to show the same kind of data is the so-called spectrogram. It is a 2D plot in which the horizontal axis represents the frequency and the vertical one the time or rotational speed. The amplitudes of the FFT are color coded. Figure 5.2 shows an example of both plots for the same case.

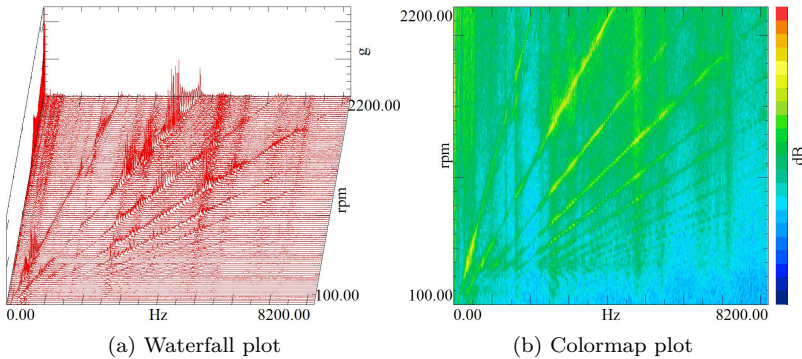


Figure 5.2: Fixed Sampling order tracking processing

Each of the FFT is calculated by considering an average rpm value over the selected block. The FFTs appear to be horizontal lines in both the colormap and waterfall plot. The rpm step defines the rpm interval between two consecutive FFTs. Of course, Finally, the order, in terms of amplitude and phase, can be extracted from the FFT spectra. The FFT kernel is given in Equation (5.3).

$$\begin{aligned}
 a_m &= \frac{1}{N} \sum_{n=1}^N x(n\Delta t) \cos(2\pi \frac{k}{p} n\Delta t) \\
 b_m &= \frac{1}{N} \sum_{n=1}^N x(n\Delta t) \sin(2\pi \frac{k}{p} n\Delta t)
 \end{aligned}
 \tag{5.3}$$

$N$  is the number of time blocks and  $n\Delta t$  represents the  $n^{th}$  time interval. The extracted orders do not normally fall on a single spectral lines. For this reason, often multiple spectral lines are summed together. The main advantage of this method is its computational efficiency. Several drawbacks could be listed. First of all, the blocksize (time interval) is not related to the rpm of the machine. This cause problems both at low and high rotational speed. In fact, at low speeds, the interval is too short to capture the low orders resulting in power leakage (smearing) between closely-spaced orders. At high speeds, the interval is too long to capture rapid variations and spikes in the signal. For minimizing the smearing problem, a Hanning window is typically applied. Figure (5.3) shows that by sampling with a constant time interval, the number of samples per rotation reduces by increasing the rotational speed.

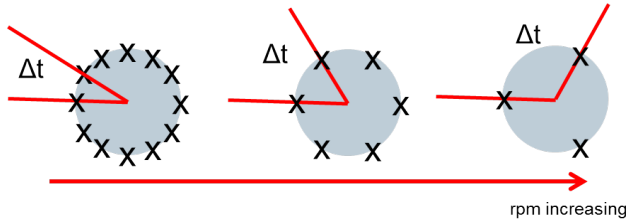


Figure 5.3: Time domain sampling based FFT order tracking concept

The procedure is shown in Figure 5.4. On top left there is the tachometer signal which means the measurement of the rotational speed of the machine. The second graph represents the time history recorded by one of the accelerometers placed on the machine under testing. FFT can be performed over a certain time block and the resultant spectrum is placed as an horizontal lined in the colormap on the right side of the figure. By considering all the time blocks the entire colormap can be built.

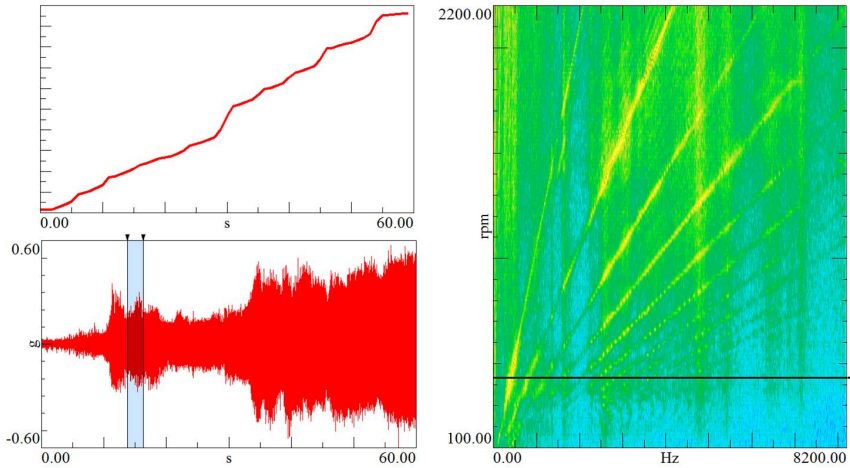


Figure 5.4: Angle domain resampling order tracking procedure

## 5.2.2 Resampling based Order Tracking

### Basic principles of resampling

The sampling Shannon-Nyquist theorem states that we can fully reconstruct a band-limited continuous signal if we sample it with a frequency that is at least two times the highest frequency component in that particular band-limited signal. Sampling, or digitization, is therefore a process that is able to convert a band-limited continuous signal into a discrete one, without loss of information. In applications like modal analysis, simple fixed sampling as a function of time is sufficient. But, when examining mechanical objects that rotate, or static objects that are influenced by nearby rotating objects, the need for another independent variable becomes obvious. What we need in this type of application is not sampling as a function of time, but sampling as a function of angle or rotational speed. Three main steps are needed in the resampling process:

- The first step is finding the relationship between the independent variable in the time domain and the one in the angle domain. In other words, this means to calculate the time as a function of the angle.
- Once the relationship is known, the moments corresponding to the angles for which we want to resample the signals can be calculated. This is normally done at equidistant angle increments.

- The last step consists in the resampling of the signals we are interested at the moments calculated in the previous steps. Aliasing must be avoided. For this reason, depending on the application, several kind of filters can be used. If the main objective is to determine the amplitude and phase of the orders, a steep filter is preferably applied. If the reconstruction of the waveform in the angle domain is more interesting, then a less steep filter with higher oversampling factor is preferred. In the second case any alias is allowed.

### **Algorithms for resampling from time to angle domain**

Several algorithms have been developed for performing the angular resampling of time domain data. In LMS Test.Lab there are two different algorithms named Order Tracking (OT) and Angle Domain (AD) techniques. As stated, the first step in the resampling process consists in finding the relation between time and angle domain. This is done in practice by measuring the so-called tachometer signal which gives the position of equidistant angles. A high sampling frequency is needed in order to avoid the aliasing problem in both domains. The resampling procedure is the main difference between the OT and AD techniques. In fact the advantage of AD if compared to OT lies in the fact that the signals are always triggered on a reference angle (since the application was initially developed for combustion engines, it is often stated that the trigger is related with the Top-Dead-Center (TDC) point of the engine). Moreover in the AD technique all the available pulses per revolutions are used in the resampling step, whereas the OT algorithm is based on a single ppr. These are the two main reasons for which AD allows to get a better precision in the results. In OT, the main interest is related to the amplitude and phase behavior of the orders. In AD the accurate reproduction of the waveform in the angle domain is also important. For this reason, a less steep filter with high oversampling is preferred in this case. The following example should clarify the conceptual differences between the two resampling methods. In both cases, after having identified the exact relationship between the time and the equidistant angles, the transformation from time to angle domain can be performed. OT is accurate enough in cases in which there are not torsional vibrations in the data. These vibrations are often one of the main concerns in power transmissions and they will be explained more in details in the following sections. They cause the engine rpm to fluctuate up to 20% within one revolution. Figure 5.5 shows the rpm oscillations within a single revolution of a shaft. As stated, OT only considers one pulse per revolution in the resampling step. This can cause an error in the angle estimation depending on the position in the revolution with respect to the average value. If the torsional vibrations are low, the value will be near the average, if they are high it can be far off. A single pulse might not be enough in this situation,



but it will allow to characterize with a certain approximation the dynamic behavior of the system. Another weak point of the OT technique lies in the fact that it is not sure that the pulse will coincide with a time domain sample, as shown in Figure 5.6. In this case the point before or the one right after will be considered for the resampling step. This is another cause of errors. On the other hand, AD considers all the samples within a single revolution helping to improve the accuracy of the results and the characterization of phenomena due to the torsional vibrations or, more in general, to rpm fluctuations within one revolution. If these phenomena are not of interests for a certain analysis, it is possible to low-pass filter the signals and the variations within a revolution will not be visible.

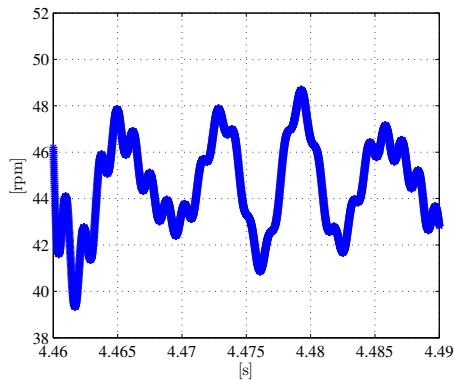


Figure 5.5: Resampling issue: rpm oscillations within a single revolution

Both techniques use an anti-aliasing filter in the last step of the resampling. A difference between the two techniques is in the filter type. In fact, the filter type depends on the application. In OT, since the main interest is in the amplitude and phase of the orders, a brick-wall filter that is flat up to 80% of the Nyquist frequency is used. In AD it is also quite interesting to extract the waveform in the angle domain from which calculating the orders by using the FFT algorithm. For this reason a less steep filter with high oversampling is preferred. While OT analyzes the system behavior over the operating range by considering an integer number of revolutions, AD allows the analysis within an operating cycle. This technique is well suited for combustion engines. It allows to focus on specific engine events like injection timing, valve open/closing or angular repetitive event.

By taking into account the Nyquist theorem, both for OT and AD, the number of pulses per revolution  $ppr$  must be higher than two times the maximum order

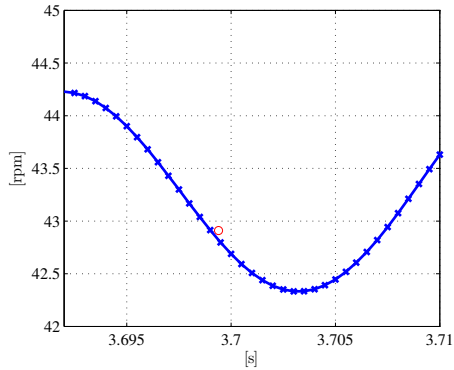


Figure 5.6: Resampling issue: pulse per revolution not coinciding with time sample

to be extracted. For this reason, for performing such an analysis high quality encoders or a high upsampling step are needed. For example, if the order of the phenomena to be analyzed in angle domain is equal to 20, at least  $40ppr$  are needed in the tachometer channel estimation. This is analogous to what happens with the sampling frequency  $f_s$ . If we want to analyze a phenomenon occurring at  $100Hz$ , a sampling frequency of at least  $200Hz$  is required for the acquisition channels.

### Mathematical description of resampling based Order Tracking

As stated previously, the time domain sampling based FFT order tracking (FS) has several drawbacks. Some of these can be solved by resampling from time to angle domain before applying the FFT to the acceleration signals. Assuming that the blocksize remains constant, the resampling implies that the signal is now sampled at a constant  $\Delta\theta$  rather than at a constant  $\Delta t$ . The resampling process requires some computational time and it includes two main steps: oversampling and then interpolating in order to get the required  $\Delta\theta$ -spaced samples. As the technique is based on the angle information, a very accurate tachometer signal is needed in this case. In fact, the resampling intervals are calculated by integrating the speed signal. After the resampling step, the variable-frequency order components are converted into regular sinusoidal signals. The DFT (or FFT) can then be used to process the resampled data and to obtain the order components as spectral lines since the transformation is based on angle domain data rather than time domain data. The kernels of the FFT are reformulated from Equation (5.3) and they are reported in Equation (5.4).

$$a_m = \frac{1}{N} \sum_{n=1}^N x(n\Delta\theta) \cos(2\pi \frac{k}{p} n\Delta\theta)$$

$$b_m = \frac{1}{N} \sum_{n=1}^N x(n\Delta\theta) \sin(2\pi \frac{k}{p} n\Delta\theta)$$
(5.4)

In this case,  $n\Delta\theta$  represents the  $n^{\text{th}}$  angular interval. The order resolution  $\Delta o$  can be found in a similar way to the frequency resolution  $\Delta f$  as the reciprocal of the total angle of rotation of the machine (Equation 5.5).

$$\Delta o = \frac{1}{N\Delta\theta}$$
(5.5)

An equivalent Nyquist-Shannon sampling theorem can be stated in the order domain (Equation 5.6).

$$o_{Nyq} = o_s = \frac{1}{2\Delta\theta}$$
(5.6)

$o_s$  is the angular sampling rate and  $o_{Nyq}$  stands for the angular Nyquist rate which corresponds to the maximum order which can be processed. It must be noticed that by choosing  $N$  such that an integer number of revolutions is described, then the smearing problem is minimized even without using any window. On the other hand, if non-harmonic components are present, then a smoothing window is required. For FFT algorithm that needs a power of 2 as blocksize, the zero-padding can be used in order to provide extra samples beyond the integer number of revolutions. Figure 5.7 shows a waterfall and a colormap for the same case analyzed in Figure 5.2 for the FS case.

The key property of angle domain data is that an order during run-up or coast-down conditions becomes constant in frequency relative to the sample rate. In other words, the order now falls on a single spectral line for all time values. Several drawbacks are still present. In fact, orders can only be tracked with reference to one rotating shaft and it is quite complicated to distinguish among crossing orders. Another limitation is due to the finite order resolution which makes the analysis of orders which do not fall on a spectral line very difficult. Furthermore, the resampling step can be quite time consuming in some cases. By using the angular resampling procedure, the same number of samples per rotation for all the rotational speeds can be obtained, as shown in Figure (5.8).

The procedure is shown in Figure 5.9. On top left there is the tachometer signal which means the measurement of the rotational speed of the machine. The

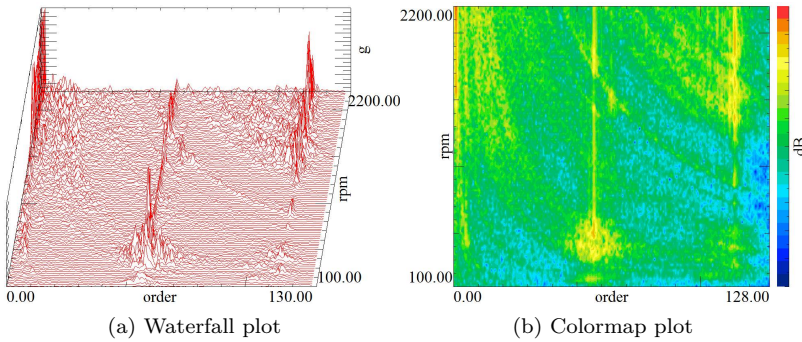


Figure 5.7: Resampled order tracking processing

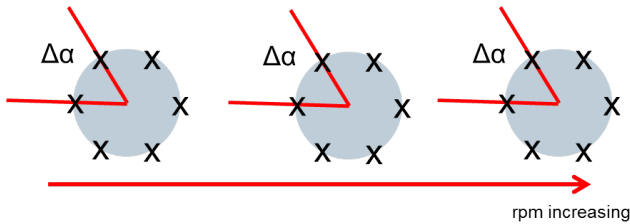


Figure 5.8: Angle domain resampling order tracking concept

second graph represents the time history recorded by one of the accelerometers placed on the machine under testing. The resampling to the angle domain yields the bottom curve. FFT can be performed over a certain angular block and the resultant spectrum is placed as an horizontal lined in the colormap on the right side of the figure. By considering all the angular blocks the entire colormap can be built.

**Phase referencing issue**

One of the main advantage of AD if compared to FS and OT is that it allows to get an absolute phase within an operating cycle for each channel. This is mainly due to the way in which it was implemented. On the other hand, both FS and OT need to be calculated with respect to a reference channel which must be synchronous with the rotational speed of the machine. In order to get a correct phase estimate for a single frequency line, it is enough to consider an

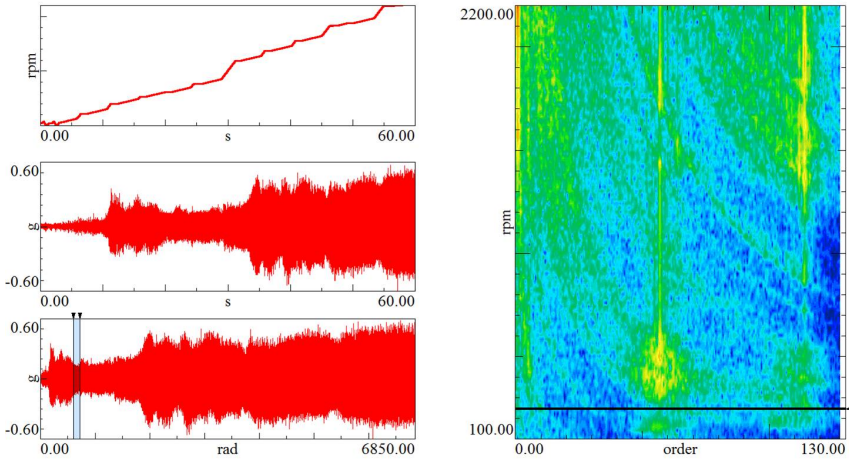


Figure 5.9: Angle domain resampling order tracking procedure

acceleration channel as reference. As consequence, the phase of all the other channels will be calculated with respect to it by considering the same angular block. More in general, from one estimate to the other it is also required that the angular block starts always at the same angular location. This can only be achieved if the phase reference channel is connected to the rotating source. For this reason, a sine sweep with frequency equal to the instantaneous rotational speed  $\omega(t)$  of the machine multiplied by the order  $o_m$  which is going to be extracted, as shown in Equation 5.7, allows to get consistent results [13].

$$\Theta_m(\tau) = \cos\left(\int_0^\tau o_m \omega(t) dt\right) \quad (5.7)$$

The next example shows the differences before and after using the mentioned phase reference channel. Figure 5.10 shows that it is very important to choose a reference channel for applying a modal parameter estimation technique to the orders. If no reference channel is chosen when calculating the orders, their phase will look random (green curve), whereas of course the estimation of the amplitude is not affected at all. Figure 5.11 and Figure 5.12 confirm that the reference channel must be chosen as shown in Equation (5.7) by taking into account the order  $o_m$  that is being extracted from the data.

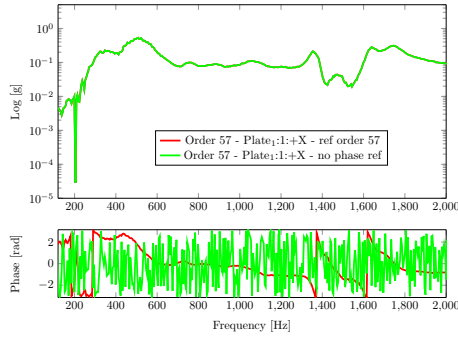


Figure 5.10: Order 57 extracted with (red) and without (green) phase reference.

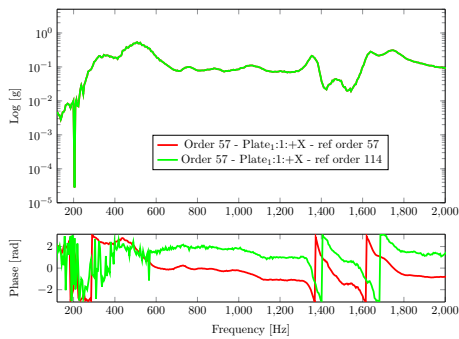


Figure 5.11: Order 57 extracted considering Order 57 as phase reference (red) and Order 114 as phase reference (green).

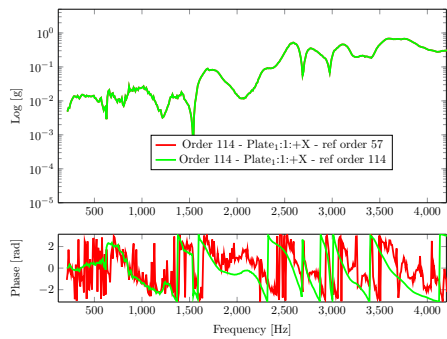


Figure 5.12: Order 114 extracted considering Order 57 as phase reference (red) and Order 114 as phase reference (green).

### 5.2.3 Time Variant Discrete Fourier Transform (TVDFT)

The previous methods allow leakage free estimates of the orders with a quite high computational effort due to the resampling step. A new order tracking method was developed by Blough [81]. It is able to get results quite similar to the ones obtained after resampling to the angle domain, but without performing the resampling step. For this reason, it allows reducing the computational effort. This method is based on a Fourier transform kernel whose frequency can vary with time. Hence the name of Time Variant Discrete Fourier Transform (TVDFT). It is basically resampling the kernel of the transform instead of resampling the data. The frequency of the kernel is instantaneously matching the one of the order to be extracted, as shown in Equation (5.8).

$$\begin{aligned}
 a_m &= \frac{1}{N} \sum_{n=1}^N x(n\Delta t) \cos \left( 2\pi \int_0^{n\Delta t} (o_m \cdot \Delta t \cdot rpm/60) dt \right) \\
 b_m &= \frac{1}{N} \sum_{n=1}^N x(n\Delta t) \sin \left( 2\pi \int_0^{n\Delta t} (o_m \cdot \Delta t \cdot rpm/60) dt \right)
 \end{aligned}
 \tag{5.8}$$

The formulation of TVDFT can be extended in order to separate close and crossing orders through a calculation to be performed as second step. There can be a leakage error using the TVDFT with constant  $\Delta t$  sampled data because it is not guaranteed that the integer revolution values required for a constant order bandwidth analysis will fall on a  $\Delta t$ . If it is not the case, it will lead to a leakage error by performing the transformation over a non-integer number of revolutions. This error can be reduced by oversampling the data which means by providing a finer  $\Delta t$ . This method contains most of the advantages of the resampling based order tracking and it can be implemented in a very efficient manner without having the computational load and complexity of the transformation from the time domain to the angle domain. The relationships in Equation 5.9 need to be valid for minimizing the leakage effects in this type of analysis.

$$\begin{aligned}
 T &= \frac{1}{\Delta o} = \text{integer} \\
 \frac{o_m}{\Delta o} &= \text{integer}
 \end{aligned}
 \tag{5.9}$$

They impose a restriction on the actual order bandwidth which may be applied in the application of the TVDFT. The second relationship further imposes a restriction on which order could be tracked with minimal leakage error. These limitations do not allow to track all the orders, but for most applications the user may track most orders of interest. More problems could arise in case of non-integer orders which could be the case of gears and gearboxes. In practice, the first step of the TVDFT algorithm consists in the calculation of the reference channel, as shown in Equation 5.7. After having generated the sinusoidal signal, the so-called "zero-crossings" are then used to identify integer number of revolutions. Any time that the sine crosses the zero with a positive slope, the index is saved and one rotation has been completed. A certain number of revolutions are taken into account to perform the transformation. This process is shown in Figure 5.13.

For enhancing the capabilities of the TVDFT for order tracking, Blough introduced also an Orthogonality Compensation Matrix (OCM). It allows

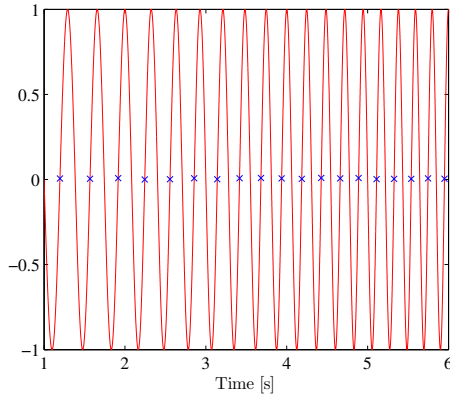


Figure 5.13: Reference signal and "zero-crossings" detection

faster sweep rates to be analyzed as well as closely spaced and crossing orders. The OCM could be applied in a post-processing step after having estimated the order by using TVDFT. The quality of the compensation is related to the quality of the original order estimates. All orders which are present in the data and have a high energy content must be tracked using the TVDFT before applying the OCM correction. In fact, any non-tracked order will lead to errors in the final results because they add noise to the linear equations.

## 5.2.4 Vold-Kalman filter based order tracking (VK)

By using all the described methods, the orders could be estimated both in terms of amplitude and phase. The main drawback is often related to the resolution and the noise of the extracted order. In fact its resolution is connected with the number of samples which can be measured by the tachometer sensor. A method which is able to extract the time history of the order was introduced by Vold and Leuridan [11]. They introduced an algorithm for high resolution, slew rate independent order tracking based on the concepts of Kalman filter. The Vold-Kalman (VK) algorithm allows tracking multiple orders at the same time and it is able to decouple close and crossing orders. This method extracts the time history of the order as well as the estimate of the amplitude and the phase of the same order. Similarly as the Kalman filter is based on the process and measurement equations, the VK filter is based on the structural and data equations. The basic idea behind the filter is the definition of local constraints stating that the unknown phase assigned orders are smooth and that the sum of the orders should approximate the total measured signal. The



smoothness condition is called the structural equation and the relationship with the measured data is called the data equation.

- Data equation:

$$y(n) = x(n)e^{j\Theta(n)} + \eta(n) \quad (5.10)$$

The data equation is shown in Equation (5.10) and it represents the link between the measured data  $y(n)$  and the complex envelope or filtered signal  $x(n)$ . In other words,  $x(n)$  represents the waveform of the order to be extracted. In practice, instead of observing  $x(n)$ , we measure the signal  $y(n)$  which is assumed to contain both the signal that satisfies the structural equation as well as noise and other periodic components. For these reasons the term  $\eta(n)$  has been introduced. The term  $e^{j\Theta(n)}$  is the complex carrier wave of the order that can be visualized as a phasor, which is a complex oscillator with an instantaneous frequency proportional to a constant multiple of the rotational speed, as can be seen from Equation (5.11).

$$\Theta(n) = \sum_{i=0}^n \omega(i)\Delta t \quad (5.11)$$

where  $\omega(i)$  is the discrete angular frequency and the sum gives the angle traveled up to the current time. The phasor is always on the complex unit circle. The product between the phasor and the complex envelope is the amplitude modulated complex order.

- Structural equation:

$$\nabla x(n) = x(n) - x(n+1) = \epsilon(n)$$

$$\nabla^2 x(n) = x(n) - 2x(n+1) + x(n+2) = \epsilon(n) \quad (5.12)$$

$$\nabla^3 x(n) = x(n) - 3x(n+1) + 3x(n+2) - x(n+3) = \epsilon(n)$$

The structural equation is an equation that describes the mathematical characteristics of the order to be extracted. The complex envelope is locally approximated by a low order polynomial. This condition is equivalent to a smoothness condition and can be represented by using multiple differentiation. The polynomial order designates the number of the filter poles (1, 2, 3 pole filters are given by Equation (5.12)). The right hand side of the equations can be seen as noise or error.

The data equation and the structural equation take the matrix form of the system represented in Equation (5.13).

$$\begin{aligned} \{y\} &= [C]\{x\} + \{\eta\} \\ [A]\{x\} &= \{\epsilon\} \end{aligned} \tag{5.13}$$

This system of equation is an undetermined system in which the unknown is given by the waveform  $\{x\}$ . The matrix  $[A]$  is explicated in Equation 5.14 for the case in which the filter has 2 poles.

$$[A] = \begin{bmatrix} 1 & -2 & 1 & 0 & \dots & 0 & 0 & 0 \\ 0 & 1 & -2 & 1 & \dots & 0 & 0 & 0 \\ \dots & \dots & \dots & \dots & \dots & \dots & \dots & \dots \\ 0 & 0 & 0 & 0 & \dots & 1 & -2 & 1 \end{bmatrix} \tag{5.14}$$

Equation 5.15 shows the same matrix when a 3 pole filter is used.

$$[A] = \begin{bmatrix} 1 & -3 & 3 & 1 & 0 & \dots & 0 & 0 & 0 & 0 \\ 0 & 1 & -3 & 3 & 1 & \dots & 0 & 0 & 0 & 0 \\ \dots & \dots & \dots & \dots & \dots & \dots & \dots & \dots & \dots & \dots \\ 0 & 0 & 0 & 0 & 0 & \dots & 1 & 3 & -3 & 1 \end{bmatrix} \tag{5.15}$$

The matrix  $[C]$  is a diagonal matrix whose diagonal elements are the signal phase samples, as reported in Equation 5.16.

$$[C] = \begin{bmatrix} e^{j\Theta(1)} & 0 & \dots & 0 \\ 0 & e^{j\Theta(2)} & \dots & 0 \\ \dots & \dots & \dots & \dots \\ 0 & 0 & \dots & e^{j\Theta(n)} \end{bmatrix} \tag{5.16}$$

As the matrix  $[C]$  is complex, then both the vectors  $\{y\}$  and  $\{\eta\}$  are complex too. The global solution can be found using the standard least square approach by minimizing the error terms  $\{\epsilon\}$  and  $\{\eta\}$ , while maintaining the given relationship between them. The weighted sum of the squares of the error vector norms can be calculated as shown in Equation (5.17) and giving the loss function  $\{L\}$ .

$$\{L\} = r^2\{\epsilon\}^T\{\epsilon\} + \{\eta\}^H\{\eta\} \quad (5.17)$$

A weighted solution can be obtained by introducing the Harmonic Confidence Factor (HCF)  $r$ . The value of this parameter is what determines the tracking characteristics of the filter. The choice of a large value for the weighting factor  $r$  leads to a highly selective filtration in the frequency domain, while by choosing  $r$  small the resolution in frequency is very small, but a fast convergence in amplitude can be obtained. The two terms can be calculated as written in Equation 5.18.

$$\begin{aligned} \{\epsilon\}^T\{\epsilon\} &= \{x\}^T[A]^T\{x\}[A] \\ \{\eta\}^T\{\eta\} &= (\{y\}^T - \{x\}^H[C]^H)(\{y\} - [C]\{x\}) \end{aligned} \quad (5.18)$$

A condition for the minimum of the loss function  $\{L\}$  can be found by deriving it with respect to the vector  $\{x\}$  and putting it equal to zero, as shown in Equation (5.19).

$$\frac{\partial\{L\}}{\partial\{x\}} = 2r^2[A]^T[A]\{x\} + 2(\{x\} - [C]^H\{y\}) = 0 \quad (5.19)$$

The final results of the derivative has been found by taking into account that the conjugate transpose or Hermitian transpose of a matrix interchanges the row and column index for each element. It reflects the element across the main diagonal. The operation also negates the imaginary part of any complex numbers. For this reason, the product  $[C]^H[C]$  is equal to the identity matrix. The unknown complex envelope results from Equation (5.20).

$$\{x\} = (r^2[A]^T[A] + [E])^{-1}[C]^H\{y\} \quad (5.20)$$

The parameter  $r$  can be related to the filter bandwidth. From the above analysis, it is quite clear that a proper Vold-Kalman filter bandwidth must be chosen before performing the order tracking filter. The selection of the bandwidth is a compromise since it has to be narrow enough to separate the different components in the signal and sufficiently wide to follow the changes in the signal amplitude. The product of the matrices  $[A]^T$  and  $[A]$  gives a symmetric positive semidefinite matrix. By adding to the matrix  $r^2[A]^T[A]$  the unity matrix  $[E]$ , the symmetric positive definite matrix  $[B] = r^2[A]^T[A] + [E]$  is obtained. Employing the Cholesky factorization of the matrix  $[B]$  into the matrix product  $[B] = [L][U]$  is the easiest way to solve the equation system

of Equation 5.20.  $[L]$  is a lower triangular matrix, whereas  $[U] = [L]^T$  is an upper triangular matrix. The value of the weighting factor  $r$  must be limited for avoiding to lose the effect of adding unity to the diagonal of the main matrix. The absolute value of the  $\{x\}$  vector gives the amplitude of the order which is going to be extracted. If the order waveform needs to be extracted, then the product between  $\{x\}$  and the phasor  $e^{j\Theta(n)}$  must be calculated.

### 5.3 Polymax method for OBMA

As underlined in Chapter 2, Operational Polymax can be combined together with Order Tracking techniques in order to apply OMA to the extracted orders. Therefore, the orders will play the role which is normally played by auto- and cross-powers. The Polymax method is robust against the hypothesis that need to be fulfilled in order to apply Order-Based Modal Analysis (OBMA) technique [12]. This method assumes that the structure is mainly excited by a rotational excitation. It can be assumed that it is excited by a rotating mass with increasing or decreasing frequency (respectively, run-up or coast-down events). This force can be represented by two correlated perpendicular forces of equal amplitude but in quadrature, as shown in Equation 5.21 and in Figure 5.14.

$$\begin{aligned}
 f_x(t) &= rm\omega_0^2 \cos(\omega_0 t + \phi) \\
 f_y(t) &= rm\omega_0^2 \sin(\omega_0 t + \phi)
 \end{aligned}
 \tag{5.21}$$

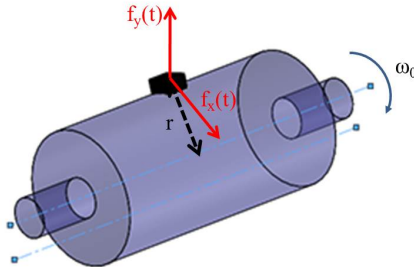


Figure 5.14: Order-Based Modal Analysis illustration

In the frequency domain, the measured response of the system can be represented in Equation 5.22.

$$Y(\omega) = H_{(:,f_x)}(\omega)F_x(\omega) + H_{(:,f_y)}(\omega)F_y(\omega) \quad (5.22)$$

In Equation (5.22),  $F_x$  and  $F_y$  represent the forces acting on the system and  $H_{(:,f_x)}$  and  $H_{(:,f_y)}$  are the corresponding columns in the transfer function matrix. By taking into account Equation (5.21) and Equation (5.22) and by considering only the positive frequency axis, Equation (5.23) can be obtained.

$$Y(\omega) \propto \omega_0^2 (H_{(:,f_x)}(\omega) - jH_{(:,f_y)}(\omega))\delta(\omega - \omega_0) \quad (5.23)$$

where  $\omega_0$  is the rotational speed. Equation (5.23) shows that the measured output is proportional to the squared rotational speed and to a complex combination of two structural FRFs related to  $x$  and  $y$  excitation. In general, a structural displacement over force FRF can be decomposed in a modal sense as shown in Equation (5.24).

$$H_{(:,bullet)}(\omega) = V(j\omega I - \Lambda)^{-1}L_{bullet} + \frac{1}{\omega^2}LR_{bullet} + UR_{bullet} \quad (5.24)$$

$LR_{bullet}$  and  $UR_{bullet}$  are respectively the real-valued lower and upper residuals which are used for modeling the influences of the modes outside of the considered frequency band.  $V$ ,  $\Lambda$  and  $L_{bullet}$  are the mode shape matrix, the diagonal matrix containing the complex poles and the modal participation factors. Inserting the modal decomposition and assuming steady-state conditions ( $\omega \rightarrow \omega_0$  into Equation (5.23) yields to Equation (5.25).

$$Y(\omega) \propto \omega^2 \left( V(j\omega I - \Lambda)^{-1}(L_x - jL_y) + \frac{1}{\omega^2}(LR_x - jLR_y) + (UR_x - jUR_y) \right) \quad (5.25)$$

This equation states that modal analysis can be applied to the orders by taking into account the following observations:

- Displacement orders are proportional to the squared rotational speed and, as consequence, acceleration orders are proportional to the fourth power of the same speed. The main difference is that in the classical modal analysis the acceleration Frequency Response Functions (FRFs) are proportional to the squared frequency axis.
- Complex upper and lower residuals, while in classical modal analysis they are assumed to be real.

- Complex participation factors both in classical and Order-Based Modal Analysis. Even in case of real modes, the participation factors are always complex.

Several Operational Modal Analysis methods could be employed for performing the modal characterization on orders. In this study, Operational Polymax has been used. It demonstrates to be robust against the listed observations because it estimates a right matrix-fraction model. This is a general curve-fitting method in which any assumption is needed on the modal model. On the other hand, methods such as the LSF (Least Squares Frequency Domain) method need to be reformulated. Operational Polymax was developed by extending to Operational Modal Analysis the well known Polymax method, also known as polyreference least-squares complex frequency domain method. Polymax works on FRFs as primary data. Operational Polymax works on auto- and cross-spectra and, after the introduction of Order-Based Modal Analysis, on orders. In all cases, the first step is the construction of the stabilization diagram from which natural frequencies, damping ratios and participation factor information can be extracted. The second step is a second least-squares step for estimating the mode shapes based on the selection of the stable poles from the previous diagram. The main advantage of such method if compared to other methods is the very clear stabilization diagram that can be obtained. It allows an easier identification of stable poles.

## 5.4 Algorithm for rotating accelerometers

It is quite interesting to point out that, in order to take into account the rotation of the accelerometers, an improved accelerometer-based method has been proposed for measuring the vibration behavior of parallel-axis high-speed gears. It is of fundamental importance to analyze the dynamics of these systems. The method can be extended also to non-parallel-axis gears. The dynamic forces at the gear mesh interfaces need to be balanced by the bearing forces. These forces are transmitted to the structure supporting the gears and cause structure-borne noise and vibrations. The fatigue life estimation of both gears and bearings is affected by the force fluctuations at the gear mesh interfaces. The proposed method implies the instrumentation of the gears by using triaxial accelerometers. They can be mounted on the gears at a given radius and  $90^\circ$  apart from each other. The acceleration signals are acquired by making use of slip rings and then they are processed by using this algorithm and divided into three main components: torsional, rotational and translational (transverse and axial directions). Several theoretical studies demonstrated that such a system shows a coupled torsional-rotational-transverse vibration motion instead of a

simple torsional one [82]. The main contribution is related to a method which allows to measure several components of gear dynamic motions:

- Dynamic Transmission Error (DTE) through measurements of motions in the torsional directions;
- Transverse motions in the transverse plane of the gears along the horizontal and vertical directions;
- Axial motions in the direction of gear motion axes;
- Rocking motions in the direction perpendicular to the transverse plane.

### 5.4.1 Motion transmission error

Nowadays, gearing transmissions are often used in many engineering systems. Several applications going from automotive transmissions to robot and aerospace engines can be mentioned. For this reason, in the market several kind of metallic gears can be found. Their main purpose is the transmission of rotation and torque between axes. If the gears were perfectly rigid and no geometrical errors or modifications were present, then the gears would transmit the motion and the torque in a perfect way resulting in a constant speed at the output shaft. No force variations would exist and, as consequence, no noise and vibration issues would be present. In reality, geometrical errors, deflections and friction are always part of the system. Hence, gears create noise and vibration problems. Transmission error is the rotation delay between driving and driven gear caused by the disturbances of inevitable random noise factors such as elastic deformation, manufacturing error, alignment error in assembly. It occurs when a traditional gear drive is operated under assembly errors. The motion Transmission Error (TE) is considered to be the primary excitation of gear noise. It is defined as the difference between the actual and the theoretical positions of the output gear. Considering Figure 5.15,  $TE$  of a gear pair can be defined as in Equation 5.26.

$$TE(t) = r_{g1}\theta_{g1}(t) + r_{g2}\theta_{g2}(t) \quad (5.26)$$

$r_{g1}$  and  $r_{g2}$  are the base circle radius of the two gears named gear  $g_1$  and gear  $g_2$ , respectively.  $\theta_{g1}$  and  $\theta_{g2}$  are the rotational displacements of the same gears.  $TE$  can be represented as a displacement excitation applied at the gear mesh along the line of action. LA is the line of action, while OLA represents the perpendicular direction named out-of-line of action.

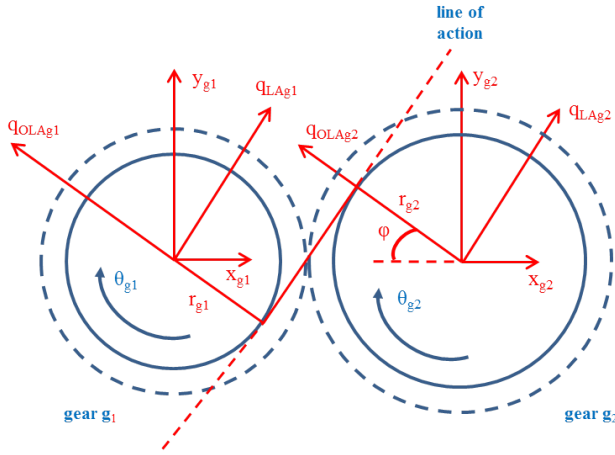


Figure 5.15: Definition of the motions of gears along the LA and OLA directions

The TE can be measured statically or dynamically, unloaded or loaded. Calculating static transmission error is a standard procedure, commercial gear calculation software are available to predict TE. As the rotational speed of the gears increase, TE changes from being a purely geometry and load dependent property to also including the dynamics of the system. As the mesh frequency and the harmonics coincide with different eigenfrequencies of the system, the resulting Dynamic Transmission Error (DTE) is a function the dynamic properties of the system. Since the DTE describes the complete system, including gears, shafts, bearings and housing, this makes the DTE more complex to analyze. DTE is often predicted by dynamic models of gear systems. Static TE is commonly used as excitation in order to calculate bearing forces, enabling the prediction of vibration and sound radiation from the housing. To make a dynamic model of a gear system it is important to have a correct model of the gear-mesh interaction.

### 5.4.2 Measurement system description

The use of uniaxial accelerometers has already been employed in several studies for gear dynamic analysis [83], [84]. Here a set of triaxial accelerometers is used to allow measurement of gear motions in all directions. Figure 5.16 shows the configuration required for applying the proposed method. Three sensors are mounted at  $0^\circ$ ,  $90^\circ$  and  $180^\circ$  at a radius  $r_g$  on each gear. Each accelerometer  $i$  measures three accelerations: tangential  $a_{iT}$ , radial  $a_{iR}$  and axial  $a_{iA}$  ( $i = 1, 2, 3$ ). So finally from each gear we get 9 measured accelerations for a total of 18 signals.



They can be used as shown in next Section for measuring the vibratory behavior of the system.

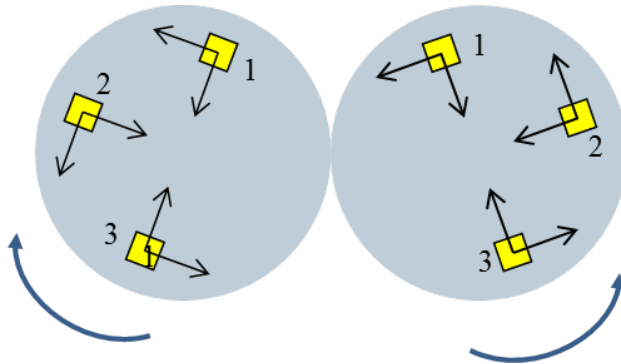


Figure 5.16: In-plane measurement system

### Measurement of DTE

Without the loss of generality, let's assume that the plane constituted by axes of the two gears is horizontal. The tangential accelerations contain both gravitational and rotational components. All the following equations are valid for both gears. Considering the accelerometers 1 and 3 we obtain Equation 5.27 and 5.28 at a given instantaneous position of the gear  $j$  ( $j = 1, 2$ ).

$$a_{1T}^j(t) = r_{gj}\ddot{\theta}_j(t) + g \sin(\omega_j t), \quad j = 1, 2 \quad (5.27)$$

$$a_{3T}^j(t) = r_{gj}\ddot{\theta}_j(t) - g \sin(\omega_j t), \quad j = 1, 2 \quad (5.28)$$

$g$  is the gravitational acceleration and  $\omega_j t$  is the angle between the horizontal reference position and the position of the 1<sup>st</sup> accelerometer on gear  $j$  at the time  $t$ .  $\omega_j$  is the rotational speed of gear  $j$ . By adding the two equations, the gravity terms get canceled out and the angular acceleration of gear  $j$  can be obtained by using Equation 5.29.

$$\ddot{\theta}_j(t) = \frac{1}{2r_{gj}} \left[ a_{1T}^j(t) + a_{3T}^j(t) \right] \quad (5.29)$$

The Transmission Error is defined in Equation 5.26 and it can be calculated in a dynamic environment by adding the signals from the two wheels and integrate them twice with respect to the time, as shown in Equation 5.30.

$$DTE(t) = \iint [r_1\ddot{\theta}_1(t) + r_2\ddot{\theta}_2(t)] dt^2 \quad (5.30)$$

### Measurement of the transverse motion of the gears

The transverse vibrations of each gear can be computed both in the horizontal and vertical directions. In order to obtain these vibrations, two radial acceleration signals from two locations that are 90° apart from each other are required. Considering  $a_{2R}$  and  $a_{3R}$  for this scope, Equation 5.31 and Equation 5.32 can be written.

$$a_{2R}^j(t) = -\ddot{x}_j(t) \sin \omega_j t - \ddot{y}_j(t) \cos \omega_j t + g \cos \omega_j t \quad (5.31)$$

$$a_{3R}^j(t) = -\ddot{x}_j(t) \cos \omega_j t + \ddot{y}_j(t) \sin \omega_j t - g \sin \omega_j t \quad (5.32)$$

$\ddot{x}_j(t)$  and  $\ddot{y}_j(t)$  are the horizontal and vertical accelerations of gear  $j$ , respectively. The angle  $\omega_j t$  represents the angle described by the first accelerometer with respect to the horizontal axis. In order to isolate the contributes in the horizontal and vertical directions, Equation 5.31 is multiplied by  $\sin \omega_j t$  and Equation 5.32 by  $\cos \omega_j t$ .

$$a_{2R}^j(t) \sin \omega_j t = -\ddot{x}_j(t) \sin^2 \omega_j t - \ddot{y}_j(t) \cos \omega_j t \sin \omega_j t + g \cos \omega_j t \sin \omega_j t \quad (5.33)$$

$$a_{3R}^j(t) \cos \omega_j t = -\ddot{x}_j(t) \cos^2 \omega_j t + \ddot{y}_j(t) \sin \omega_j t \cos \omega_j t - g \sin \omega_j t \cos \omega_j t \quad (5.34)$$

Equation 5.33 and Equation 5.34 can be added and solved for  $\ddot{x}_j(t)$ , as shown in Equation 5.35.

$$\ddot{x}_j(t) = -a_{2R}^j(t) \sin \omega_j t - a_{3R}^j(t) \cos \omega_j t \quad (5.35)$$

By multiplying Equation 5.31 by  $\cos \omega_j t$  and Equation 5.32 by  $\sin \omega_j t$  and subtracting the resultant equations,  $\ddot{y}_j(t)$  can be computed.

$$\ddot{y}_j(t) = g - a_{2R}^j(t) \cos \omega_j t + a_{3R}^j(t) \sin \omega_j t \quad (5.36)$$

### Measurement of the axial and rocking motions of the gears

For the determination of the axial and rocking components of the gear  $j$  about the  $x$  and  $y$  axes, the axial components of the accelerometers 1 and 3 can be used. So the acceleration  $a_{1A}^j$  and  $a_{3A}^j$  can be used to calculate the rotational acceleration of gear  $j$  about the rotating diametral axis connecting the points 1 and 3, as shown in Equation 5.37. Figure 5.17 can help to better understand the accelerations taken into account.

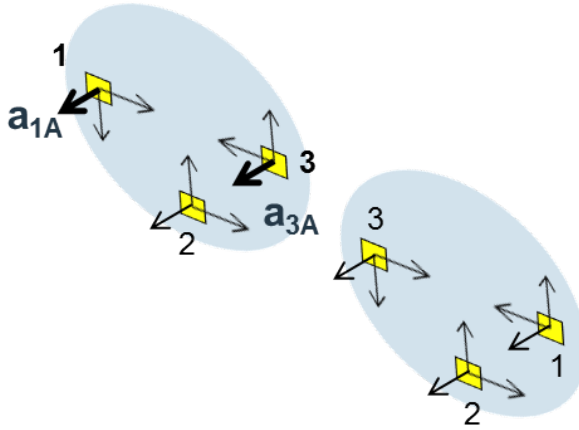


Figure 5.17: Out-of-plane measurement system

$$\ddot{\psi}_j(t) = \frac{1}{2r_{gj}} [a_{1A}^j(t) - a_{3A}^j(t)] \quad (5.37)$$

This acceleration can be decomposed in the two main directions  $x$  and  $y$  and integrated twice with respect to the time for obtaining the respective angular rocking displacements, as shown in Equation 5.38 and 5.39.

$$\psi_{xj}(t) = \iint \ddot{\psi}_j(t) \cos(\omega_j t) dt^2 \quad (5.38)$$

$$\psi_{x_j}(t) = \iint \ddot{\psi}_j(t) \sin(\omega_j t) dt^2 \quad (5.39)$$

While the rocking motion is given by acceleration components which are opposite in directions, the axial motion of gear  $j$  is simply given by the average of the two accelerations  $a_{1A}^j$  and  $a_{3A}^j$ , as written in Equation 5.40.

$$z_j(t) = \frac{1}{2} \left[ a_{1A}^j(t) + a_{3A}^j(t) \right] \quad (5.40)$$

### Remarks

The proposed method is quite general and it must be noticed that it is valid for any gear ratio between the two gears. The DTE is independent of the gear ratio, while the transverse and axial motions are derived independently for each gear  $i$ . In case of unity gear pair (which is the case for the experimental validation) the position angle between the reference accelerometers can be established so that only one of the two angles is needed for measuring the vibratory behavior of the gear pair. It can also be noticed that out of the 18 measured quantities, only 12 have been used for the post-processing calculations. Table 5.1 lists the sensor assignment for each type of measurement. The channels 1R, 2T, 2A have not been exploited for both gears.

## 5.5 Best practice for OBMA

The OBMA technique shows to be very powerful for identifying the modal parameters in operational conditions in case of rotating machineries. Basically there are two fundamental steps: a very good measurement of the tachometer signal and the correct extraction of the orders, both in amplitude and phase.

### 5.5.1 Best practice for tachometer measurements

In order to perform a proper tachometer measurement, several alternatives are possible. The sensors to be used are depending from both the application and the objective of the study. For this reason, several sensors can be found in the market with a huge variety of costs and performances. The best sensor can then be selected for each individual application based on the type of analysis, the

Gear	Sensor	Direction	DTE	x	y	Rocking	Axial	
gear 1	Accel 1	1T	X					
		1R						
		1A				X	X	
	Accel 2	2T						
		2R			X	X		
		2A						
	Accel 3	3T	X					
		3R			X	X		
		3A					X	X
gear 2	Accel 1	1T	X					
		1R						
		1A				X	X	
	Accel 2	2T						
		2R			X	X		
		2A						
	Accel 3	3T	X					
		3R			X	X		
		3A					X	X

Table 5.1: Sensor assignment for each type of measurement

accessibility of the shaft, the ease of instrumentation and the required accuracy or level of detail [85].

### Accelerometers and strain gauges

Two linear accelerometers are fixed in parallel on the rotating shaft as shown in Figure 5.18. The two accelerometers measure the tangential acceleration. They move in two opposite directions in the fixed reference frame of the rotation axis. As consequence, any translational acceleration gets canceled by averaging the two signals.

The angular displacement, velocity and acceleration can be computed by using Equation 5.41.

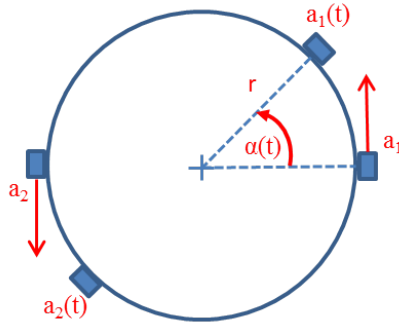


Figure 5.18: Linear accelerometers configuration

$$\begin{aligned}
 r\alpha &= \iint \frac{a_1 + a_2}{2} dt^2 \Rightarrow \alpha = \iint \frac{a_1 + a_2}{2r} dt^2 \\
 \Rightarrow \dot{\alpha} &= \omega = \int \frac{a_1 + a_2}{2r} dt \Rightarrow \ddot{\alpha} = \frac{a_1 + a_2}{2r}
 \end{aligned}
 \tag{5.41}$$

For Noise, Vibration and Harshness (NVH) analysis, the *rpm* quantity can be calculated by using Equation 5.42.

$$rpm = \frac{60}{2\pi} \int \frac{a_1 + a_2}{2r} dt
 \tag{5.42}$$

The main advantages of this configuration are related to the fact that the dynamic range is determined directly by the accelerometers and that, if they are properly aligned, there is a very low sensitivity to the shaft-translational vibrations. There are several drawbacks which can be listed:

- the telemetry system can be very expensive or slip rings are needed for transferring the acceleration signals from the rotating shaft to the measurement hardware
- in case of small shafts, the mass loading due to the presence of the two accelerometer can modify the dynamic behavior of the shaft
- the accelerometers can get lost in a dangerous way in case of big shafts due to the higher centrifugal forces

- angle domain processing is not possible online because accelerations are measured and angle and speed can only be derived by integration afterwards (offline processing).

In the market, fully-integrated angular accelerometers can be found. They need to be fixed on the shaft extremities and they include both the sensor and the slip ring. Also the strain gauges can be used for this application. Their advantage is mainly due to the direct measurement of the torsional elongation or stress. This is the reason why these sensors are often used in durability tests for estimating the torsional fatigue. The same drawbacks listed for the accelerometers are valid also for strain gauges.

### Laser interferometers

Laser manufacturers propose specific systems for rotating machineries based on the dual-beam techniques to cancel the effect of translational movement of the shaft. Laser interferometers can be used for the purpose of measuring the rotational speed of a machine. The technique is based on the Doppler effect and allows computing the angular velocity from the velocity measured in the direction of the laser beams on the two pointed areas in Figure 5.19.

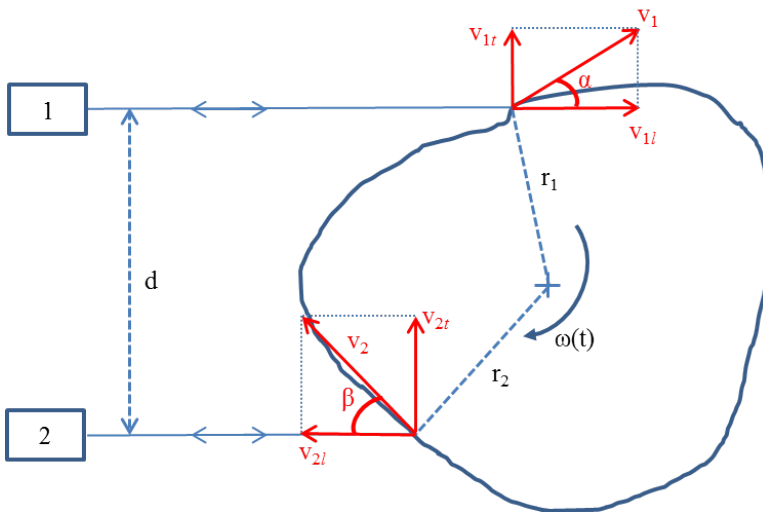


Figure 5.19: Torsional laser principle based on Doppler effect

Several advantages can be mentioned for what concerns the lasers. In fact they allow a contactless measurement and an easy instrumentation. They also have a

low sensitivity both to shaft-translation vibration and to the shape of the shaft itself. On the other hand we are talking about very expensive devices. This is an important drawback because for several applications (i.e. torsional vibrations) more than one device is needed which enormously increase the costs. Also in this case the exact angular speed and position are not known in an absolute sense because the velocity is measured and the angle can only be derived by integration. Their use in a real-life environment is very difficult or close to impossible because the devices are not very small and they cannot be used in case in which the working environment is not big enough.

### Coder-based techniques

In order to apply a coder-based technique, equidistantly-spaced markers need to be placed on the shaft or, more in general, on the rotating part. The sensor measures every time a marker passes in front of the sensor and the time difference between two markers is used for estimating the angular velocity as shown in Equation 5.43.

$$rpm_i = \frac{60}{(t_i - t_{i-1})ppr} \quad (5.43)$$

$ppr$  represent the number of pulses per revolution and  $(t_i - t_{i-1})$  is the time difference between two markers. This technique delivers both the  $rpm$  and the angular position. The data resolution is determined by the number of markers: the more markers, the more accurate information. Different types of setups are used to provide markers (coder); for example, stripes drawn on the shaft or the teeth of the gears. Also, different sensors are available to detect the markers, such as electro-magnetic pickup or optical sensors. Incremental encoders are devices combining the coder and the sensor in a single hardware.

**Magnetic pickups** Magnetic pickups detects changes in the magnetic field or flux resulting from metallic teeth passing the sensor, as shown in Figure 5.20. Since they are very robust and reliable, they are used quite often in the industrial world. Just to give an example, these sensors are employed in most of the combustion engines for measuring torsional vibrations. The setup is not very difficult to prepare. In fact the gear sets can be used as coder and the sensor will be able to measure the time difference between the passage of a marker in front of it and the successive passage of a second marker. The number of markers defines the angular resolution: the more markers, the more accurate information can be obtained. The number of teeth on the gear set limits the number of pulses per rotation which could be insufficient to capture all torsional



content. The sensor must be placed very close to the rotating shaft and this is not always possible. Another drawback could be due to shaft bending that can generate a fictive torsional vibration.

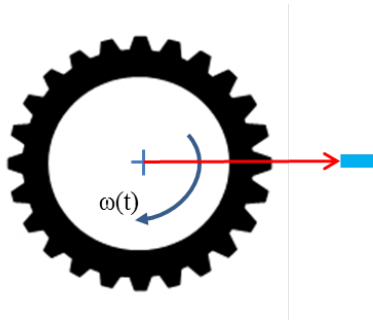


Figure 5.20: Coder-based measurement principle

**Optical sensors** Most of the optical sensors available in the market are used for object detection. In order to use them for measuring the rotational speed  $\omega$ , a high resolution is needed. In fact, they need to detect a high rate of events per second with a very good timing accuracy. An optical sensor converts light rays into electronic signals. It measures the physical quantity of light and then translates it into a form that is readable by an instrument. Optical fibers are used to conduct the light from the emitter to the sensor head, and back from the sensor head to the receptor. These sensors have several advantages:

- The instrumentation is not very difficult. In fact the sensor is typically fixed on non-rotating components, while the code needs to rotate.
- They can be instrumented on gears as for magnetic pickups
- Coders can be implemented on the shaft by using contrasted paint or zebra tape configurations
- Quick response and phase accuracy of good quality optical sensor allows the measurement of a very high pulse rate

On the other hand, some disadvantages could also be listed:

- The instrumentation of gears could be complicated by the sensitivity to ambient light or by the quality of the material reflection

- The sensor must be placed very close to the rotating shaft and this could not be always possible and problems could arise if the shaft has an important translational movement

**Zebra tapes** Black and white tapes are increasingly used to quickly implement a coder on a shaft. It can be used to create a coder where no gear wheel is available or when a higher number of pulses per rotation are needed. There are two families of tape depending if it must be glued around the shaft (zebra tape) or on the extremity (zebra disc). Zebra tapes and discs exist in multiple-stripe width to adapt to the number of pulses per revolution in the functioning of the shaft diameter. An example of a zebra tape instrumentation is shown in Figure 5.21. The rotating velocity can be measured by timing the duration of the passage of the alternating light and dark stripes glued to the shaft. Such systems are able to overcome the limitations of other measurement systems which are either expensive or require time-consuming and difficult shaft modifications. Zebra tapes however suffer from the fact that the last stripe at the butt joint has in general a different width if compared with the other stripes, as shown in Figure 5.22. This will cause an error that disturbs the data analysis. A butt joint correction algorithm is needed and it must be able to deal with high rotational speed and strong torsional vibrations. The algorithms proposed by [86] identifies the position and the angular interval at the butt joint by using an angle estimator function and a dedicated spline interpolation and FIR bandpass filter. This information allows to reconstruct the exact angle evolution and perform a proper torsional vibrations analysis. The algorithm has been validated and it is now a standard for zebra tape measurements.



Figure 5.21: Zebra tape shaft instrumentation

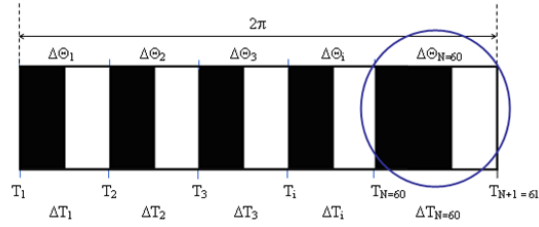


Figure 5.22: Zebra tape butt joint correction

**Incremental encoders** Incremental encoders are devices combining the coder and the sensor in a single hardware. This means in practice that it consists of both a rotating (rotor) and a static (stator) component and the full sensor needs to be mounted on the setup. They are typically used for accurate detection of shaft positions. Their high accuracy make them very interesting for all those applications which require a high resolution tachometer measurements, such as Order Based Modal Analysis.



Figure 5.23: Incremental encoder

The incremental encoder uses three embedded coders: one (called C) detecting a single pulse/revolution as an absolute angle reference, and two more high-resolution encoders called A and B. The A and B signals have the exact same number of pulses, but the B signal is phase-shifted with a quarter of a pulse cycle (90 degrees) compared to A. Combining these two coder signals allows detection of the sense of rotation of the coder. The work principle is illustrated in Figure 5.24.

Incremental encoders are mainly used when working on test benches in which the instrumentation is part of the test bench itself. Because of its relatively complex instrumentation, it is rarely used for in-vehicle or mobile measurements. On the other hand, several advantages are obtained by applying this fully-integrated approach. In fact, a very high pulse rate can be obtained and normally incremental encoders can be delivered with the appropriate number of pulses depending on the application and the desired accuracy. very high number can be reached (up to 5000). The sense of rotation can be of great help

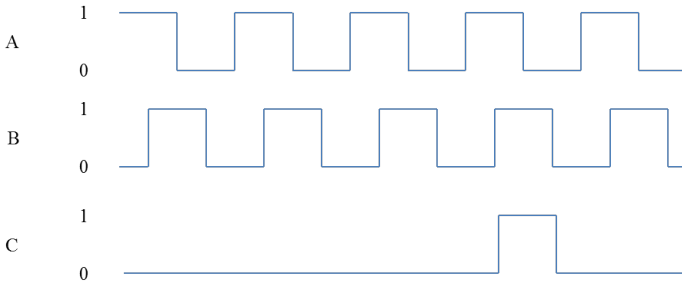


Figure 5.24: Incremental encoder signals

for several applications.

### Final considerations about tachometer measurements

In Section 5.5 several sensors for an accurate measurement of the tachometer signal have been introduced. Among them surely the coder-based techniques are the most used in the industrial environment. Depending on the application, it could be enough to instrument the rotating shaft with a zebra tape and using an optical sensor to detect the rotational speed. For some other applications a high number of pulses per revolution could be needed. In this case an incremental encoder built for the particular application could give better results. The use of accelerometers or strain gauges has many drawbacks and it is not suggested for demanding cases. In our applications, we mainly used coder-based techniques. Both the use of a zebra tape and of incremental encoders has been tested for different application cases. In both cases it must be considered that each pulse detection moment corresponds to a known increase in angular position. In other words, at each tacho moment, the angular position is known with respect to the first tacho moment. This means that interpolation techniques are needed to estimate the position or the speed between two tacho moments and to generate time-equidistant rpm trace at the desired sampling frequency. Digital reconstruction filters are also needed to avoid aliasing. Another point which must be taken into account is that the quality of coder-based measurements is affected by the correct selection of a minimum number of pulses per rotation. In case too few markers per revolution are present, an error named angle-domain aliasing will be added. Three main principles can be used for identifying the minimum coder resolution:

- Nyquist-Shannon sampling theorem: The required number of samples per revolution  $M$  is obtained by applying the Nyquist theorem to an angle

domain acquisition. It states that the number of samples per rotation  $M$  must be at least two times higher than the maximum order  $O_{max}$ .

$$M > 2O_{max} \quad (5.44)$$

- Relation order bandwidth for rotating machinery: The maximum order observed  $O_{max}$  is a function of the bandwidth  $bw$  of the system and the rotational speed  $rpm$ . For varying speeds such as in case of runups, rundowns, etc., the  $rpm_{min}$  determines the maximum observed order.

$$O_{max} = 60 \frac{bw}{rpm_{min}} \quad (5.45)$$

- Optimal number of pulses per rotation: Based on the previous principles, the optimal coder resolution can be estimated as in Equation 5.46.

$$M = 2O_{max} = 120 \frac{bw}{rpm_{min}} \quad (5.46)$$

In many cases, test engineers are not free to choose the optimal coder for the test. For example, in cases in which the teeth of a gear in a gearbox are used as coders, it is fundamental to estimate the error made by using few pulses. The reversed Equation 5.47 is used to estimate the bandwidth of the coder for specific  $rpm$  conditions.

$$bw = M \frac{rpm_{min}}{120} \quad (5.47)$$

## 5.5.2 Best practice for order estimation

The Order Based Modal Analysis technique requires a very good order estimation which can only be obtained if an accurate tachometer measurement took place. There are several parameters and considerations which must be taken into account when choosing the order tracking technique to apply to the acquired data. Chapter 6 will give several examples in this sense by comparing the order tracking techniques in different cases, both in a simulation and in a test environment. Anyhow the main considerations can already be listed at this point and they will be extensively discussed during the application cases analysis:

- Purpose of the order tracking step  
It is important to know which is the reason why an order tracking step is going to be performed. For instance, if the aim is the dynamic analysis of

the rotating system by means of OBMA technique, then a particular care need to be reserved to the phase of the orders. In fact it is an essential part of the signal especially for modal analysis. If the main scope is just to analyze at which frequencies orders are facing a resonance or at which frequency the highest order amplitude is obtained, then most of the listed techniques will be able to give these kind of information.

- Computational time

The choice of the order tracking technique is always a compromise between the computational effort and the good quality of the results. For example, the FS technique allows to get a good approximation of the orders in a simple and numerically efficient way even if it does not take into account the fact that the frequencies of orders are changing with the time. It suffers from the problems due to fast sweep rates. On the other hand, OT and AD need a higher computational time but they provide leakage free estimates of orders. Furthermore, TVDFT estimates orders which closely match those of the resampling based methods with much less computational load. In fact, this technique is essentially resampling the kernel of the Fourier transform instead of resampling the data. The VK filter is able to extract the time histories of the orders and for this reason it is quite computationally demanding.

- Presence of close/crossing orders

The presence of close/crossing orders can be known in advance and it is important for choosing the best technique for the analysis. In fact, only TVDFT (with OCM compensation) and VK are able to separate close/crossing orders. All the other techniques will have some troubles in these cases.

## Chapter 6

# Order Based Modal Analysis: application cases

This Chapter introduces several simulation and test cases to underline the improvements obtained by applying the OBMA method instead of classical modal analysis techniques. Section 6.1 shows a simple 2D model built by using Matlab to show the basic concepts. Section 6.2 is focused on the application of OBMA to an industrial gear test-rig and compares EMA, ODS, OMA and OBMA results. Finally, a very industrially oriented example will be presented in Section 6.3 by considering a wind turbine gearbox in a test-rig configuration before being installed in a wind turbine.

### 6.1 2D model

The main purpose for which a numerical model has been built by using Matlab is the validation of the proposed approach. The order tracking techniques introduced in the previous discussion were used for extracting orders. Then Operational Polymax was employed for identifying a modal model.

#### 6.1.1 Model description

The model is a 8 degree-of-freedom (DOF) mass-spring-damper planar system which is composed of 4 masses connected by means of springs and dampers.

The directions  $x$  and  $y$  are coupled [14]. A schematic representation of the model is shown in Figure (6.1).

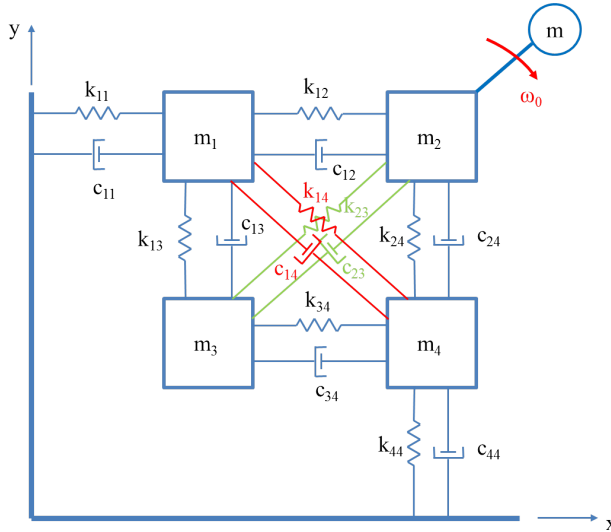


Figure 6.1: Schematic representation of the numerical model

A rotating mass excitation has been applied on mass  $m_2$  for simulating the effect of a rotating force which can be represented by two perpendicular forces of equal amplitude, but with a  $90^\circ$  phase shift, as shown in Equation (6.1).

$$\begin{aligned}
 f_x(t) &= rm\omega_0^2 \cos(\omega_0 t + \phi) \\
 f_y(t) &= rm\omega_0^2 \sin(\omega_0 t + \phi)
 \end{aligned}
 \tag{6.1}$$

$\omega_0$  is the rotational speed, while  $r$  is the distance of the mass  $m$  from the mass  $m_2$ . The natural frequencies, damping ratios and mode shapes of this system can be numerically identified by constructing the mass, damping and stiffness matrices  $[M]$ ,  $[C]$ ,  $[K]$ . Table 6.1 lists the values used for masses, springs and dampers.

Table 6.2 lists the natural frequencies (in Hz) and damping ratios (in %) for the 2D system by using the input parameters listed in Table 6.1. Since we have a 8 DOF system, then 8 modes are identified.



---

$m_1 = m_2 = m_3 = m_4$	10 kg
$c_{11} = c_{12} = c_{34}$	60 Ns/m
$c_{13} = c_{24}$	50 Ns/m
$c_{44}$	250 Ns/m
$c_{14}$	20 Ns/m
$c_{23}$	40 Ns/m
$k_{11} = k_{12} = k_{34}$	150000 N/m
$k_{13} = k_{24} = k_{44}$	200000 N/m
$k_{14}$	100000 N/m
$k_{23}$	90000 N/m

---

Table 6.1: 2D model: input parameters

Natural frequency [Hz]	Damping ratio [%]
6.69	1.13
14.78	1.45
18.45	3.39
23.76	3.12
30.88	3.88
34.62	4.04
36.84	3.40
40.95	5.78

---

Table 6.2: Modal parameters identification

## 6.1.2 Operational Modal Analysis

Several run-ups were simulated by using the same sampling frequency ( $f_s=200\text{Hz}$ ) and by varying the sweep rate or, in other words, the simulation time to go from 1Hz to 25Hz: 10s, 100s, 1000s. Most of the order tracking techniques are very sensitive to the sweep rate variation. In fact, by sweeping through the resonances with a lower sweep rate, the modal parameters such as the natural frequencies and the damping ratios can be identified with a better precision. Two orders have been generated (Order 1 and Order 2). First of all, the "end-of-order" effect can be highlighted by applying classical OMA to

the acquired accelerations. Figure (6.2) shows the time-frequency plot (bottom picture) in which the rotational speed is increasing from 0 to 1500rpm in 1000s. The two orders are crossing several resonances as it can be noticed by their magnification at several frequencies. The top picture in Figure 6.2 shows the overall spectra of the same channel. The two "end-of-order" peaks are quite evident and they appear at 25Hz and 50Hz (as expected, they correspond to the frequencies at which the Order 1 and Order 2 are ending when the maximum rotational speed is reached).

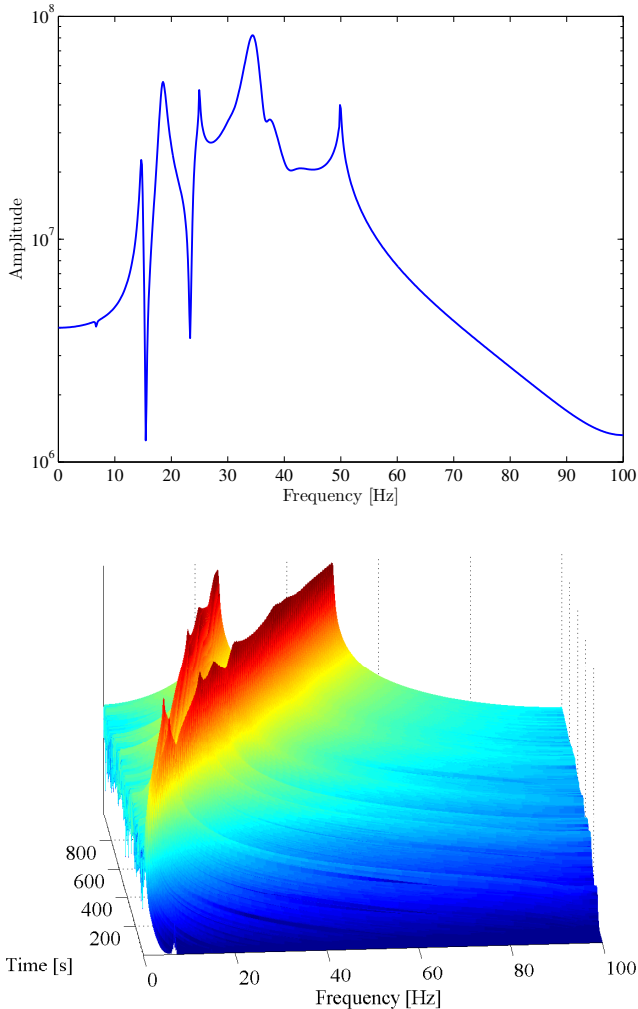


Figure 6.2: Time-Frequency plot for the 8-DOF model

Both Operational Modal Analysis and Order-Based Modal Analysis have been employed for estimating the modal parameters of the 8-DOF model. For what concerns OMA, a frequency band from 1Hz to 60Hz has been considered. This frequency band includes all the 8 modes of the system. Figure (6.3) shows the stabilization diagram obtained by applying Operational Polymax to the auto- and cross-powers in the selected frequency band.

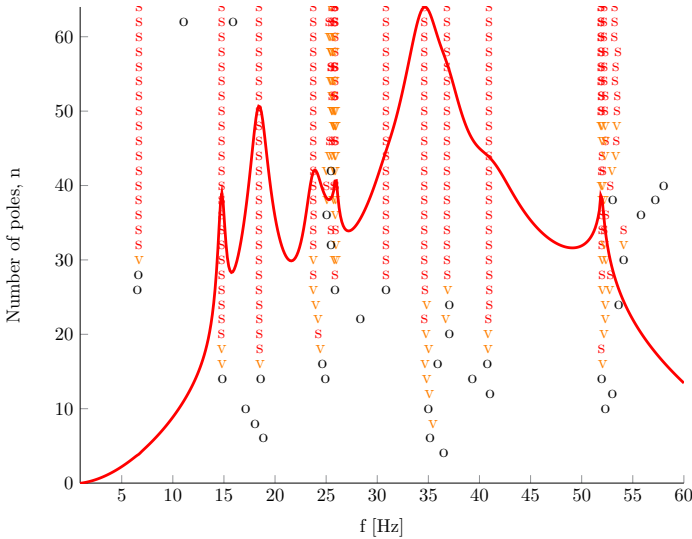


Figure 6.3: Stabilization diagram obtained by applying Operational Polymax.

The accelerations of mass 1 in both x and y directions are used as reference for the calculation of the spectra. An exponential window equal to 10% has been applied and a modal order equal to 64 has been chosen. The main differences by using the classical OMA procedure and the OBMA one are related with the fact that the Polymax method is applied to the spectra in the first case and to the orders in the second case. For calculating the spectra, one or more reference channels need to be defined among the acquired accelerations. In case of order calculation, the reference is chosen with respect to the rotational speed. The spectrum of the input forces is shown in Figure 6.4. The two peaks at 25Hz and 50Hz are clearly visible and this demonstrates the origin of the "end-of-order" effect. OMA cannot be applied because one of its main assumptions is not respected. In fact the two "end-of-order" peaks are such that the input spectrum cannot be considered as a white noise spectrum.

The results are listed in Table 6.3 where 2 different OMA cases are compared with the modal parameters identified numerically in the previous Section.

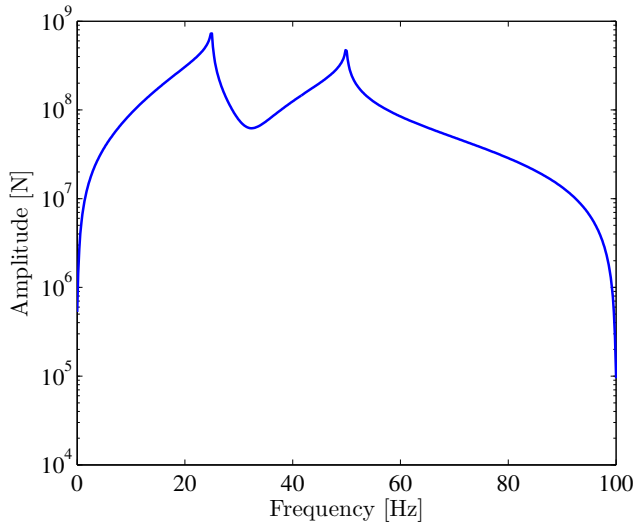


Figure 6.4: Spectrum of the input forces exciting the 8DOF system

Numerical Analysis		OMA (0-1500rpm)		OMA (0-1020rpm)	
Natural frequency [Hz]	Damping ratio [%]	Natural frequency [Hz]	Damping ratio [%]	Natural frequency [Hz]	Damping ratio [%]
6.69	1.13	6.69	1.86	6.69	1.86
14.78	1.45	14.79	1.78	14.79	1.78
-	-	-	-	16.94	0.62
18.45	3.39	18.45	3.65	18.45	3.65
23.76	3.12	23.76	3.32	23.77	3.33
-	-	24.90	0.43	-	-
30.88	3.88	30.88	4.04	30.89	4.04
34.62	4.04	34.62	4.18	-	-
-	-	-	-	33.89	0.50
36.84	3.40	36.85	3.54	-	-
40.95	5.78	40.96	5.90	-	-
-	-	49.96	1.42	-	-

Table 6.3: OMA - Modal parameters identification and comparison with numerical analysis

The 8 modes are well identified by 8 columns of stable poles, but on top of them two more poles are identified by two sharp peaks (very low damping ratios) in both cases. In the first case (0-1500 rpm), they appear at frequencies very close to 25Hz and 50Hz. They are the frequencies at which the two orders are stopping at the maximum rpm. A comparison between the measured crosspower and the synthesized one after having applied OMA is shown for a channel in Figure (6.5). The fitted model looks very good, but two more modes at 25Hz and 50Hz have been estimated as poles of the system, whereas they are not.

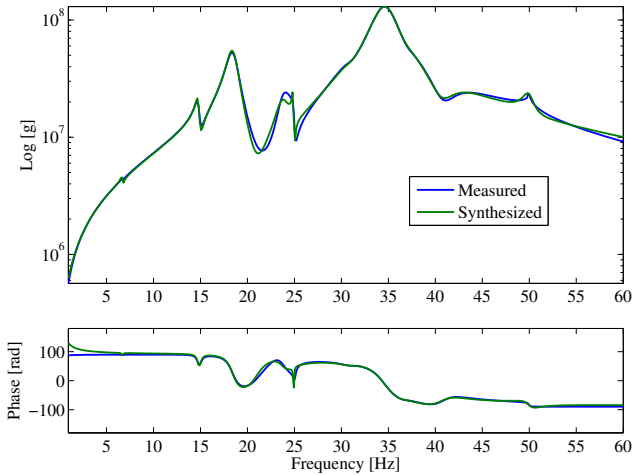


Figure 6.5: Measured vs. synthesized crosspower after having applied Operational Polymax.

The two sharp "*end-of-order*" peaks can be clearly identified. In this case they are not corresponding to any of the natural frequencies of the model and they can be ignored since their frequencies will be known in advance. A more challenging case is shown in the stabilization diagram in Figure (6.6). In this case the rotational speed is increasing and reaching a maximum value of 1020rpm, which allows the orders to end very close to two structural modes. In this case, the modal identification becomes more complex and it is not very easy to distinguish between physical and mathematical poles. It can be noticed that the last two modes cannot be identified since they are masked by the "*end-of-order*" pole which is very close in frequency to them.

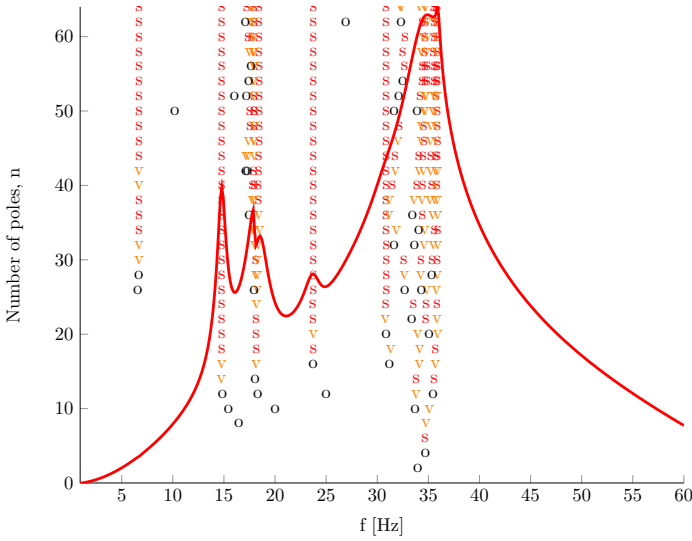


Figure 6.6: Stabilization diagram obtained by applying Operational Polymax.

### 6.1.3 Order-based Modal Analysis

After having shown the difficulties that could be encountered by applying the regular OMA process to run-up data, the results of OBMA will be shown by considering the order tracking techniques listed and described in the previous chapter.

#### Order Tracking step

Several run-up speeds have been considered also in this case. In all situations, the  $2^{nd}$  order is crossing all the 8 resonances of the system. First of all the three techniques implemented in the LMS Test.Lab software will be used for extracting the orders: Fixed Sampling (FS), Order Tracking (OT) and Angle Domain (AD). Afterwards both Time Variant Discrete Fourier Transform (TVDFFT) and Vold-Kalman filter order tracking (VK) will be employed. The parameters used for the different cases (10s, 100s, 1000s) and for all the techniques (FS, OT, AD, TVDFFT, VK) are listed in Table (6.4). The main parameter to be set for FS is the frequency resolution  $f_{res}$ . For what concerns the OT technique, the order resolution  $o_{res}$  and the maximum order  $o_{max}$  need to be defined. AD is based upon the number of cycles  $n_{cyc}$  used for the calculation. Finally the main parameter for the TVDFFT order tracking is the number of revolutions ( $n_{rev}$ ) to

be considered in the algorithm. On the other hand, the main parameter for VK order tracking is the bandwidth of the filter ( $bw$ ). All the parameters shown in Table 6.4 have been employed and the ones listed in Table 6.5 have been selected for being used in the three different cases of slow, medium and fast run-ups. Figure 6.7 shows the tachometer signals for two run-ups cases (10s and 100s). A linear run-up has been considered in all cases.

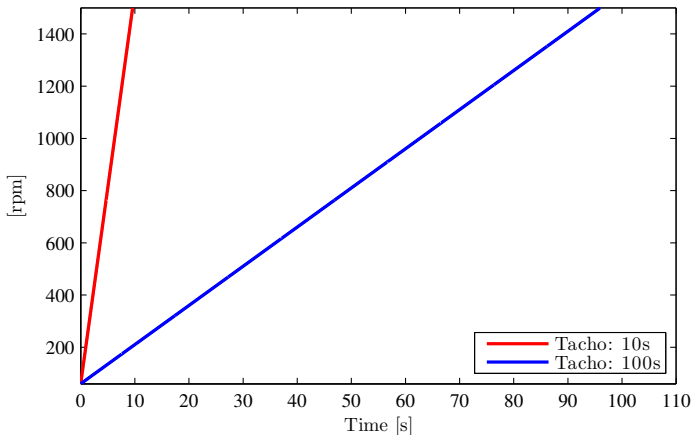


Figure 6.7: rpm signals: 10s vs 100s runup.

<b>FS</b>	$f_{res}$	1Hz	2Hz	4Hz
<b>OT</b>	$o_{res}$	0.25	0.5	1
<b>AD</b>	$o_{max}$	8	16	32
<b>TVDF</b>	$n_{cyc}$	1	4	16
<b>TVDF</b>	$n_{rev}$	1	4	16
<b>VK</b>	$bw$	1Hz	3Hz	5Hz

Table 6.4: Order Tracking step: sensitivity analysis parameters

<b>FS</b>	$f_{res}$	1000s	100s	10s
<b>OT</b>	$o_{res}$	4Hz	2Hz	2Hz
<b>OT</b>	$o_{res}$	0.25	0.25	1
<b>AD</b>	$o_{max}$	8	8	32
<b>AD</b>	$n_{cyc}$	4	4	1
<b>TVDF</b>	$n_{rev}$	4	4	1
<b>VK</b>	$bw$	1Hz	3Hz	5Hz

Table 6.5: Order Tracking step: selection of the optimal parameters

The first case is the one in which the run-up lasts 1000s. Since it is a quite slow run-up, none of the mentioned techniques has problems in extracting the correct orders. Figure 6.8 shows a comparison between the three techniques (FS, OT and AD) and the theoretical order (True) in terms of amplitude and phase for what concerns the extraction of order 2. All the techniques can extract the order with a very good approximation. On the other hand a small delay in phase can be highlighted in all cases. This is mainly due to the fact that all techniques need to wait a certain time before acquiring the first sample.

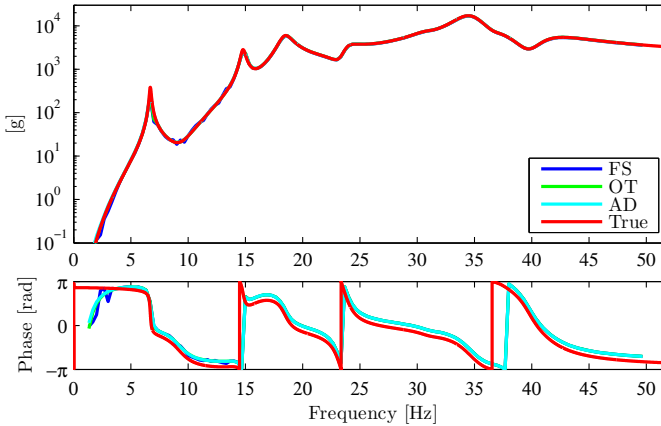


Figure 6.8: 1000s runup: comparison between order tracking techniques (FS, OT, AD) and the theoretical order (True).

A comparison among the orders extracted by using TVDFT and VK with the True order is shown in Figure 6.9. In this case, curves which are very similar to the previous cases can be obtained. We could then conclude that all the order tracking techniques perform very well and are able to extract properly the dominant order (except for the small phase delay in the entire frequency band).

In general we could state that TVDFT and VK techniques demonstrate to be more powerful in cases in which a rpm signal is obtained in a simulation environment. AD, on the other hand, is an excellent technique when the rpm is measured by means of a high quality encoder. This will be demonstrated in the next Section on the industrial test-rig data. OT can perform as well as AD in many cases, but it only exploits 1 pulse per revolution which can be enough in several applications (e.g. when the torsional vibrations are negligible). FS is a very quick tool to verify that the data are consistent, but it has several limitations if compared with the other techniques. The situation becomes more complicated if the sweep rate is higher. Figure 6.10 compares FS, OT and AD



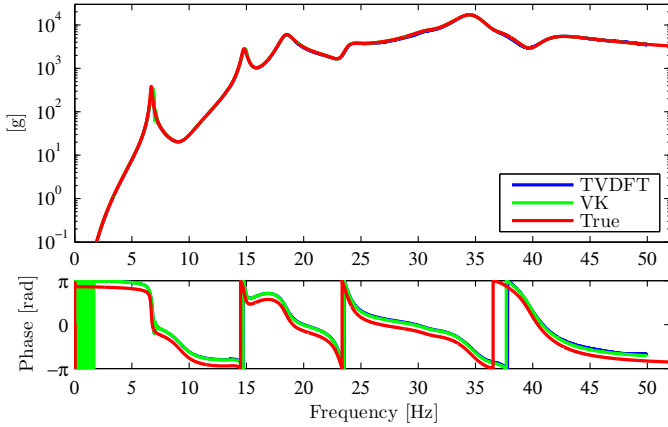


Figure 6.9: 1000s runup: comparison between order tracking techniques (TVDFDT, VK) and the theoretical order (True).

with the True order in case of a run-up which lasts 100s instead than 1000s. Figure 6.11 shows how TVDFDT and VK perform in this more challenging case.

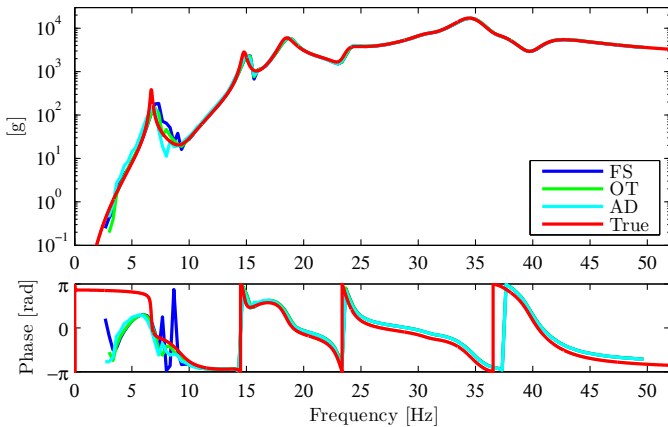


Figure 6.10: 100s runup: comparison between order tracking techniques (FS, OT, AD) and the theoretical order (True).

It can be noticed that below 10 Hz there are too few samples by using FS, OT and AD to describe properly the order. The situation improves at higher frequencies. Same considerations for what concerns TVDFDT and VK. In fact, in

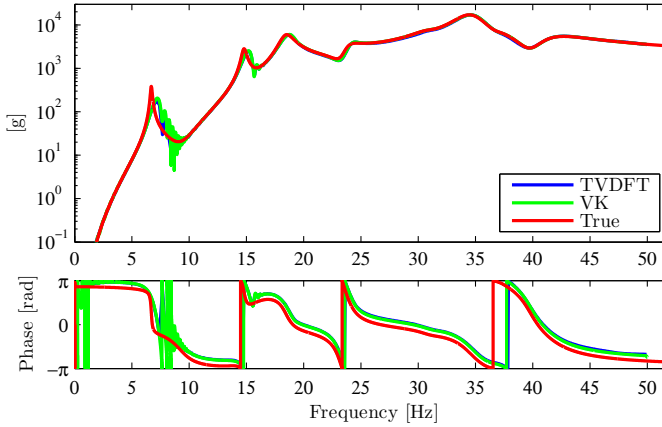


Figure 6.11: 100s runup: comparison between order tracking techniques (TVDFT, VK) and the theoretical order (True).

these cases the beating phenomena is quite evident. This is due to the fact that the system crosses the resonance without having the time to excite it properly. Finally, let's move to a very challenging case. The run-up takes, in this case, 10s to accelerate up to 1500rpm. Figure 6.12 and Figure 6.13 illustrate the extracted orders. In a very fast run-up, the effects of small irregularities in the tachometer signal are less important, but it becomes very difficult to describe the dynamic of the system at low frequencies. The parameters for each technique need to be modified a bit in order to properly extract the needed orders. In general, for all techniques a small time interval need to be considered for the estimation. Otherwise only few samples are collected and the order estimation becomes too coarse.

For this reason, a sensitivity study has been performed for all the techniques. Here the results for FS, OT and AD are shown by varying the frequency resolution  $f_{res}$ , the order resolution  $o_{res}$  and the number of cycles  $n_{cyc}$  respectively. Figure 6.14, 6.15 and Figure 6.16 represent the use of FS technique for the three different run-ups (1000s, 100s and 10s). Figure 6.17, 6.18 and Figure 6.19 show the OT technique results by varying the order resolution and finally in Figure 6.20, 6.21 and Figure 6.22 the AD curves are shown for the three different run-ups (1000s, 100s and 10s).

The influences of the frequency resolution  $f_{res}$ , the order resolution  $o_{res}$  and the number of cycles  $n_{cyc}$  are quite evident. It's difficult to predict in advance which are the best parameters to choose. In general, a trial and error procedure is the suggested one, even if some preliminary considerations can be drawn.

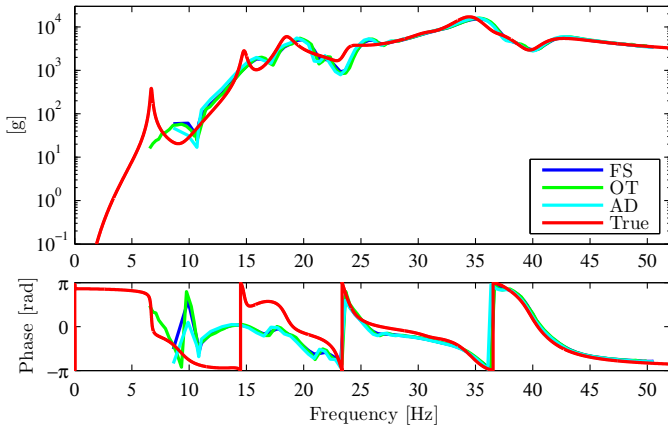


Figure 6.12: 10s runup: comparison between order tracking techniques (FS, OT, AD) and the theoretical order (True).

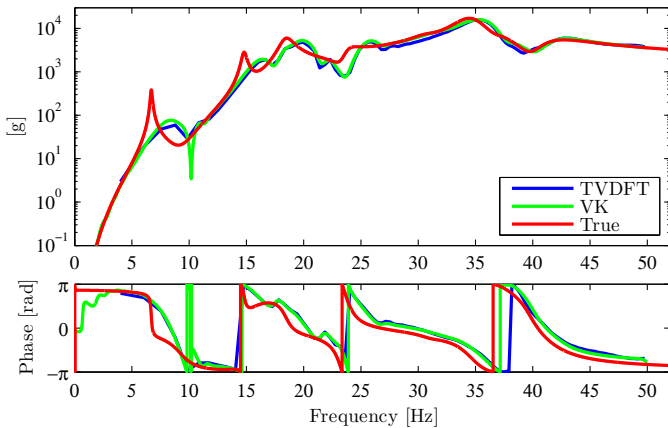


Figure 6.13: 10s runup: comparison between order tracking techniques (TVDFFT, VK) and the theoretical order (True).

In fact the rotational speed, the sweep rate, the number of samples are the main actors and they need to be taken into account when defining the order tracking parameters. A machine rotating at a very high speed allows to choose a high value for the number of cycles because there will be enough rotations to characterize the dynamics of the system. If the rotational speed is quite low and the measurement does not last very long, then by considering a high

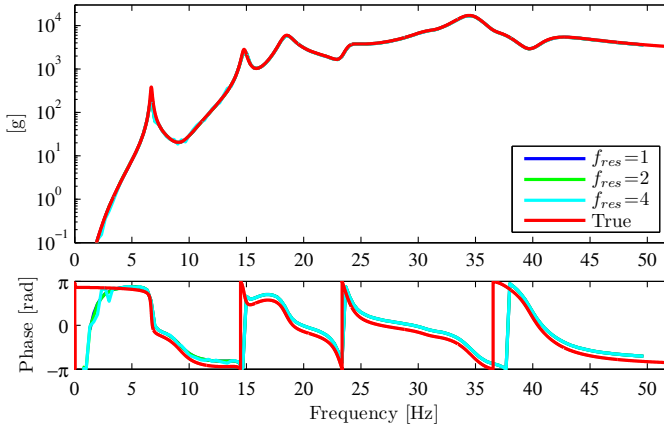


Figure 6.14: 1000s runup: Influence of input parameters for FS order.

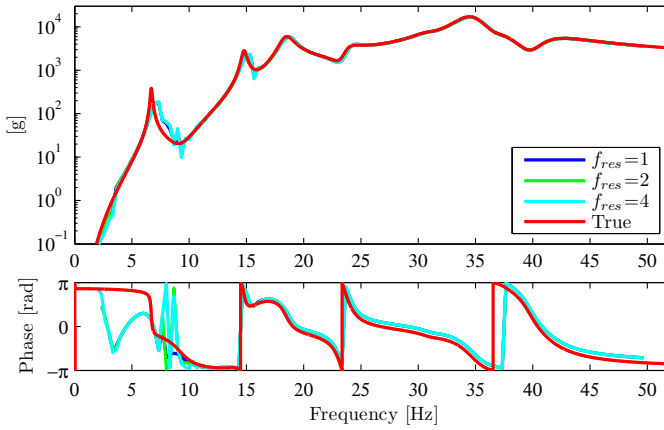


Figure 6.15: 100s runup: Influence of input parameters for FS order.

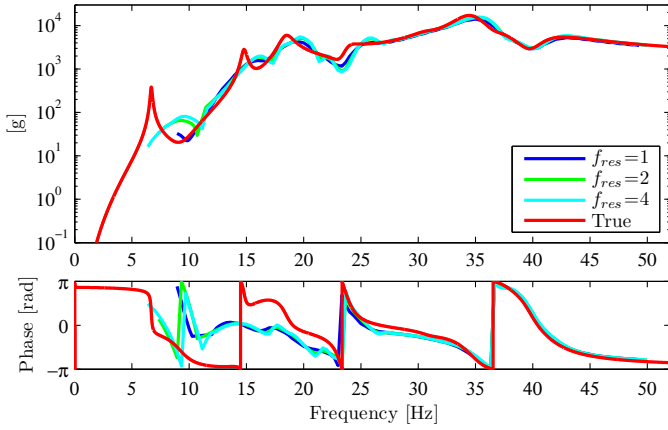


Figure 6.16: 10s runup: Influence of input parameters for FS order.

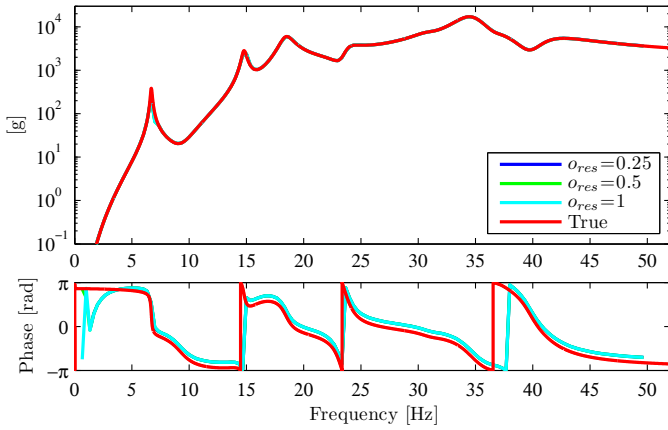


Figure 6.17: 1000s runup: Influence of input parameters for OT order.

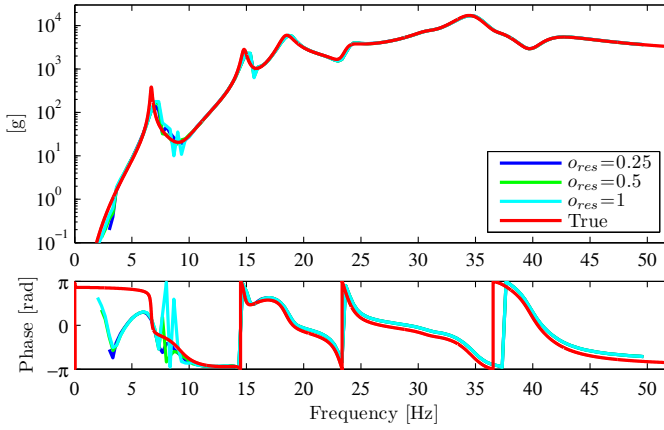


Figure 6.18: 100s runup: Influence of input parameters for OT order.

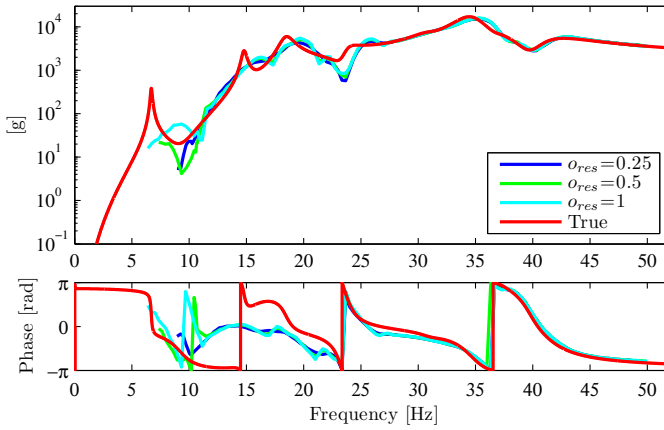


Figure 6.19: 10s runup: Influence of input parameters for OT order.

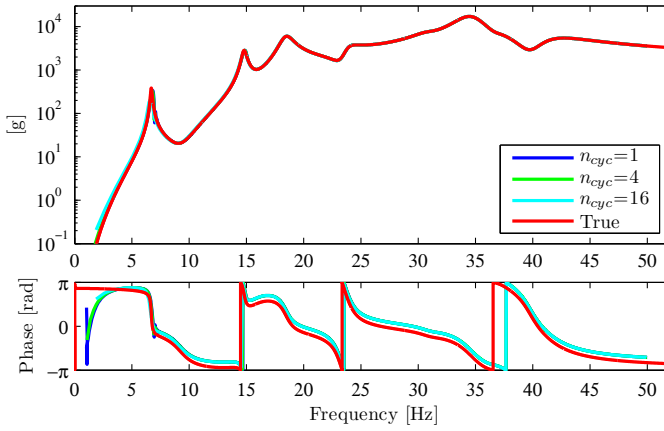


Figure 6.20: 1000s runup: Influence of input parameters for AD order.

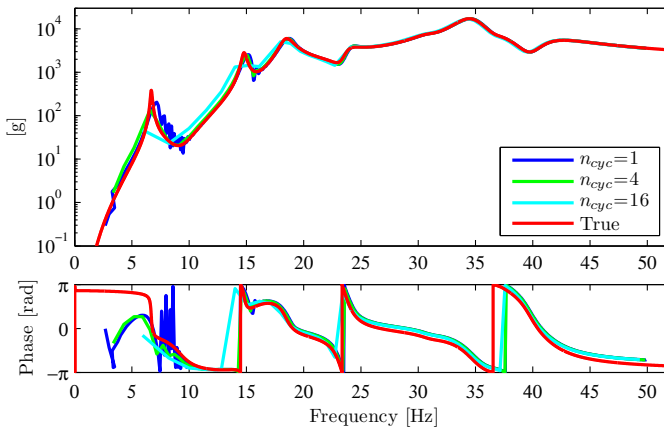


Figure 6.21: 100s runup: Influence of input parameters for AD order.

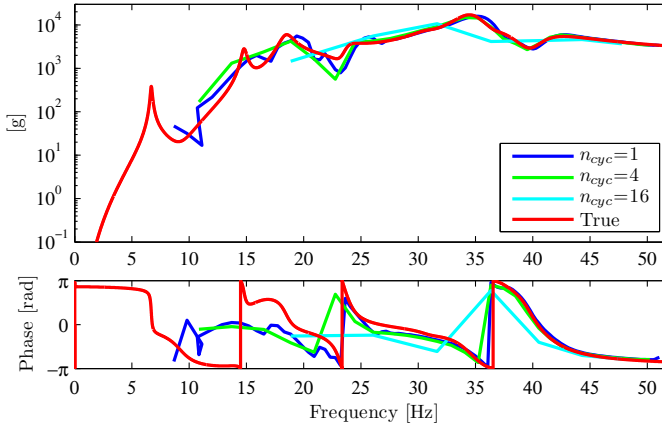


Figure 6.22: 10s runup: Influence of input parameters for AD order.

number of cycles we will get only few samples along the entire measurement.

### Operational Polymax step

After having analyzed the performances of each of the implemented order tracking techniques, the next natural step in the framework of the OBMA method is the combination of these techniques with Operational Polymax. The final objective is to get the best possible modal parameters estimation. The parameters listed in Table 6.5 are the ones considered in this Section as baseline for each of the presented techniques. Figure 6.23, Figure 6.24 and Figure 6.25 show the stabilization diagrams for the long run-up (1000s) by using the 5 order tracking techniques.

In this very long and slow runup, there are no differences among the order tracking techniques. All of them are able to extract the exact order and Operational Polymax estimates the modal parameters (natural frequencies, damping ratios and mode shapes) which are very close to the numerical ones, as it is shown in Table 6.6 and 6.7 for the natural frequencies and the damping ratios respectively. A very good match has been found for all the modes in terms of natural frequencies. For what concerns the damping ratios, there are some errors mainly at low frequencies where it becomes a bit more complicated to describe the peak related to the first mode.

The results shown in Table 6.8 and Table 6.10 are related to the natural frequency identification in case of faster run-ups (100s and 10s). On the other



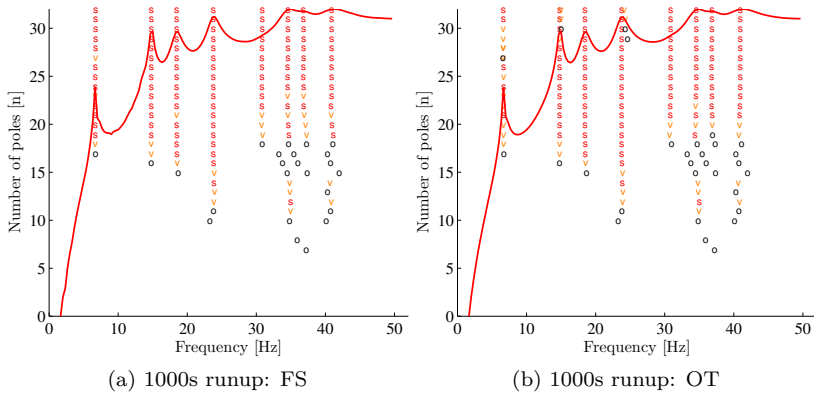


Figure 6.23: Stabilization diagrams for different order tracking techniques

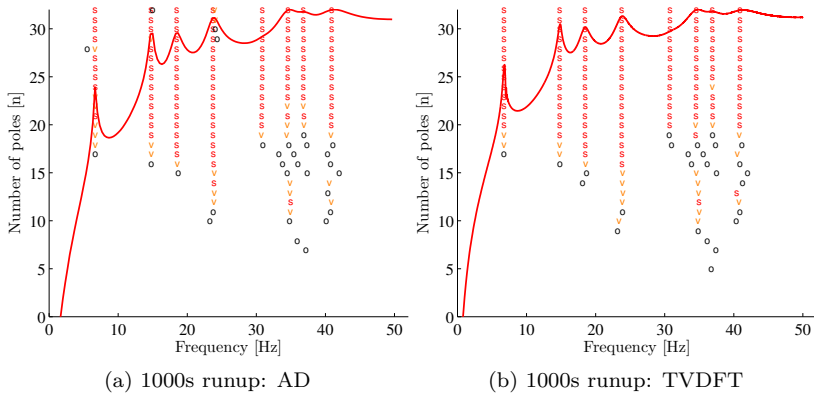
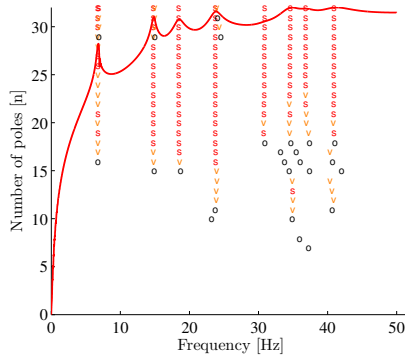


Figure 6.24: Stabilization diagrams for different order tracking techniques

hand, Table 6.9 and Table 6.11 show the damping ratios identified in case of faster run-ups (100s and 10s). In case of very fast run-up it is much more complicated to identify correctly the modal parameters. It can be noticed that most techniques (FS, OT, AD) fails in identifying the first mode, while TVDFT and VK methods allow to identify it, but the damping ratio is much higher in both cases. Basically, in order to allow the identification of the first mode, a large bandwidth  $bw$  for the VK technique and the minimum  $n_{rev}$  had to be considered. This translates into a mode with a higher damping ratios because its peak get larger and spread among several frequency lines.



(a) 1000s runup: VK

Figure 6.25: Stabilization diagrams for different order tracking techniques

Numerical [Hz]	FS [Hz]	OT [Hz]	AD [Hz]	TVDFFT [Hz]	VK [Hz]
6.69	6.75	6.68	6.68	6.77	6.72
14.78	14.80	14.79	14.79	14.81	14.79
18.45	18.47	18.47	18.46	18.49	18.46
23.76	23.78	23.77	23.76	23.78	23.76
30.88	30.87	30.89	30.88	30.78	30.89
34.62	34.60	34.62	34.61	34.60	34.62
36.84	36.84	36.84	36.84	36.93	36.85
40.95	40.92	40.95	40.94	40.91	40.95

Table 6.6: OBMA - Natural frequencies identification - 1000s

The performances of all techniques when combined with Operational Polymax can be evaluated by means of the stabilization diagrams. Figure 6.26, Figure 6.27 and Figure 6.28 show these curves for the different techniques and for the 100s runup. Also in this case it is quite difficult to appreciate differences among the 5 order tracking techniques employed for identifying the modal parameters. On the other hand, in case of a very fast runup (10s) the techniques have quite some difficulties in identifying the first mode and some more divergences between them can be underlined. For instance, the first mode is identified only by TVDFFT and VK, as already explained previously. Here it becomes more evident the reason of the high damping ratio. It can also be highlighted the reason why FS, OT and AD cannot identify this mode. In fact it is clear that there are not enough samples to characterize the dynamic of the system below

<b>Numerical</b> [%]	<b>FS</b> [%]	<b>OT</b> [%]	<b>AD</b> [%]	<b>TVDFT</b> [%]	<b>VK</b> [%]
1.13	1.65	1.97	1.78	1.28	1.99
1.45	1.45	1.67	1.62	1.45	1.74
3.39	3.48	3.41	3.41	3.30	3.39
3.12	3.11	3.17	3.18	3.09	3.21
3.88	3.83	3.89	3.88	3.30	3.88
4.04	3.96	4.05	4.05	3.56	4.05
3.40	3.29	3.38	3.38	3.05	3.39
5.78	5.82	5.78	5.78	5.75	5.78

Table 6.7: OBMA - Damping identification - 1000s

<b>Numerical</b> [Hz]	<b>FS</b> [Hz]	<b>OT</b> [Hz]	<b>AD</b> [Hz]	<b>TVDFT</b> [Hz]	<b>VK</b> [Hz]
6.69	6.92	6.79	6.33	6.97	7.01
14.78	14.90	14.88	14.79	14.91	14.92
18.45	18.59	18.60	18.51	18.62	18.63
23.76	23.82	23.85	23.78	23.86	23.81
30.88	30.99	30.99	30.94	30.91	30.99
34.62	34.73	34.74	34.70	34.75	34.73
36.84	36.98	36.98	36.95	37.03	36.98
40.95	40.96	41.00	40.95	40.97	41.01

Table 6.8: OBMA - Natural frequencies identification - 100s

10Hz. OT and AD need at least one cycle in order to get the first sample. This is the reason why they are not able to catch it. This is a limitation of all techniques that use the transformation from time to angle domain. VK extracts the time histories of the orders. For this reason the orders extracted by using this technique possess as many samples as the time domain signal. The comparison has been performed by keeping constant the number of poles  $n$  of the system. If this parameter increases, it is possible that a better stabilized pole is identified by TVDFT and VK.

<b>Numerical</b> [%]	<b>FS</b> [%]	<b>OT</b> [%]	<b>AD</b> [%]	<b>TVDFT</b> [%]	<b>VK</b> [%]
1.13	3.12	1.84	3.06	2.95	1.90
1.45	2.05	2.36	2.43	2.43	2.16
3.39	3.57	3.56	3.62	3.37	3.46
3.12	3.09	2.93	3.01	2.96	3.50
3.88	3.83	3.81	3.78	3.39	3.82
4.04	4.00	4.03	3.98	3.77	3.96
3.40	3.30	3.32	3.34	3.20	3.28
5.78	5.73	5.76	5.71	5.69	5.75

Table 6.9: OBMA - Damping identification - 100s

<b>Numerical</b> [Hz]	<b>FS</b> [Hz]	<b>OT</b> [Hz]	<b>AD</b> [Hz]	<b>TVDFT</b> [Hz]	<b>VK</b> [Hz]
6.69	-	-	-	8.20	7.69
14.78	15.72	15.91	15.58	15.99	15.43
18.45	19.73	19.18	19.65	19.47	19.66
23.76	24.51	24.69	24.42	24.76	24.62
30.88	31.83	31.99	31.88	32.15	31.97
34.62	35.33	35.41	35.37	35.37	35.51
36.84	37.69	37.83	37.61	37.90	37.94
40.95	41.73	41.75	41.62	41.86	41.70

Table 6.10: OBMA - Natural frequencies identification - 10s

<b>Numerical</b> [%]	<b>FS</b> [%]	<b>OT</b> [%]	<b>AD</b> [%]	<b>TVDFT</b> [%]	<b>VK</b> [%]
1.13	-	-	-	4.08	8.07
1.45	5.90	5.26	5.72	2.83	5.88
3.39	2.13	2.07	0.50	2.78	3.26
3.12	5.39	4.11	4.35	3.51	3.63
3.88	4.61	2.63	3.48	0.85	3.83
4.04	5.02	4.24	4.56	4.04	4.40
3.40	3.26	2.57	3.10	2.53	2.97
5.78	5.41	5.22	5.06	5.04	5.00

Table 6.11: OBMA - Damping identification - 10s

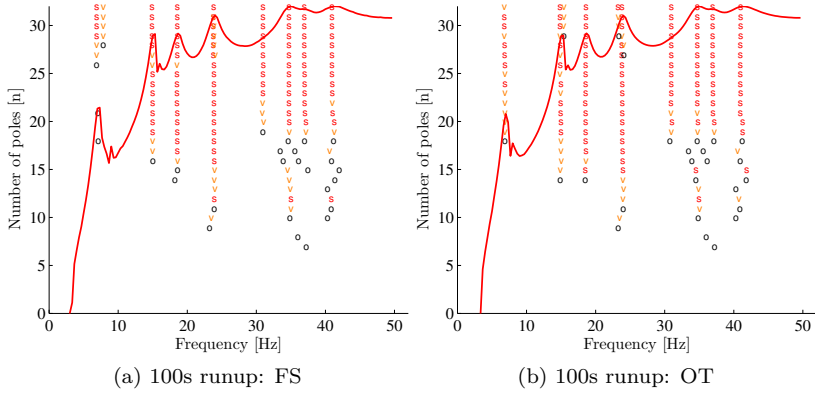


Figure 6.26: Stabilization diagrams for different order tracking techniques

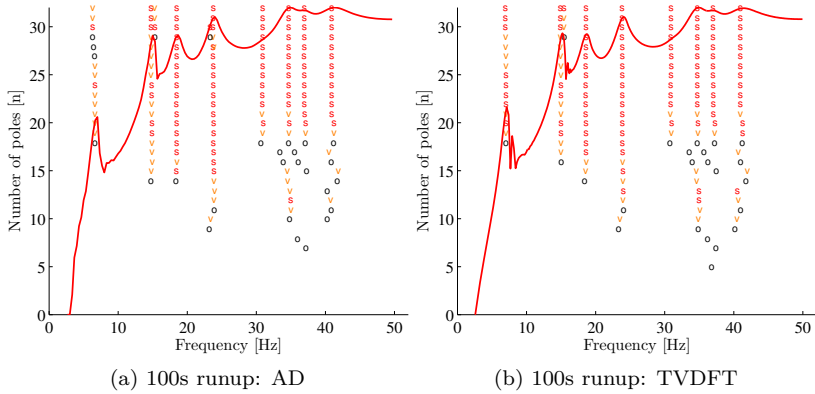
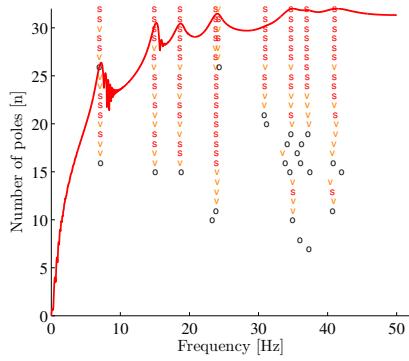


Figure 6.27: Stabilization diagrams for different order tracking techniques



(a) 100s runup: VK

Figure 6.28: Stabilization diagrams for different order tracking techniques

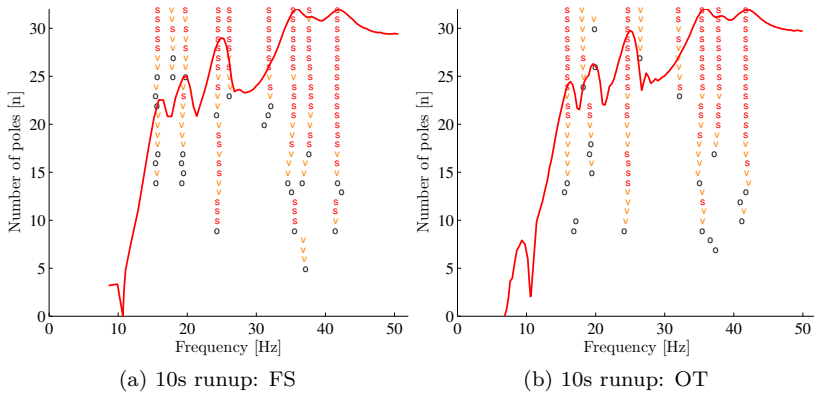


Figure 6.29: Stabilization diagrams for different order tracking techniques

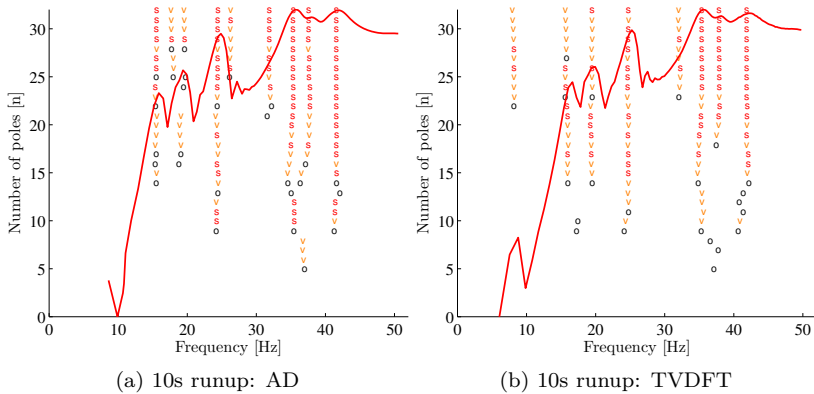
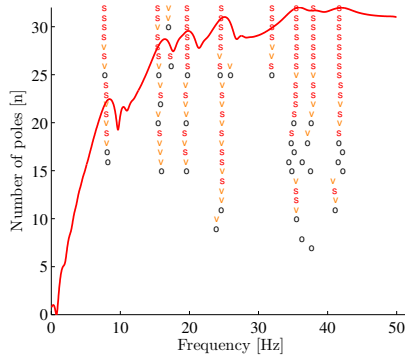


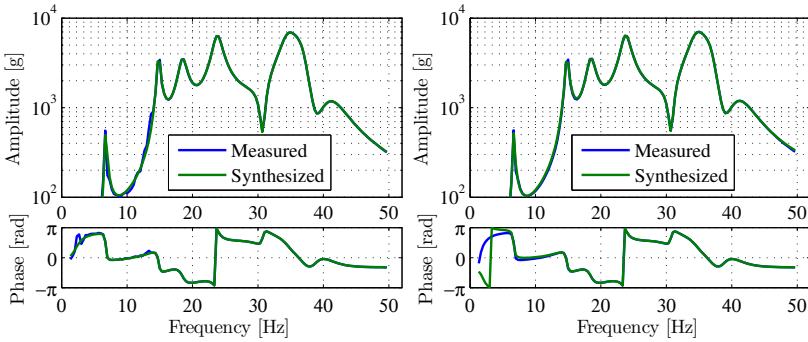
Figure 6.30: Stabilization diagrams for different order tracking techniques

Figure 6.32, Figure 6.33 and Figure 6.34 show that measured and synthesized orders are corresponding with each other for all the techniques in case of a long runup(1000s). It means that the Operational Polymax works very well on good estimates of the orders. In fact, once very good orders have been estimated, the modal parameter identification will allow to correctly estimate the modal parameters of the structure under-test. The same considerations done with regard to the stabilization diagrams can also be drawn for the synthesis curves. Figure 6.35, Figure 6.36 and Figure 6.37 show the same synthesized curves but for a 100s runup and finally Figure 6.38, Figure 6.39 and Figure 6.40 show the



(a) 10s runup: VK

Figure 6.31: Stabilization diagrams for different order tracking techniques



(a) 1000s runup: FS

(b) 1000s runup: OT

Figure 6.32: Synthesized vs measured models for different order tracking techniques

challenging case of a 10s runup. The quality of the synthesis is always acceptable even for the fast runup, but of course its quality decreases by accelerating the runup.



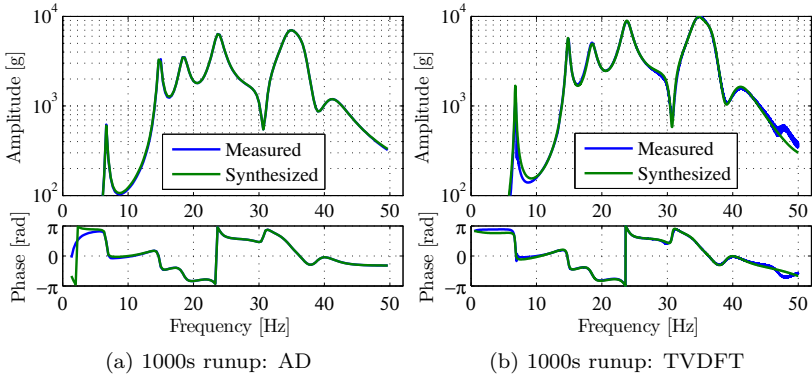


Figure 6.33: Synthesized vs measured models for different order tracking techniques

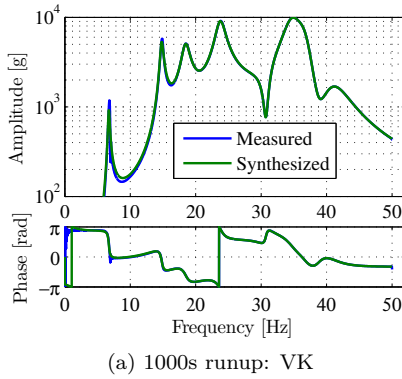


Figure 6.34: Synthesized vs measured models for different order tracking techniques

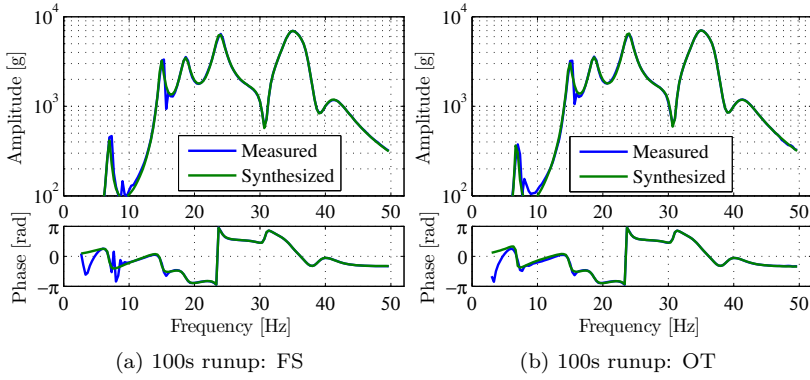


Figure 6.35: Synthesized vs measured models for different order tracking techniques

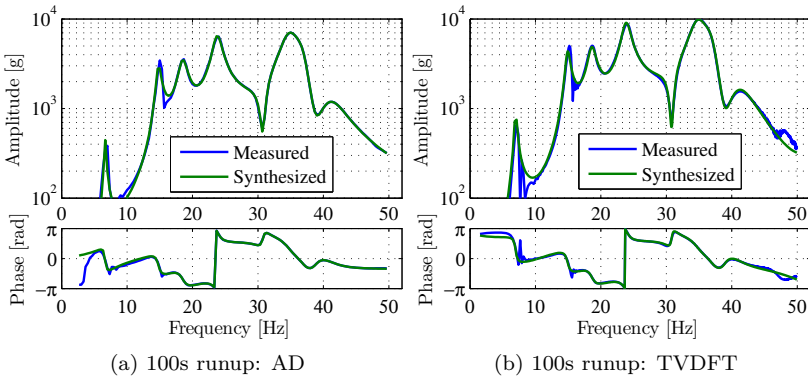
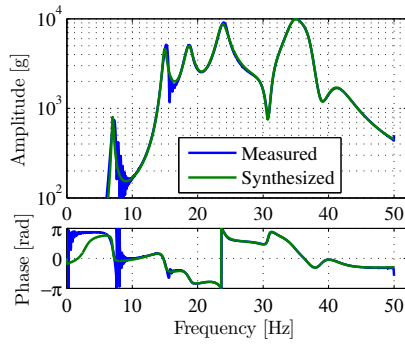
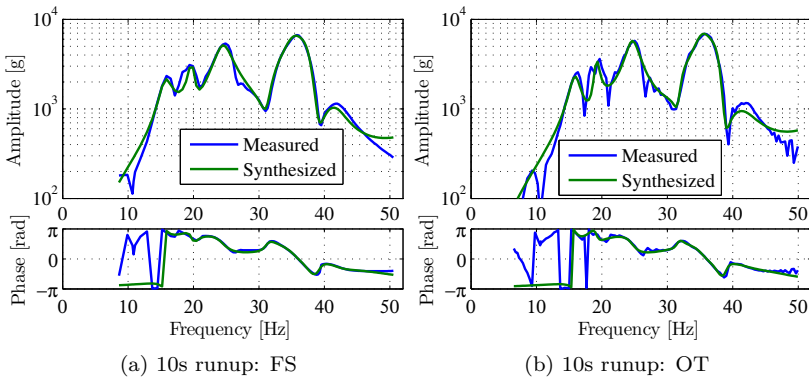


Figure 6.36: Synthesized vs measured models for different order tracking techniques



(a) 100s runup: VK

Figure 6.37: Synthesized vs measured models for different order tracking techniques



(a) 10s runup: FS

(b) 10s runup: OT

Figure 6.38: Synthesized vs measured models for different order tracking techniques

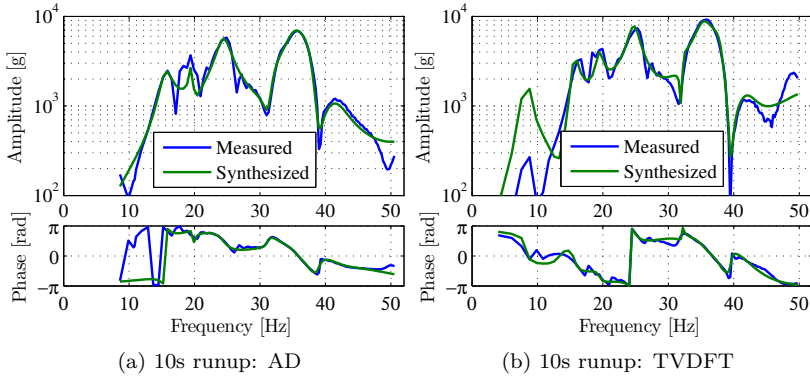


Figure 6.39: Synthesized vs measured models for different order tracking techniques

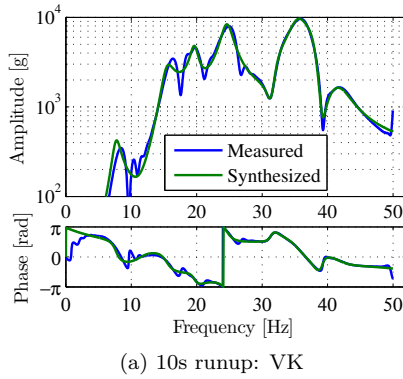


Figure 6.40: Synthesized vs measured models for different order tracking techniques

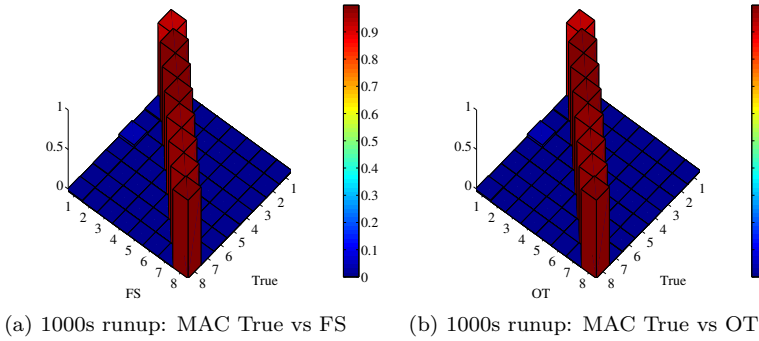
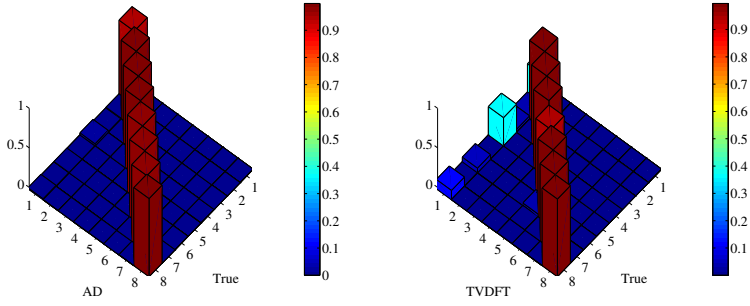


Figure 6.41: MAC diagram comparison between different order tracking techniques

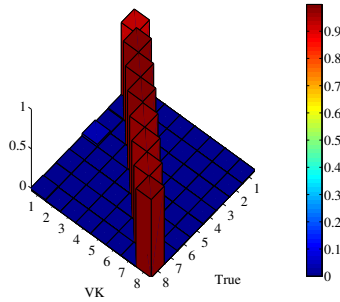
Figure 6.41, Figure 6.42 and Figure 6.43 illustrate the comparison in terms of Modal Assurance Criterion (MAC) between the mode shapes obtained by using OBMA technique (and the 5 order tracking techniques) for the 1000s case and the true mode shapes extracted from the numerical model. The modes agree quite well with each other and this can be highlighted by almost perfectly diagonal matrices. The same comparison is shown for the 100s and 10s in Figure 6.44, Figure 6.45, Figure 6.46, Figure 6.47, Figure 6.48 and Figure 6.49. Also for what concerns the mode shapes, it is evident that problems arise in case of a fast runup even at higher frequencies. Regardless of the fact that Operational Polymax is able to identify the modes, their shapes are not perfectly overlapping with the numerical ones.

The sweep rate is the main issue for most of the techniques. If we increase the rotational speed in a very fast manner, not all the natural frequencies are excited enough for being identified by a modal parameter estimation technique. Moreover the resolution of the orders become another issue. In fact, it can be that the resolution is very coarse especially at lower frequencies both in terms of amplitude and phase. This is a problem for all the modal identification techniques which are not able to fit any modal model to the measured system.



(a) 1000s runup: MAC True vs AD    (b) 1000s runup: MAC True vs TVDFT

Figure 6.42: MAC diagram comparison between different order tracking techniques



(a) 1000s runup: MAC True vs VK

Figure 6.43: MAC diagram comparison between different order tracking techniques

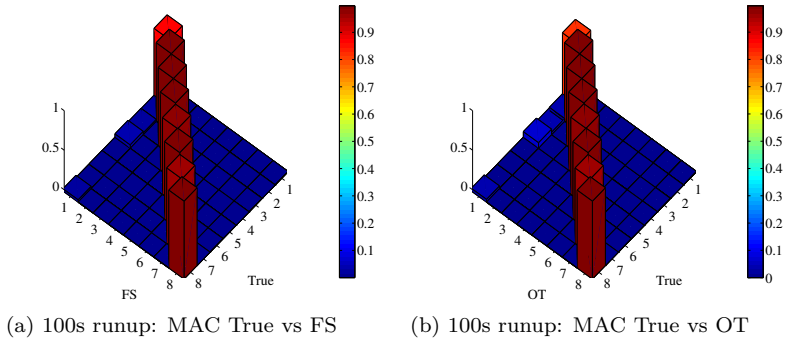


Figure 6.44: MAC diagram comparison between different order tracking techniques

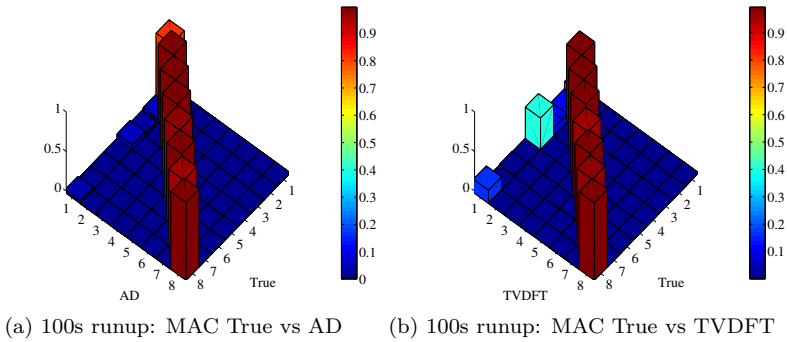
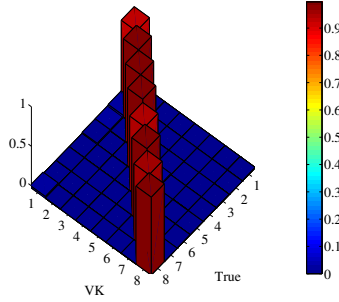
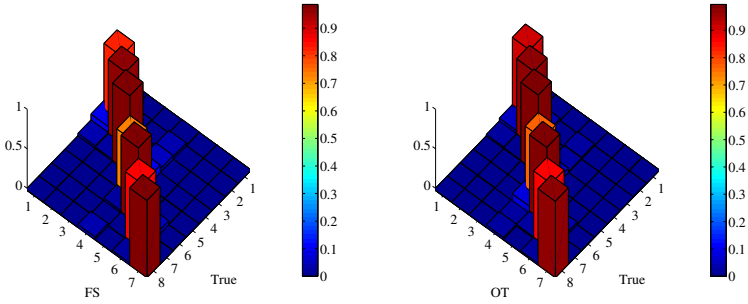


Figure 6.45: MAC diagram comparison between different order tracking techniques



(a) 100s runup: MAC True vs VK

Figure 6.46: MAC diagram comparison between different order tracking techniques

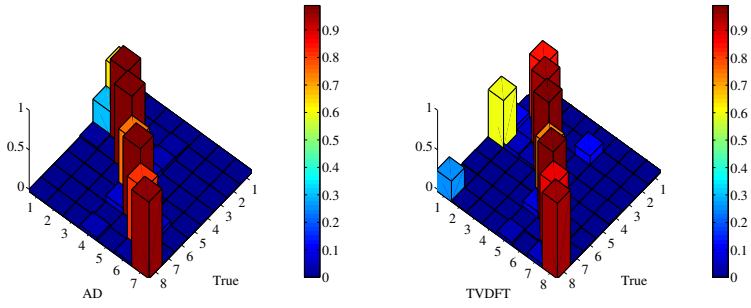


(a) 10s runup: MAC True vs FS

(b) 10s runup: MAC True vs OT

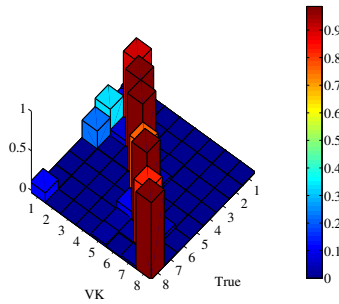
Figure 6.47: MAC diagram comparison between different order tracking techniques





(a) 10s runup: MAC True vs AD      (b) 10s runup: MAC True vs TVDFT

Figure 6.48: MAC diagram comparison between different order tracking techniques



(a) 10s runup: MAC True vs VK

Figure 6.49: MAC diagram comparison between different order tracking techniques

## 6.2 Industrial gear test-rig

After having validated the OBMA technique by considering a numerical example, a dedicated test rig has been used for performing an experimental validation. It has also been used for evaluating the performances of the order tracking techniques available in commercial software and of the ones implemented in a Matlab environment. The test rig has been built for simulating different working conditions for the gears at a subsystem level without any other influence coming from the interaction with other systems. A very precise and highly instrumented device is needed in order to get reliable results [87], [88]. Only a few precision gear test rig have been used for research so far.

### 6.2.1 Test-rig description

Figure 6.50 shows the CAD model of the test rig and Figure 6.51 shows its picture. It is composed by two main parts: the test side, which is dedicated to testing a cylindrical gear pair, and the reaction side, that is needed for retaining a torque preload in the system by means of a second gear pair. Its specifications are reported in Table 6.12.

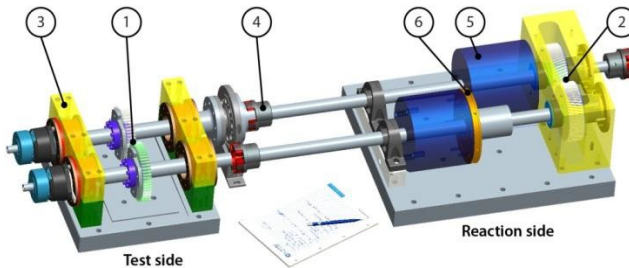


Figure 6.50: Test rig three-dimensional representation. 1. Test gears; 2. Reaction Gears; 3. Bearings support plates; 4. Flexible couplings; 5. Flywheel; 6. Clutch flange for preload.

The test rig is mounted on a concrete base suspended on air springs which allows to isolate the overall system and separate the two sides for avoiding the propagation of stray vibrations between them. Such vibrations are damped through the concrete. A temperature-controlled pressurized lubrication system feeds oil to the test and the reaction side bearings and gears. High-precision spherical roller bearings are chosen to support test gears and maximize stiffness. Several different gears are used for the test side and they provide a very repeatable meshing excitation due to two main reasons: the gear ratio is equal



Figure 6.51: Test rig picture.

Parameter	Range	Uncertainty
Speed	0 to 4500 rpm (0 to 75 Hz)	Measured
Torque	0 to 500 Nm	0.05 %
Angular misalignments	0 to 2 mrad	0.1 mrad
Parallel misalignments	0 to 0.3 mm	0.020 mm

Table 6.12: Test rig specifications

to 1 and gears are precision ground to ISO 1328 Quality 3 standard. Furthermore, test gears and reaction gears are designed to have a different number of teeth to be able to distinguish the excitation belonging to each gear pair. Test gears have 57 teeth, while reaction gears have 64. Angular misalignment in an arbitrary plane and parallel misalignment in the transverse plane can be imposed thanks to the bearings: they are mounted in eccentric caps that can be turned to orient the eccentricity at a given angle. Same angles for the two caps on the same shaft result in imposing a parallel misalignment, while opposite angles result in imposing angular misalignment.

## 6.2.2 Experimental Modal Analysis

In order to characterize the dynamic behavior of the entire test rig, an Experimental Modal Analysis (EMA) campaign was carried out. Several three-axial accelerometers were placed on the structure and the signals were acquired by using the LMS SCADAS acquisition system in a master-slave configuration

(Figure 6.52). This means that two acquisition systems were connected to each other in order to increase the number of channel that could be measured simultaneously. The source of excitation was an electro-dynamic shaker. It was acting along the line of action on the clamping point of one of the two gears, as shown in Figure 6.53. The choice of this direction is not casual, but it is justified by the fact that it is the same direction of the gear contact force which is the main source of excitation for gear pairs. A chirp signal from  $20Hz$  to  $8kHz$  with  $5N$  amplitude and a duration of 1 minute was chosen to excite the structure.



Figure 6.52: SCADAS measurement system.

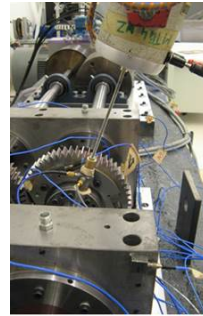


Figure 6.53: Shaker installation.

The accelerometers were placed according to the need of having a high spatial resolution in order to get the mode shapes of the structure especially at high frequencies. On the other hand, the complexity of a measurement with a lot of sensors and their availability limits the number of sensors used during the measurements. Several runs have been performed by shifting the location of most of the accelerometers and leaving the reference ones in the same place as phase references. Figure 6.54 shows the accelerometers locations along the test rig. In order to check if the measurements were comparable among different runs, the Frequency Response Functions (FRFs) coming from the same accelerometer and the same measurement point, but from different runs, have been superimposed and shown in Figure 6.55. The curves are almost perfectly overlapped showing that the system response was not affected by the fact that most of the accelerometers were moved from a location to another one. Afterwards, EMA has been performed considering all the measured channels together. Polymax algorithm has been used for estimating the modal model of the whole structure in standing still conditions. The frequencies and damping ratios are shown in Table 6.13, while Figure 6.56 shows the comparison between a measured FRF and the correspondent synthesized one. An example of a mode shape involving the whole structure is finally shown in Figure 6.57.

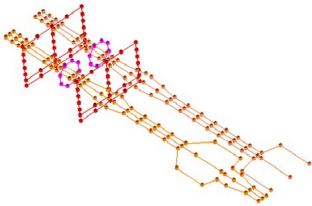


Figure 6.54: Accelerometers locations along the test rig.

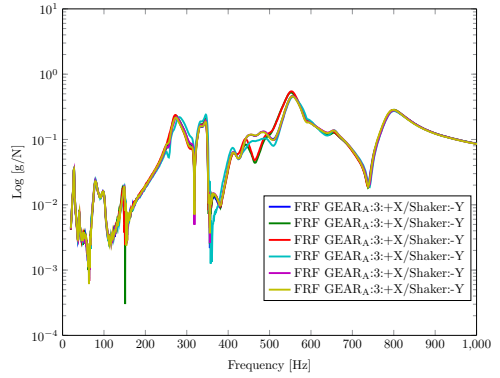


Figure 6.55: Frequency Response Function (FRF): test repeatability and consistency.

no.	Natural frequency [Hz]	Damping ratio [%]	no.	Natural frequency [Hz]	Damping ratio [%]
1	253.9	1.55	11	650.4	2.07
2	274.7	2.40	12	792.9	3.03
3	300.2	2.64	13	1191.8	0.17
4	329.2	2.11	14	1467.1	1.35
5	346.7	0.55	15	1637.7	1.22
6	409.1	2.39	16	1795.8	3.25
7	432.9	2.42	17	2135.5	2.25
8	449.1	2.47	18	2360.1	0.72
9	488.7	3.79	19	2746.7	0.26
10	557.8	2.86			

Table 6.13: EMA - Modal parameters identification

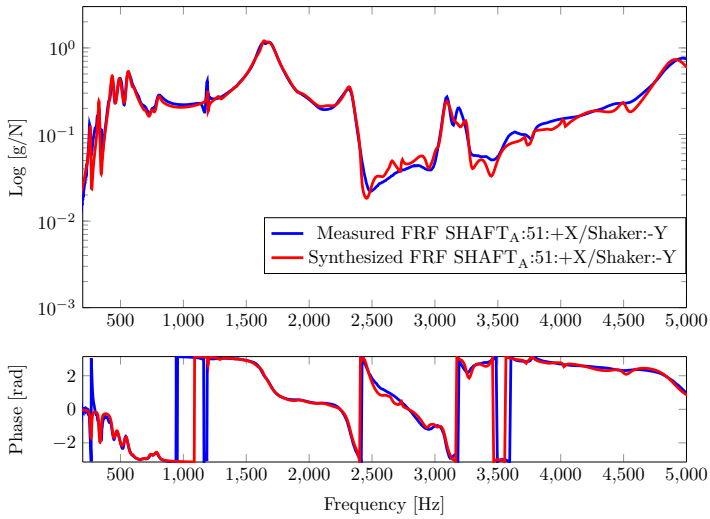


Figure 6.56: Measured FRF vs. Synthesized FRF

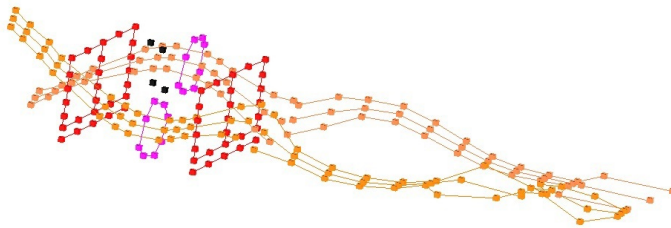


Figure 6.57: Mode shape example

### 6.2.3 Analysis in operating conditions

The EMA modeset has been considered in the following analysis as a reference dataset for a comparison of the natural frequencies, damping ratios and mode shapes identified by Order-Based Modal Analysis [13]. Operational Polymax will be applied to the orders extracted by using 5 different order tracking techniques. The entire procedure could be divided into two main parts. The first step is the orders extraction. It is a key step for OBMA since the quality of the orders will have a significant impact on the modal parameter estimation. The phase of the orders, as discussed previously, has also a very high importance. In fact, the mode shapes will be influenced by the choice of the phase. Normally a phase reference which is related to the instantaneous rotational speed has been considered as the best possible option. A measurement campaign has been carried out using the gear test-rig. Its main scope was the validation of the OBMA technique together with the algorithm for rotating accelerometers. For this reason, the test-rig was instrumented using 35 accelerometers of which 22 were placed on the plates housing the bearings. The gears were instrumented with 3 tri-axial accelerometers each. Finally, 7 more accelerometers were placed on the reaction side. The entire test geometry is illustrated in Figure 6.58. The analysis consists in two different parts. The first step consists in the validation of the OBMA procedure. For this reason, only the fixed accelerometers will be considered. The rotating ones will be considered in a second phase for validating the approach developed in Chapter 6.

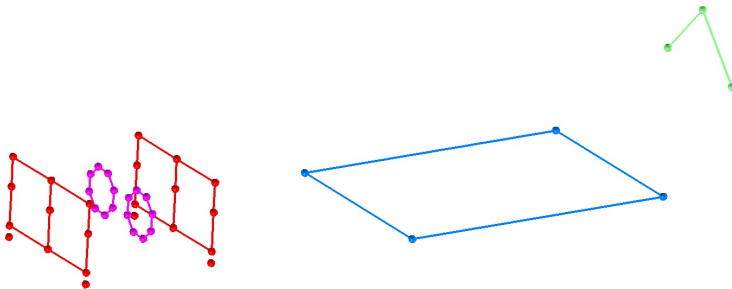


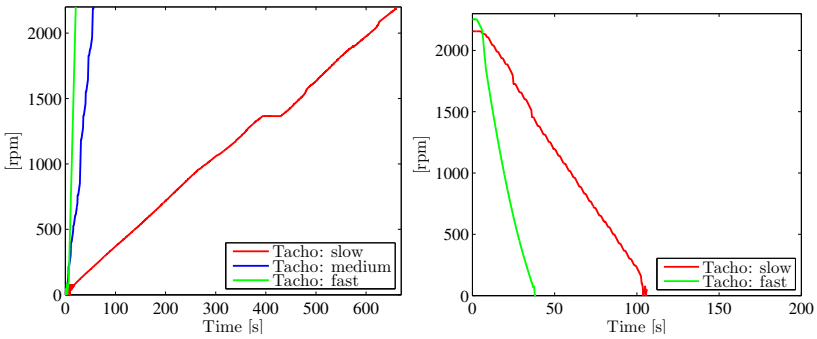
Figure 6.58: Test rig measurement points.

During the measurement campaign, several configurations in terms of applied torque and run-up/run-down sweep rates have been performed. Next Sections will show the results obtained by applying OBMA technique and varying torque and sweep rates and directions. Especially the sweep rate, as underlined in the previous Sections, is a key parameter. In fact most of the Order Tracking

techniques have difficulties in extracting the orders if the run-up/run-down speed goes too fast through the resonances. The effect of the torque load variation will also be discussed in details.

**Order-Based Modal Analysis: changes of sweep rates**

First of all, let us consider the different sweep rates. Figure 6.59 shows the tachometer signals acquired by using a high quality and very accurate encoder (5000 pulses per revolution). Three different run-up cases are shown. In all cases the speed increases from 0rpm to 2200rpm and they can be identified as: fast run-up (20s), medium run-up (60s) and slow run-up (660s). Also two different run-down conditions are shown in Figure 6.59: a slow (110s) and a fast (40s) ones.



(a) Different run-up configurations (slow, medium and fast). (b) Different run-down configurations (slow and fast).

Figure 6.59: Run-up and run-down cases

The colormaps (Frequency vs Time) in Figure 6.60 and Figure 6.61 have been obtained from four different datasets (two run-up and two run-down cases). From these curves, the most excited orders which are related with the gear mesh frequencies can be extracted. The curves have been plotted in the frequency domain where the orders are clearly identifying a run-up or a run-down, whereas the resonances can be seen as vertical lines at a fixed frequency along the entire measurement time. On the other hand, in the order domain, the orders are vertical lines and the resonances can be seen as lines describing hyperbolas. It can be noticed that several resonances are crossed and they can be evidenced on the extracted orders. Since the gears have both 57 teeth, then the orders 57, 114 and their multiples are the ones excited by the rotation of the gears.



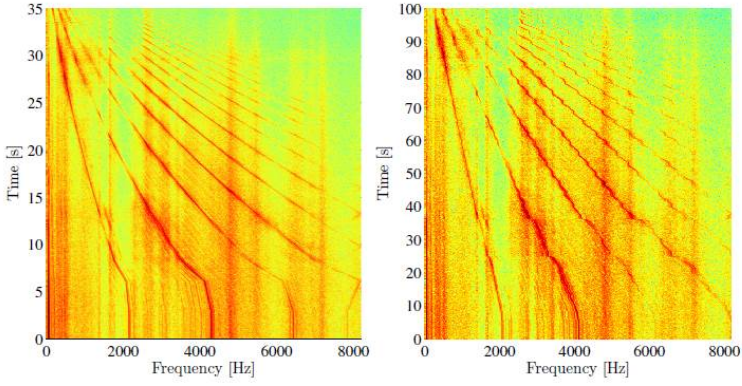


Figure 6.60: Rundown colormap plot (left: fast; right: slow).

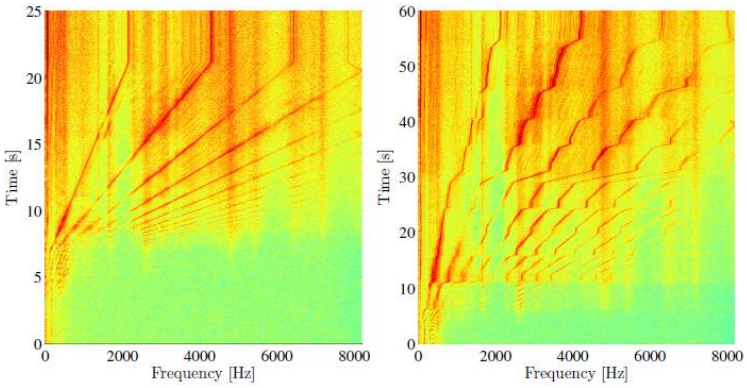


Figure 6.61: Runup colormap plot (left: fast; right: medium).

After having identified the most excited orders, the next natural step consists in their extraction by means of the order tracking techniques used also for the 2D model case. Their comparison in a more challenging experimental environment can bring some more insights into the OBMA technique and its requirements for being successfully applied.

**Order-Based Modal Analysis: Order Tracking step**

As first step, in order to validate the procedure in an experimental environment, the rotating accelerometers and the reaction side ones will not be taken into account. As discussed previously, it is very important for some of the order tracking techniques to choose a proper reference channel. If no reference channel is chosen when calculating the orders by using FS and OT techniques, then their phase will look random whereas the estimation of the amplitude will not be affected at all. As well as for the 2D model, also in this case a parameter sensitivity analysis has been performed and the parameters reported in Table 6.14 have been chosen for all the cases. The measurements taken into account in the following discussion are two different runups (medium and fast) and two different rundowns (slow and fast). The advantage of using a very long and slow run-up is close to zero since the medium run-up is giving very similar results.

<b>FS</b>	$f_{res}$	4Hz
<b>OT</b>	$o_{res}$	0.25
	$o_{max}$	128
<b>AD</b>	$n_{cyc}$	4
<b>TVDFT</b>	$n_{rev}$	4
<b>VK</b>	$bw$	3Hz

Table 6.14: Order Tracking step: selection of the optimal parameters

First of all, the orders extracted by means of the 5 order tracking techniques will be compared with each other. For sake of clarity they will be shown in two different plots for each condition (fast runup and medium runup). Figure 6.62 illustrates the order 57 estimated by using FS, OT and AD. This order spans a frequency band from 100Hz to 2000Hz. Figure 6.63 shows the same order 57 extracted by using TVDFT and VK techniques. Results are quite similar in terms of amplitude among the different order tracking techniques. The phase behavior especially at lower frequencies is not very clear in case of FS and OT where a channel needs to be defined as phase reference for the acquired accelerations . The TVDFT and AD resolution is quite coarse at low frequencies both in terms of amplitude and phase. VK describes the orders in a better way also in the low frequency range.

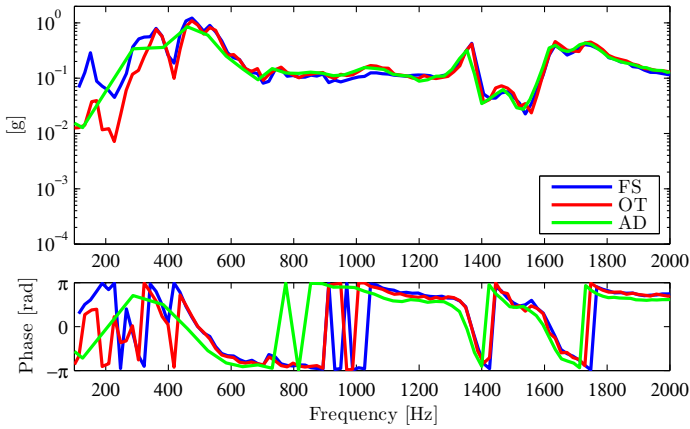


Figure 6.62: FS vs OT vs AD - Fast run-up - Order 57.

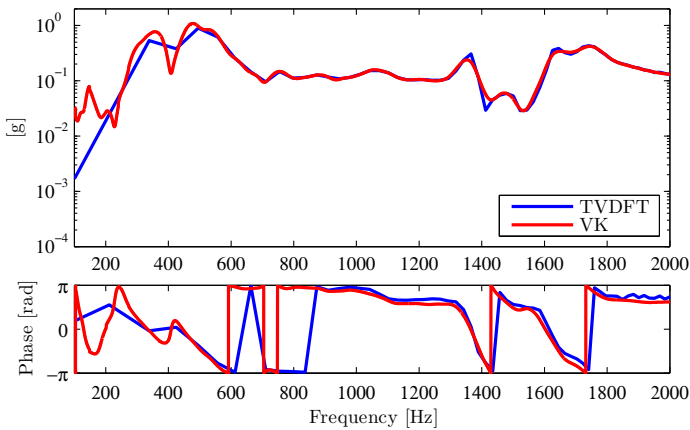


Figure 6.63: TVDFT vs VK - Fast run-up - Order 57.

Orders 114 (second gear mesh frequency) are shown in Figure 6.64 and Figure 6.65 in an analogous manner. They span a larger frequency band from 200Hz to 4000Hz. The same considerations can be drawn also in this case. Anyhow before giving some final conclusions and remarks, it is a good idea to analyze the medium run-up and understand if these limitations keep being present even if the rotational speed is slowly increasing in the same range. For this reason, Figure 6.66, Figure 6.67, Figure 6.68 and Figure 6.69 show the order 57 and 114 extracted for the medium run-up. It is quite clear that at high rotational

speed the curves are very similar to the ones of the fast runup case. On the other hand, at low speed there are much more samples in case of slower runups and this can allow a better modal parameter estimation.

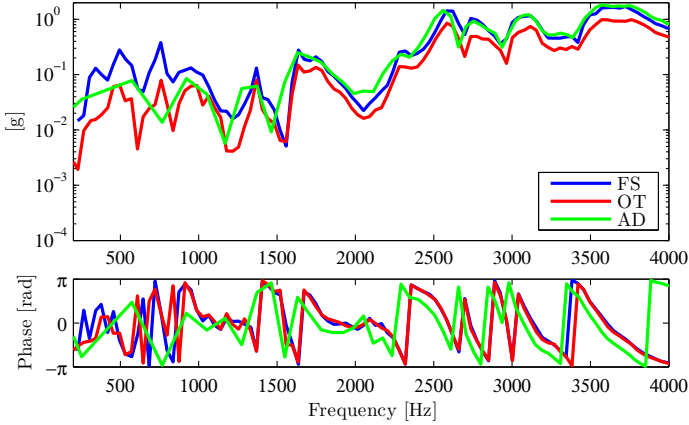


Figure 6.64: FS vs OT vs AD - Fast run-up - Order 114.

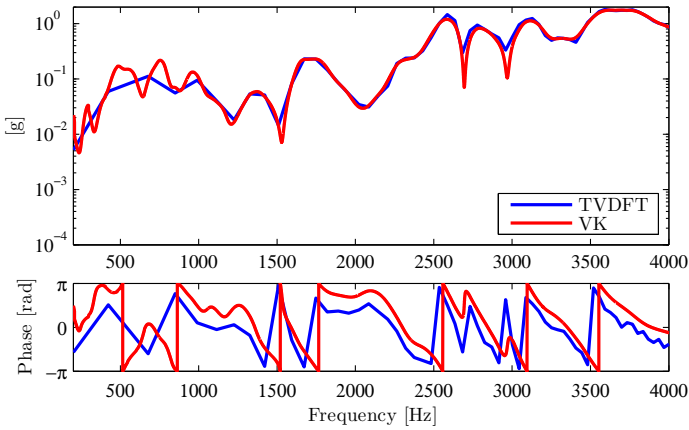


Figure 6.65: TVDFT vs VK - Fast run-up - Order 114.

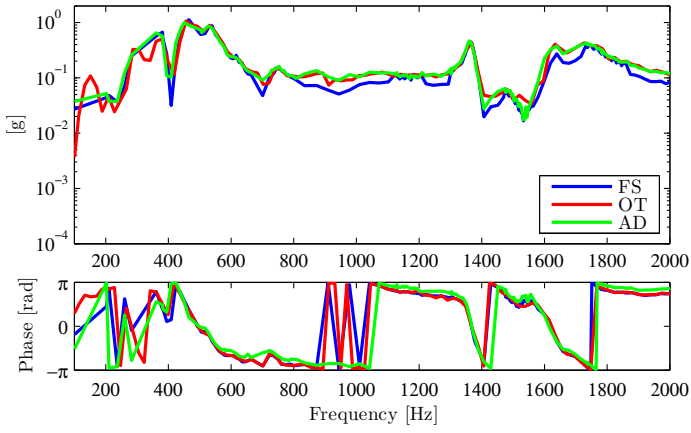


Figure 6.66: FS vs OT vs AD - Medium run-up - Order 57.

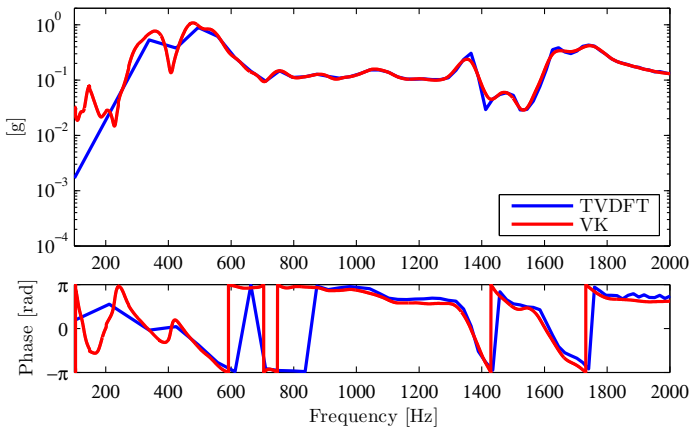


Figure 6.67: TVDFT vs VK - Medium run-up - Order 57.

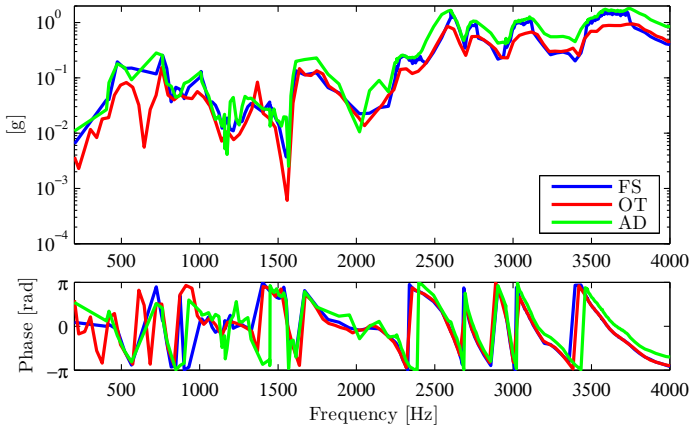


Figure 6.68: FS vs OT vs AD - Medium run-up - Order 114.

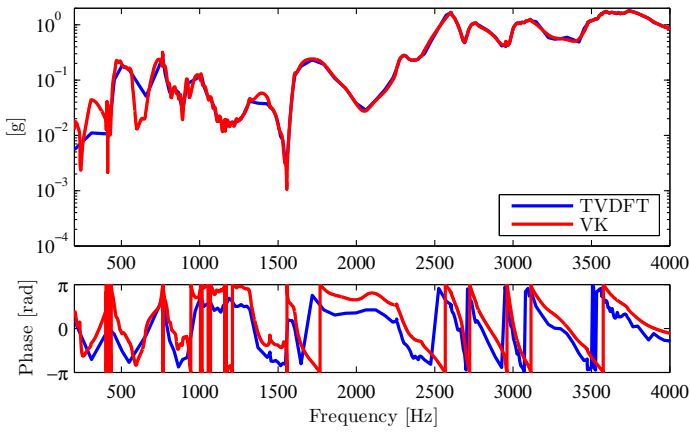


Figure 6.69: TVDFT vs VK - Medium run-up - Order 114.

### Order-Based Modal Analysis: Operational Polymax step

Once the orders have been extracted for all the channels and for different experimental cases, the next step consist of the modal characterization of the dynamic system under study. The two different runup cases have been analyzed by using the 5 order tracking techniques. The stabilization diagrams are shown in Figure 6.70, Figure 6.71 and Figure 6.72 for the fast runup.

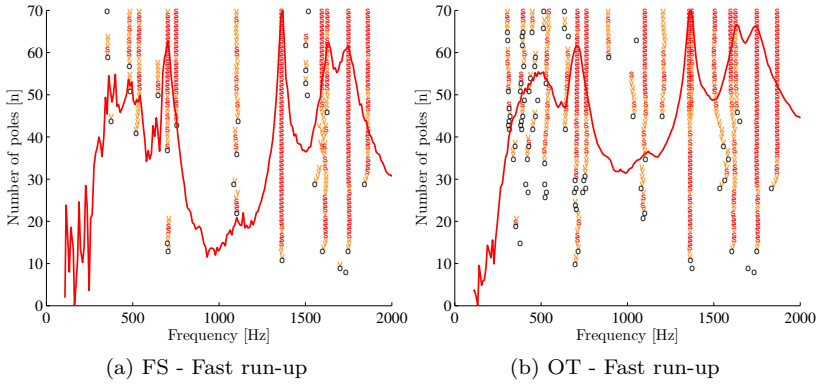


Figure 6.70: Stabilization diagrams for different order tracking techniques

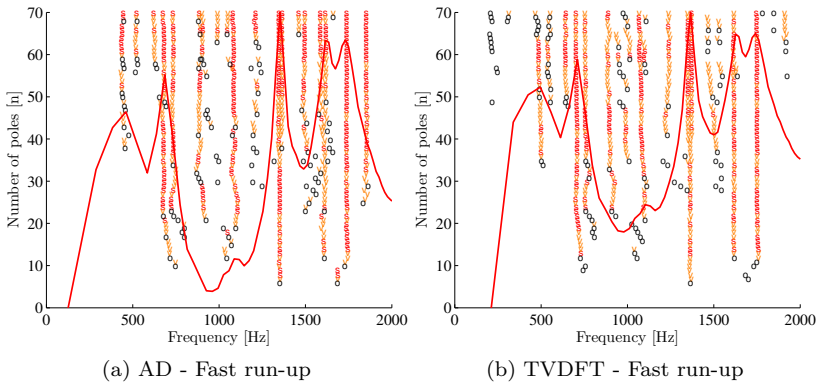
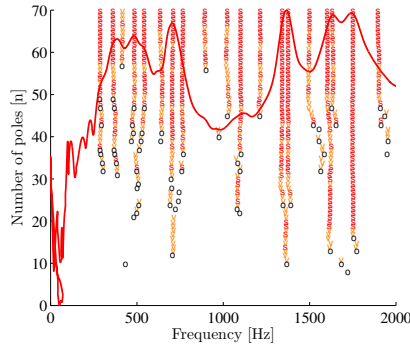


Figure 6.71: Stabilization diagrams for different order tracking techniques

It is quite clear by analyzing these curves that in case of a quite high sweep rate (around 100 rpm/s) all the techniques have difficulties in identifying the correct modal parameters especially at low speed. Except for the VK method,



(a) VK - Fast run-up

Figure 6.72: Stabilization diagrams for different order tracking techniques

all the other techniques need a certain number of revolutions or time samples to calculate a sample in the frequency/order domain. The identified natural frequencies and damping ratios are listed in Table 6.15 and Table 6.16. Some comments can be done regarding to the modal parameter identification. OT, AD and VK allow to identify a higher number of modes. The natural frequencies are quite similar to each other by using the different techniques. A systematic shift toward lower frequencies can be noticed by using AD. This shift is more severe in the first part of the frequency range and it tends to stabilize at low values for the most interesting and dominant modes above 1000 Hz.

The damping ratios are identified with higher uncertainties. For this reason it is difficult to establish the technique which is giving the best results in terms of damping ratios. The influence of the parameters used for the order estimation step for each order tracking technique is also very important. Techniques such as AD, TVDFT and VK tend to have very high damping ratio values for the first modes.

After having identified the modal parameters, it is important to check if the modal model respects the measured one. The synthesized curves for one of the channels are compared to the measured orders. For all techniques a very good match has been found in the second half of the spanned frequency band (from 1000Hz to 2000Hz). Until 1000Hz it is evident from Figure 6.70 and Figure 6.71 that for a fast runup it is difficult to identify the correct amplitude and phase behavior by using FS. OT, AD and TVDFT give results quite comparable with each other. VK is giving the best possible behavior from 300Hz until 2000Hz, which is a quite large frequency band as shown in Figure 6.75.

The tool used for comparing the mode shapes obtained by using different order



<b>FS</b> [Hz]	<b>OT</b> [Hz]	<b>AD</b> [Hz]	<b>TVDFT</b> [Hz]	<b>VK</b> [Hz]
352.8	-	-	-	362.4
486.9	453.7	438.2	486.6	486.7
538.9	535.9	522.2	-	543.8
-	629.1	-	644.5	635.5
704.3	712.7	680.7	701.6	710.6
751.3	764.1	734.9	756.2	766.7
-	890.3	888.3	896.4	892.7
1098.3	1101.6	1085.1	1070.7	1100.7
-	1212.7	-	1241.3	1214.3
-	1357.3	1346.2	1349.4	1341.6
1362.5	1373.9	1365.3	1371.3	1376.4
-	1508.0	1496.8	-	1499.7
1596.0	1597.4	1585.7	-	1602.7
1627.0	1625.5	1616.2	1616.8	1632.0
1749.9	1749.3	1738.3	1746.7	1750.2
1863.5	1867.4	1852.8	-	1888.1

Table 6.15: OBMA - Natural frequencies identification - Fast run-up

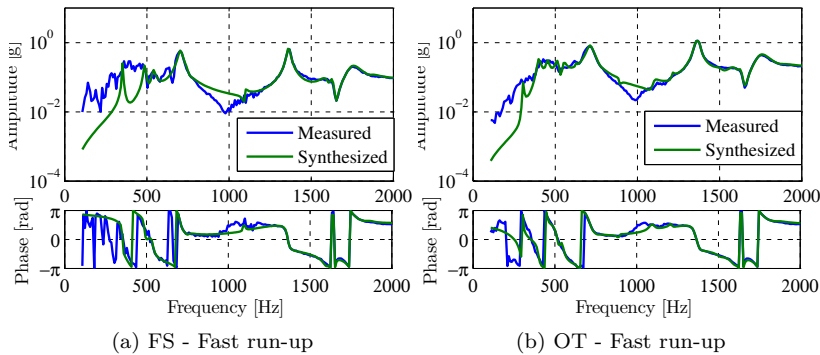


Figure 6.73: Synthesized vs measured models for different order tracking techniques

tracking techniques is the MAC (Figure 6.76, Figure 6.77, Figure 6.78, Figure 6.79). In general an expected diagonal behavior can be highlighted. This means that the modes which are more or less at the same frequencies are similar also

<b>FS</b> [%]	<b>OT</b> [%]	<b>AD</b> [%]	<b>TVDFFT</b> [%]	<b>VK</b> [%]
0.55	-	-	-	5.26
1.21	0.78	6.18	7.17	5.02
1.98	2.64	3.29	-	4.19
-	1.23	-	3.78	1.90
1.88	2.54	3.52	3.87	2.55
1.98	2.90	4.07	2.72	3.03
-	0.55	1.60	1.14	0.76
0.60	1.83	3.92	4.07	3.17
-	0.58	-	1.26	1.71
-	0.96	1.15	1.29	2.15
0.70	0.64	0.87	0.80	1.95
-	1.74	2.33	-	1.42
1.76	2.08	1.93	-	2.48
0.76	0.97	1.18	1.58	1.26
2.42	2.48	2.45	1.92	2.73
1.76	2.71	2.79	-	2.89

Table 6.16: OBMA - Damping identification - Fast run-up

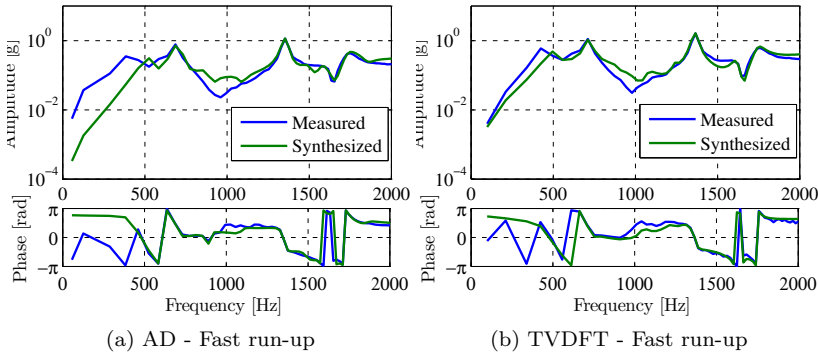
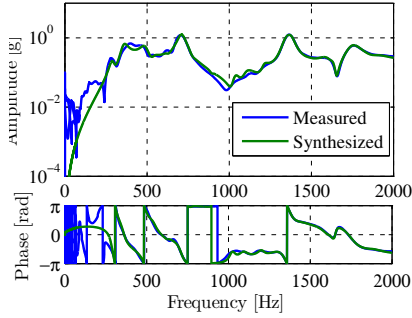


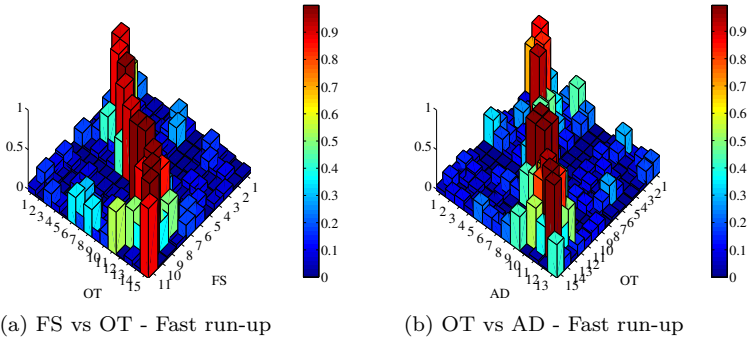
Figure 6.74: Synthesized vs measured models for different order tracking techniques

from a mode shape point of view.



(a) VK - Fast run-up

Figure 6.75: Synthesized vs measured models for different order tracking techniques



(a) FS vs OT - Fast run-up

(b) OT vs AD - Fast run-up

Figure 6.76: MAC diagram comparison between different order tracking techniques

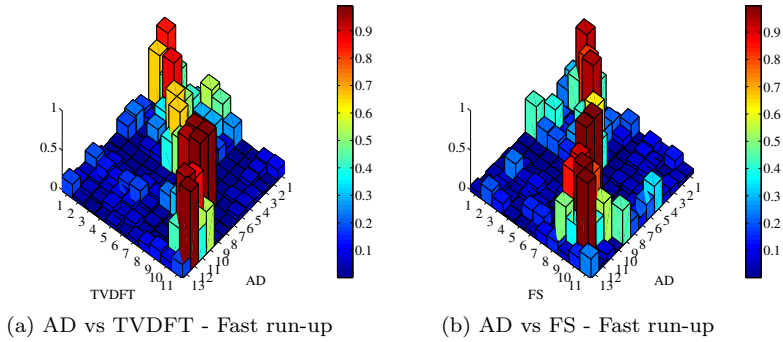


Figure 6.77: MAC diagram comparison between different order tracking techniques

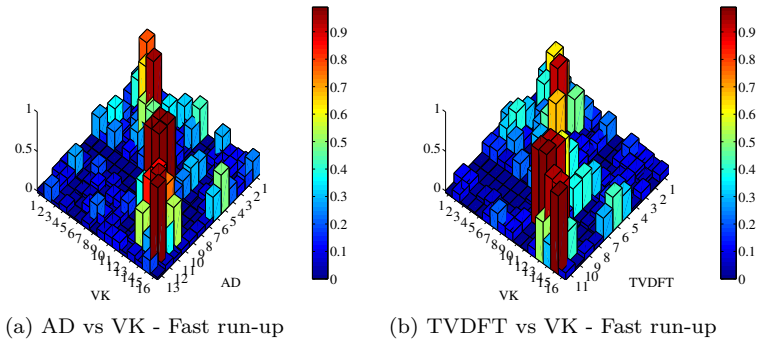


Figure 6.78: MAC diagram comparison between different order tracking techniques

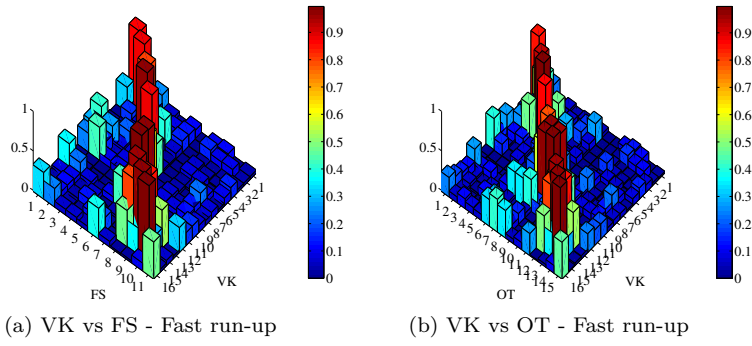


Figure 6.79: MAC diagram comparison between different order tracking techniques

The case analyzed until now is quite challenging because it is a very fast runup (high sweep rate). The next step consists of the analysis of another challenging case. It is a slower runup, but with an irregular sweep rate (the speed of the test rig was increased manually from 0 to 2200 rpm). Being a slower runup, the stabilization diagrams allow to identify the poles of the system with very nice stable columns in all cases. FS, OT, AD and TVDFT curves are highly improved if compared to the fast runup (Figure 6.80 and Figure 6.81). On the other hand VK seems to be very sensitive to the irregular shape of the rpm curve, as shown in Figure 6.82.

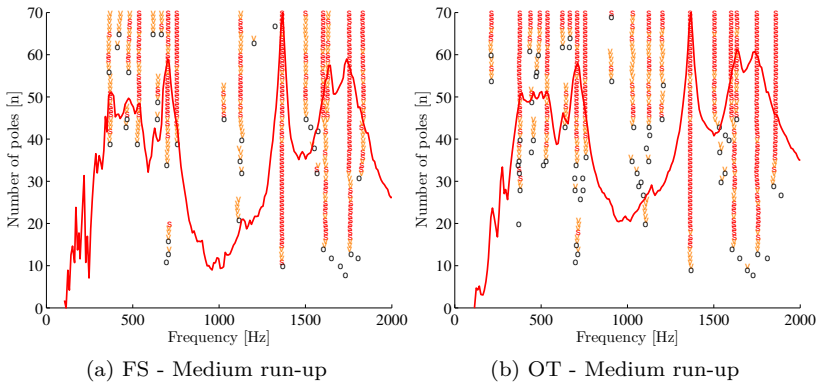


Figure 6.80: Stabilization diagrams for different order tracking techniques

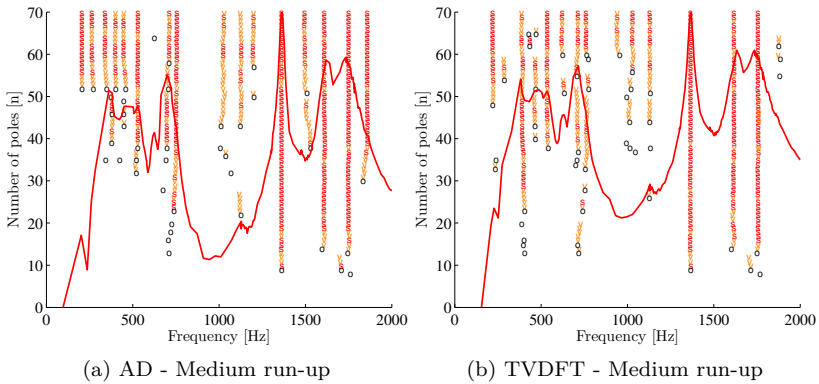
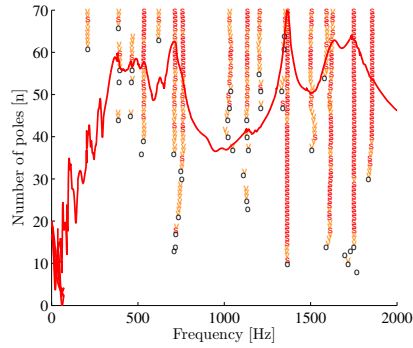


Figure 6.81: Stabilization diagrams for different order tracking techniques



(a) VK - Medium run-up

Figure 6.82: Stabilization diagrams for different order tracking techniques

Table 6.17 and Table 6.18 list the natural frequencies and the damping ratios obtained in the medium runup case. Because of the slow sweep rate, most of the modes are identified by all techniques with less differences both in terms of damping and natural frequencies.

<b>FS</b> [Hz]	<b>OT</b> [Hz]	<b>AD</b> [Hz]	<b>TVDFFT</b> [Hz]	<b>VK</b> [Hz]
366.1	378.9	340.6	389.7	395.1
483.5	493.1	448.3	467.4	467.6
538.2	538.9	530.5	536.8	536.6
-	624.1	-	622.3	622.7
705.2	710.8	711.9	714.5	716.0
755.5	755.9	755.7	760.2	759.9
-	1031.7	1023.5	1030.1	1030.3
1126.1	1124.2	1129.1	1129.7	1134.9
-	1203.7	1201.0	-	1207.6
1365.4	1364.2	1361.8	1365.3	1366.0
1501.8	1504.5	1495.7	-	1514.0
1603.9	1600.8	-	-	1584.5
1632.6	1635.1	1609.9	1616.7	1629.6
1754.3	1749.3	1750.2	1755.1	1748.7
1831.9	1860.9	1858.9	-	1896.5

Table 6.17: OBMA - Natural frequencies identification - Medium run-up

<b>FS</b> [%]	<b>OT</b> [%]	<b>AD</b> [%]	<b>TVDFFT</b> [%]	<b>VK</b> [%]
2.04	4.03	6.18	2.36	0.21
2.58	2.73	1.48	1.33	0.52
3.00	3.12	2.59	2.55	2.45
-	0.99	-	1.02	1.18
1.89	2.32	0.72	1.62	2.45
1.85	1.98	2.08	1.48	2.21
-	0.48	0.42	1.23	1.91
1.12	1.01	0.62	0.44	0.64
-	0.86	0.60	-	0.76
0.58	0.65	0.68	0.46	0.54
0.70	1.65	0.68	-	0.79
2.16	2.45	-	-	1.67
0.52	0.90	1.74	1.44	1.66
2.11	2.19	2.35	1.78	2.56
1.29	2.58	2.32	-	2.45

Table 6.18: OBMA - Damping identification - Medium run-up

The comparison between the synthesized and the measured models are reported in Figure 6.83, Figure 6.84 and Figure 6.85. The curves overlap with each other, which means that the modal models are corresponding to the measured ones.

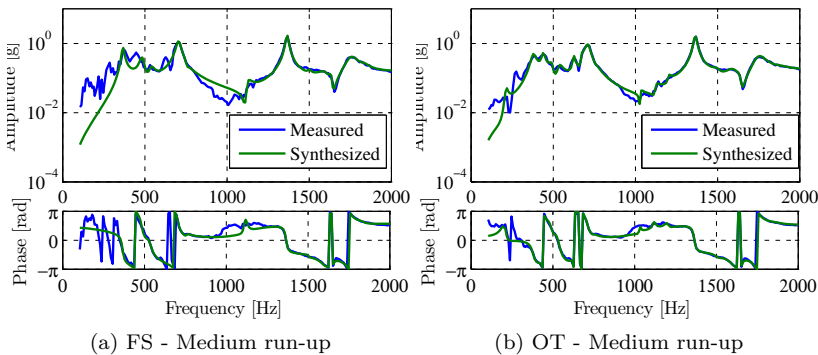


Figure 6.83: Synthesized vs measured models for different order tracking techniques



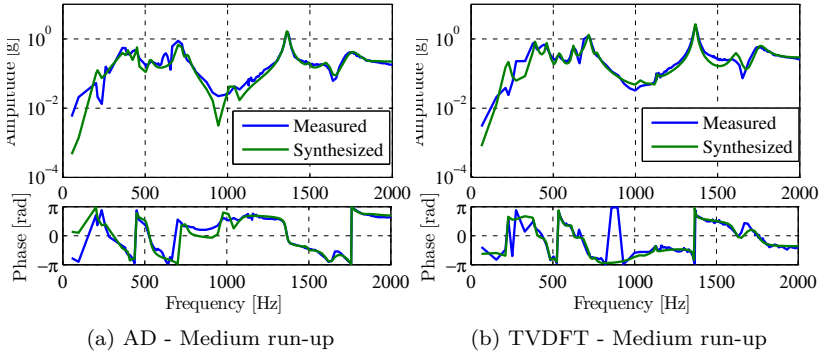


Figure 6.84: Synthesized vs measured models for different order tracking techniques

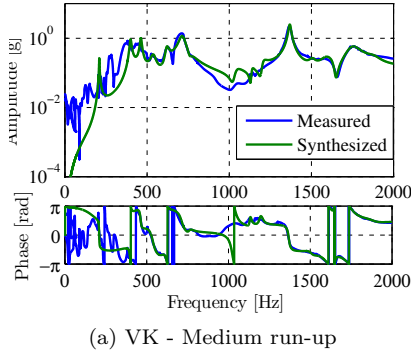
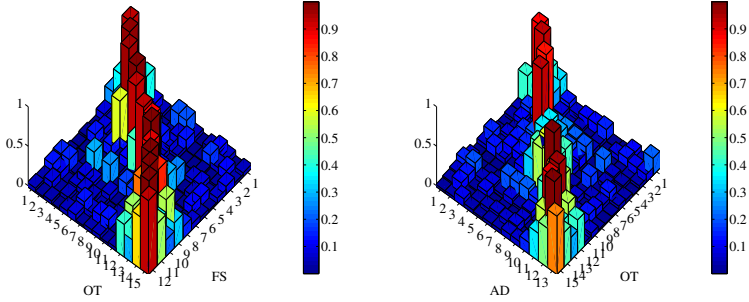


Figure 6.85: Synthesized vs measured models for different order tracking techniques

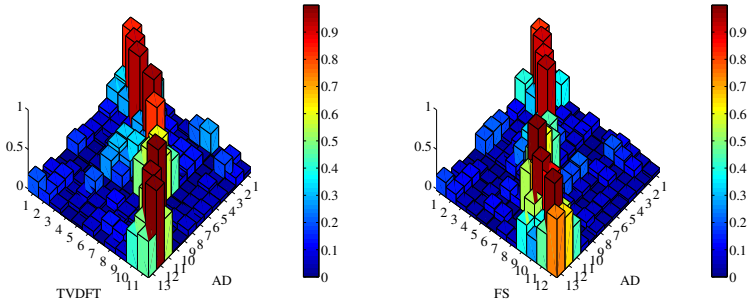
Finally, the mode shapes obtained by using the different techniques (Figure 6.86, Figure 6.87, Figure 6.88, Figure 6.89)



(a) FS vs OT - Medium run-up

(b) OT vs AD - Medium run-up

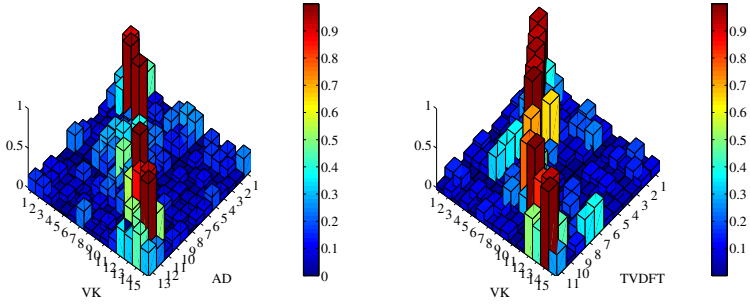
Figure 6.86: MAC diagram comparison between different order tracking techniques



(a) AD vs TVDFT - Medium run-up

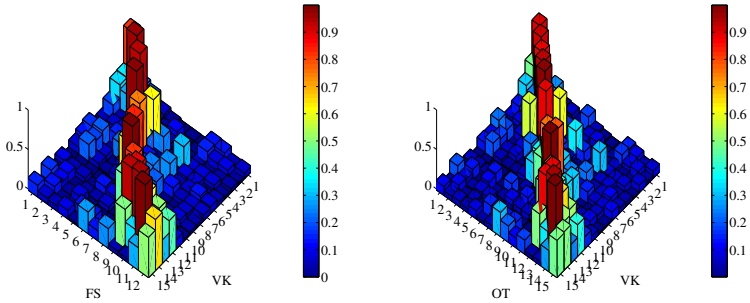
(b) AD vs FS - Medium run-up

Figure 6.87: MAC diagram comparison between different order tracking techniques



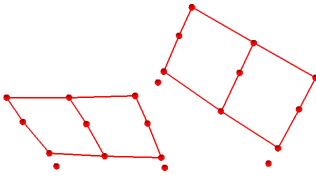
(a) AD vs VK - Medium run-up (b) TVDFT vs VK - Medium run-up

Figure 6.88: MAC diagram comparison between different order tracking techniques

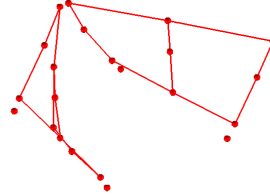


(a) VK vs FS - Medium run-up (b) VK vs OT - Medium run-up

Figure 6.89: MAC diagram comparison between different order tracking techniques

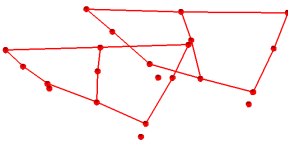


(a) Mode 5: 716.0 Hz

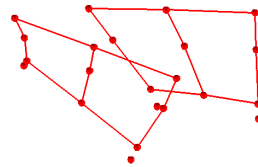


(b) Mode 10: 1366.0 Hz

Figure 6.90: Test rig plate mode shapes



(a) Mode 13: 1629.6 Hz



(b) Mode 14: 1748.7 Hz

Figure 6.91: Test rig plate mode shapes

## 6.2.4 Rotating accelerometers post-processing

Without considering the rotating accelerometers in the processing, only the main modes of the support structure can be identified. By considering also the instrumented gears, the preprocessing steps presented in Chapter 5 need to be applied. The dynamic behavior of the gears can be identified during operational measurements. For the gear test rig case the different order tracking techniques give very similar results. Therefore, in order to illustrate the gears behavior, only the Vold-Kalman filter has been used. The same considerations can be done by using any of the other techniques. The following bandwidth has been chosen:  $bw = 3$  and the gears accelerations have been decomposed in the vertical, horizontal and axial directions. Some more modes are identified which were not present by looking only at the plates accelerometers. On the other hand most of the modes keep being present. The plates modes cause a motion of the gears, but also the gears can influence the motion of the supporting structure. Of course the first situation is more evident than the second one because of the high stiffness of the supporting structure. Table 6.19 lists the natural frequencies and damping ratios for the mentioned case. The results have been obtained by using the Order 57. The values can be compared to the ones listed in Table 6.15 and Table 6.16.

no.	Natural frequency [Hz]	Damping ratio [%]	no.	Natural frequency [Hz]	Damping ratio [%]
1	310.0	0.30	11	1339.7	2.33
2	481.2	2.08	12	1378.5	2.01
3	535.4	1.17	13	1480.9	0.94
4	638.6	1.09	14	1579.7	1.94
5	703.1	2.63	15	1634.1	1.84
6	767.6	2.25	16	1735.3	2.05
7	969.2	3.12	17	1785.3	0.98
8	1078.9	2.26	18	1883.4	1.44
9	1144.8	2.47			
10	1235.7	0.82			

Table 6.19: OBMA - Modal parameters identification by considering rotating accelerometers

Figure 6.92 shows the order extracted for two different gear accelerations. The order is compared with the synthesized one obtained by using OBMA. Some difficulties are encountered as in the previous cases to fit the model at lower

frequencies. Figure 6.93 shows the auto-MAC between the calculated modes and it shows that all the modes are different from each other. Therefore, no double poles have been selected. Some of the mode shapes which are related to the gears are shown in Figure 6.94 and Figure 6.95. The modes shown are the ones in horizontal direction, along the line of action and out of the line of action.

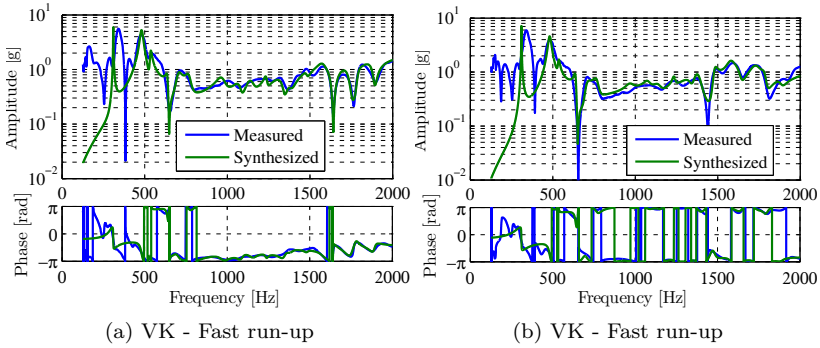


Figure 6.92: Synthesized vs measured models in rotating conditions

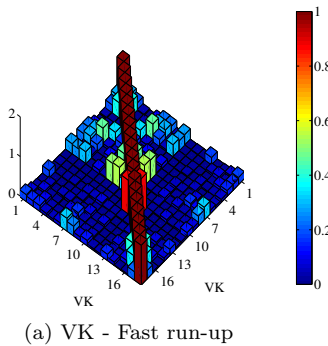


Figure 6.93: Auto-MAC diagram

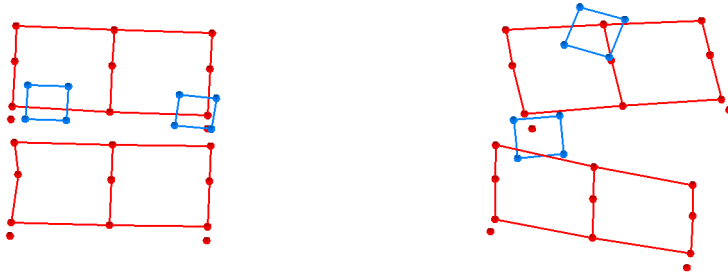


Figure 6.94: Test rig mode shapes - Fast run-up: 310.0 Hz and 481.2 Hz

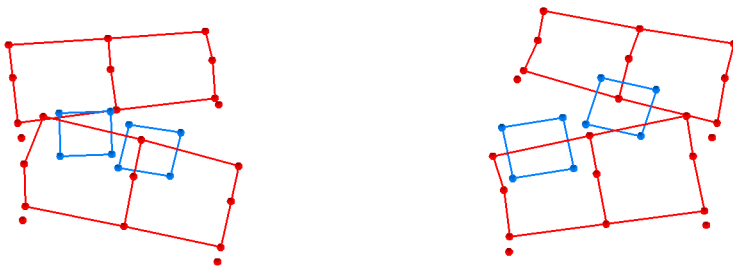


Figure 6.95: Test rig mode shapes - Fast run-up: 638.6 Hz and 767.6 Hz

## 6.3 Wind turbine gearbox

The gearbox is one of the key subsystems in a geared wind turbine providing the task to transfer power from the low speed shaft connected to the rotor to the high speed shaft connected to the generator. In the past years, the number of wind farms has increased and some of them were installed quite close to residential areas. This is one of the main reasons for which noise emission levels are a matter of public interest. The airborne rotor noise had a drastic reduction based on improved blade design, new control strategies and tip speed limitations. However, mechanical noise resulting from gearbox, generator etc. - primarily tonal of nature - can become a new sound challenge. In the case of the gearbox, the sound originates from gear excitations which are transmitted through shafts, bearings and the housing [89]. A deep knowledge into gearbox dynamics becomes of fundamental importance and noise and vibration measurements are demanded [90]. The demanded measurements are mainly quality estimation methods for gear mesh vibrations and overall sound power levels. They are based on standard techniques for the estimation of dynamic characteristic in general applications and are not focusing on the wind turbine gearbox case. Order-Based Modal Analysis has been successfully applied to this challenging case and several interesting conclusions has been made.

### 6.3.1 Experimental campaign

With the main objectives of characterizing the gearbox dynamic response in different operating conditions and obtaining experimental data for model validation and updating, a measurement campaign took place on the 13.2 MW dynamic test rig available at ZF Wind Power in Lommel, Belgium [91]. This is one of the world's largest test facilities in its kind matching the wind turbine power growth in the market. Gearboxes can be tested under representative loading conditions using parameterized load cases implemented in the controller. The life testing can be accelerated and potential technical risks can be identified in an early stage of the gearbox development. The main objective is to increase their reliability. During the measurement campaign, two gearboxes were placed in a back-to-back configuration in order to limit the energy requirements needed to operate the test rig. In fact, the energy used to drive the gearboxes in the motor is recovered by the generator and fed back into the system. A picture taken during the measurement campaign is shown in 6.96.

The gearbox under test (3.2 MW, named P3) operates in the so-called "generator mode" as in the wind turbine, whereas the second one (3 MW, names P2) is in the "motor mode". They have slightly different gear ratio, which means that





Figure 6.96: Picture taken during the measurement campaign at ZF Wind Power, Lommel, Belgium

the motor mode gearbox does not run at its nominal speed when the generator mode one is being tested. The tested gearbox (P3) is driven at a certain time varying speed corresponding to variable wind speeds and loaded with a certain time varying torque by the generator corresponding to the loading from the grid. It experiences test conditions very similar to the ones that it would experience in the wind turbine in operating conditions.

In this case, the following scenarios were tested:

- Shaker sine sweep during standstill and in operating conditions at 1200 rpm.
- Stationary operating conditions at 1200 and 800 rpm.
- Runup from 200 to 1500 rpm with a sweep rate equal to 5 rpm/s.

All these measurements were repeated under different torque loading conditions (33%, 66% and 100% of the nominal torque).

An extensive grid of 250 points on both the gearboxes and the test rig was measured using tri-axial accelerometers. The schedule test was repeated 7 times in order to measure all points. The available sensors were roving in order to cover the whole grid. A set of 7 uni-axial accelerometers were kept in the same position along the entire measurement campaign. They were used to ensure that the different datasets were consistent with each other. Furthermore, 3 optical sensors (zebra tape + laser) were respectively installed on the Low Speed Shaft (LSS) and on the High Speed Shaft (HSS) of each of the two gearboxes. Table 6.20 lists all the measurement points and associate them to the P3 and P2 gearboxes and to the test rig. Figure 6.97 and Figure 6.98 show the gearbox P3 and the counter gearbox P2, respectively.

The data measured during shaker excitation with the gearbox in standstill conditions have been analyzed. One of the main objectives was to compare

Component	Abbreviation	Number of points
<b>Tested gearbox P3</b>		
Torque Arm Cover	TAC	12
Torque Arm	TA	30
Low Speed Stage Ring Wheel	LSRW	12
Intermediate Bearing Housing	IBH	24
Intermediate Speed Stage Ring Wheel	ISRW	12
Bearing Housing	BH	36
High Speed Stage Housing	HSH	76
<b>Counter gearbox P2</b>		
Counter gearbox	P2	27
Test rig	CASS	27

Table 6.20: Measurement points list

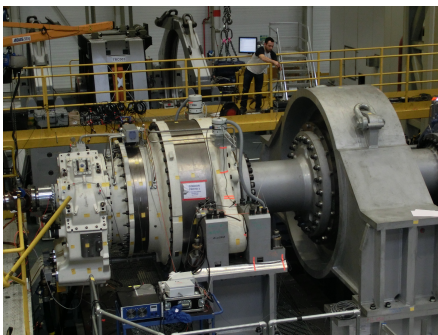


Figure 6.97: P3 gearbox picture.

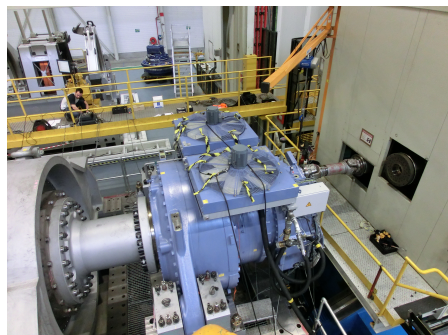


Figure 6.98: P2 gearbox picture.

the modal parameters obtained by using different operating conditions. A similar processing was also performed on the data collected applying the sine sweep via the shaker during stationary operating conditions. However, although some of the modes could still be identified, the main conclusion was that the shakers were not powerful enough to excite most of the modes of the structure. Therefore a meaningful modal parameter estimation could not be performed [92].

Accelerations were also acquired during stationary conditions (constant speed). The vertical lines in Figure 6.99 in the time-frequency diagram represent the harmonics of the fundamental rotational speed. They can all be related to the different shafts and stages composing the gearboxes. It can be noticed how all these harmonics are very close to each other. They are dominating the response of the system and for this reason it is impossible to apply standard OMA. As a consequence, ODS could be applied but this is the typical case in which it cannot be distinguished whether the high response at the receiver is due to the system or the source. A possible solution could be the comparison with the natural frequencies identified by applying shaker excitation. However, since the boundary conditions are quite different between the two cases, erroneous conclusions might be drawn. In the runup case (Figure 6.100), as explained also for the 2D model and the gear test rig, both OMA and OBMA could be applied to the data. In fact, the harmonics become orders sweeping through a certain frequency band. The excitation is similar to that of a multi-sine sweep.

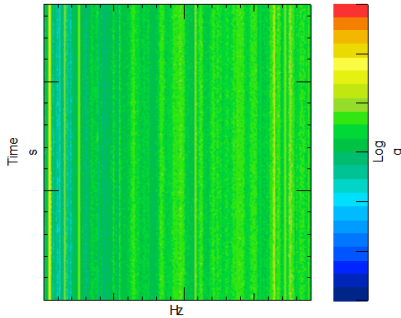


Figure 6.99: Time-frequency plot during stationary conditions (constant speed).

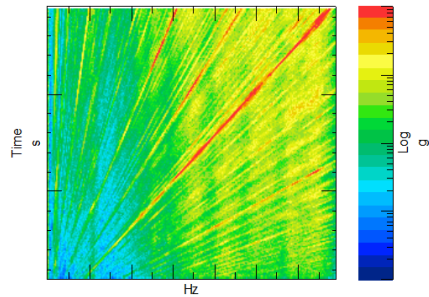


Figure 6.100: Time-frequency plot during runup conditions (increasing speed).

### 6.3.2 Operational Modal Analysis

The input data for Operational Modal Analysis are the time histories collected during operational conditions. These time histories are then converted into auto and cross-spectra and they can be analyzed by using a curve-fitting method such as Operational Polymax. By combining the response at the different orders, the resulting spectra can be considered as the response to a "flat" broadband excitation. Therefore, these spectra will be compliant with the fundamental OMA assumption. However, the results might be wrongly interpreted if the data are not carefully analyzed. The "end-of-order" phenomena was already highlighted by using the 2DOF system. A comparison of the two graphs in Figure 6.101 shows again that some of the peaks in the spectrum (and in particular the sharpest one) originate from order components suddenly stopping at the maximum rpms. Cursors were added to the pictures at frequencies that were identified as poles of the gearbox by classical OMA analysis. Moreover, as the two gearboxes have a slightly different gear ratio, they rotate at slightly different speeds generating a doubling of these "end-of-order" related poles. This is the main weakness of the method: it is able to identify the physical poles of the system, but on top of them it also identifies the "end-of-order" poles which are physically not present in the system. The four identified frequencies correspond to some of the main order components ending at that frequency. The estimated modal model is then not correct because it considers them as poles of the system. In some cases they can just be ignored a-posteriori, but in cases where many orders are present (such this one) they can also affect the estimation of close modes reducing the confidence in the identified modal model.

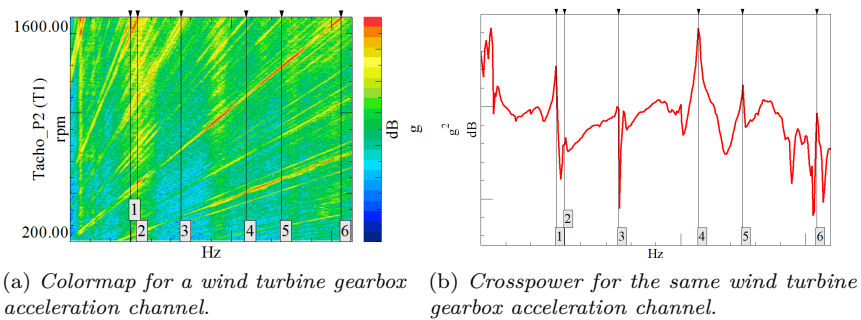


Figure 6.101: "End-of-order" effect.

### 6.3.3 Order-Based Modal Analysis: order tracking step

These conclusions about the use of OMA in this challenging case motivated the development of the Order-Based Modal Analysis (OBMA) method to identify the modal model of a rotating machine in operating conditions. The main concept was introduced in the previous Sections. In this particular case, some more challenges are present. In fact, a clean tachometer signal is needed for having good orders estimates. The three shafts (two high-speed shafts and one low-speed shaft) on the test rig were instrumented by using zebra tapes combined with Keyence FU-10 probes. The rotating speed is then measured by timing the duration of the passage of the alternating light and dark stripes glued to the shafts [86]. The main advantage of this system is that it is less expensive than other existing systems and it does not require shaft modifications or time consuming installations. On the other side, zebra tapes suffer from the fact that the last stripe has a different width than the others causing an erroneous signal that disturbs the analysis of the data. The angle discontinuities lead to spikes in the rpm data, making the order analysis impossible. In [86] a butt joint algorithm has been developed in order to deal with fast rotating shafts. The algorithm is able to identify the location and the angular interval at the butt joint of a zebra tape from the tacho moments measured on a rotating shaft. This information allows the reconstruction of the exact angle evolution to be used for order tracking purposes. The algorithm makes use of an angle estimator function and a dedicated spline interpolation and FIR band-pass filter. After having pre-processed the tachometer signal, the order tracking techniques can be applied to extract the orders of interest. On each of these orders operational modal identification can then be applied and the modal parameters from the different orders combined to obtain the modal response in the frequency band of interest.

The most excited orders (according to the colormap shown in Figure 6.100) are the second gear mesh frequency of the intermediate speed stage (Order 12.36) and the first gear mesh frequency of the high speed stage (Order 27) of the wind turbine gearbox. Unfortunately during this measurement campaign not all the tachometer signals were measured successfully. As a consequence the tacho measurements of the counter gearbox are taken into account for the further processing. This causes the presence of a multiplication factor (0.9413) for all the extracted orders due to the gear ratio difference between the two gearboxes. Hence, the two main orders are now: Order 11.63 and Order 25.41.

For sake of conciseness, only the TVDFT and VK methods will be applied to this use case. After properly taking care of the processing of non-integer orders, the data could also be processed with commercially available tools in Test.Lab. The two orders (11.63 and 25.41) are shown respectively in Figure 6.102 and Figure 6.103.

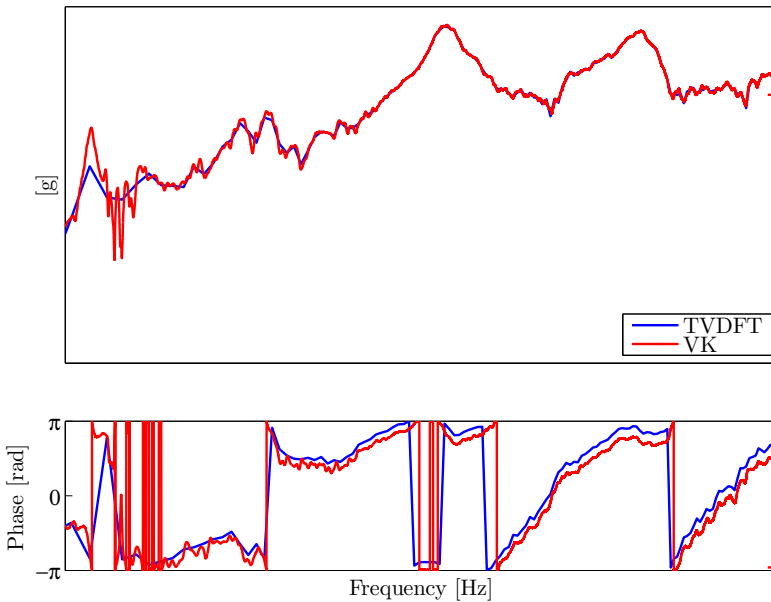


Figure 6.102: TVDFT vs VK - Order 12.36.

The amplitude behavior is described in the same manner by the two techniques. On the other hand the phase behavior is very similar, but in both cases there is a slight shift between the two orders. This is mainly due to the fact that the TVDFT technique considers integer number of revolutions during the processing. For non-integer orders, the number of revolutions is rounded to the closest integer number.

### 6.3.4 Order tracking for harmonic removal purpose

The orders shown in Figure 6.102 and Figure 6.103 have been selected with care. In fact, they are not affected by harmonic disturbances. However, in this case, several harmonics are present in many of the channels. They are due to a bad electrical insulation of cables and sensors during the measurements. It is not rare to have the 50 Hz (or 60 Hz if in the US) component and its odd multiples which are masking a great part of the dynamics of the system. A solution could be the one of selecting small frequency bands and excluding the frequencies at which harmonics are showing. For example, if an harmonic is present at 50 Hz and at its odd multiples, the identification process could be completed by selecting two frequency bands: from 0 Hz to 49 Hz, from 51 Hz to

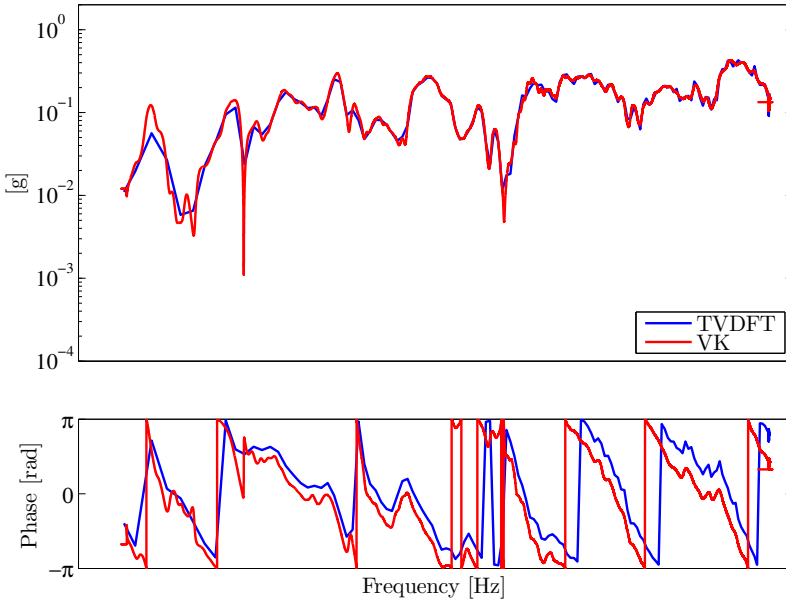


Figure 6.103: TVDFT vs VK - Order 27.

149 Hz and so on. This is normally possible because harmonics (especially the electrical ones) are represented by very sharp peaks that do not spread energy on many frequency lines around them. Different harmonic removal tools could be employed to filter out the harmonics before the modal analysis step takes place. In this dissertation, the potential of Vold-Kalman filter order tracking has been used for filtering out harmonics before using OMA techniques. In the literature this filter is normally used as order tracking technique, but with some adaptations it could be easily used for filtering out harmonics instead of extracting the orders. Figure 6.104 and Figure 6.105 show respectively the Order 12.36 and the Order 27 for a channel in which the electrical disturbance is quite high. It is impossible to perform modal analysis by including this channel in the dataset. Unfortunately many channels are influenced by the same components. For this reason, VK filter has been used as pre-processing step to filter out these sharp peaks. It acts quite effectively, as shown in Figure 6.104 and Figure 6.105 where the same orders are represented after having applied the filter to them. At this point the OMA step can be performed to identify the modal parameters of the wind turbine gearbox in a test rig configuration.

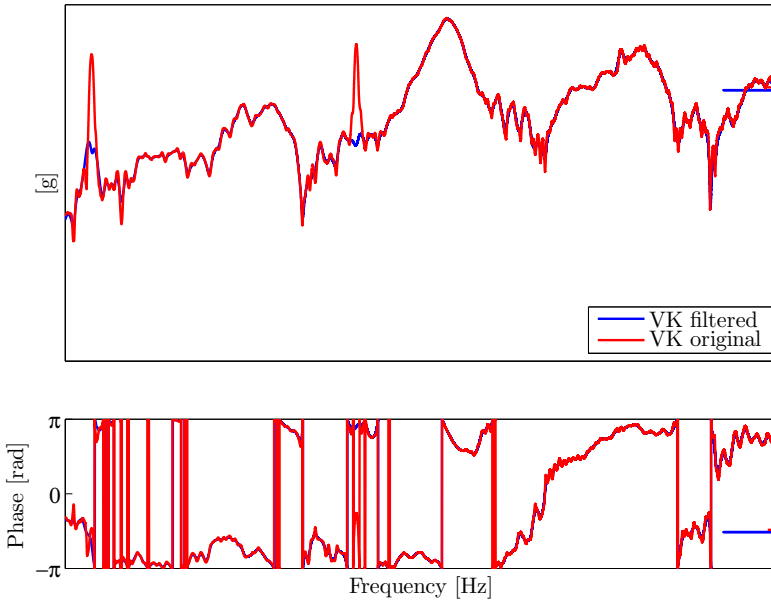


Figure 6.104: Harmonic removal filter - Order 12.36.

### 6.3.5 Order-Based Modal Analysis: modal analysis step

Several modes are identified by using both techniques in the OBMA processing (after having applied the proper harmonic removal tool). Before applying any filter to the data the stabilization diagram shown in Figure 6.106 is obtained. The same processing was performed after the use of the VK filter to delete the harmonics at 50Hz and 150Hz and better results were obtained (Figure 6.107). In general some more modes are found which were hidden behind those harmonics.

The same processing was repeated for different load levels to investigate possible system non-linearities resulting in variations of modal parameters. The results are summarized in Figure 6.108 and Figure 6.109, for TVDFT and VK respectively. They show the relative variations of the natural frequencies for the 3 cases by using as reference load case the one with 100% load. The general trend from the results shows an increase of the natural frequencies with the torque value.

Generally, almost all modes are identified in the 3 cases. It is clear that OBMA on the VK tracked orders is the process which is able to identify the highest



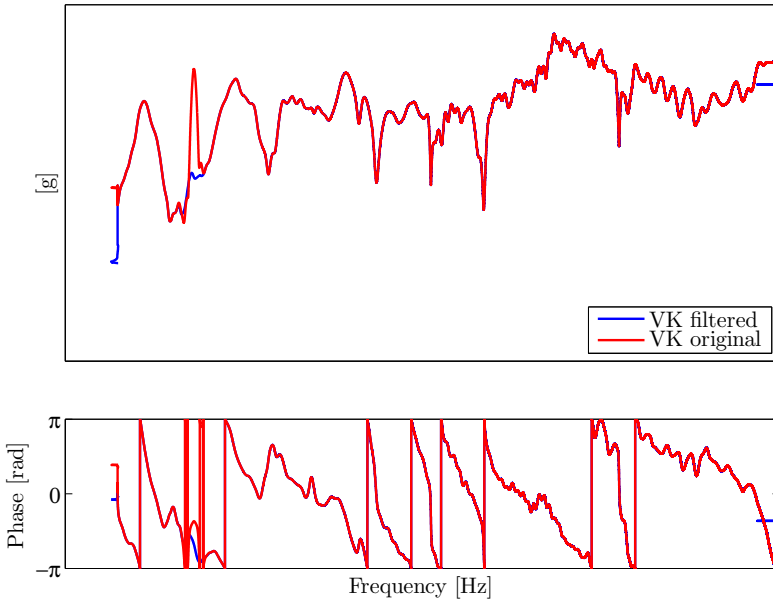


Figure 6.105: Harmonic removal filter - Order 27.

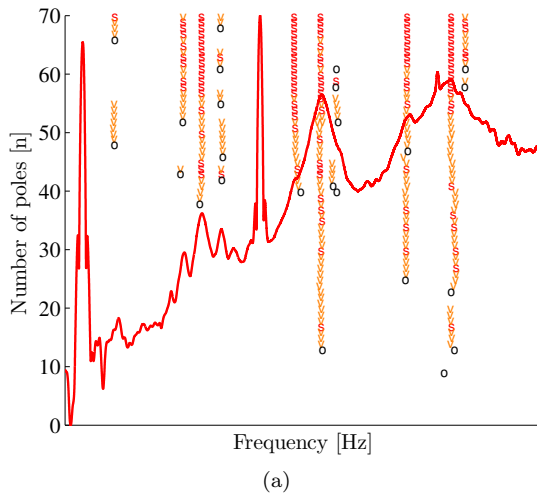
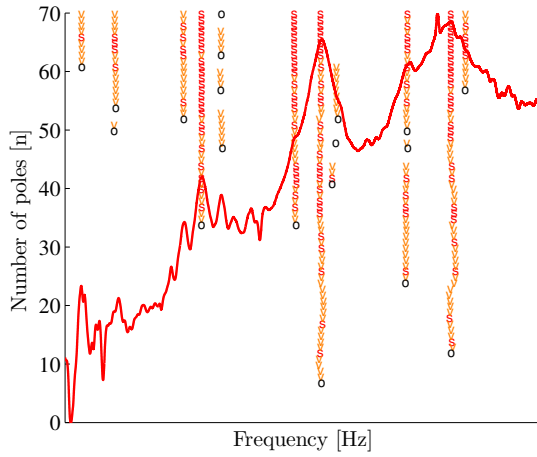


Figure 6.106: Stabilization diagram before applying VK as harmonic removal filter



(a)

Figure 6.107: Stabilization diagram after applying VK as harmonic removal filter

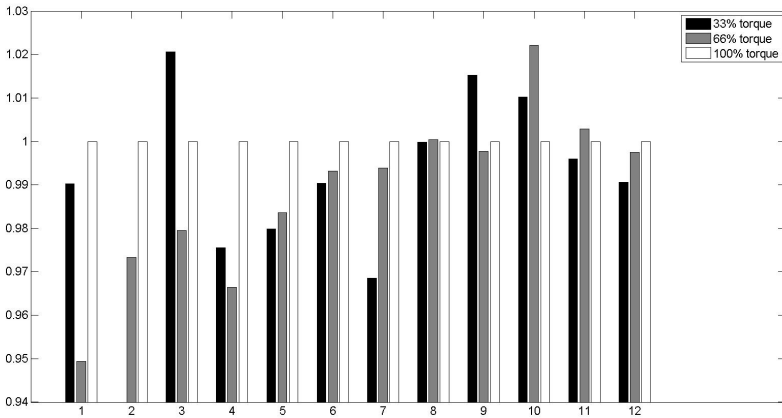


Figure 6.108: Order-based Modal Analysis with TVDFT order tracking - relative variation of natural frequencies with torque level.

number of modes in the selected frequency band.

A way of validating the obtained results is to compare the measured order with the synthesized one computed by applying Operational Polymax. In the

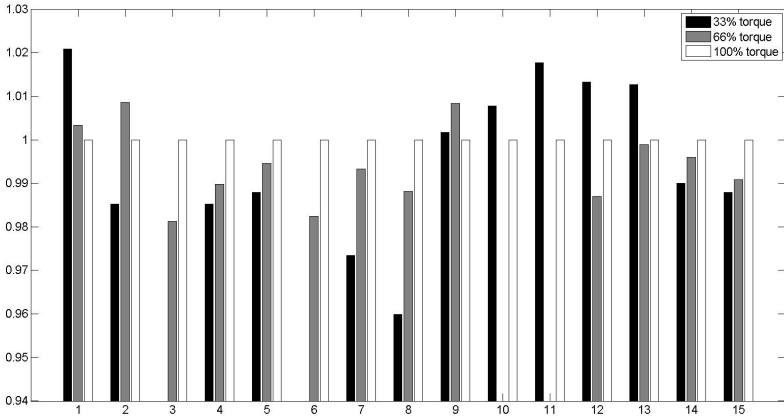


Figure 6.109: Order-based Modal Analysis with VK order tracking - relative variation of natural frequencies with torque level.

mid-high frequency band, the identified modal models are able to accurately describe the measured orders. However, at lower frequencies, where the number of available samples for the TVDFT order estimation is smaller, VK performs significantly better as expected.

Figure 6.110 and Figure 6.111 show the synthesized models for two different acceleration channels calculated by means of OBMA processing. It is quite clear that even in a noisy case as the one in Figure 6.111, the modal model is reproducing quite accurately the dynamic behavior of the system.

A further comparison between the different methods can be performed by computing the MAC between the mode sets. Figure 6.112 and Figure 6.113 show respectively the auto-MAC functions obtained for what concerns the VK and the TVDFT mode shapes.

In both cases a diagonal behavior can be underlined. All the identified modes are then different from each other. Finally, the MAC between the two datasets is shown in Figure 6.114. The main difference is that by using VK much more modes are identified because of the better resolution in the frequency domain. For this reason, the wind turbine gearbox case confirms that among the two techniques for order tracking, the VK filter has the best performances.

The mode shapes obtained for the entire challenging dataset are mainly related with the high-speed stage of the gearbox. Two of them are shown in Figure 6.115 and Figure 6.116. In the first one a symmetric behavior of the entire test

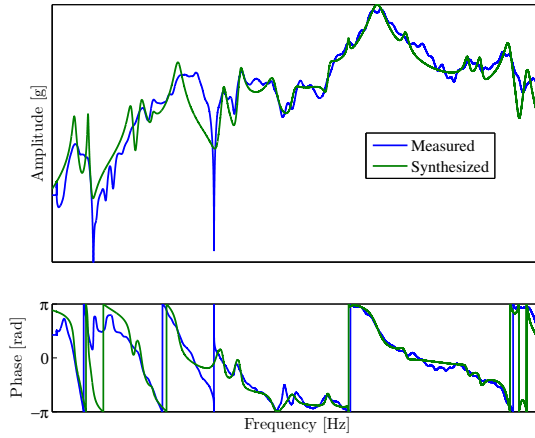


Figure 6.110: Synthesized vs measured models for VK order tracking technique

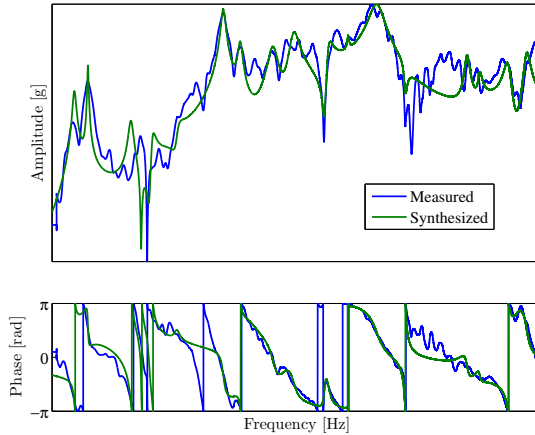


Figure 6.111: Synthesized vs measured models for VK order tracking technique

rig can be underlined since both gearboxes are moving in phase. The second mode is higher in frequency and it shows a bending/twisting movement of the high-speed housing and a rotation of the torque arms.

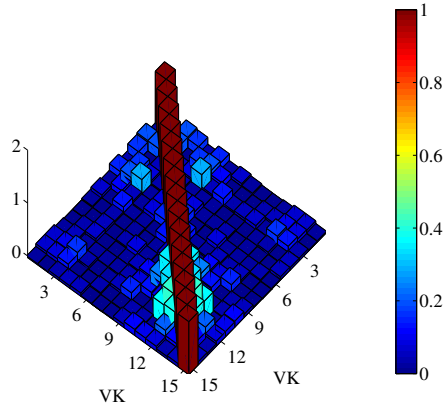


Figure 6.112: Auto-MAC for VK order tracking technique

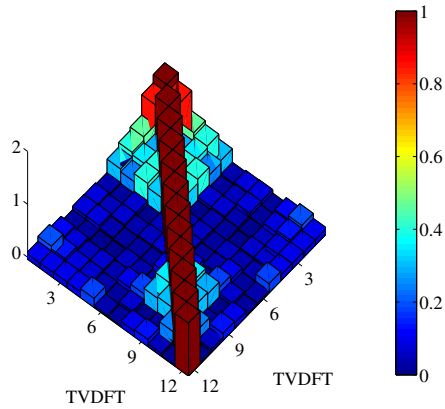


Figure 6.113: Auto-MAC for TVDFT order tracking technique

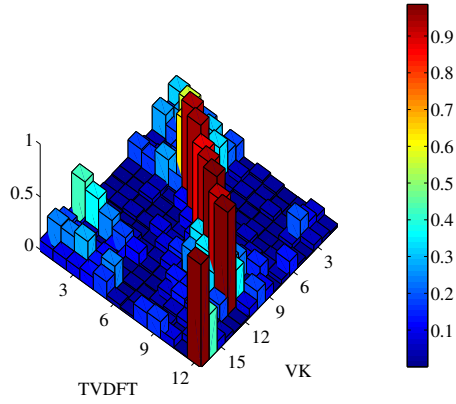


Figure 6.114: MAC comparison between VK and TVDFT order tracking techniques

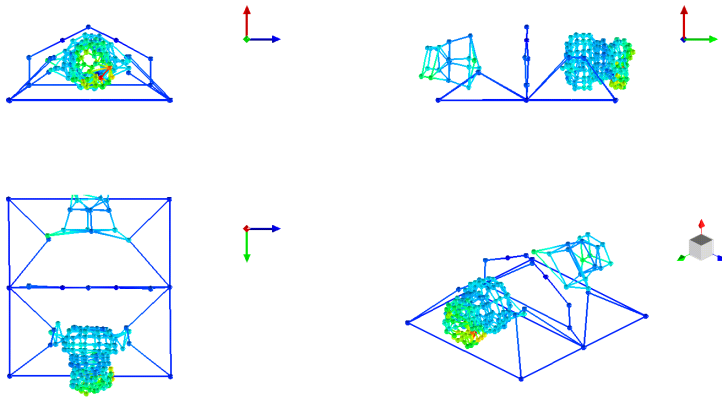


Figure 6.115: Wind turbine gearbox mode shape: test-rig symmetric mode.

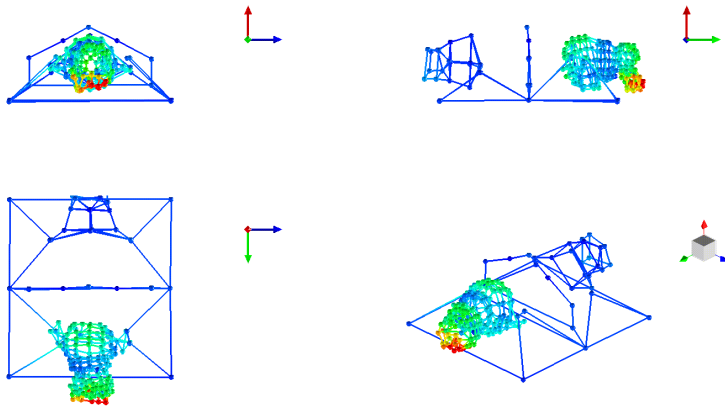


Figure 6.116: Wind turbine gearbox mode shape: bending/twisting movement of the high-speed housing.





# Chapter 7

## Conclusions and Recommendations

The main objective of this dissertation is to fully understand and propose solutions to the challenges and the limitations occurring when trying to use Operational Modal Analysis (OMA) in a rotating machinery context. In fact, some of the hypothesis needed in order to apply classical OMA are not valid when one or several parts of the structure are rotating with respect to each other or when the entire system is rotating. In some cases the use of dedicated pre-processing techniques is mandatory before performing OMA. In other cases existing methods need to be re-adapted to overcome some of the limitations. In this final conclusions the most important findings for each chapter are illustrated and recommendations for further research are given. The thesis can be divided into three main topics which will be discussed separately:

- OMA for LTP systems;
- OMA for SHM purposes;
- Order-Based Modal Analysis.

### 7.1 Conclusions on OMA for LTP systems

Chapter 3 describes the use of OMA for Linear Time Periodic (LTP) systems. This is the case of a wind turbine or an helicopter in operating conditions at

their nominal speed. In this case the OMA hypothesis for which the system must be Linear Time Invariant (LTI) is not valid. For this reason two main techniques have been proposed in order to be able to apply OMA to LTP data:

- Multi-Blade Coordinate transformation;
- Harmonic Power Spectrum method.

These techniques can be used as a pre-processing step for OMA. They are able to combine LTI and LTP datasets together by transforming the LTP part of the system into a LTI one. The limitation due to the time varying nature of the structure is then overcome and standard techniques for estimating the modal parameters can be used. MBC technique performs very well if the rotational speed is constant and it has also another important advantage: it allows to filter out all the periodic terms except those which are multiple of the 3P component. This is not true if the rotational speed is highly variable during the observation time. In this case the harmonics continue being present even after applying the MBC pre-processing technique. On the other hand, HPS results are also very satisfactory, but some a priori knowledge of the system is needed. In fact new harmonics are introduced by this method since the output signals are exponentially modulated. The procedure to be followed in both cases has been defined and the results on simulation models have demonstrated the applicability of both techniques on wind turbines in operating conditions. The main findings are related to the whirling modes identification. They are among the most identifiable modes in a wind turbine context and their frequency varies with the rotational speed. For this reason it is quite important to identify and track them in order to avoid structural damages. They are also quite sensitive to structural modifications. For this reason, some SHM considerations have been discussed in the second part of the thesis. The influence of the icing phenomena has also been tackled in the dissertation. On the other hand, the influence of the temperature and environmental effects on the natural frequencies and damping ratios has not been taken into account.

## 7.2 Conclusions on OMA for SHM purposes

Chapter 4 looks into Structural Health Monitoring (SHM) which is often a reason for which OMA is used in industrial environment. In fact, it is common practice to define SHM strategies based on the differences among the modal parameters in "healthy" and "damaged" conditions. Two main strategies have been defined for rotating machines (e.g. wind turbines):

- Whirling modes as damage indicators;
- Mode shape curvature as damage indicators.

The first one is based upon the well-known (in the rotating machinery community) whirling phenomenon. The whirling modes appear to be very sensitive to changes in stiffness and they are among the most identifiable modes in operating conditions. The changes of stiffness are identified and localized by considering the differences among the three blades. The whirling mode shapes (both backward and forward) are affected by these changes. It can be clearly noticed how the phase lag between the blades is not anymore equal to  $120^\circ$  and the amplitude of the damaged blade is higher than the ones of the other two blades. So finally, both amplitude and phase of these modes can be used as damage indicators since they are able to detect even small changes in the stiffness of the blades. The second strategy is based on the curvature of the mode shapes (second derivative) which demonstrated to be a very good damage indicator for beam-like structures such as a wind turbine blade. It allows to identify the presence of a damage, its position and its extension. The intersection between the curvature in the undamaged and damaged case indicate the beginning and the end of the damaged area. Many sensors are needed in this case because at least one of them needs to be placed in the damaged area in order to detect the damage. For this purpose the suggested sensors are the fiber optics which can have several interrogators along the blade without adding too many cables to the structure.

The first technique has been proved in a simulation environment by using aeroelastic wind turbine models results. The second technique has also been tested in a simulation environment by considering a very accurate wind turbine blade model. Then, the same blade has been tested by means of OMA before and after that a damage occurred (pre-buckling and post-buckling). The effectiveness of the method has been demonstrated in localizing damages in beam-like structures and it could be extended to other cases. In both cases a relatively high number of sensors need to be used to instrument the blades and furthermore all the blades must be instrumented in the same manner to identify changes between them.

### **7.3 Conclusions on Order-Based Modal Analysis**

Chapter 5 and Chapter 6 introduce the Order Based Modal Analysis technique from a theory and a practical point of view. As suggested by its own name, this technique is a combination of Order Tracking and Operational Modal Analysis. This is an alternative method which can be used when the dominant excitation

is due to rotating components and the rotational speed can be accurately measured during run-up/down non-stationary operations. In this case OBMA can be successfully applied to identify the modal model of the structure under test in operational conditions. This method is able to overcome the limitation of classical OMA to interpret the "end-of-order" poles. The advantages and drawbacks of several order tracking techniques have been extensively described. The Angle Domain technique demonstrated to be very efficient both in terms of quality of the results and computational time consumption. Its main advantage, if compared to other commercially implemented techniques (Fixed Sampling, Order Tracking), is that it allows to get an absolute phase within an operating cycle for the calculated orders. On the other hand, the other techniques need to calculate the orders with respect to a reference channel which must be synchronous with the rotational speed of the machine.

An algorithm to take into account rotating accelerometers has also been implemented and tested in a controlled test environment. Its results have been combined with OBMA and the mode shapes of gears in contact during operational conditions have been estimated.

Another finding which is described in this part of the dissertation is related to the use of order tracking techniques to filter out sharp harmonics (e.g. due to electrical disturbance). VK filter performs very well this step and it is used as a pre-processing step before applying OBMA in cases in which the electrical component is masking the dynamics of the system.

Finally, in Chapter 6, the OBMA technique has been successfully applied to three different challenging cases. First of all, most of its advantages and drawbacks are shown for a simulated 2D model. Finally, it proved to be applicable in a test environment to identify the modal parameters of an industrial test-rig in a controlled environment and of a wind turbine gearbox in a test-rig configuration. In this chapter the rotating accelerometer algorithm has been applied in practice to identify the gear modes. The potential of order tracking techniques for harmonic removal scopes is also discussed and VK is successfully applied to remove the electrical disturbances from the measured accelerations.

## 7.4 Recommendations and future directions

**Recommendations** This brings to the end of this dissertation. Before putting the last point it is worth to give some recommendations about the use of the implemented techniques. It is also important to describe future challenges and research that is still ongoing.

The main aspects of the dynamic characterization of operating rotating machines have been covered in this thesis. Several guidelines have been drawn to help

structural dynamics engineers to estimate the modal parameters of this type of systems.

- In order to perform OMA on an operating wind turbine, both MBC and HPS can be used in combination with a modal parameter estimation technique. The procedure consists in acquiring the data by means of sensors (which can be accelerometers, strain gauges, optical fibers, etc.) at several locations along the blades and the tower-nacelle subsystems. The sensors placement is quite important. In fact, in order to successfully apply the two techniques, the sensors must be placed at the same location along the three blades. Errors in the position or angle of one or more sensors will cause an apparent anisotropic behavior of the rotor. This situation must be avoided or, if it is too late to replace/move the sensors, the errors must be taken into account when applying the techniques. MBC and HPS can be applied to the rotating blade sensors by taking into account the azimuth angle. For this reason, the measurement of the rotational speed of the wind turbine is also playing a very important role. It's mandatory to have an accurate rpm trace to be able to apply the techniques and to accurately track the modes of interest. The set of fixed sensors and rotating sensors can then be combined and OMA can be applied to estimate the modal parameters in operating conditions. Finally a post-processing step is needed to get back the physical coordinates.
- For what concerns the SHM for beam-like structures, several type of sensors can be used(e.g. acceleration or displacement based sensors). Accelerometers are the most common sensors for vibration measurements, but several more information can be obtained by combining them with other types of sensors. Nowadays, for blade monitoring the strain gauges and the embedded fiber optics are very attractive because the wires along the blades could be reduced or eliminated and problems in case of lightning can be avoided. In order to successfully apply the proposed techniques, accelerometers or strain gauges can be used in a straightforward manner by using classical OMA or Strain-Based Modal Analysis, respectively. Both SHM strategies do not have any problem in dealing with these types of sensors. The strategy based on the whirling modes is very accurate, but it only allows to identify which blade is damaged by analyzing the differences among the three blades. The technique based on the curvature of the mode shapes, on the other hand, is able to identify the damaged zone in a single blade. A complete SHM system should have different type of sensors installed in order to get as many information as possible out of it for SHM purposes. The two techniques could be combined with each other in order to identify cracks and damages as soon as they are occurring in operational conditions.

- The use of several sensors for an accurate measurement of the tachometer signal of a rotating machine have been discussed. The coder-based techniques are the most used in the industrial environment. For applications in which there is no need of a high number of pulses per revolution (e.g. absence of torsional vibrations, only low order present in the data) a zebra tape suffices to measure the rotational speed of the machine. On the other hand, if a very high number of samples is needed or in case of gears in which higher orders are present in the data, an incremental encoder must be used to get better results.
- The Order-Based Modal Analysis technique requires a very good order estimation which can only be obtained if an accurate tachometer measurement took place. There are several parameters and considerations which must be taken into account when choosing the order tracking technique to apply to the acquired data. It is important to know which is the reason why an order tracking step is going to be performed. For instance, if the aim is the dynamic analysis of the rotating system by means of OBMA technique, then a particular care need to be reserved to the phase of the orders. In fact it is an essential part of the measurement function especially when curve-fitting methods are used afterwards (like in modal analysis). If the main scope is just to analyze at which frequencies orders are facing a resonance or at which frequency the highest order amplitude is obtained, then most of the techniques will be able to give these kind of information.
- The choice of the order tracking technique for modal analysis purposes is a compromise between the computational effort and the good quality of the results. For example, the FS technique allows to get a good approximation of the orders in a simple and numerically efficient way even if it does not take into account the fact that the frequencies of orders are changing with the time. It suffers from the problems due to fast sweep rates. On the other hand, OT and AD need a higher computational time but they provide leakage free estimates of orders. Furthermore, TVDFT estimates orders which closely match those of the resampling based methods with much less computational load. The VK filter is able to extract the time histories of the orders and for this reason it is quite computationally demanding, but it allows to get very accurate results. The last two techniques are also able to separate close and crossing orders and to extract the proper phase behavior in case of non-integer orders which is normally a difficult step.

**Future directions** Several research paths are still under study and several topics connected with the ones discussed in this thesis are going to be studied in the next future. The first one concerns the study of the dynamic behavior of

LTP systems (e.g. wind turbines). By taking into account the considerations done in Chapter 3 and Chapter 4, a vibration-based condition monitoring system for wind turbine blades could be put in place. This solution aims at significantly progress the blade monitoring state of the art by combining together advanced techniques and solution into a dedicated environment. Figure 7.1 shows the proposed concept idea. The tool consists of 3 main elements: a Condition Monitoring System (CMS), advanced blade and rotor data processing tools (MBC, HPS, OMA, Damage detection methods) and a numerical model of the wind turbine (virtual sensing approach). The use of simulation can be integrated in the process to enrich the information to be used to assess the health of the structure. First of all non-linear multibody hydro-aero-elastic simulation software can be used to derive reference operational response of the wind turbine under different environmental conditions. In parallel, simulation models of the blade, rotor or the turbine can also be used in real time in combination with the measured data in a real-time hybrid monitoring approach. (Augmented) Kalman filtering, modal expansion and joint-input-state estimation techniques will be used to determine the otherwise difficult to measure loads as well as strains and accelerations at location where no sensors are available. Beside increasing the accuracy, this approach will allow to drastically reduce the number of physical sensors required and the associated instrumentation time. The model used in these virtual sensing approaches can originate from preliminary measurements using more extensive instrumentation Although each of these elements does not represent a novelty, the aim of the proposed innovation is to combine them as a whole to allow a much more reliable monitoring of the blade, with timely detection and localization of damage and estimation of the actual remaining life based on the load history.

An idea consist of the extension of the OBMA technique to torsional vibrations problems (e.g. car engine). The Torsional Order Based Modal Analysis (TOBMA) technique can then be developed. It allows the identification of torsional modes of a shaft by applying OBMA to orders obtained from the rpm measured trace. In other words, instead of analyzing acoustics or vibration channels, it takes into account only the measured tachometer signal. If this is measured with a good accuracy, it will allow the torsional modes identification in terms of natural frequencies and damping ratios. This tool will be helpful in the automotive domain, where the problem of torsional vibrations is quite important.

Another problem to tackle concerns the user-friendliness of the OBMA technique in the software implementation. At the actual state, Order-Based Modal Analysis is addressed to few users who need to be expert both in Order Tracking and Operational Modal Analysis domains. In order to increase the ease of use of the software, a dedicated pre-processing step need to be put in place so that

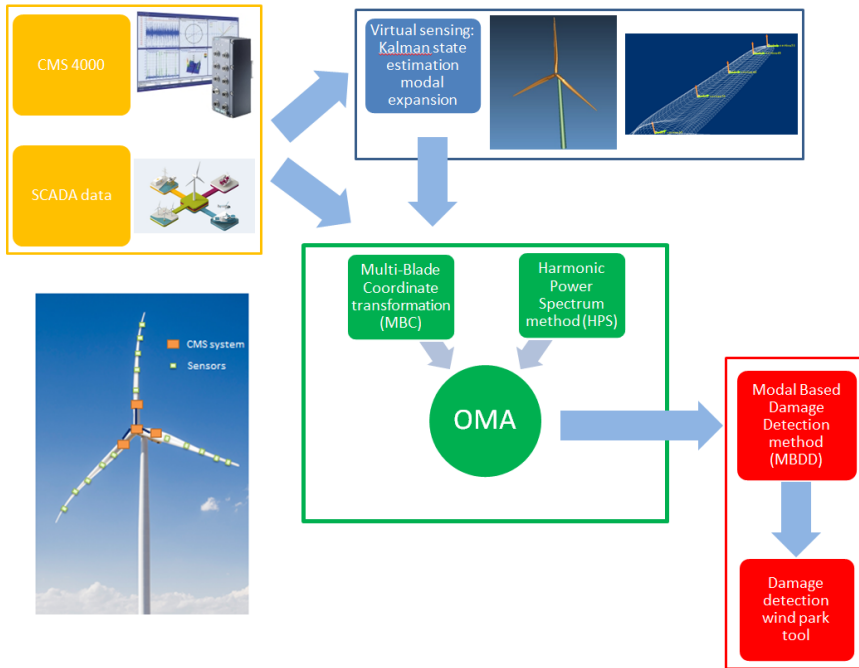


Figure 7.1: Condition monitoring system + Virtual sensing + OMA + Damage detection

even non-expert users could successfully use the tool to estimate the modal parameters of rotating machines.



# Bibliography

- [1] W. Heylen, S. Lammens, and P. Sas. *Modal Analysis Theory and Testing*. KU Leuven, Department Werktuigkunde, Leuven, Belgium, 2007. pages 3, 14, 17, 22
- [2] D.J. Ewins. *Modal Testing: theory, practice and application*. Research Studies Press LTD, 1985. pages 3, 14
- [3] N. Maia and J. Silva. *Theoretical and Experimental Modal Analysis*. Research Studies Press LTD, 1997. pages 3, 14, 24
- [4] R. Brincker and C. Ventura. *Introduction to Operational Modal Analysis*. John Wiley and Sons LTD, 2015. pages 3, 14
- [5] G. Floquet. Sur les equations differentielles lineaires a coefficients periodiques. Technical Report 12, Annales scientifiques de l'ENS, 1883. pages 4, 35
- [6] J.J. Dacunha and J.M. Davis. A unified floquet theory for discrete, continuous, and hybrid periodic linear systems. *Journal of Differential Equations*, 251, 2011. pages 4, 35
- [7] G. Bir. Multiblade coordinate transformation and its application to wind turbine analysis. In *Proceedings of ASME Wind Energy Symposium*, Reno, Nevada, USA, 2008. pages 4, 37
- [8] R.P. Coleman. Theory of self-excited mechanical oscillations of hinged rotor blades. Technical Report G29, NACA, 1943. pages 4, 37
- [9] N.M. Wereley. *Analysis and control of linear periodically time varying systems*. PhD thesis, Massachusetts Institute of Technology, Department of Aeronautics and Astronautics, USA, 1991. pages 4, 41
- [10] M.S. Allen, M.W. Sracic, S Chauhan, and M.H. Hansen. Output-only modal analysis of linear time periodic systems with application to wind turbine

- simulation data. *Mechanical Systems and Signal Processing*, 25:1174–1191, 2011. pages 4, 44
- [11] H. Vold and J. Leuridan. High resolution order tracking at extreme slew rates, using Kalman tracking filters. In *Proceedings of Society of Automotive Engineers Noise and Vibration Conference, SAE paper number 931288*, 1993. pages 6, 140
- [12] K. Janssens, Z. Kollar, B. Peeters, S. Pauwels, and Van der Auweraer. H. Order-based resonance identification using operational PolyMAX. In *Proceedings of 24<sup>th</sup> International Modal Analysis Conference (IMAC)*, Saint Louis, MO, USA, 2006. pages 6, 30, 127, 144
- [13] E. Di Lorenzo, A. Palermo, S. Manzato, A. Dabizzi, B. Peeters, W. Desmet, and F. Marulo. Gear dynamics characterization by using Order-Based Modal Analysis. In *Proceedings of 34<sup>th</sup> International Modal Analysis Conference*, Orlando, FL, USA, 2016. pages 7, 137, 203
- [14] E. Di Lorenzo, S. Manzato, B. Peeters, F. Vanhollebeke, W. Desmet, and F. Marulo. Order-Based Modal Analysis: a modal parameter estimation technique for rotating machineries. In *Proceedings of 6<sup>th</sup> International Operational Modal Analysis Conference (IOMAC)*, Gijon, Spain, 2015. pages 7, 164
- [15] E. Di Lorenzo, G. Petrone, S. Manzato, B. Peeters, W. Desmet, and F. Marulo. Damage detection in wind turbine blades by using operational modal analysis. *Structural Health Monitoring*, 15(3):289–301, 2016. pages 7, 104
- [16] G. Bir. Understanding Whirl Modal Behavior of a Wind Turbine Rotor. In *Proceedings of 21<sup>st</sup> International Modal Analysis Conference (IMAC)*, Orlando, FL, USA, 2003. pages 7, 45
- [17] E. Reynders. *System Identification and Modal Analysis in Structural Mechanics*. PhD thesis, KU Leuven, Leuven, Belgium, 2009. pages 14
- [18] J.S. Bendat and A.G. Piersol. *Engineering Applications of Correlation and Spectral Analysis*. John Wiley and Sons LTD, 1993. pages 20
- [19] A.J. Felber. *Development of a hybrid bridge evaluation system*. PhD thesis, University of British Columbia, Vancouver, Canada, 1993. pages 20
- [20] R. Brincker, L. Zhang, and P. Andersen. Modal identification from ambient responses using frequency domain decomposition. In *Proceedings of 18<sup>th</sup> International Modal Analysis Conference (IMAC)*, San Antonio, TX, USA, 2000. pages 20

- [21] P. Guillaume, L. Hermans, and H. Van der Auweraer. Maximum Likelihood Identification of Modal Parameters from Operational Data. In *Proceedings of 17<sup>th</sup> International Modal Analysis Conference (IMAC)*, Kissimmee, FL, USA, 1999. pages 21
- [22] B. Cauberghe. *Applied Frequency-Domain System Identification in the Field of Experimental and Operational Modal Analysis*. PhD thesis, Vrije Universiteit Brussel, Brussels, Belgium, 2004. pages 21, 26
- [23] C. Devriendt and P. Guillaume. The use of Transmissibility Measurements in Output-Only Modal Analysis. *Mechanical Systems and Signal Processing*, 21(7):2689–2696, 2007. pages 21
- [24] P. Guillaume, P. Verboven, S. Vanlanduit, H. Van der Auweraer, and B. Peeters. A Poly-Reference Implementation of the Least-Squares Complex Frequency-Domain Estimator. In *Proceedings of 21<sup>st</sup> International Modal Analysis Conference (IMAC)*, Kissimmee, FL, USA, 2003. pages 21, 28
- [25] B. Peeters, H. Van der Auweraer, P. Guillaume, and J. Leuridan. The PolyMAX Frequency-Domain Method: a New Standard for Modal Parameters Estimation? *Shock and Vibration*, 11:395–409, 2004. pages 21, 28
- [26] B. Peeters, H. Van der Auweraer, F. Vanhollebeke, and P. Guillaume. Operational modal analysis for estimating the dynamic properties of a stadium during a football game. *Shock and Vibration*, 14:283–303, 2007. pages 22
- [27] J.N. Juang and R.S. Pappa. An eigen system realization algorithm for modal parameter identification and modal reduction. *J. Guidance*, 8(5):620–627, 1985. pages 22
- [28] G. James, T. Carne, and J. Lauffer. The Natural Excitation Technique (NExT) for Modal Parameter Excitation from Operating Wind Turbines. Technical Report 921666, SANDIA National Laboratories, Albuquerque, NM, USA, 1992. pages 22
- [29] B. Peeters. *System Identification and Damage Detection in Civil Engineering*. PhD thesis, KU Leuven, Leuven, Belgium, 2000. pages 22
- [30] P. Van Overschee and B. De Moor. *Subspace Identification for Linear Systems*. Kluwer Academic Publishers, Leuven, Belgium, 1996. pages 22
- [31] P. Welch. The use of fast Fourier transform for the estimation of power spectra: A method based on time averaging over short, modified

- periodograms. *IEEE Transactions on Audio and Electroacoustics*, 15(2):70–73, 1967. pages 25
- [32] L. Hermans, H. Van der Auweraer, and P. Guillaume. A Frequency-Domain Maximum Likelihood Approach for the Extraction of Modal Parameters from Output-Only Data. In *Proceedings of 23<sup>rd</sup> International Conference on Noise and Vibration Engineering (ISMA)*, Leuven, Belgium, 1998. pages 26
- [33] E. Parloo. *Application of Frequency-Domain System Identification Techniques in the Field of Operational Modal Analysis*. PhD thesis, Vrije Universiteit Brussel, Brussels, Belgium, 2003. pages 26, 28
- [34] G. Genta. *Dynamics of Rotating Systems*. Springer, 2005. pages 34
- [35] W. Johnson. *Helicopter theory*. Princeton University Press, 1980. pages 37
- [36] G. Bir, A.D. Wright, and S. Butterfield. Stability Analysis of Variable-Speed Wind Turbines. In *Proceedings of ASME Wind Energy Symposium*, Reno, Nevada, USA, 1997. pages 37
- [37] M.H. Hansen. Aeroelastic Instability Problems for Wind Turbines. *Wind Energy*, 10:551–577, 2007. pages 37
- [38] G. Bir and J. Jonkman. Aeroelastic instabilities of large offshore and onshore wind turbines. *Journal of Physics: Conference Series*, 2007. pages 37
- [39] D. Tcherniak, S. Chauhan, M. Rossetti, I. Font, J. Basurko, and O. Salgado. Output-only modal analysis on operating wind turbines: application to simulated data. In *Proceedings of European Wind Energy Conference*, Warsaw, Poland, 2010. pages 40
- [40] E. Di Lorenzo, S. Manzato, B. Peeters, and F. Marulo. Modal parameter estimation for operational wind turbines. In *Proceedings of 7<sup>th</sup> European Workshop on Structural Health Monitoring (EWSHM)*, Nantes, France, 2014. pages 40
- [41] D. Tcherniak and G.C. Larsen. Application of OMA to an operating wind turbine: now including vibration data from the blades. In *Proceedings of 5<sup>th</sup> International Operational Modal Analysis Conference (IOMAC)*, Guimaraes, Portugal, 2013. pages 40
- [42] E. Di Lorenzo, S. Manzato, B. Peeters, and F. Marulo. Structural health monitoring techniques applied to operating wind turbines. In *Proceedings of 9<sup>th</sup> International Conference on Structural Dynamics*, Porto, Portugal, 2014. pages 40

- [43] H. Stiesdal. Extreme Wind Loads on Stall-Regulated wind Turbines. In *Proceedings of 16<sup>th</sup> British Wind Energy Association Conference*, 1994. pages 45
- [44] M.H. Hansen, K. Thomsen, and J.T. Petersen. Rotor Whirling Modes and Their Relation to Their Aerodynamic Damping. In *Proceedings of European Wind Energy Conference*, Copenhagen, Denmark, 2001. pages 45
- [45] J.T. Petersen, K. Thomsen, and H. Madsen. Local Blade Whirl and Global Rotor Whirl. Technical Report R-1067, Riso National Laboratory, Roskilde, Denmark, 1998. pages 45
- [46] J.T. Petersen, H. Madsen, P. Bjorck, A. Enevoldsen, S. Oye, H. Ganader, and D. Winkelaar. Prediction of Dynamic Loads and Induced Vibrations in Stall. Technical Report R-1045, Riso National Laboratory, Roskilde, Denmark, 1998. pages 45
- [47] J. Jonkman, S. Butterfield, W. Musial, and G. Scott. Definition of a 5-MW Reference Wind Turbine for Offshore System Development. Technical Report TP-500-38060, NREL National Laboratory, USA, 2009. pages 50, 63
- [48] C. Bak, F. Zahle, R. Bitsche, T. Kim, A. Yde, L.C. Henriksen, A. Natarajan, and M.H. Hansen. Description of the DTU 10 MW reference wind turbine. Technical Report I-0092, Riso National Laboratory, Roskilde, Denmark, 2013. pages 50, 63
- [49] G. Kosova. Operational Modal Analysis of Wind Turbines in Rotating Conditions. Master's thesis, University of Naples, Department of Aerospace Engineering, 2015. pages 50
- [50] R.J. Allemang. *Investigation of Some Multiple Input-Output Frequency Response Function Experimental Modal Analysis Techniques*. PhD thesis, University of Cincinnati, Department of Mechanical Engineering, 1980. pages 56
- [51] P. Agarwal and L. Manuel. Simulation of Offshore Wind Turbine Response for Extreme Limit States. In *Proceedings of 26<sup>th</sup> International Conference on Offshore Mechanics and Arctic Engineering*, San Diego, CA, USA, 2007. pages 65
- [52] G.R. Fulton, D.J. Malcolm, and E. Moroz. Design of a Semi-Submersible Platform for a 5MW Wind Turbine. In *Proceedings of 44<sup>th</sup> AIAA Aerospace Sciences Meeting and Exhibition*, Reno, NV, USA, 2006. pages 65

- [53] J. Jonkman. *Dynamics Modeling and Loads Analysis of an Offshore Floating Wind Turbine*. PhD thesis, University of Colorado, Department of Aerospace Engineering Sciences, USA, 2007. pages 65
- [54] J.C. Kaimal, J.C. Wyngaard, Y Izumi, and R.O. Cote. Spectral characteristics of surface layer turbulence. *Journal of the meteorological society*, 98(417):563–589, 1972. pages 66
- [55] U. Musella. Design and Operational Modal Analysis of a New 10-MW Offshore Wind Turbine. Master's thesis, University of Naples, Department of Aerospace Engineering, 2015. pages 80
- [56] G. James. Development of Structural Health Monitoring techniques using dynamic testing. Technical Report 960810, SANDIA National Laboratories, Albuquerque, NM, USA, 1996. pages 92
- [57] K. Worden, C.R. Farrar, J. Haywood, and M. Todd. A review of nonlinear dynamics applications to structural health monitoring. *Structural Control Health Monitoring*, 15(4):540–567, 2007. pages 92
- [58] B. Hahn, M. Durstewitz, and K. Rohrig. Reliability of wind turbines. In *Wind Energy: Proceedings of the Euromech Colloquium*, 2007. pages 92
- [59] D. Adams, J. White, M. Rumsey, and C.R. Farrar. Structural health monitoring of wind turbines: method and application to a HAWT. *Wind Energy*, 4:603–623, 2011. pages 92, 97
- [60] H.N. Li, D.S. Li, and G.B. Song. Recent applications of fiber optic sensors to health monitoring in civil engineering. *Engineering Structures*, 26(11):1647–1657, 2004. pages 93
- [61] C.R. Farrar and K. Worden. An introduction to structural health monitoring. *Philosophical Transactions of the Royal Society*, 365(1851):303–315, 2007. pages 93
- [62] J. Shieh, J.E. Huber, N.A. Fleck, and M.F. Ashby. The selection of sensors. *Progress in Material Science*, 46:461–504, 2001. pages 93
- [63] B.F. Sorensen, L. Lading, P. Sendrup, M. McGugan, C.P. Debel, O.J.D. Kristensen, G. Larsen, A.M. Hansen, J Rheinlander, J. Rusborg, and J.D. Vestergaard. Fundamentals for remote structural health monitoring of wind turbine blades. Technical Report R-1336, Riso National Laboratory, Roskilde, Denmark, 2002. pages 93
- [64] P. Joosse, M. Blanch, A. Dutton, A.G. Kouroussis, T.P. Philippidis, and P.S. Vionis. Acoustic Emission Monitoring of Small Wind Turbine Blades. *Journal of Solar Energy Engineering*, 124(4):446–454, 2002. pages 96

- [65] H. Sutherland, A. Beattle, B. Hansche, W. Musial, J. Allread, J. Johnson, and M. Summers. The Application of Non-Destructive Techniques to the Testing of a Wind Turbine Blade. Technical Report 931380, SANDIA National Laboratories, Albuquerque, NM, USA, 1994. pages 96, 97
- [66] A. Ghoshal, M.J. Sundaresan, M.J. Schulz, and P.F. Pai. Structural health monitoring techniques for wind turbine blades. *Journal of Wind Engineering and Industrial Aerodynamics*, 85:309–324, 2000. pages 96, 97
- [67] M.A. Rumsey and J.A. Paquette. Structural health monitoring of wind turbine blades. In *Proceedings SPIE*, volume 6933, 2008. pages 96, 97
- [68] K. Roy and S. Ray-Chaudhuri. Fundamental mode shape and its derivatives in structural damage localization. *Journal of Sound and Vibration*, 332:5584–5593, 2013. pages 96
- [69] A.K. Pandey and M. Biswas. Damage detection from changes in curvature mode shapes. *Journal of Sound and Vibration*, 145:321–332, 1991. pages 96
- [70] R.P.C. Sampaio, N.M. Maia, and J.M.M. Silva. Damage detection in structures from mode shape to frequency response function methods. *Journal of Sound and Vibration*, 226:1029–1042, 1999. pages 96
- [71] M.P. Limongelli. Frequency response function interpolation for damage detection under changing environment. *Mechanical Systems and Signal Processing*, 24:2898–2913, 2010. pages 96
- [72] K. Schroeder, W. Ecke, J. Apitz, E. Lembke, and G. Lenschow. A fibre Bragg grating sensor system monitors operational load in a wind turbine rotor blade. *Measurement Science and Technology*, 17(5):1167–1172, 2006. pages 97
- [73] B. Peeters and G. De Roeck. One-year monitoring of the Z24-Bridge: environmental effects versus damage events. *Earthquake Engineering and Structural Dynamics*, 30:149–171, 2001. pages 97
- [74] Loya J., L. Rubio, and J. Fernandez-Saez. Natural frequencies for bending vibrations of Timoshenko cracked beams. *Journal of Sound and Vibration*, 290:640–653, 2006. pages 101
- [75] Davini C., A. Morassi, and N. Rovere. Modal analysis of notched bars: tests and comments on the sensitivity of an identification technique. *Journal of Sound and Vibration*, 179(3):402–416, 1995. pages 101
- [76] O. Salawu. Detection of structural damage through changes in frequency: a review. *Engineering Structures*, 19(9):718–723, 1997. pages 101

- [77] A. Cutolo. Operational Modal Analysis for Structural Health Monitoring of a Wind Turbine Blade. Master's thesis, University of Naples, Department of Aerospace Engineering, 2015. pages 104
- [78] R.L. Bielawa. Rotary wing structural dynamics and aeroelasticity. *AIAA Educational Series*, 1992. pages 120
- [79] M. Reymond. DMAP Programmer's guide. Technical Report 10113, MSC Software, 2013. pages 122
- [80] J. Blough. *Improving the analysis of operating data on rotating automotive components*. PhD thesis, University of Cincinnati, USA, 1998. pages 127
- [81] J. Blough, D.L. Brown, and H. Vold. The time variant discrete Fourier transform as an order tracking method. In *Proceedings of Society of Automotive Engineers Noise and Vibration Conference, SAE paper number 972006*, 1997. pages 138
- [82] M.R. Kang and A. Kahraman. Measurement of vibratory motions of gears supported by compliant shafts. *Mechanical Systems and Signal Processing*, 29:391–403, 2012. pages 147
- [83] A. Kahraman and G.W. Blankenship. Experiments on nonlinear dynamic behavior of an oscillator with clearance and periodically time-varying parameters. *Journal of Applied Mechanics*, 64:217–226, 1997. pages 148
- [84] D.J. Croasmun. Development of an integrated encoder and accelerometer-Based gear transmission error measurement methodology. Master's thesis, University of Toledo, Columbus, Ohio, USA, 2002. pages 148
- [85] Identifying best practices for measuring and analyzing torsional vibration. Technical Report White paper, Siemens PLM Software, 2016. pages 153
- [86] K. Janssens, P. Van Vlierberghe, P. D'Hondt, T. Martens, B. Peeters, and W. Claes. Zebra tape butt joint algorithm for torsional vibrations. In *Proceedings of 28<sup>th</sup> International Modal Analysis Conference (IMAC)*, Orlando, FL, USA, 2010. pages 158, 233
- [87] A. Palermo, J. Anthonis, D. Mundo, and W. Desmet. A novel gear test rig with adjustable shaft compliance and misalignments. Part I: Design. and Part II: Instrumentation. In *Proceedings of the 3<sup>rd</sup> International Conference on Condition Monitoring of Machinery in Non-Stationary Operations (CMMNO)*, Ferrara, Italy, 2013. pages 198
- [88] A. Palermo, A. Toso, G.H.K. Heirman, R. Cerda, M. Gulinelli, D. Mundo, and W. Desmet. Structural coupling and non-linear effects in the



- experimental modal analysis of a precision gear test rig. In *Proceedings of the International Gear Conference*, Lyon, France, 2014. pages 198
- [89] S. Goris, F. Vanhollebeke, A. Ribbentrop, M. Markiewicz, L. Schneider, S. Wartzack, W. Hendrickx, and W. Desmet. A validated virtual prototyping approach for avoiding wind turbine tonality. In *Proceedings of 5<sup>th</sup> International Conference on Wind Turbine Noise*, Denver, USA, 2013. pages 228
- [90] J. Helsen. *The dynamics of high power density gear units with focus on the wind turbine application*. PhD thesis, KU Leuven, Leuven, Belgium, 2012. pages 228
- [91] B. Marrant. Validation of MBS Multi-Megawatt Gearbox Models on a 13.2 MW Test Rig. Technical report, SIMPACK newsletter, 2012. pages 228
- [92] S. Manzato, E. Di Lorenzo, A. Medici, F. Vanhollebeke, B. Peeters, and W. Desmet. Order Based Modal Analysis vs. standard techniques to extract modal parameters of operational wind turbine gearboxes. In *Proceedings of 33<sup>rd</sup> International Modal Analysis Conference (IMAC)*, Orlando, FL, USA, 2015. pages 231



# Curriculum vitae

Emilio Di Lorenzo  
18<sup>th</sup> February 1987, Naples, Italy  
dilorenzo.emilio@gmail.com

## Education

*November 2012 - April 2017*

PhD candidate in a Joint doctoral program in:

- Engineering Science, Department of Mechanical Engineering, KU Leuven, Belgium
- Aerospace, Naval and Quality Engineering, Department of Industrial Engineering, University of Naples "Federico II", Italy

*September 2008 - May 2012*

M.Sc. Aerospace and Astronautic Engineering, University of Naples "Federico II", Italy, *110/110 cum laude*

Thesis title: "Virtual shaker testing: Sine controller application"

*September 2009 - September 2010*

Erasmus student in Aerospace Engineering, Institute Polytechnique des Sciences Avancées (IPSA), Paris, France

*September 2005 - September 2008*

B.Sc. Aerospace Engineering, University of Naples "Federico II", Italy, *110/110 cum laude*

Thesis title: "Prestazioni ed utilizzo applicativo di sensori elettroottici aviotrasportati"

*September 2000 - May 2005*

Scientific High School, Mondragone, Italy, *100/100*

## **Professional Experiences**

*November 2012 - ...*

Research Engineer, Siemens Industry Software NV, Leuven, Belgium

*September 2011 - March 2012*

Trainee, LMS International, Leuven, Belgium

*March 2010 - September 2010*

Trainee, Office National d'études et de recherches aérospatiales (ONERA), Chatillon, France

## **Awards**

Special mention by the Head of the Engineering faculty as one of the best bachelor graduates in 2008 at the Engineering faculty of the University of Naples "Federico II"

# List of publications

## Articles in international journals

1. E. Di Lorenzo, S. Manzato, B. Peeters, H. Van der Auweraer. Virtual structural health monitoring of wind turbines using Operational Modal Analysis techniques. *Key Engineering Materials*, 569:523-530, 2013
2. F. Vanhollebeke, P. Peeters, J. Helsen, E. Di Lorenzo, S. Manzato, J. Peeters, W. Desmet. Large scale validation of a flexible multibody wind turbine gearbox model. *Journal of Computational and Nonlinear Dynamics*, 10(4), 041006, 2015.
3. E. Di Lorenzo, G. Kosova, U. Musella, S. Manzato, B. Peeters, F. Marulo, W. Desmet. Structural health monitoring challenges on the 10-MW offshore reference wind turbine model. *Journal of Physics: Conference Series*, 628 012081, 2015.
4. E. Di Lorenzo, G. Petrone, S. Manzato, B. Peeters, W. Desmet, F. Marulo. Damage detection in wind turbine blades by using Operational Modal Analysis. *Structural Health Monitoring*, 15:289-301, 2016.

## Book chapter

1. E. Di Lorenzo, S. Manzato. Experimental characterization of wind turbine gearbox in operation. *MARE-WINT: New Materials and Reliability in Offshore Wind Turbine Technology*, 147-166, 2016.

## Articles in international conference proceedings

1. E. Di Lorenzo, S. Manzato, B. Peeters, H. Van der Auweraer. Virtual assessment of damage detection techniques for operational wind turbine.

- In *Proceedings of 3<sup>rd</sup> International Conference on Condition Monitoring of Machinery in Non-Stationary Operations (CMMNO 2013)*, Ferrara, Italy, May 2013
2. E. Di Lorenzo, S. Manzato, B. Peeters. Virtual assessment of structural health monitoring techniques for wind turbines using vibration data. In *Proceedings of 9<sup>th</sup> International Workshop on Structural Health Monitoring (IWSHM 2013)*, Stanford, CA, USA, September 2013.
  3. E. Di Lorenzo, S. Manzato, J. Houben, F. Vanhollebeke, S. Goris, B. Peeters. Wind turbine gearbox dynamic characterization using Operational Modal Analysis. In *Proceedings of 32<sup>nd</sup> International Modal Analysis Conference (IMAC 2014)*, Orlando, FL, USA, February 2014.
  4. S. Manzato, C. Devriendt, W. Weijtjens, E. Di Lorenzo, B. Peeters, P. Guillaume. Removing the influence of rotor harmonics for improved monitoring of offshore wind turbines. In *Proceedings of 32<sup>nd</sup> International Modal Analysis Conference (IMAC 2014)*, Orlando, FL, USA, February 2014.
  5. E. Di Lorenzo, S. Manzato, B. Peeters, F. Marulo. Structural health monitoring techniques applied to operating wind turbines. In *Proceedings of 9<sup>th</sup> International Conference on Structural Dynamics (EURODYN 2014)*, Porto, Portugal, July 2014.
  6. E. Di Lorenzo, S. Manzato, B. Peeters, F. Marulo. Modal parameter estimation for operational wind turbines. In *Proceedings of 7<sup>th</sup> European Workshop on Structural Health Monitoring (EWSHM 2014)*, Nantes, France, July 2014.
  7. F. Marulo, G. Petrone, V. D'Alessandro, E. Di Lorenzo. Operational modal analysis on a wind turbine blade. In *Proceedings of 26<sup>th</sup> International Conference on Noise and Vibration Engineering (ISMA 2014)*, Leuven, Belgium, September 2014.
  8. E. Di Lorenzo, S. Manzato, F. Vanhollebeke, S. Goris, B. Peeters, W. Desmet, F. Marulo. Dynamic characterization of wind turbine gearboxes using Order-Based Modal Analysis. In *Proceedings of 26<sup>th</sup> International Conference on Noise and Vibration Engineering (ISMA 2014)*, Leuven, Belgium, September 2014.
  9. E. Di Lorenzo, S. Manzato, F. Vanhollebeke, S. Goris, B. Peeters, W. Desmet, F. Marulo. Dynamic characterization of wind turbine gearboxes in operational conditions. In *Proceedings of 9<sup>th</sup> International Conference on Rotor Dynamics (IFTToMM 2014)*, Milan, Italy, September 2014.

10. S. G. Horcas, E. Di Lorenzo, J. Martinez, R. Mehdi, D. Mehta, G. Pereira, R. Soman. MARE-WINT: New Materials and Reliability in Offshore Wind Turbines Technology. In *Proceedings of 10<sup>th</sup> EAWE PhD Seminar on Wind Energy in Europe*, Orléans, France, October 2014.
11. S. Manzato, E. Di Lorenzo, A. Medici, F. Vanhollebeke, B. Peeters, W. Desmet. Order Based Modal Analysis vs. standard techniques to extract modal parameters of operational wind turbine gearboxes. In *Proceedings of 33<sup>rd</sup> International Modal Analysis Conference (IMAC 2015)*, Orlando, FL, USA, February 2015.
12. E. Di Lorenzo, S. Manzato, B. Peeters, F. Vanhollebeke, W. Desmet, F. Marulo. Order-based modal analysis: a modal parameter estimation technique for rotating machineries. In *Proceedings of 6<sup>th</sup> International Operational Modal Analysis Conference (IOMAC 2015)*, Spain, May 2015.
13. F. Marulo, G. Petrone, E. Di Lorenzo, A. Cutolo. Operational modal analysis for SHM of a wind turbine blade. In *Proceedings of 7<sup>th</sup> International Conference on Structural Health Monitoring of Intelligent Infrastructure (SHMII 2015)*, Turin, Italy, July 2015.
14. E. Di Lorenzo, S. Manzato, B. Peeters, F. Marulo, W. Desmet. Structural health monitoring considerations on offshore wind turbine models. In *Proceedings of 10<sup>th</sup> International Workshop on Structural Health Monitoring (IWSHM 2015)*, Stanford, CA, USA, September 2015.
15. E. Di Lorenzo, A. Palermo, S. Manzato, A. Dabizzi, B. Peeters, W. Desmet, F. Marulo. Gear dynamics characterization by using Order-Based Modal Analysis. In *Proceedings of 34<sup>th</sup> International Modal Analysis Conference (IMAC 2016)*, Orlando, FL, USA, January 2016.
16. M. Choukri, S. Manzato, E. Di Lorenzo, B. Peeters, J. Lau. Estimation of operational modal parameters of a vehicle from transient run up engine data. *Society of Automotive Engineers of Japan*, Yokohama, Japan, May 2016.
17. E. Di Lorenzo, S. Manzato, A. Dabizzi, F. Vanhollebeke, B. Peeters, F. Marulo, W. Desmet. Order-Based Modal Analysis: a technique for estimating the modal parameters in the rotating machinery field. In *Proceedings of 27<sup>th</sup> International Conference on Noise and Vibration Engineering (ISMA 2016)*, Leuven, Belgium, September 2016.
18. A. Dabizzi, G. H. K. Heirman, A. Palermo, S. Manzato, E. Di Lorenzo, S. Shweiki, A. Toso. Multibody modeling of a high precision gear test rig and correlation to experiments. In *Proceedings of 27<sup>th</sup> International*

*Conference on Noise and Vibration Engineering (ISMA 2016)*, Leuven, Belgium, September 2016.

19. E. Di Lorenzo, S. Manzato, B. Peeters, F. Marulo, W. Desmet. Best practices for using Order-Based Modal Analysis for industrial applications. In *Proceedings of 35<sup>th</sup> International Modal Analysis Conference (IMAC 2017)*, Garden Grove, CA, USA, January 2017.

### **Abstracts in international conference proceedings**

1. E. Di Lorenzo, S. Manzato, B. Peeters, F. Marulo, W. Desmet. Operational Modal Analysis for rotating machines: challenges and solutions. *7<sup>th</sup> International Operational Modal Analysis Conference (IOMAC 2017)*, Ingolstadt, Germany, May 2017.
2. E. Di Lorenzo, S. Manzato, B. Peeters, F. Marulo, W. Desmet. Structural Health Monitoring strategies based on the estimation of modal parameters. *10<sup>th</sup> International Conference on Structural Dynamics (EURODYN 2017)*, Rome, Italy, September 2017.
3. E. Di Lorenzo, S. Manzato, B. Peeters, F. Marulo, W. Desmet. Structural Health Monitoring techniques for detecting wind turbine rotor faults. *35<sup>th</sup> International Conference on Structural Engineering Dynamics (ICEDYN 2017)*, Ericeira, Portugal, July 2017.





FACULTY OF ENGINEERING SCIENCE  
DEPARTMENT OF MECHANICAL ENGINEERING  
NOISE & VIBRATION RESEARCH GROUP  
Celestijnenlaan 200A box 2402  
B-3001 Leuven  
<https://www.mech.kuleuven.be/en/research/mod>

